

Injection and Separation Evaluation for Microfluidic Protein and DNA Separation

by

Pegah Pezeshkpour

A thesis
presented to the University of Waterloo
in fulfillment of the
thesis requirement for the degree of
Doctor of Philosophy
in
Mechanical and Mechatronics Engineering

Waterloo, Ontario, Canada, 2018

© Pegah Pezeshkpour 2018

Examining Committee Membership

The following served on the Examining Committee for this thesis. The decision of the Examining Committee is by majority vote.

| | |
|--------------------------|--|
| External Examiner | NAME: Neelesh Patankar TITLE: Professor, Mechanical Engineering |
| Supervisor(s) | NAME: Gerry Schneider TITLE: Professor, Mechanical Engineering NAME: Carolyn Ren TITLE: Professor, Mechanical Engineering |
| Internal Member | NAME: Fue-Sang Lien TITLE: Professor, Mechanical Engineering |
| Internal Member | NAME: Sean Peterson TITLE: Professor, Mechanical Engineering |
| Internal-external Member | NAME: Marios Ioannidis TITLE: Professor, Chemical Engineering |

AUTHOR'S DECLARATION

I hereby declare that I am the sole author of this thesis. This is a true copy of the thesis, including any required final revisions, as accepted by my examiners.

I understand that my thesis may be made electronically available to the public.

Abstract

Electrophoresis is the separation of charged particles under an applied electric field and is applied for macromolecules such as DNA, proteins, RNA and peptides through a solvent. It has been one of the most widely used analytical separation techniques since the early 1900s. Traditionally, capillary zone electrophoresis and gel electrophoresis have been used in laboratories, however, with the advent of the Lab-on-a-Chip (LOC) and the Micro Total Analysis System (μ TAS) concepts in the early 1990s, the focus has been on shrinking the entire laboratory with all its functions onto a microchip. The miniaturization of traditional, cumbersome laboratory equipment onto microchip devices offers the potential for decreased analysis times, reduced sample volumes, reduced operating and manufacturing costs, as well as portability. However, such downsizing necessitates a fundamental study of microscale fluid transport, microchip design, channel geometries, and sample manipulation and detection methods.

This thesis reports theoretical and numerical investigations into microfluidic transport in protein and DNA separation. The thesis begins with a background chapter about electrophoresis, reviewing the fundamentals concepts of operation in microchannels. Different chip designs and electric potential configurations are discussed as well as the concepts of electroosmotic and electrophoretic velocities, diffusivity, and separation resolution.

Next, the dimensional problem formulation is provided for a basic cross-linked chip, including an injection and a separation channel by assuming slip boundary conditions on the channel walls. This assumption is made after considering the details of the ion distribution in the electric double layer (EDL) adjacent to the walls as provided by the detailed derivation of the Poisson-Boltzmann equation from a statistical approach as presented in Appendix A. The non-dimensional formulation of the problem, as determined in Appendix B, was used to guide the numerical simulations and further analysis, using two numerical tools: Ansys CFX 15.0 and Matlab R2017.

With the significant role that sample plug shape and size play, with regard to separation, the quality of the sample was investigated. A model was developed for evaluating the sample shape and size at the intersection of the injection and separation channels of cross-linked microchannels. A shape factor was developed to quantify the sample plug shape and size. A variety of sample plug shapes was analyzed and criteria to assess the sample plug were identified. Higher quality sample plugs result in increased separation resolution and this is predominantly possible when a rectangular sample plug is achieved at injection.

A new definition of the separation resolution was developed which considers the detector sensitivity and the peak-to-valley magnitude of the sample species concentration. In the conventional definition of resolution, a significant distance between the adjacent peaks of concentration graphs, relative to the sum of peak half-widths, represents good separation. However, such a definition ignores the drop from the initial sample concentration, which plays a significant role in identification of sample peaks. Therefore, a new factor, the ratio of peak-to-valley magnitude to the detector sensitivity, is introduced. This modified resolution represents a clearer demonstration of resolving sample constituents and shows resolution improvement.

The grid independence and validation studies were performed to validate the numerical predictions with results available in the literature. For the spatial grids, the grid at the $50 \times 50 \mu\text{m}^2$ cross, in the primary design, was examined from a coarse mesh of 10×10 cells to 60×60 cells. The results show that the numerical solution for three electric, flow and concentration fields are grid independent when the cross has 40×40 mesh cells within 0.5% error, second order accuracy. For the transient concentration field, the time scale was examined from 0.01s to 0.0005s. The solution was independent of the temporal step when the time step was 0.001s with 0.35%, first order accuracy. The spatial and temporal grid-independent results were validated with experimental results in the literature for the injection of a single constituent sample. The validation demonstrated the accuracy of the implemented numerical simulations and showed promising results for further analysis of injection and separation.

Having established a confident numerical model, results are then presented providing more analysis for electric potential configurations at injection and separation. The basic geometry is modified to a new design with channels of equal lengths and a reduced width of the separation channel to 50% of that of the original. Further, it was discovered that under certain conditions a steady-state sample plug shape is formed at the cross; this revelation led to a two-step injection procedure that was subsequently implemented for injecting the sample plug to the separation channel. Different separation configurations are studied for this procedure and results show an improved separation resolution, by both the conventional and modified definitions. With the high quality sample achieved, the effect of potentials at the side reservoirs of separation channel was studied for separation. The results show increasing these potentials to 25% – 40% of the driving potential for separation increases the resolution.

Conclusions are drawn in the final chapter with regard to the contributions made and development activities taken during the course of this research. With the modified chip design including

channels of equal lengths and a narrowed separation channel, and by implementing the two-step injection procedure, the ideal rectangular plug was achieved. The separation resolution was improved by the two-step process and thresholds of potential configurations at separation for achieving higher resolution were identified.

Acknowledgements

I would like to take this opportunity to thank the many people who helped me during the course of my Ph.D. research and study.

First and foremost, I would like to thank my supervisors Professor Gerry Schneider and Professor Carolyn Ren. I am deeply grateful to Prof. Schneider who accepted me as his student, supported me, and patiently guided me to grow into a better researcher. I have learned so much from you. You taught me the significance of the fundamentals and to improve my critical thinking skills. I would also like to express my gratitude to Prof. Ren, for her advice throughout this study, for encouraging women in engineering and for teaching me to have a big picture of the problem. You taught me to have passion for research, ahead-of-time planning and the importance of applications.

I hereby acknowledge my thesis examining committee members, Professor Neelesh Patankar from Northwestern University, Professor Sean Peterson, Professor Fu-Sang Lien and Professor Marios Ioannidis, from University of Waterloo.

I would never have had the opportunity to do this research if it was not for the generous support of Natural Resources and Engineering Research Council (NSERC), University of Waterloo Graduate Scholarships, Ontario Graduate Scholarship (OGS) and UW President's Graduate Scholarship (PGS).

I am deeply grateful to my family and friends whose support is truly appreciated. I would specially thank to my husband Ehsan Hashemi whose love and support was always encouraging. You were a good company along this bumpy road and made great discussions in our after-meeting coffee time. Special thanks to my heart, my son Bardia who gave me the chance of improving my time-management skills. I appreciate your understanding of the busy world of a PhD-student mom.

I am very grateful to my parents who did their best to pave my way to success, to my late father who watches me from the other world, to my dear mom who has been devoting her life to her children, and to my dearest sister Pantea for her unlimited love and support. Many thanks to UW microfluidic lab members, Dr. Cody Chen, Dr. Ning Qin, Dr. Pei Zhao, Anna Nguyen, Marie Hebert and Matt Courtney for their great discussions in our group meetings. I would also like to extend thanks to Mary McPherson at UW Writing and Communication Center for patiently helping me to revise this thesis.

Dedicated to my beloved ones, Ehsan and Bardia

Table of Contents

| | |
|---|-----|
| Examining Committee Membership | ii |
| AUTHOR'S DECLARATION..... | iii |
| Abstract | iv |
| Acknowledgements | vii |
| List of Figures | xi |
| List of Tables..... | xiv |
| Chapter 1 | 1 |
| 1.1 Introduction..... | 1 |
| 1.2 Research Motivation..... | 1 |
| 1.3 Research Objectives..... | 2 |
| 1.4 Thesis Outline..... | 2 |
| Chapter 2 Background..... | 5 |
| 2.1 Literature Review | 5 |
| 2.1.1 Electrophoretic Separation | 9 |
| 2.1.2 Capillary Electrophoresis | 10 |
| 2.1.3 Microfluidic Separation Chips | 11 |
| 2.2 Electroosmotic and electrophoretic mobilities..... | 18 |
| 2.3 Diffusivity..... | 22 |
| 2.4 Separation Resolution..... | 23 |
| 2.4.1 Detection methods..... | 25 |
| 2.4.2 Ways to improve limits of detection and flow visualization..... | 26 |
| 2.5 Other Techniques to Couple with Electrophoresis | 27 |
| Chapter 3 Problem Formulation | 32 |
| 3.1 Introduction..... | 32 |
| 3.2 Chip Configuration | 32 |
| 3.3 Problem Formulation, Dimensional Governing Equations and Boundary Conditions..... | 33 |
| 3.3.1 Electric Field Equation..... | 33 |
| 3.3.2 Flow Field Equations | 34 |
| 3.3.3 Concentration Field Equation..... | 36 |
| 3.3.4 Energy Equation..... | 37 |
| 3.4 Conclusions..... | 39 |

| | |
|---|-----|
| Chapter 4 Injection and Separation Evaluation | 41 |
| 4.1 Introduction..... | 41 |
| 4.2 Literature Review | 42 |
| 4.3 Shape Factor Introduction..... | 42 |
| 4.3.1 Development of a Shape Factor-Guiding Principles | 44 |
| 4.3.2 Conclusion for the Shape Factor Value..... | 55 |
| 4.3.3 Assessment of Shape Factor Model with Experiments in Literature | 56 |
| 4.3.4 Injection and Separation of 5 Cases | 58 |
| 4.3.5 Time to stop injection..... | 60 |
| 4.4 Assessment of Resolution | 65 |
| 4.4.1 Solution to Concentration Equation for a Finite Body..... | 65 |
| 4.4.2 Detection Sensitivity, Peak to Valley factor | 66 |
| 4.5 Conclusions..... | 69 |
| Chapter 5 Validation and Analysis..... | 70 |
| 5.1 Introduction..... | 70 |
| 5.2 Convergence Study | 70 |
| 5.3 Validation | 78 |
| 5.4 Injection and Separation Analysis | 79 |
| 5.4.1 Modified Geometry | 79 |
| 5.4.2 Injection Configurations for the Final Geometry | 81 |
| 5.4.3 Comparison among Different ϕ_{inj} * Configurations | 92 |
| 5.4.4 Separation Configurations..... | 92 |
| 5.4.5 Modified Injection Procedure..... | 97 |
| 5.4.6 Separation of the modified injection ($\Phi_{inj1} *= 1, \Phi_{inj2} *= 0.5$) | 99 |
| 5.5 Conclusions..... | 113 |
| Chapter 6 Conclusions and Recommendations | 115 |
| 6.1 Contributions of This Thesis..... | 115 |
| 6.2 Recommendations for Extension of Work..... | 118 |
| Letters of Copyright Permissions' | 120 |
| References | 124 |
| Appendix A- EDL and Poisson-Boltzmann Equation in Microfluidics | 138 |
| Appendix B-Non-Dimensionalization of Problem and Numerical Model Formulation..... | 167 |

List of Figures

| | |
|--|----|
| FIGURE 1: CONVENTIONAL GEL ELECTROPHORESIS (WIKIMEDIA)..... | 9 |
| FIGURE 2: SCHEMATIC OF CAPILLARY ELECTROPHORESIS | 10 |
| FIGURE 3: SAMPLE CHIP CONFIGURATION FOR ELECTROPHORETIC SEPARATION | 11 |
| FIGURE 4: SCHEMATIC OF INJECTION AND SEPARATION IN CROSS-LINKED CHANNELS; S: SAMPLE, B: BUFFER, SW: SAMPLE WASTE, AND BW: BUFFER WASTE..... | 11 |
| FIGURE 5: ELECTRIC DOUBLE LAYER(EDL) IN MICROCHANNELS | 13 |
| FIGURE 6: DRIVING FORCE IN ELECTRIC DOUBLE LAYER (EDL)..... | 14 |
| FIGURE 7: SCHEMATIC OF CHANNEL GEOMETRIES (SOLID ARROWS: INJECTION AND DASHED ARROWS: SEPARATION) | 15 |
| FIGURE 8: SCHEMATIC OF VOLTAGE-CONTROLLED CONFIGURATIONS, S: SAMPLE, SW: SAMPLE WASTE, B: BUFFER, BW: BUFFER WASTE; SOLID ARROWS: SAMPLE, DOTTED ARROWS: BUFFER..... | 17 |
| FIGURE 9: SCHEMATIC OF SEPARATION OF SAMPLE COMPONENTS DUE TO THEIR DIFFERENT ELECTROPHORETIC MOBILITIES | 18 |
| FIGURE 10: THE BALANCE OF ELECTRICAL AND VISCOUS FORCES ON A PARTICLE..... | 18 |
| FIGURE 11: COMPARISON OF VARIOUS BIOLOGICAL ASSEMBLIES AND TECHNOLOGICAL DEVICES | 19 |
| FIGURE 12: CHARGE TO SIZE RATIO IS THE PRINCIPLE OF THE ELECTROPHORETIC SEPARATION | 20 |
| FIGURE 13: VELOCITY PROFILES OF EOF VERSUS PRESSURE DRIVEN FLOW | 21 |
| FIGURE 14: OBSERVED VELOCITY AS THE RESULT OF ELECTROOSMOTIC AND ELECTROPHORETIC VELOCITIES | 21 |
| FIGURE 15: PRINCIPLE OF THE ELECTROOSMOTIC MEASUREMENT WITH CURRENT MONITORING METHOD (1 μ A CURRENT \rightarrow 10mV VOLTAGE DROP) [75] | 22 |
| FIGURE 16: DEFINITION OF RESOLUTION FOR TWO ADJACENT PEAKS | 23 |
| FIGURE 17: PEAK OVERLAPS FOR A GAUSSIAN DISTRIBUTION IN RESOLUTIONS OF 1 AND 1.5..... | 24 |
| FIGURE 18: SCHEMATIC OF CAPILLARY ELECTROPHORESIS VS. FREE-FLOW ELECTROPHORESIS | 28 |
| FIGURE 19: SCHEMATIC OF FIELD-AMPLIFIED SAMPLE STACKING (FASS) TECHNIQUE TO INCREASE THE CONCENTRATION OF SAMPLE [102] | 29 |
| FIGURE 20: ISOTACHOPHORESIS | 30 |
| FIGURE 21: ISOELECTRIC FOCUSING (IEF)..... | 30 |
| FIGURE 22: CROSS-CHANNEL GEOMETRY OF THE MICROCHIP..... | 32 |
| FIGURE 23: EDL BOUNDARY CONDITIONS..... | 35 |
| FIGURE 24: HEAT TRANSFER FROM FLUID IN MICROCHANNEL..... | 37 |
| FIGURE 25: POSSIBLE SAMPLE PLUG SHAPES AT THE CROSS | 43 |
| FIGURE 26: SAMPLE PLUG SHAPE OPTIMIZATION | 43 |
| FIGURE 27: A SAMPLE CONCENTRATION CONTOUR FOR A HORIZONTAL INJECTION | 44 |
| FIGURE 28 : DIFFERENT SHAPES AT THE TOP-HALF OF SAMPLE PLUG AT THE CROSS ($A_0 = 1$) | 47 |
| FIGURE 29 : DIFFERENT SHAPES BASED ON ASCENDING Σ IN ROWS, ROW-COLUMN BOX NUMBERS FROM FIGURE 28... | 48 |
| FIGURE 30 : MORE SHAPES WITH $0 \leq \Sigma \leq 0.2$ | 51 |
| FIGURE 31: TRENDS OF ASCENDING Σ , S_{Y1} , S_{Y2} AND S_Y FOR 50 DIFFERENT SHAPES | 52 |
| FIGURE 32: TRENDS OF ASCENDING Σ AND $S_Y = 1.7 \Sigma$ FOR 50 DIFFERENT SHAPES..... | 52 |
| FIGURE 33: ZOOM OF TRENDS FOR ASCENDING Σ [$0 \leq \Sigma \leq 0.2$], S_{Y1} , S_{Y2} AND S_Y | 53 |
| FIGURE 34 : MORE SAMPLE SHAPES OF FIGURE 28 WITH $A_0 = 2$ | 54 |
| FIGURE 35 : EXTRA SAMPLE SHAPES FOR $A_2 = 4$ | 54 |
| FIGURE 36 : LEFT TO RIGHT COMPARISON OF FOUR RANDOM CASES FOR $A_0 = 1$ VS $A_0 = 2$ | 55 |
| FIGURE 37 : EXPERIMENTAL RESULTS OF FU ET AL. [61] FOR VERIFICATION OF SHAPE FACTOR MODEL..... | 56 |
| FIGURE 38 : EXPERIMENTAL RESULTS OF FU ET AL. [61] FOR VERIFICATION OF SHAPE FACTOR MODEL..... | 56 |
| FIGURE 39 : SHAPE FACTOR MODEL ON EXPERIMENTAL RESULTS OF REN ET AL. [111] | 57 |
| FIGURE 40 : SHAPE FACTOR MODEL ON EXPERIMENTAL RESULTS OF BOUSSE ET AL. [30] | 57 |
| FIGURE 41 : SHAPE FACTOR MODEL ON EXPERIMENTAL RESULTS OF CHANG ET AL.[112] | 57 |
| FIGURE 42 : SHAPE FACTOR MODEL ON EXPERIMENTAL RESULTS OF TAYLOR ET AL.[25] | 58 |
| FIGURE 43: GENERAL MAP OF CASES A TO E, APPLIED ELECTRIC FIELDS, SAMPLE PLUG SHAPES AT INJECTION | 59 |
| FIGURE 44: CASE B , TIME FRAMES WHEN THE SAMPLE APPROACHES THE CROSS..... | 60 |
| FIGURE 45 CONFIGURATIONS OF ELECTRIC POTENTIAL AND FIELD APPLIED TO FIVE CASES A TO E | 61 |
| FIGURE 46: CONCENTRATION CONTOURS FOR THE SEPARATION OF FLUORESCEIN AND RHODAMINE IN CASE B | 61 |

| | |
|---|----|
| FIGURE 47: CASE B- SPATIAL SEPARATION GRAPHS FOR c^* AT $t = 1, 2$ AND $4s$ FOR FLUORESCEIN AND RHODAMINE ALONG SEPARATION CHANNEL AT $y = 0.025, 0, -0.025 \text{ mm}$, STOPPED INJECTION TIME: $6.6s$ | 62 |
| FIGURE 48: CASE B- TEMPORAL SEPARATION GRAPHS FOR AVERAGED c^* VS. c^* AT $y = 0.025, 0, -0.025 \text{ mm}$ AT DETECTION SPOTS OF $x = 0.1, 0.2$ AND 0.3 mm | 63 |
| FIGURE 49: HEISLER CHARTS FOR MID-PLANE TEMPERATURE OF A SLAB | 65 |
| FIGURE 50: PEAK TO VALLEY DIFFERENCE | 66 |
| FIGURE 51: CONVENTIONAL RESOLUTION | 68 |
| FIGURE 52: MODIFIED RESOLUTION BASED ON NO THRESHOLD FOR DETECTABILITY AND NORMALIZED DETECTOR SPOT BY CHANNEL WIDTH ($50\mu\text{m}$) | 68 |
| FIGURE 53: MAKING THE MESH FINER FROM 10×10 TO 60×60 AT THE CROSS | 71 |
| FIGURE 54: GRID INDEPENDENCY FOR CENTERLINE ELECTRIC FIELD ALONG INJECTION CHANNEL | 72 |
| FIGURE 55: GRID INDEPENDENCY FOR CENTERLINE VELOCITY ALONG INJECTION CHANNEL | 72 |
| FIGURE 56: TIME-STEP INDEPENDENCY FOR MEDIUM AND FINE GRID SIZES 20×20 (LEFT) AND 60×60 (RIGHT) | 73 |
| FIGURE 57: SAMPLE CONCENTRATION REGION $C^* \geq 0.5$ (WHITE), $dt = 0.001s$ FOR TWO DIFFERENT GRIDS | 74 |
| FIGURE 58: $x0.5c-1/N, dt = 0.001s$ | 74 |
| FIGURE 59: $x0.5c-1/N2$, AND $dt = 0.001s$ | 74 |
| FIGURE 60: $x0.5c-1/N$, AND $dt = 0.001s$ | 75 |
| FIGURE 61: $x0.5c-1/N2$, AND $dt = 0.001s$ | 75 |
| FIGURE 62: ZOOM OF $x0.5c-1/N$, AND $dt = 0.001s$ | 75 |
| FIGURE 63: ZOOM OF $x0.5c-1/N2$, AND $dt = 0.001s$ | 75 |
| FIGURE 64: TIME STEP CONVERGENCE, $\Delta t = 0.001s$ FOR THE FINEST GRID AT THE CROSS (60×60) | 76 |
| FIGURE 65: ELECTRIC POTENTIAL RMS CONVERGENCE FOR GRIDS 10×10 TO 60×60 AT THE CROSS | 77 |
| FIGURE 66: ELECTRIC POTENTIAL CONVERGENCE ERROR FOR GRIDS 10×10 TO 50×50 AT THE CROSS | 77 |
| FIGURE 67: CHIP CONFIGURATION IN EXPERIMENTS OF REN ET AL. FOR VERIFICATION OF INJECTION MODEL | 78 |
| FIGURE 68: DIRECT EXPERIMENTAL IMAGE OF CONCENTRATION FIELD IN GREY SCALE | 78 |
| FIGURE 69: VERIFICATION OF INJECTION SIMULATION OF A SINGLE-COMPONENT SAMPLE WITH EXPERIMENTS | 79 |
| FIGURE 70: MODIFICATIONS ON CHIP GEOMETRY | 80 |
| FIGURE 71: NEW GEOMETRY OF CHANNELS WITH EQUAL LENGTH AND NARROW SEPARATION CHANNEL | 81 |
| FIGURE 72: CONFIGURATION $\phi_{inj} = 1$ ($\phi = 100V$) | 82 |
| FIGURE 73: ELECTRIC FIELD VECTORS AND FLOW FIELD STREAM LINES ($\phi = 1$) | 82 |
| FIGURE 74: SAMPLE PLUG SHAPES FOR RHODAMINE (1 ST AND 2 ND ROWS) AND FLUORESCEIN (3 RD AND 4 TH ROWS) AT DIFFERENT TIMES FOR TWO CONFIGURATIONS $\phi_{inj} = 1$ AND 0.75 | 83 |
| FIGURE 75: SHAPE FACTORS FOR BOTH CONSTITUENTS AT $\phi = 1$ | 84 |
| FIGURE 76: SAMPLE PLUG SHAPES FOR RH (1 ST AND 2 ND ROWS) AND FL (3 RD AND 4 TH ROWS) AT DIFFERENT TIMES | 85 |
| FIGURE 77: WIDE RHODAMINE SAMPLE PLUG AT $\phi_{inj} = 0.25$ | 86 |
| FIGURE 78: RECTANGULAR PLUG (AT 50% CONTOUR LINE) FOR $\phi_{inj} = 0.5$ CONFIGURATION | 86 |
| FIGURE 79: STOP-INJECTION TIME, MAX c^* AT THE CROSS, RH (LEFT), FL (RIGHT), $\phi_{inj} = 0.5$ | 87 |
| FIGURE 80: RECTANGULAR PLUG AND ZERO SHAPE FACTOR | 88 |
| FIGURE 81: SAMPLE PLUG SHAPES FOR RHODAMINE (LEFT) AND FLUORESCEIN (RIGHT) AT DIFFERENT TIMES, $\phi_{inj} =$: FLOATING | 88 |
| FIGURE 82: STOP-INJECTION TIME ($T = 22.1s$) AND MAX c^* AT THE CROSS FOR $\phi_{inj} =$: FLOATING | 89 |
| FIGURE 83: A COMPARISON BETWEEN $\phi = 0.5$ AND FLOATING INJECTION CONFIGURATIONS FOR FLUORESCEIN SAMPLE PLUG SHAPES AT $T = 21.9s$ | 89 |
| FIGURE 84: CONCENTRATION CONTOURS, INJECTION $\phi_{inj} = 0.4$ | 90 |
| FIGURE 85: CONCENTRATION CONTOURS AND SHAPE FACTOR AT $t = 20.5s$ FOR INJECTION $\phi_{inj} = 0.4$ | 90 |
| FIGURE 86: CONCENTRATION CONTOURS, INJECTION $\phi_{inj} = 0.6$ | 91 |
| FIGURE 87: CONCENTRATION CONTOURS AND SHAPE FACTOR AT $t = 25.5s$ FOR INJECTION $\phi_{inj} = 0.6$ | 91 |
| FIGURE 88: A COMPARISON OF SHAPE FACTOR AND SAMPLE PLUG WIDTH FOR DIFFERENT $\phi_{inj} =$ CONFIGURATIONS | 92 |
| FIGURE 89: SEPARATION CONFIGURATIONS | 93 |
| FIGURE 90: CONCENTRATION CONTOURS OF SEPARATION FOR $\phi_{inj} = 0.5$ AND $\phi_{sep} = Floating$ | 94 |
| FIGURE 91: SEPARATION GRAPHS AT DIFFERENT DETECTION SPOTS $x = 0.1, 0.2, 0.3$ AND 0.5 mm FOR $\phi_{inj} = 0.5$ AND $\phi_{sep} = F$ | 94 |
| FIGURE 92: CONCENTRATION CONTOURS, INJECTION $\phi_{inj} = 0.5$ AND SEPARATION $\phi_{sep} = Floating$ VS $\phi_{sep} =$ $0.25, t = 0.7s$ | 95 |

| | |
|--|-----|
| FIGURE 93: SEPARATION GRAPHS AT DIFFERENT DETECTION SPOTS $x = 0.1, 0.2, 0.3$ and 0.5 mm FOR $\phi_{inj} = 0.5$ AND $\phi_{sep} = 0.25$ VS. FLOATING | 96 |
| FIGURE 94: SEPARATION RESOLUTION (LEFT: CONVENTIONAL, RIGHT: MODIFIED) FOR RHODAMINE AND FLUORESC EIN AT DIFFERENT DETECTION SPOTS; $\phi_{inj} = 0.5$; $\phi_{sep} = 0.25$ VS. FLOATING | 97 |
| FIGURE 95: CONCENTRATION CONTOURS FOR TWO-STEP INJECTION WITH CONFIGURATIONS OF $\phi_{inj} * 1 = 1$ AND $\phi_{inj} * 2 = 0.5$ | 98 |
| FIGURE 96: σ AT T=32S FOR TWO-STEP INJECTION WITH CONFIGURATION $\phi_{inj} * 1 = 1$ AND $\phi_{inj} * 2 = 0.5$ | 98 |
| FIGURE 97: SEPARATION CONFIGURATIONS; YELLOW ARROWS SHOW FLOW/ELECTRIC FIELD INTENSITY..... | 99 |
| FIGURE 98: SEPARATION GRAPHS AT DIFFERENT DETECTION SPOTS $x = 0.1, 0.2, 0.3$ and 0.5 mm FOR TWO-STEP INJECTION ($\phi_{inj1} = 1$ AND $\phi_{inj2} = 0.5$) AND $\phi_{sep} = Floating$ (GREY LINES REPRESENT ONE-STEP INJECTION)..... | 100 |
| FIGURE 99: SEPARATION RESOLUTION (LEFT: CONVENTIONAL, RIGHT: MODIFIED) FOR RH AND FL AT DIFFERENT DETECTION LOCATIONS; TWO-STEP ($\phi_{inj1} = 1$ AND $\phi_{inj2} = 0.5$) VS. DIRECT INJECTION ; $\phi_{sep} = Floating$ | 101 |
| FIGURE 100: COMPARISON OF SEPARATION CONTOURS AT $t = 2s$ ($\phi_{sep} = 0.25$ VS. $\phi_{sep} = floating$) | 102 |
| FIGURE 101: COMPARISON OF SEPARATION CONTOURS AT $t = 4s$ ($\phi_{sep} = 0.25$ VS. $\phi_{sep} = floating$) | 102 |
| FIGURE 102: SEPARATION GRAPHS AT DIFFERENT DETECTION SPOTS $x = 0.1, 0.2, 0.3$ and 0.5 mm FOR TWO-STEP INJECTION ($\phi_{inj1} = 1$ AND $\phi_{inj2} = 0.5$) AND COMPARISON OF $\phi_{sep} = Floating$ (GREY LINES) VS. $\phi_{sep} = 0.25$ (RED AND GREEN)..... | 103 |
| FIGURE 103: SEPARATION RESOLUTION (LEFT: CONVENTIONAL, RIGHT: MODIFIED) FOR RHODAMINE AND FLUORESC EIN AT DIFFERENT DETECTION SPOTS; TWO-STEP INJECTION ($\phi_{inj1} = 1$ AND $\phi_{inj2} = 0.5$) ; $\phi_{sep} = Floating$ VS. 0.25 | 103 |
| FIGURE 104: INITIAL NON-DIMENSIONAL CONCENTRATION, $t = 0s$, FOR ALL SEPARATION CONFIGURATIONS ($\phi_{sep} = 0, 0.25, 0.4, Floating$ AND 0.6)..... | 104 |
| FIGURE 105: ELECTRIC FIELD STREAMLINES FOR DIFFERENT SEPARATION CONFIGURATIONS | 105 |
| FIGURE 106: FLOW FIELD FOR DIFFERENT SEPARATION CONFIGURATIONS | 105 |
| FIGURE 107: SPATIAL SEPARATION PEAKS AT $t = 2$ AND $4s$ ($\phi_{sep} = 0.25, 0.4, Floating$ AND 0.6) | 106 |
| FIGURE 108: C *CONTOURS AT $t = 0.1, 0.3$ and $0.5s$ FOR $\phi_{sep} = 0.25, 0.4, Floating$ AND 0.6 | 107 |
| FIGURE 109: ZOOM OF 50% C * CONTOUR LINES AT $t = 0.1$ AND $0.5s$ FOR $\phi_{sep} = 0.25, 0.4, Floating$ AND 0.6 | 108 |
| FIGURE 110: C *CONTOURS AT THE CROSS AT $t = 2s$; $\phi_{sep} = 0.25, 0.4, Floating$ AND 0.6 LEFT: FL; RIGHT: RH .. | 108 |
| FIGURE 111: C *CONTOURS AT $t = 2s$ FOR $\phi_{sep} = 0, 0.25, 0.4, Floating$ AND 0.6 | 109 |
| FIGURE 112: C *CONTOURS AT $t = 4s$ FOR $\phi_{sep} = 0, 0.25, 0.4, Floating$ AND 0.6 | 110 |
| FIGURE 113: SEPARATION GRAPHS AT DIFFERENT DETECTION SPOTS $x = 0.1, 0.2, 0.3mm$ FOR TWO-STEP INJECTION ($\phi_{inj1} = 1$ AND $\phi_{inj2} = 0.5$) AND COMPARISON OF $\phi_{sep} = 0, 0.25, 0.4, Floating$ AND 0.6 | 111 |
| FIGURE 114: EFFECT OF SEPARATION CONFIGURATION ON SEPARATION RESOLUTION FOR TWO-STEP INJECTION..... | 112 |
| FIGURE 113: COMPARING PEAK DISTANCES (LEFT) AND SUM OF HALF-WIDTH MAXIMUMS (RIGHT) AT DIFFERENT SEPARATION CONFIGURATIONS $\phi_{sep} = 0, 0.25, 0.4, 0.6$ AND FLOATING | 113 |
| | |
| FIGURE A- 1: SUMMARY OF POISSON-BOLTZMANN EQUATION DERIVATION | 139 |
| FIGURE A- 2: SUMMARY MAP OF THE DERIVATION OF POISSON-BOLTZMANN EQUATION | 140 |
| FIGURE A- 3: DEPENDENCE OF THE NUMBER OF DISTRIBUTIONS ON THE NUMBER OF PARTICLES | 143 |
| FIGURE A- 4: ENSEMBLE AVG. OF PARTICLES DISTRIBUTION OVER ENERGY LEVELS, CHANGING N FOR $E = 10e$ | 146 |
| FIGURE A- 5: ENSEMBLE AVERAGE OF PARTICLES DISTRIBUTION OVER ENERGY LEVELS, N=10, CHANGING E | 147 |
| FIGURE A- 6: ω vs. $\ln(\omega_{max}\omega)$ FOR $N = 4$ to 11 and $E = 11e$ | 148 |
| FIGURE A- 7: ELECTROOSMOTIC POTENTIAL DISTRIBUTION WITHIN EDL AS A FUNCTION OF THE INNER-LAYER SCALE χ (LEFT)IN NORMAL AND (RIGHT) LOGARITHMIC SCALING [125]..... | 164 |
| | |
| FIGURE B- 1: SAMPLE CONCENTRATION ALONG THE CENTERLINE OF THE INJECTION CHANNEL (T=4.5s)..... | 173 |
| FIGURE B- 2: ILLUSTRATION OF THE DIFFUSION PROCESS AND SCALES OF DIFFUSION (GULLIVER 2007)..... | 176 |
| FIGURE B- 3: A SAMPLE CONCENTRATION CONTOUR FOR A HORIZONTAL INJECTION AT T=4.5 AND 9S | 177 |
| FIGURE B- 4: CONTROLLING POTENTIALS AT INJECTION AND SEPARATION | 180 |
| FIGURE B-5: CHIP GEOMETRY (PRELIMINARY STUDY)..... | 184 |
| FIGURE B-6: BOUNDARY CONDITIONS..... | 185 |

List of Tables

| | |
|---|-----|
| TABLE 1: A FEW REFERENCES FOR CHANNEL DIMENSIONS IN LITERATURE | 15 |
| TABLE 2: SHAPE FACTORS (PARAMETERS) USED TO CHARACTERIZE SAMPLE PLUG SHAPE | 45 |
| TABLE 3: PARAMETERS VALUES BASED ON INCREASING σ | 49 |
| TABLE 4: COMPARISON OF FL (GREEN) AND RH (RED) SEPARATION FOR CASES A- E ALONG SEPARATION CHANNEL ... | 64 |
| TABLE 5: MODIFIED RESOLUTION FOR CASES A TO E | 67 |
| TABLE 6: SPATIAL GRID REFINEMENT INFORMATION | 71 |
| TABLE 7: ELECTRIC FIELD AND GRID INDEPENDENCY | 72 |
| TABLE 8: TIME-STEP GRID INDEPENDENCY OF 50% C LOCATION FOR FINE AND COARSE GRIDS | 76 |
| TABLE 9: A COMPARISON OF SHAPE FACTOR AND SAMPLE PLUG WIDTH FOR DIFFERENT ϕ_{inj} * | 92 |
| TABLE 10: A COMPARISON OF SHAPE FACTOR FOR BEST RESULTS OF ONE STEP AND TWO STEP INJECTION | 99 |
| | |
| TABLE A- 1: ENSEMBLE AVERAGE TABLES FOR 3 DIFFERENT SYSTEMS | 145 |
| TABLE A- 2: EXAMPLE OF SHOWING VALUES FOR COSH(X) AND SINH(X) | 162 |
| TABLE A- 3: ANALYTICAL AND SIMPLIFIED SOLUTIONS OF POISSON-BOLTZMANN EQUATION | 163 |
| | |
| TABLE B- 1 : GEOMETRIC BOUNDARIES BASED ON LENGTH SCALE lr | 169 |
| TABLE B- 2: LIST OF PARAMETERS | 172 |
| TABLE B- 3: PARAMETERS | 174 |
| TABLE B- 4: SUMMARY OF PARAMETER RANGES | 179 |
| TABLE B- 5: NON-DIMENSIONAL GEOMETRIC PARAMETERS | 180 |
| TABLE B- 6: NON-DIMENSIONAL POTENTIAL PARAMETERS | 180 |
| TABLE B- 7: NON-DIMENSIONAL VELOCITY PARAMETERS | 180 |
| TABLE B- 8: NON-DIMENSIONAL CONCENTRATION PARAMETERS | 181 |
| TABLE B-9: BOUNDARY CONDITIONS | 186 |

Chapter 1

1.1 Introduction

As the entropy of the world is increasing, mixing and chaos can feel natural. On the other hand, much effort is devoted to separating and sorting mixed systems.

Separation scientists have developed different separation techniques with much success in industrial scale applications such as the oil industry and food processing. For biological samples, separation science is focused on laboratories, which, with the advent of micro- and nanofluidics, are being revolutionized to “lab-on-a-chip” devices with all their promising potential to deal with small sample amounts and several advantages like portability, reduced analysis time, and lower costs.

However, miniaturizing separation techniques is not just a matter of downsizing. Physical transport phenomena can be drastically different at microscopic length scales, necessitating theoretical and computational examination.

1.2 Research Motivation

Microfluidics and Lab-on-a-chip (LOC) devices serve as a platform for many diagnostic, clinical, biomedical, nutritional, cosmetic and forensic applications. Indeed, miniaturization of conventional devices to microchip scale, enables sample manipulation and study to be performed much faster, with significantly lower sample size and cost. LOC systems for diagnostic applications are rapidly developing higher performance for sample injection, separation with high resolution, and improved detection sensitivity. Sample separation is the heart of DNA and protein based diagnostic assays and purification methods for biologics, particularly in the development of customized, portable devices for personalized health-care diagnostics and point-of-use production of treatment.

DNA screening and separation of DNA and protein have been improved through microfluidic chip based electrophoretic separation with the precise control of the injected sample shape and volume for separation. Although numerous microfluidic chips have been reported for DNA and protein separation, a

comprehensive understanding of the physics that dominates sample injection and separation is still lacking, which calls for systematic studies on the parameters that influence these processes.

1.3 Research Objectives

This thesis reports the theoretical and computational investigations of on-chip electrophoretic separation. This thesis is to apply an injection and separation model to a cross-link microchip to study protein and DNA separation. Experimental and numerical studies revealed that the sample plug shape and size play a significant role in improving the separation resolution. To achieve our main goal of producing a rectangular sample plug at the intersection of the injection and separation channels, we conducted studies with various applied potentials and chip designs. With the significant role of the injected sample plug in the separation process, this study quantifies the shape and size of the sample plug. Moreover, to assess the separation performance, a modified definition of resolution is proposed that better identifies the quality of the sample separation. This modified definition includes peak-to-valley magnitude of the sample species concentration. In addition to assessing sample shape and separation quality, new separation procedures and chip geometries are to be explored with the objective of sample separation optimization. In support of the above, the work performed in this thesis is both theoretical and computational.

1.4 Thesis Outline

Having introduced the research motivation and research objectives, the rest of this chapter lays out the thesis outline.

Chapter 2 reviews the background and relevant literature on electrophoresis separation in microfluidic chips, including an overview of the separation techniques in molecular biology, capillary electrophoresis to the present electrophoretic chips. The first phenomenon considered is electrophoresis, where an applied electric field moves charged macromolecules (such as DNA) through a solvent. This is a very natural idea; however, the results of doing this simple act are often surprising and depend on many parameters such as physical properties, geometrical conditions, and applied electric fields.

The review outlines the fundamentals of electrophoresis separation and the various mechanisms used to separate and detect different biochemical samples through microfluidic networks. Moreover, different geometries of the microchannel networks as well as some common configurations for applied electric

potentials are addressed. Moreover, the separation resolution, a few detection methods, ways to improve detection and finally other separation techniques are addressed briefly.

Chapter 3 formulates the problem's four parts: the electric field, flow field, concentration, and energy fields. The initial chip geometry and dimensional forms of governing equations and boundary conditions, assuming an electric double layer (EDL), are presented first, then the thin EDL is neglected and its effect is reflected on flow boundary conditions.

Several parts of this thesis refer to a cross-linked microchannel. It includes injection and separation channels, a cross at the intersection of those channels, and four reservoirs for loading sample and buffer solutions. Initially, the channels are filled with the buffer solution. Then, by applying the electric potentials, the sample is electrokinetically loaded until it reaches the cross. Once the sample is at the cross, the electric potentials are applied on the separation channel.

For greater ease, all the equations and boundary conditions are non-dimensionalized. For this purpose, the choice of reference parameters is first discussed in detail. Also presented is the choice of time and length scales to be implemented in the numerical simulation of the problem. Regardless of the choice of time and length scales, the number of parameters are the same and in accordance with Buckingham-Pi theorem.

Following the non-dimensionalization, the details of the numerical simulation tool and solver, ANSYS CFX, are presented.

Chapter 4 is the main contribution of this thesis and evaluates the injection and separation. The required fundamentals of on-chip electrophoretic separation of a DNA and protein sample are presented in the first four chapters. Many techniques proposed for this goal and successful separation have been reported in the literature. All addressed the role of a good shape for the injected sample as it results in a high separation resolution. This begged the questions "What is a good shape for the sample plug?" and "What is a high resolution for resolving sample components?"

My supervisors, Prof. Schneider and Prof. Ren, and I attempted to answer these questions by quantifying the sample plug shape at the cross. We presented the parameters for quantifying the sample plug shape and introduced a "shape factor" as an individual parameter for assessing the shape of the plug. Results of a Matlab code for the possible shapes at the cross are presented and the shape factor model is assessed with experimental results in literature. We studied five different plug shapes by controlling the applied electric potentials/fields at injection and investigated the effect of time to stop injection on the sample plug shape. Following the separation analysis for these five cases, we introduced a modified separation resolution that includes the conventional resolution and the factor of detector sensitivity.

Chapter 5 provides the analysis of the injection and separation. First, the grid independency of the solution is discussed. Then, the injection model is validated with experimental results in literature. At injection, in addition to the applied electric potential as a key controlling parameter, the effects of separation channel width and the injection channel length are also studied. We modified the chip design and much simulation work was done to develop a shape factor model for sample injection prior to switching to separation and resolving sample constituents. For the final chip geometry, different configurations of applied electric potentials at injection are presented, and we achieved a rectangular sample plug shape through a two-step injection procedure. For such an ideal plug, different configurations of applied electric potentials at separation are analyzed. At the onset of separation analysis in Chapter 6, the shape factor-resolution correlation was not certain, but the final results in this chapter show the study of this correlation for different configurations.

The last chapter, Chapter 6, summarizes this work and outlines recommendations to further improve the separation performance of microfluidic devices in electrophoretic separation analysis.

The distribution of ions and electric potential in electric double layers in microchannels and non-dimensionalization of problem formulation, more details are provided in appendices. Appendix A looks at the electric double layer and its effect on problem formulation. The fundamentals of probability and ion distribution in an electric double layer (EDL), that is, the thin ion layer adjacent to the microchannel wall, are presented. To find out the distribution of ions and electric potential, the derivation of the Poisson-Boltzmann equation is provided. This appendix clarifies theoretical microfluidics from the statistical and classical thermodynamics perspective. The Poisson-Boltzmann equation is derived in this work because microfluidic literature lacks a detailed derivation of this equation all in one place. This derivation fills the gap between theoretical and experimental studies in a comprehensive way. Solutions to this equation are provided, with the assumptions, and finally, simplifications are addressed to reflect the effect of the EDL as a finite slip wall in the velocity boundary conditions.

Appendix B presents the non-dimensional form of the problem formulation, governing and boundary conditions, discussed in Chapter 3. It is explained why the equations for three electric, flow and concentration fields can be decoupled. All the geometric, electric, flow and concentration parameters are presented. The choice of time and length scales are thoroughly discussed.

Appendix C provides the copy right permissions for the figures used for validation studies in this thesis.

Chapter 2

Background

2.1 Literature Review

Electro-osmotic flow (EOF), or the fluid motion through the application of an electric field, was first reported by Reuss [1] in 1809 in experiments that demonstrated that water could be made to percolate through porous clay diaphragms. The observed mobility of water occurred because the clay particles (and many other solid substrates such as glass, silicon, polymeric materials, minerals of various kinds, etc.) acquire a surface charge when in contact with an electrolyte. The immobile surface charge in turn attracts a cloud of free ions of the opposite sign, creating a thin (1–10 nm) layer of mobile charges next to the surface charge, which is called an electric double layer (EDL). In the presence of an external electric field, the fluid in this charged layer (the Debye layer) acquires a momentum which is then transmitted to adjacent layers of fluid through the effect of viscosity. If the fluid phase is mobile, it causes the fluid to flow (electro-osmosis) [2]. In late 1800, Helmholtz [3] also conducted experiments on a glass tube containing aqueous salt solution and observed the fluid motion under the applied electric field. Through this work, he pioneered the governing principles of electroosmotic flow.

Electrophoresis is the science of a variety of separation techniques based on different migration speeds of ions and/or charged particles under the influence of an applied electric field. The migration velocity of an ion is determined by two factors: the intensity of the electric field and the electrophoretic mobility. The former is a user-controlled parameter, and the latter is a characteristic of the ions in the given sample.

The history of electrophoresis is rooted in 1937 when Tiselius [4], the Chemistry Nobel prize winner in 1948, developed this method into one of the most used analytical separation techniques in analytical chemistry. Then capillary electrophoresis (CE), where electrophoretic separation is performed in capillaries of 10 – 100 μm , turned into a common separation technique and became well established. Later on, with the advent of micro-total analysis systems (μ -TAS) and device miniaturization, microchip capillary electrophoresis was developed and attracted attention in many fields such as pharmaceuticals, biology, energy and nutrition. Reduced analysis time (a few minutes) and lower sample and reagents consumption (picoliters and microliters) are the primary benefits of miniaturization in devices for analytical separation. High sample throughput is also possible by using arrays of microchips by fabricating multiple chips. These are significant merits in comparison to the conventional slab gel electrophoresis, which is a time consuming laborious procedure for DNA or protein sample separation.

Electrokinetic phenomena have been mentioned in the literature from the beginning of the 19th century. In 1808, Reuss [1] discovered electrokinetic flow through a capillary. Then in 1964, Burgreen and Nakache [5] provided a theoretical work on the fundamentals of electrokinetics in capillaries with rectangular cross sections which mainly focused on charge and potential distribution. The detailed derivation of the P-B equation was not presented. In 1965, Rice and Whitehead [6], presented the net charge density in a capillary based on the Boltzmann distribution. In 1982, Neukirchen et al. [7] presented experimental results on high resolution micro-scale protein analysis but did not address the underlying theory. In 1995, Finkelstein et al. [8] showed why protein structures follow the Boltzmann distribution which emphasizes the importance of a thorough understanding of the Boltzmann equation. Later in 1998, Patankar and Hu [9] presented an excellent numerical study of electroosmotic flow for a cross-linked microchannel, considering the EDL in their simulations. The driving force is determined by the applied electrical field and the ion density of the working fluid, described the Poisson-Boltzmann (P-B) equation. The P-B equation has been used in many books and publications, but no detailed derivation is available in the microfluidic literature at one place. Kirby and Bruus , [10] [11], provided a derivation of the Poisson equation in their books, but there is a dearth of understanding in microfluidics when it comes to the derivation of the Boltzmann equation from a statistical thermodynamics perspective. However, understanding this, derivation provides insight into the ion distribution in the nanometer-scaled electric double layer (EDL) in microchannels, and a solid justification for replacing the EDL influence with slip boundary conditions in the solution of the Navier-Stokes (N-S) equation for the prediction of the bulk region flow field. The N-S equations are applicable to most Newtonian fluids such as those commonly used in microfluidic applications. Derivation of the P-B equation requires the knowledge of Statistical Physics and Thermodynamics, Chemical Engineering, Mathematics, and Mechanical Engineering. The strongly interdisciplinary nature is reflected by the lack of a detailed derivation in the microfluidic literature. This fundamental study is motivated by the need to fill this gap and to establish the basis for further experiments. The intellectual merit and broader impact of this study will be to narrow the research regarding specific health issue applications that comes from the non-dimensionalized governing equations, parametric studies, and precise boundary conditions.

A survey of the microfluidics literature shows that devices used in electrophoresis separation are largely designed based on experimental study [12]–[15]. Examples include the chip designed for protein pre-concentration [16], the chip for acupuncture sample injection in capillary electrophoresis (CE), designed by Ha and Hahn in 2016 [17], and the novel instrumentation for potentiostatically controlled voltammetry applied in the presence of high external voltages and electric fields by Zaino et al. [18]. Experimental studies are, however, expensive, and usually much iteration is usually needed to achieve an optimized design for one particular application. The performance of experiments also requires lab facilities, experimental apparatus, test material, and knowledge of chip fabrication.

Computational fluid dynamics (CFD) simulation is a useful tool for reducing both the time and cost of experiment. Numerical simulation in microfluidics can be performed by considering several mutually independent cases. Identifying such cases in turn requires knowledge of the important governing parameters for the problem. Understanding these parameters minimizes the number of cases that need consideration, which in turn, minimizes the cost associated with microchip design. An optimized simulated design can then be verified and refined with experimental studies. Patankar and Hu pioneered the use of numerical simulation in electroosmotic flow [9]. They studied the electroosmotic injection characteristics of a cross-channel device for capillary electrophoresis and observed that the desired rectangular shape of the sample plug at the intersection of the cross-channel can be obtained when the injection is carried out at high electric field intensities. Bianchi et al. performed finite element simulation of electroosmotic flow at a T-Junction [19]. A physical and numerical study of various injection systems in microfluidic chips was presented by Fu et al. [20], and for the evolution of the resulting sample plug, good agreement between simulation and experimental results was obtained. In *Electrophoresis* 2015 [21], a computer simulation study described the impact of complex mobilities on electrophoretic separation. An analytical and parameterized model was presented for examining the effects of Joule heating on analyte dispersion in electrophoretic separation microchannels [22].

Valuable experimental results are available in literature, however, little research is carried out through numerical analysis in this field, and yet the literature lacks a general model for on-chip separation of DNA and protein. According to literature, one key factor that plays a significant role in the efficiency of on-chip electrophoresis separation is the initial shape of the sample plug at injection [23]–[27]. For microchips involved in separation, injection is a key step in efficient analysis. Patankar and Hu [9] stated that the shape of the inserted sample is an important parameter that influences the resolution of the separated zones during the electrophoresis and depends primarily on the electroosmotic flow pattern at the intersection of the channels. Mohammadi and Santiago [28] presented shape optimization techniques for minimizing dispersion in extraction and separation fluidic devices using the control parameter. This parameter may be either the potential differences applied during the pinching and pull-back steps, or the turn geometries devoted to keeping the dispersion minimal by reducing the skew of the advected band. The literature shows that a distorted sample plug has a negative impact on the quality of separation [29], [25],[24] and optimal injection depends on the shape and size of the sample plug at the intersection of injection and separation channels during injection [30]. The shape of the sample plug depends primarily on the electroosmotic flow pattern at the intersection of the channels and plays an important role in determining the separation resolution.

In this thesis, I start with the background of electrophoretic separation including gel electrophoresis, and capillary electrophoresis, then focus on microchip electrophoresis with the ultimate goal of Lab-On-Chip (LOC) systems. Over hundreds of publications are available in literature in microfluidic electrophoretic separation for biological samples in particular DNA and protein. Because of the charged nature of these molecules, they migrate with different pace, depending on their charge and size, under the applied electric field. This causes the separation of different constituents of such biological samples. To analyze the efficiency of separation, different research areas have been extensively developed, including: Choice of chip material and surface properties [31] [32], type of background electrolyte (buffer solution) [33], pre-concentration methods for samples with low initial concentration [34]–[36], chip design at injection and separation [37]–[42], electric potential configurations [43]–[47], detection methods [48]–[52] and the shape and size of the sample plug at injection prior to separation. Shape and size of the sample plug at injection is the main focus of this research. Much research is being carried out on microchip electrophoretic separation, few studies have examined sample shape from a theoretical perspective and a detailed analysis of the effect of sample plug shape at injection on separation efficiency is still lacking. In literature, it is stated to be difficult to attain a rectangular and narrow sample shape only by adjusting electric voltages. This goal is achieved in the current research and in Chapter 4 I present the role of sample plug shape thoroughly, and the effective factors in evaluating good injection.

2.1.1 Electrophoretic Separation

Figure 1 shows the conventional method for sample separation, gel electrophoresis, which suffers from several disadvantages. Despite the ability to resolve the components of complex samples, it suffers from the low speed of separation, which is limited by Joule heating due to the applied high electric fields. Poor dissipation of Joule heat in slab systems, the cumbersome and time-consuming preparation process, and poor reproducibility have motivated the capillary electrophoresis approach in sample separation. These issues are solved in microchip electrophoresis requiring a thorough study of downsizing.

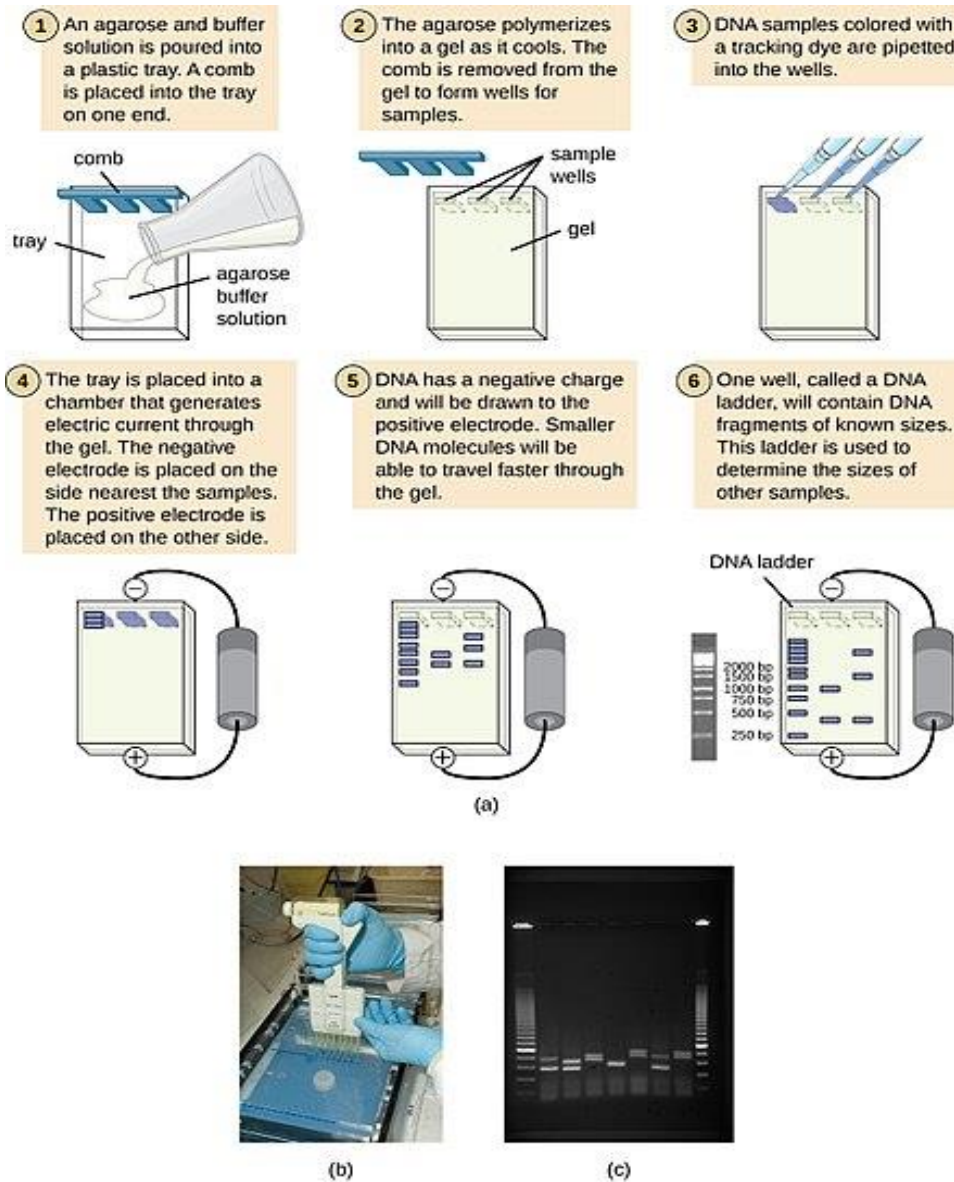


Figure 1: Conventional gel electrophoresis (Wikimedia)

2.1.2 Capillary Electrophoresis

The schematic of CE is shown in Figure 2. In CE, both ends of a capillary are immersed in buffer reservoirs that include the electrodes that provide electrical contact between the high voltage power source and the capillary. Then one of the buffer reservoirs is replaced by the sample reservoir, and by applying the electric field, the sample is loaded onto the capillary. After sample injection the reservoirs are replaced again, and the electric field is applied to process separation.

Close to the end of the capillary, a detector is installed to detect sample components through UV, fluorescent, mass spectroscopy or other detection techniques.

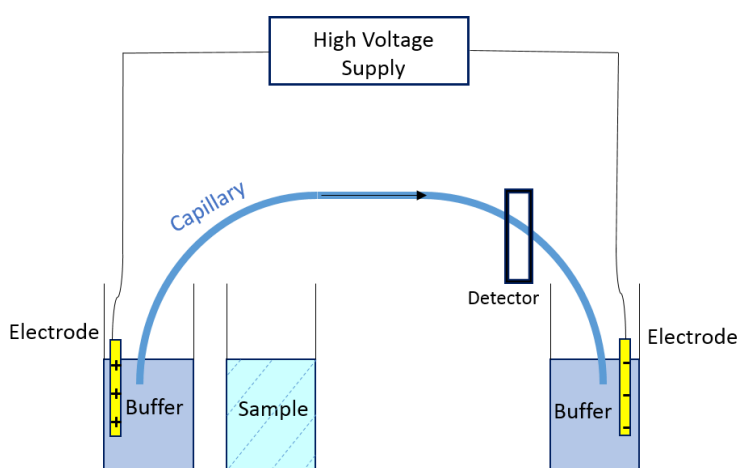


Figure 2: Schematic of capillary electrophoresis

A typical capillary has the internal diameter of $20 - 100 \mu\text{m}$ and length of $20 - 100 \text{ cm}$ [53]. The high surface-to-volume ratio of capillaries allows the dissipation of Joule heat generated from large applied electric fields, which is shown in detail in section 3.3.4. As a result of its ability to dissipate heat, capillary electrophoresis can deal with up to 30 KV/m when in contact with the ambient temperature [53]. Moreover, downsizing from gel electrophoresis to capillary and microfluidic electrophoresis results in low sample and reagent (buffer) consumption, on the order of nano to picoliters, and rapid analysis time, on the order of minutes instead of days and weeks.

2.1.3 Microfluidic Separation Chips

For microchip electrophoresis, much research has been done on chip geometry. The most common design is the cross-linked chip, which includes the injection and separation channels as well as sample and buffer reservoirs, as shown in Figure 3 and Figure 4. Both figures show a microchip consisting of the injection and separation channels, arranged in a cross shape. Fluid reservoirs are placed at each end of the channels two for the sample and buffer solution (electrolyte solution) and the other two as the waste reservoirs. To apply the electric fields, electrodes are positioned in all the reservoirs to make connections with the high voltage power source. First the buffer solution is injected into the channels; then, the electric potentials are applied at the injection channel reservoirs, and the sample is loaded electrokinetically until it reaches the cross or the intersection of the channels. This cross is the main part of the sample injector. Once enough sample plug is available at the cross, it is subjected to separation through the application of an electric field along the separation channel. To achieve a better sample plug shape, consequently a higher separation resolution, side electric fields offer additional control during the injection and separation steps. The on-chip detection of the separation of sample components (constituents) is made in the final part of the separation channel.

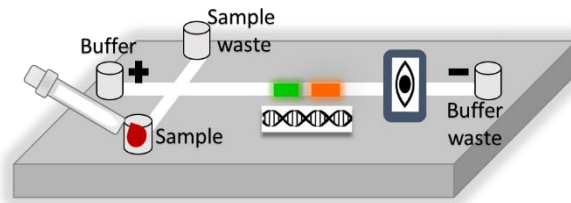


Figure 3: Sample chip configuration for electrophoretic separation

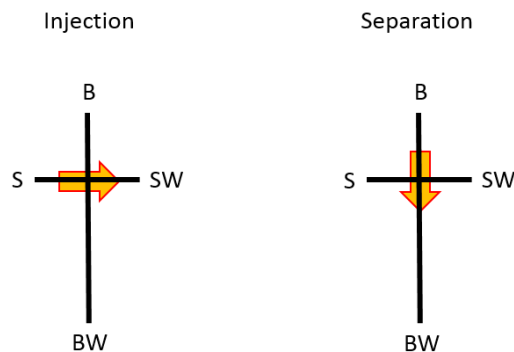


Figure 4: Schematic of injection and separation in cross-linked channels;
S:Sample, B: Buffer, SW: Sample waste, and BW: Buffer waste

The goal of electrophoretic separation is to achieve high separation efficiency, that is, to ensure that system can resolve sample constituents based on their different electrophoretic mobilities. To achieve an efficient system, much effort should be dedicated to the injection step prior to starting the separation. In that respective, the initial size of the sample as well as its initial concentration have a significant effect on separation resolution. Band broadening of the sample happens due to the longitudinal diffusion from the interface sides of both the sample and buffer. Shorter separation time gives the sample less time to diffuse. A short sample plug results in less overlapping of sample components and consequently better resolution; however, very short sample plugs need pre-concentration to achieve detection sensitivity.

Designing an optimal injector necessitates a detailed study of the size and the shape of the sample plug at the cross, which is the main objective of this thesis. It is necessary to have an insight into the distribution of charges in the microchannel, in the bulk flow region and in the thin layer adjacent to the wall, (EDL).

2.1.3.1 Electric Double Layer (EDL)

To benefit from microchips by performing biological, medical, diagnostics, etc. tests, requires an understanding of the physics of the problem and its governing equations. In a microchannel, where an electrolyte solution is adjacent to a charged surface (a dielectric surface with static charges), the counterions in the solution are attracted to the surface while the co-ions are repelled from the surface; as a result, an electric double layer is formed where a net charge difference exists. Considering glass and water, silica is brought into contact with an aqueous solution; therefore, depending on the PH value of the electrolyte solution, the surface could have positive, neutral or negative charges. If the channel surface is negatively charged (such as with deionized water), the net charge would be positive keeping the bulk of the liquid far away from the wall electrically neutral [54] an EDL is thus formed, and then the electric field in the double layer results in a potential difference across it [55]. Figure 5 shows what we call an electric double layer consisting of two regions: the first (Stern) layer is compact, and acts as an inner region with ions that tightly adhere to the surface. The second layer is composed of mobile ions which, due to the Coulomb force, are attracted to the surface charges next to the wall. This second layer is named the diffuse layer and includes free ions which move in the fluid under the influence of an external electric field, causing bulk electroosmotic flow (EOF). The rigid, stationary ions attached to the wall in the Stern layer, create a potential difference with diffuse-layer mobile ions. The electric potential on the interface surface of the Stern and diffuse layers, or at the solid-liquid interface is called the “Zeta potential”, ζ . Factors such as the solution concentration, PH value, and ionic concentration, as well as temperature, may affect the Zeta potential.

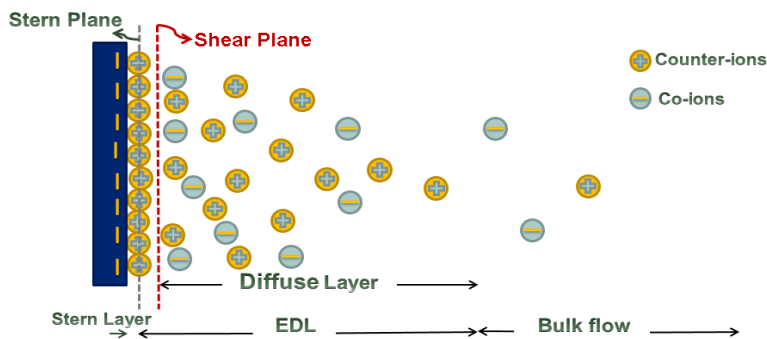


Figure 5: Electric Double Layer(EDL) in microchannels

With a better insight into the electric double layer, we have to determine out the distribution of charges and the electric potential in order to determine ion and concentration distributions. At equilibrium, the ion distribution represents the most probable state in the EDL and also in the bulk flow. Classical thermodynamics is inherently limited in explaining the microscopic behavior of even the simplest thermodynamic system [56] and is deficient for the atomic behavior of materials. Therefore, it is necessary to understand some basic concepts of probability and statistical thermodynamics, such as microstates and macrostates of energy, distinguishable and indistinguishable particles, and Lagrangian multipliers. Knowing the exact position and momentum of atoms and particles is not an easy task given the huge number of atoms on the order of 10^{23} . Consequently, finding the energy of individual atoms as defined by quantum mechanics approaches is a different approach from that of continuous system properties in classical thermodynamics. The objective here is to find the distribution of ions, in equilibrium, in the presence of an applied electric field. Moreover, to find the electric potential distribution, Poisson's equation should be solved in two regions - the EDL and the bulk flow - following a fundamental law in physics, Coulomb's law. Electro-osmotic flow (EOF), a key feature in CE, is the movement of the bulk flow and sample components in the capillary, regardless of their charge or size. For capillaries made from silicon groups, the negatively charged capillary wall attracts the positive charges in the solution; therefore, an electric double layer (EDL) is formed as shown in Figure 6 . The applied electric field causes the movement of the cations of the diffuse part of the EDL towards the cathode. Due to the cations movement, the molecules of the bulk solution are dragged too, and EOF occurs. The magnitude of EOF velocity depends on the intensity of the applied electric field, as well as the EOF mobility which is affected by parameters such as surface potential, the PH and ionic strength of the buffer solution, and the temperature and capillary surface properties, preferably with permanent coating modifications.

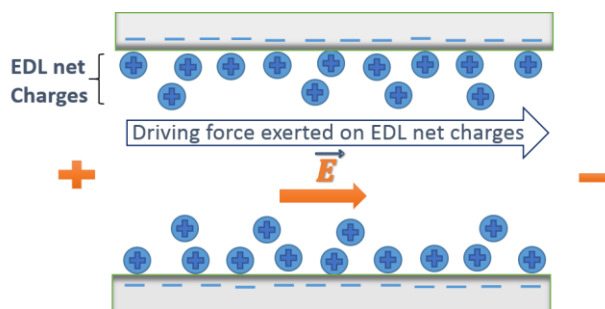


Figure 6: Driving force in Electric Double Layer (EDL)

2.1.3.2 Geometries of electrophoretic chips and injectors

Different chip configurations have been reported in the literature, and the design of the chips has undergone significant development. The schematics of a few cases are shown in Figure 7. Surveying the literature shows that the chip configurations (channel geometries) are mixed up with electric potential (electric fields) configurations in some cases. A map of both of these key factors in electrophoretic separations are briefly discussed in this section and Section 2.1.3.4. In Figure 7, type “a” is a simple cross-linked chip, which is the most common geometry implemented in electrophoretic separation so far. It is an appropriate and easy-to-fabricate chip for the purpose of separation, and with the cross size on the order of the width of the channels, the sample plug volume is controllable by the applied electric fields [57] [58]. The type “b” configuration is called a double-T chip. In 1994, Effenhauser et al. [59] implemented this geometry to ensure a low baseline signal as a consequence of preventing sample leakage from the two T junctions of the injection channel during separation. Later, in 2003, the double-T injection geometry was used in sample pre-concentration applications like Jung et al.’s research in Stanford [60]. In such geometry, the minimum size of the sample plug is limited to the length in which a sample is trapped between two T channels, which could have negative effects on the detection of sample-constituent separation. Type “c”, the double-cross injection chip, is the geometry Fu et al. [61] designed for their research. They showed that the proposed system is not only capable of performing the same function as the single-cross injection system but is also able to generate sample plugs of different volumes. Their chip results in slightly better separation detection. Zhuang et al. [29] showed the results of a double-focusing injection configuration, similar to type “d”, used to generate regular and non-distorted sample-plug shapes and deliver the variable-volume sample plugs by electrokinetic focusing. They claimed that the detection peak in the proposed injection system is uniform regardless of the position of the detection probe in the separation channel, and the peak resolution is greatly enhanced. Type “e”, similar to what Tsai et al. [62] and Fu et al. [63], was presented as a new design with an expansion chamber located at the inlet of the separation channel. Both groups demonstrated

that for a particular expansion ratio and expansion length, the peak intensities of the sample are sharp and clearly distinguishable.

More-complicated designs, like the serpentine separation channel and arrays of microchannels, are addressed in a review paper by Dolnik et al.[39].

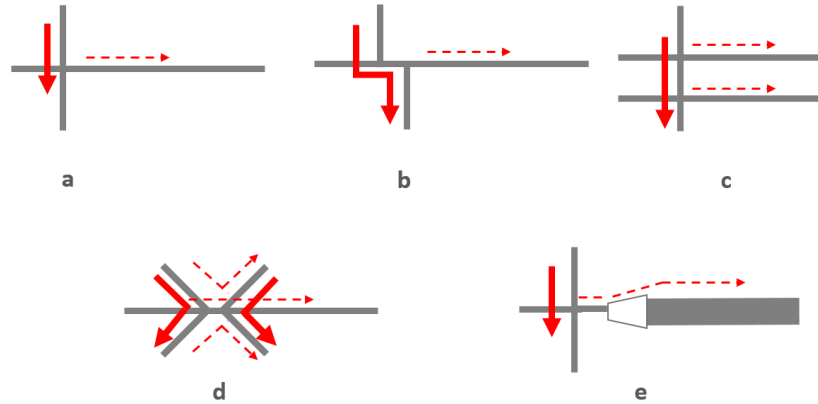


Figure 7: Schematic of channel geometries (solid arrows: injection and dashed arrows: separation)

2.1.3.3 Microchannel Dimensions

According to literature, the typical channel depth is $10 - 50 \mu m$ and the width of the channels are $30 - 200 \mu m$.([64]–[66]). Table 1 shows the dimensions of the channels and chip material for a few cases in literature.

Table 1: A few references for channel dimensions in literature

| | Length | | Width (μm) | Depth (μm) | Reference | Chip Material |
|---|-------------|------------|----------------------|----------------------|----------------------------------|------------------|
| | Injection | Separation | | | | |
| 1 | 280 mm | 70 mm | 30 | 10 | Fan and Harrison [66] | Glass |
| 2 | $150 \mu m$ | $90 \mu m$ | 30 | 10 | Patankar and Hu computations [9] | Glass |
| 3 | 13 mm | 50 mm | 100 | 20 | Zhuang et al. [67] | silica glass |
| 4 | 12.5 mm | 12.5 mm | 120 | 20 | Xuan et al. [58] | PDMS |
| 5 | 20 mm | 37 | 40 | 18 | Wang et al.[68] | PDMS |

2.1.3.4 Electric potential/field configurations at injection and separation

Several voltage-controlled (electric field-controlled) configurations have been reported in the literature to improve the sample plug shape and consequently the separation resolution.

The first row in Figure 8, shows an uncontrolled simple/direct injection method. The sample disperses into the separation channel, and depending on the width of the sample plug and the concentration drop, while passing by the detector, could result in poor resolution. Ideally, the rectangular plug at the cross provides the best separation resolution due to one-dimensional diffusion at the interface of the sample and buffer. The effect of sample shape is thoroughly discussed in Chapter 4. The applied electric fields at injection are the controlling feature of the shape of the sample plug. Therefore, to limit the dispersion of the sample into the separation channel at injection, the pinched/focusing/triangular injection configuration [64] is applied, as shown in the second row of Figure 8. In this injection method, pinching voltages are applied to the buffer reservoirs of the separation channel during the sample injection phase. The pinching electric forces counteract the diffusion of the sample into the separation channel. In the following separation phase, back voltages are applied at the sample and sample waste reservoirs of the injection channel to draw the injected extra sample back to the reservoirs, preventing sample leakage into the separation channel during separation. The drawback of the pinched injection method is the difficulty of determining the exact amount of sample, but it has good injection reproducibility. A narrow sample zone in this configuration will be resolved better than the uncontrolled sample zone. The third-row configuration shows a floating injection configuration [64], in which the sample is migrated in injection phase with no voltage control at the buffer reservoirs of the separation channel. The separation is controlled similar to in the pinched configuration to avoid leakage. During floating injection, due to the diffusion of the sample into the separation channel and also the duration of floating voltages, more high-concentration sample is pushed to the separation channel. Thus, the floating method forms a compromise between reproducibility and detection sensitivity.

Another configuration, shown in the last row of Figure 8, represents so-called gated-injection [69]. In contrast with previous configurations, gated injection has a permanent flow of the sample and buffer solution, each making a 90-degree turn flow at separation, whereas the buffer flow is interrupted at injection. The gated valve is capable of dispensing sample plugs of variable volume and provides unidirectional flow in the separation channel. The continuous buffer flow in separation prevents sample leakage into the separation channel. The periodic sample injection from a continuous flow of the analytes is advantageous, especially for coupling the electrophoresis process with on-chip derivatization [70]. Besides the fast injection, it is also possible to change the sample for continuing injection. However, the very limited volume of the sample results in poor detection sensitivity. The gated configuration also requires two HV sources and two HV switches.

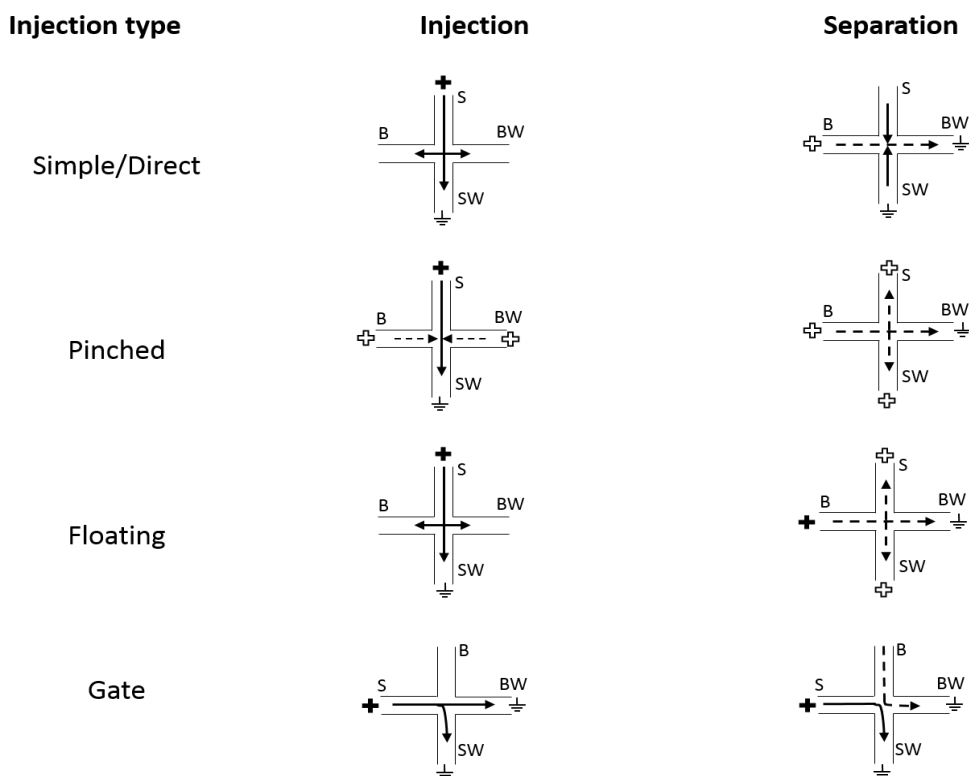


Figure 8: Schematic of voltage-controlled configurations, S:sample, SW: sample waste, B:buffer, BW: buffer waste; solid arrows: sample, dotted arrows: buffer

2.1.3.5 Limits of applied electric fields, electric safety

Increasing the applied voltages or indeed the electric fields has some benefits in electrophoretic separation. A higher electric field moves the sample faster and decreases analysis time. Giving the sample less chance to diffuse through faster migration, can also improve the separation resolution and resolved peaks. However, in very high electric fields, the Joule heat may not be dissipated efficiently. High temperature can result in sample denaturation, decreased viscosity, which leads to increase in EOF and ion mobility as well as faster sample diffusion, resulting in band broadening and loss of resolution. The electrical fields typical in microfluidic applications are on the order of $10\text{ kV}/m$, with the typical channel dimensions on the order of 10 mm , the potential differences between reservoirs will be on the order of $100V$. High electric fields are not only detrimental to biological samples, but can also cause the

electrolytes to lose their dielectric properties. They can also cause chip breakage due to a high local electric field and consequent high local temperature.

2.2 Electroosmotic and electrophoretic mobilities

As previously discussed, once the voltages are applied to the reservoirs of the separation channel, the electroosmotic flow is created, causing bulk flow movement from the injection point towards the cathode when the walls are negatively charged. Based on their differing mobilities or velocities, all sample components are carried with the buffer solution in a migration order which depends on the difference between the electroosmotic and electrophoretic mobilities (Figure 9). EOF is generated at the surface-solution interface, and the relative velocity between each component and buffer flow leads into the separation of sample components.

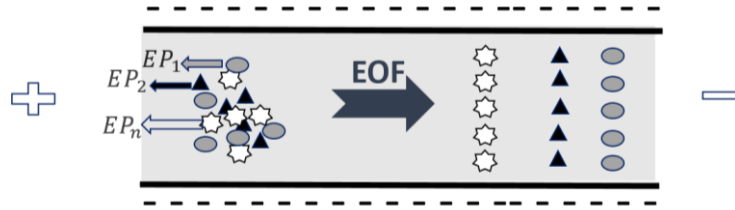


Figure 9: Schematic of separation of sample components due to their different electrophoretic mobilities. Electrophoretic mobility is the migration characteristic of the charged particles under an applied electric field. For a charged particle, the balance of electrical force and liquid viscous drag force are presented in Figure 10. The electrophoretic mobility will be proportional to the applied electric field as well as the net charge of particles. Since drag force is an opposing force, it will be inversely proportional to the viscosity of the liquid.

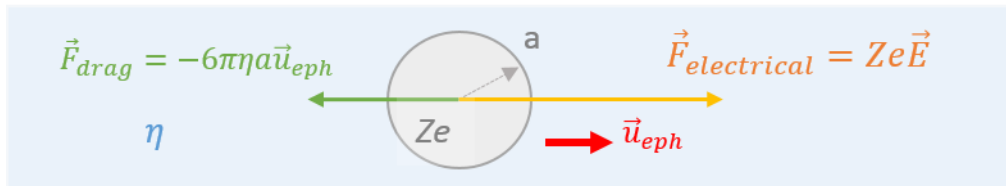


Figure 10: The balance of electrical and viscous forces on a particle

In a low conductivity liquid with viscosity η , where the migration velocity of the particle is \vec{u}_{eph} , the drag force in the Stokes flow around the spherical particle equals to $\vec{F}_{drag} = -6\pi\eta a \vec{u}_{eph}$, where a is the Stokes radius of the particle. On the other hand the driving electrical force equals to $\vec{F}_{electrical} = Ze\vec{E}$, where Ze

is the total net charge of the analyte. The balance of the forces on the moving particle is as $\Sigma \vec{F} = \vec{F}_{drag} + \vec{F}_{electrical} = 0$; therefore, the electrophoretic velocity appears as

$$\vec{u}_{eph} = \frac{Ze}{6\pi\eta a} \vec{E} \quad (1)$$

The coefficient of the electric field on the R.H.S of (1) is defined as electrophoretic mobility

$$\mu_{ep} = \frac{Ze}{6\pi\eta a} \quad (2)$$

which shows the motion of a charged particle in an electrolyte solution under the applied electric field

$$\mu_{ep} = \frac{\vec{v}_{ep}}{\vec{E}} \quad (3)$$

Atkinson [71] provided experimental values for ionic mobilities for small ions in aqueous solutions at low concentrations. Bruus and Kirby, [10] [11], reproduced the table of electrophoretic mobilities for a few ions like H^+ , K^+ , Na^+ and Cl^- , OH^- ranging from $(36.2 - 20) \times 10^{-8} \left[\frac{m^2}{V.s} \right]$. For $Z = 1$, $\eta = 1 \text{ mPa.s}$ and $a = 0.2 \text{ nm}$, $\mu_{ep} = 4 \times 10^{-8} \left[\frac{m^2}{V.s} \right]$. Figure 11 shows the size comparison of DNA and protein particles and other biological assemblies. In this research, Fluorescein and Rhodamine are used instead of biological samples and their electrophoretic mobilities are taken as $-3.3 \times 10^{-8} \left[\frac{m^2}{V.s} \right]$ and $-1.65 \times 10^{-8} \left[\frac{m^2}{V.s} \right]$ respectively.

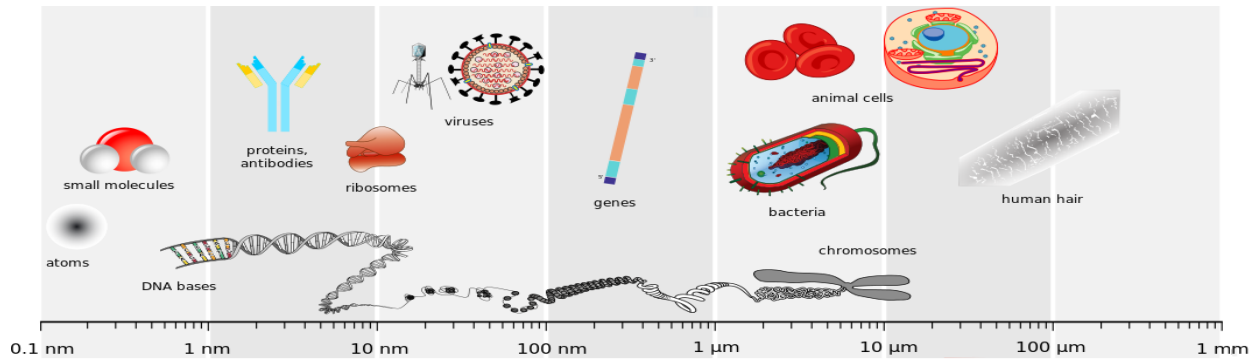


Figure 11: Comparison of various biological assemblies and technological devices

In addition to the size of particles, equation (2) shows the significance of the charge to size ratio, as shown in Figure 12, is an important factor in the mobility of a particle. In an electrophoretic separation, based on Newton's second law, the particle acceleration under the applied electric field equals $\vec{a} = \vec{E}q/m$, which shows the role of charge to mass ratio in electrophoretic separation.

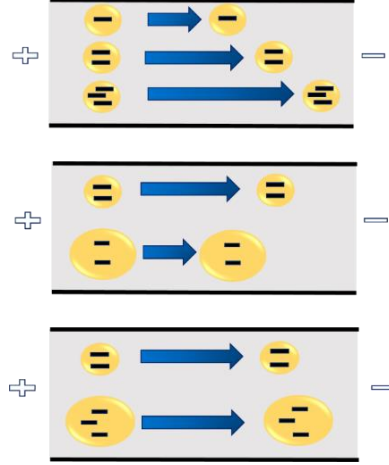


Figure 12: Charge to size ratio is the principle of the electrophoretic separation

This ratio shows that for the purpose of biological sample separation through electrophoresis, the smallest particles with the highest charge move faster in the separation channel. For DNA sample particles, which are negatively charged, shorter DNA molecules move faster than longer ones. Proteins, which are more complicated and carry both positive and negative charges, generally separate based on their charge, which is determined by the PH of the sample solution.

The electroosmotic mobility of a solution, $\mu_{eof} = \frac{\vec{v}_{efo}}{E}$, is defined as

$$\mu_{eof} = \frac{-\epsilon\zeta}{\eta} \quad (4)$$

where, ϵ is the relative electric permittivity of material, ζ is zeta potential and is an experimentally observed quantity that has units of volts, and η is the viscosity of the fluid. In this thesis the electroosmotic mobility of buffer solution is set to $4.5 \times 10^{-8} \left[\frac{m^2}{V.s} \right]$. According to Kirby, [10], a typical magnitude observed for electroosmotic mobility in aqueous systems is on the order of $1 \times 10^{-8} \left[\frac{m^2}{V.s} \right]$. He provided a table for different wall materials like glass, silicon, PDMS and polycarbonate, $1mM$ of $NaCl$ buffer solution at neutral pH, with μ_{eof} in range of $(1 - 3) \times 10^{-8} \left[\frac{m^2}{V.s} \right]$. It is noted that the permittivity of the region can be measured with respect to the vacuum permittivity, i.e. $\epsilon = \epsilon_r \epsilon_0$, where ϵ_r is the relative permittivity and ϵ_0 is the permittivity in a vacuum.

In comparison with the velocity profiles in a microchannel in the pressure driven flow, EOF velocity is a plug like, which is the main reason for using electrokinetic transport to achieve the plug shape sample at injection (Figure 13). Pressure driven flows will add more Taylor-Aris dispersion effect, in which a shear flow can increase the effective diffusivity of species. Essentially, the shear acts to diffuse the concentration distribution in the direction of the flow, by enhancing the rate at which it spreads in the flow direction.

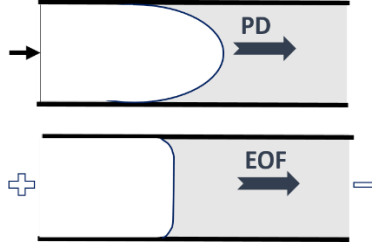


Figure 13: Velocity profiles of EOF versus pressure driven flow

Taking the effect of both electroosmotic and electrophoretic mobilities into account, the apparent velocity, which is the observed velocity of the sample components, is expressed in (5). Figure 14 demonstrates that, depending on the charge of the particle, the electrophoretic and electroosmotic velocities could be in the same or opposite directions.

$$\vec{v} = (\mu_{eof} + \mu_{ep})\vec{E} \quad (5)$$

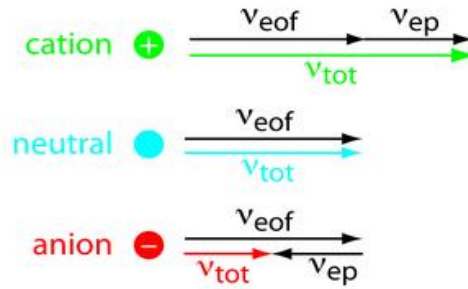


Figure 14: Observed velocity as the result of electroosmotic and electrophoretic velocities

Therefore, for particles with negative charge, which migrate in the opposite direction of the applied electric field, the difference in the magnitude of EOF and EP mobilities is the pace at which the sample components pass by the detector.

One way to measure EOF mobility is to monitor current method. With the important role of electroosmotic velocity in EOF and EP separation, accurate measurements of electroosmotic mobility are significant. The earliest measurement method reported in the literature relies on the injection of an electrically neutral compound, followed by the recording of its migration time through capillaries [72]. This measurement method is independent of the electrolyte or channel walls. However, a fluorescent marker method will be a more precise method, but suffers from issues in detecting the fluorescent agent. The most widely used method so far is the current monitoring method, which measures the electrophoretic current change as electrolytes of different ionic strengths fill the microchannel [73] [74]. The time required to reach a steady-state separation current is used to calculate EOF mobility. The reported precision for average EOF rates measured by this method in CE and microchip CE ranges between 5% and 15%. Based on a similar

measurement principle, conductivity detection monitors the change in bulk solution conductivity between two electrodes, when an analyte band passes through the electrode gap.

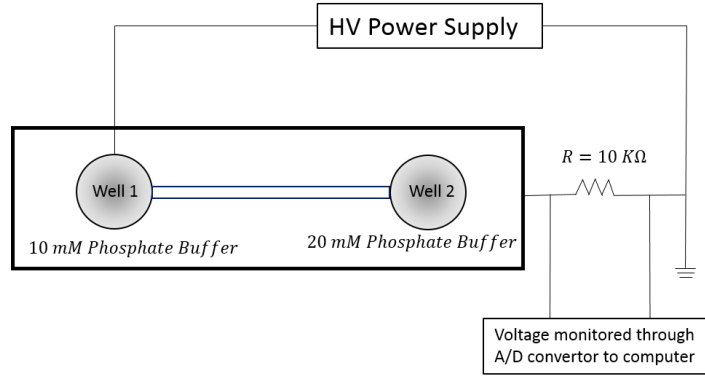


Figure 15: Principle of the electroosmotic measurement with current monitoring method ($1\mu A$ current \rightarrow $10mV$ voltage drop) [75]

2.3 Diffusivity

At the interface of the biological sample and the solvent (buffer solution), diffusion plays an opposing role in the separation of sample constituents. In electrophoresis separation, diffusivity and electrophoretic mobility are related phenomena and can be calculated from one another. Diffusivity is a measure of random motion of species because of random thermal molecular motion, Brownian motion. Electrophoretic mobility is a measure of species' motion because of an electric field. Moreover, diffusion plays a key role when there is a concentration gradient between the sample and buffer solution. The dependence of the diffusion coefficient on the viscosity can be modeled by the Stokes-Einstein relation. According to this equation, the diffusion coefficient is related to particle mobility, as shown below

$$D = \mu K_B T \quad (6)$$

where, μ is the "mobility" of a particle under applied electric field, K_B is the Boltzmann constant (Appendix A) and T is temperature. There are two ways of defining diffusion coefficient based on the Stokes-Einstein relation: One is diffusion of spherical particles through a liquid with low Reynolds number

$$D = \frac{K_B T}{6\pi\eta a} \quad (7)$$

where, a is the radius of the particle and η is the buffer viscosity, and the other way is through electrical mobility equation, for diffusion of charged particles with μ_{ep} mobility which based on the balance of electrical and drag forces becomes

$$D = \frac{\mu_{ep} K_B T}{q} \quad (8)$$

In Chapter 3, we show how diffusivity is related to concentration gradient. For the diffusion of a single solute, the diffusion constant D , diffusivity, determines how fast a concentration diffuses a certain distance. For example, the diffusivity of sugar molecules in water or 30-base-pair DNA molecules in water is respectively 5×10^{-11} or $4 \times 10^{-11} \left[\frac{m^2}{s} \right]$. The diffusivity in all simulations in this thesis is $4.37 \times 10^{-10} \left[\frac{m^2}{s} \right]$.

2.4 Separation Resolution

The conventional definition of resolution is explained in this section; however, in Chapter 4 a modified definition of that is introduced and discussed in details. In electrophoretic separation, resolution is defined as the efficiency of resolving sample components. Experimentally, when the sample components go through the separation process and pass by the detector, the distance between the adjacent peaks as well as the distance between the baselines of those peaks are good benchmarks of resolving sample components. Giddings [76] was one of the pioneers to address the definition of resolution in terms of the number and height of theoretical plates in electrophoresis. Later Jorgenson et al. [77] expanded the definition of Giddings' resolution to a parameter involving the applied electric field as well as sample properties such as electrophoretic mobilities and diffusion coefficient. Luckey et al. [78] also determined the resolution by the width of DNA bands in capillary gel electrophoresis. There are much research carried out in electrophoretic separation which pointed out to the definition of resolution. A few could be named as the research presented by Effenhauser et al. [59] for a high-speed gel electrophoretic separation due to very high electric fields of 2300 V/cm in DNA sequencing. Molho et al., [40], Bharadwa et al., [79], David Ross, [80], Viefhues et al., [81] and Simhadri et al. [82] all addressed the same definition of resolution as separation efficiency in electrophoresis. As shown in Figure 16, the resolution is defined as the ratio of the distance between the centers of two adjacent peaks to the average of the base widths for those peaks, therefore:

$$R_s = \frac{\Delta x}{0.5 * (w_{B,1} + w_{B,2})} \quad (9)$$

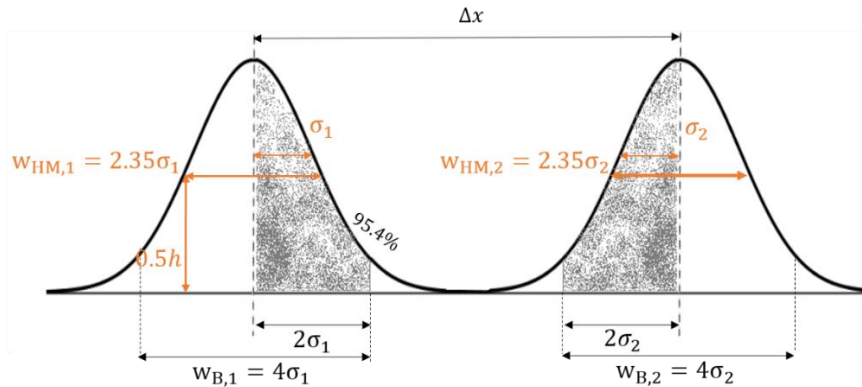


Figure 16: definition of resolution for two adjacent peaks

However, with no clear edges at the interface of the sample and the buffer solution, measuring the base width is not possible experimentally. For this purpose, by seeing the peaks clearly the full width at half maximum is applied. To correlate the base width with the width at half maximum point, a Gaussian concentration distribution with standard deviation of σ_i is assumed for each component. For such distribution, the width of the baseline for 95.4% of the distribution is $4\sigma_i$ and $w_{HM,i} = 2.35\sigma_i$. Therefore, the definition of resolution in terms of full-width at half maximums becomes $(\sqrt{2\ln 2}) \frac{\Delta x}{(w_{HM,1} + w_{HM,2})}$ or:

$$R_s = \frac{\Delta x}{0.85 (w_{HM,1} + w_{HM,2})} \quad (10)$$

As shown in Figure 17, for a Gaussian distribution, 4σ encompasses the base width for 95.4 %, such that the peaks overlap by 2.3 % $((100 \% - 95.4 \%)/2)$. This indicates that 2.3 % of the peak intrudes into the adjacent peak for a resolution of one. Similarly, a resolution of 1.5 indicates a difference in retention time of $1.5 \times 4\sigma = 6\sigma$, which corresponds to 99.7% of the distribution and an overlap of 0.15 % $((100 \% - 99.7 \%)/2)$.

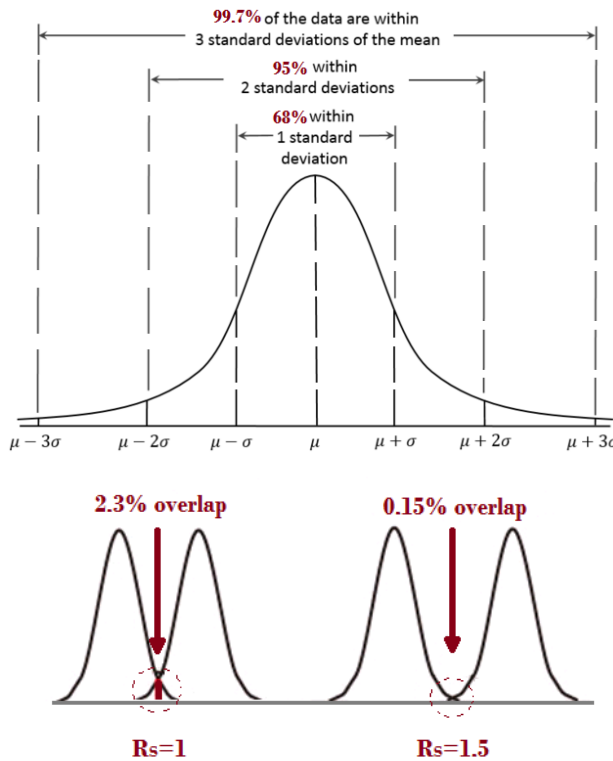


Figure 17: Peak overlaps for a Gaussian distribution in resolutions of 1 and 1.5

To achieve a good separation of sample components, the detection method and sensitivity of the detector play key roles. For the purpose of separation resolution, chapter 5, an introductory knowledge of detection methods is presented in the following.

2.4.1 Detection methods

Identification of the unknown analytes is carried out by comparing the recorded UV/Vis absorption spectrum with spectral libraries. The detection is a single point detection at separation channel; however, whole-column imaging detection (WCID) can be applied for specific applications [83] [84].

UV absorption: This traditional indirect detection method is very popular in electrophoresis. It employs strongly UV-absorbing fluorescent markers, but has high limits of detection because the shallow channel sizes demand small path lengths. The fluorescent markers are added to the entire buffer to provide a uniform background signal, then in the separation channel, the non-fluorescent sample displaces the fluorescent buffer, and the local reduction in the signal marker ions indirectly detects the sample of interest [53] [85]. In addition to its low sensitivity due to small depth of microchannels and therefore small path wave length, this method is susceptible to false identifications due to the presence of system peaks [86].

Laser Induced Fluorescent (LIF): The history of micro total analysis systems shows that fluorescence detection has been the most-popular detection method for microfluidic platforms. Fluorescent labeling has been used due to its high sensitivity and ease of application in microfluidic devices [64]. In electrophoresis, the most common detection method for fast separations is LIF, which necessitates sample derivatization with fluorescent material if the sample of interest is not a native fluorescent material. After derivatization, a laser is used to induce fluorescence for intensity measurement. This method has high sensitivity. However, scattering of light from microchannels can cause noise and decrease signal-to-noise ratios. Moreover, due to lack of fluorophore nature in most of the analytes, derivatization is required, which is time consuming and has some sample compatibility challenges.

Miniaturizing both UV and LIF detection systems is problematic for portable devices, whereas electrochemical detection aligns well with miniaturization goals because small electrodes can be fabricated to work on chip.

Electro-Chemical Detection (ECD): This alternative to optical detection methods in rapid electrophoretic separations suits microchips well, has high sensitivity and requires no derivatization. It can be carried out

for different detection modes: amperometry, voltammetry, conductometry, and potentiometry. Among these modes, amperometric detection is the most popular ECD method for on-chip electrophoresis due to its easy operation and minimal background-current contributions. [87]. This method is based on measuring oxidation or reduction currents of the analytes on a working electrode and is therefore restricted to electro-active species [88]. Its main drawback is that noise from the separation of electrodes and high voltage sources must be minimized. After grounding the separation voltage before the electrodes, no EOF and consequent band-broadening due to diffusion occurs [89].

Mass spectrometry (MS): Another useful method in analytical chemistry is mass spectrometry by coupling the microchip with a mass spectrometric detector. However, the detection of low mass samples, coupling of the separation channel to the mass spectrometer and the micro-scale fabrication of ionized interfaces are still challenging.

2.4.2 Ways to improve limits of detection and flow visualization

Many macroscale-flow visualization techniques have been successfully adapted to microscale flows. Particle-based or dye-based visualization with different methods of acquiring data and flow analysis have been developed for microfluidics applications, including Laser Doppler Velocimetry (LDV), Particle Streak Velocimetry (PSV), Particle Image Velocimetry (PIV), all in microscales and using fluorescently labelled particles with the challenges of micro-size particles. Due to their small size however, molecular tracers have much higher diffusion coefficients than micro-sized particles, which can lower the spatial resolution and velocity resolution of the measurements [90]. On the other hand, in dye-based measurements, the electrokinetic migration of the charged dye species should be considered. A few dye-based methods are Laser-Induced Fluorescence (LIF), Flow Tagging Velocimetry (FTV), and Molecular Tagging Velocimetry (MTV). The mechanism in all these techniques is based on fluorescent characteristic of the labelling/tagging dyes. A photon is absorbed by the fluorophore, increases its energy to an excited state, and remains in that state for a finite period of its lifetime. Then, the absorbed energy of the fluorophore starts dissipating, and finally the fluorophore releases the photon of energy and returns to its ground state. For dye-free detection, new phluorophores like silver nanoclusters (Ag NCs) are used as labelling material and are even smaller than semiconductor quantum dots. Yeh et al. [91] , showed that theses nanoclusters have better photo stability and brightness than commonly used organic dyes. Yang and Vosch [92] also presented DNA/AgNC probes as simple and inexpensive tools for rapid, specific, and sensitive detection of micro RNAs, which is an important field of research in disease diagnosis.

Photo-bleaching or losing fluorescence properties due to over exposure is also an issue in these flow visualization or detection methods [93]. To overcome this issue, Caged-fluorescent dye method is applied to fluorophore molecules with additional chemical groups that cause rendering non-fluorescent effect. A caged fluorophore is “uncaged” by exposure to certain electromagnetic radiation that breaks the bonds attaching the caging groups. With a photolysis process, the original fluorescent dye is then recovered, and it can be tracked indefinitely using ordinary fluorescence imaging approaches. David Sinton [94] clearly explains the variety of microfluidics methods as briefly mentioned above.

2.5 Other Techniques to Couple with Electrophoresis

As previously mentioned, in electrophoretic separation, based on Newton’s second law, the particle acceleration under the applied electric field is $\vec{a} = \vec{E}q/m$, which represents the charge to mass ratio. Since the charge of DNA is proportional to its size, the q/m ratio remains constant for different DNA sizes. Thus, with no buffer, all the DNA particles (small to large) move at the same pace. Adding a sieving matrix like the buffer solution creates different resistances to different-sized DNA fragments; therefore, size-based separation occurs. In electrophoretic separation, the right choice of buffer is essential. First of all, a buffer must be selected that does not interfere with the detectability of the sample components and maintains solubility of the sample. If UV absorbance detection is used, the buffer should result in low-absorbance at the desired detection wavelength. If electrochemical detection methods are used, the buffer should be compatible with the sample and also have a stable background conductivity. The pH of the buffer should also be close to neutral and increasing the pH to between 4 and 9 results in increasing the EOF. According Landers et al. [95] increasing the buffer pH from 8.61 to 11.64 results in identifying a greater number of peaks, i.e. five peaks for a sample with five peptides. So, at a given pH, the choice of buffer effects the separation resolution due to the buffer’s electroosmotic mobility. Moreover, buffer concentration has a significant effect on mobility. This effect has been reported in the literature several times. Bruin, et al. [96] studied overall mobility versus buffer concentration. Nashabeh and El-Rassi [97]also presented data on buffer concentration effects on mobility. In the results presented by Issaq et al. [33], the migration time of any solute increases and the separation factor improves with increasing concentration. The linear relationship between solute migration time and the square root of concentration suggests that the migration time will double for every four-fold increase in buffer concentration. The bigger the difference in the net mobility of two neighboring solutes, the larger their separation factor at higher concentrations. Issaq et al. [33] determined the maximum applied voltage that works best for each buffer concentration. The maximum buffer concentration and applied voltage was determined for each buffer concentration, then

Ohm's law (current versus voltage curve) was plotted. From each plot, the maximum voltage at which the curve begins to deviate from linearity was recorded. The generated data was then plotted as maximum voltage versus buffer concentration. The results represents a practical guide for the selection of buffer concentrations and applied voltages for phosphate and acetate buffers.

2.5.1.1 Free Flow Electrophoresis (FFE)

Another technique used in separation of biomolecules based on sample electrophoretic mobilities is Free Flow Electrophoresis (FFE). An electric field is applied perpendicularly to the direction of flow to deflect analytes into distinct streams [98][99]. In FFE, pressure is used to drive a sample stream through a planar separation channel. Unlike CE, sample injection, separation, and collection can take place continuously because the direction of the separation is different from that of the bulk flow. The continuous nature of this technique provides a high-throughput separation mechanism. This technique could be coupled with electrophoretic separation as two-dimensional separation to promise separation of sample constituents with marginal electrophoretic mobilities. Figure 18 shows a Schematic of capillary electrophoresis vs. free-flow electrophoresis.

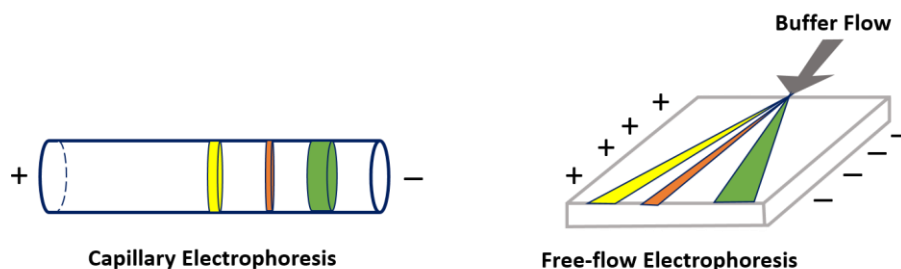


Figure 18: Schematic of capillary electrophoresis vs. free-flow electrophoresis

2.5.1.2 Field-Amplified Sample Stacking (FASS)

Buffer conductivity and conductivity gradient are studied in much research to improve separation. A one-dimensional analogy holds in resistive electrical networks and electroosmotic and electrophoretic transport in microchannels with long axial-to-radial dimension ratios. In such an analogy, Kirchhoff's current and voltage laws can be used to predict flow rates in a network of electroosmotic channels under applied voltages at the reservoirs at the end of channels. All of the current, and hence all of the flow, entering a node must also leave that node, and the resistance of each part of the network can be determined by knowing the cross-sectional area, the conductivity of the liquid buffer, and the length of that part. One

way to improve the limits of the detection in on-chip electrophoresis, especially for low concentration samples, is Field-Amplified Sample Stacking (**FASS**), shown in Figure 19. Additionally, an on-line pre-concentration process can be integrated for sample analytes. Sample pre-concentration offers higher sensitivity assays, robust electrokinetic injection schemes, and the use of detection modes less sensitive than fluorescence, such as electrochemical detection [2]. This technique was first discussed by Mikkers et al. [100] and also presented by Santiago's group at Stanford [101]. In FASS, conductivity gradients between the injected sample and the background buffer are leveraged to increase sample concentration. However, a major challenge in applying FASS to on-chip assays is the initial setup of high conductivity gradient boundaries in the region of the injected sample volume. Jung et al. [101] overcame this challenge by facilitating a porous polymer structure in the separation channel. This porous structure enabled them to use a pressure-injection scheme for the introduction of a high-conductivity gradient in the separation channel and thus prevented the flow instabilities associated with high-conductivity gradient electrokinetics.

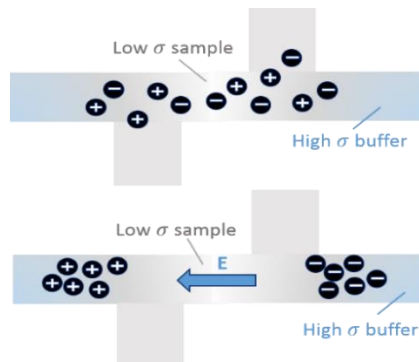


Figure 19: Schematic of Field-amplified Sample Stacking (FASS) technique to for increase the concentration of sample [102]

2.5.1.3 Isotachopheresis (ITP)

Another technique used to increase separation by means of heterogeneous buffer solutions is **Isotachopheresis**, whereby a sample is sandwiched between a trailing buffer and a leading buffer, and so sample ions move faster than the trailing buffer but slower than the leading buffer Figure 20. Then, under the applied electric fields, sample zones are formed based on their electrophoretic mobilities. With defined conductivity boundaries, each zone migrates at a certain velocity, and ions in that zone migrate with the same velocity; therefore, the phenomenon is called Isotachopheresis. This method is presented in several studies [103]–[106].

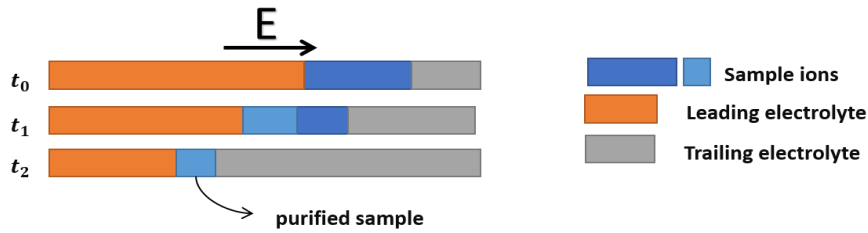


Figure 20: Isotachopheresis

2.5.1.4 Isoelectric focusing (IEF)

Utilizing heterogeneous buffers allows varying many physical properties to be varied, including the buffer pH. Isoelectric focusing (IEF), is another electrophoretic technique which employs a background buffer containing molecules that can be either negatively charged, neutral, or positively charged, depending on the buffer pH. The pH at which a molecule is neutral is called the isoelectric point, or pI. Under an applied electric field, a pH gradient is formed along the channel. When a sample is injected into a channel filled with buffer, the sample migrates up to a location where the sample pH equals to the pI of its molecules. Thus IEF concentrates initially dilute amphoteric samples and separate out their constituent parts according to their isoelectric point. Because of this behavior, IEF is often used as the first dimension of multidimensional separations [107] [34].

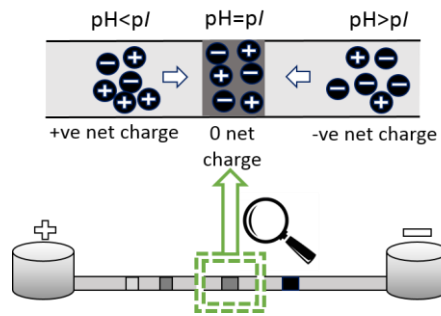


Figure 21: Isoelectric focusing (IEF)

Another technique in electrophoretic separation, by controlling the non-physical parameters, is temperature-gradient focusing (TGF).

2.5.1.5 Temperature gradient

Another method of sample stacking is Temperature Gradient Focusing (TGF), whereby an axial temperature gradient applied axially along a microchannel produces a gradient in electrophoretic velocity. When opposed by a net bulk flow, charged analytes focus at points where their electrophoretic velocity and

the local, area-averaged liquid velocity sum to zero. More details of this method are presented in studies by Ross and Locascio [108] and also by Shameli et al. [109], [110].

In the next chapter, the problem formulation for the electrokinetic migration of the sample in the microchannels is provided. To understand the details of the thin electric double layer adjacent to the microchannel walls and its effect on the bulk flow, the distribution of ions and electric potential are discussed in detail in Appendix A.

Chapter 3

Problem Formulation

3.1 Introduction

In this chapter, problem formulation for the cross-linked microchannels is presented. Assuming the Electric Double Layer (EDL), all the governing equations and boundary conditions are provided. Then in the following chapter, more details of the EDL are addressed. Then, the problem formulation in non-dimensional form is presented when the effect of EDL is seen on boundary conditions.

3.2 Chip Configuration

For the electrophoretic separation in microchannels, a sample is injected from the injection channel by an applied voltage, with electroosmosis as the driving force. The applied potential is switched from the injection channel to the separation channel, then, after the sample is situated in the separation channel, the sample species start to separate based on the differences in their electrophoretic velocities. Figure 22 shows the geometry of the cross-channel, which is the first geometry studied this research.

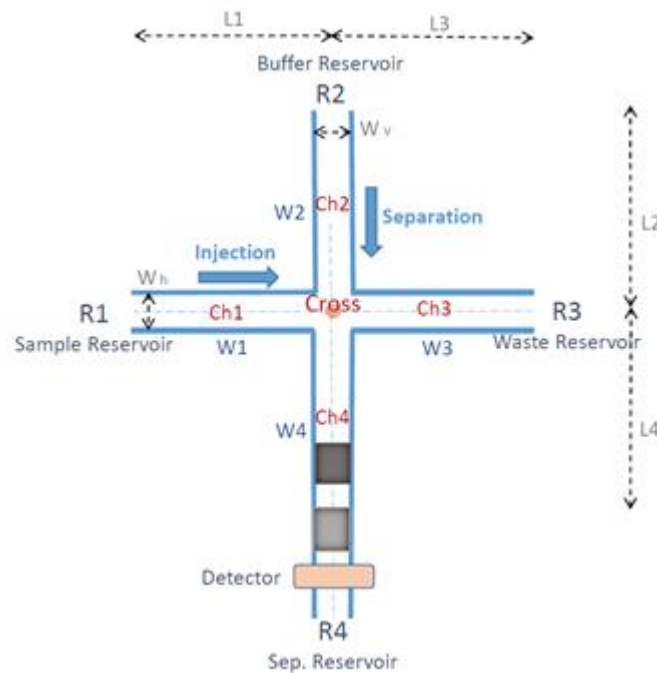


Figure 22: Cross-channel geometry of the microchip

3.3 Problem Formulation, Dimensional Governing Equations and Boundary Conditions

As discussed previously, Electroosmotic flow (EOF) problem can be modeled by considering electric body force term, exerted on ions appearing in right hand side of Navier–Stokes equation. This force is observed by applying external electric potential on any electrolyte fluid. In other words, by applying an external electric field in presence of EDL, ions motion begins and the external electric field interaction with EDL forms an electrokinetic body force on bulk flow which is considered as body force term in right hand side of fluid momentum equation. Since governing equations are coupled and the effect of EDL is narrowly confined to the wall (Appendix A), we have to solve $\nabla^2 \phi = 0$ for externally applied electric field as well as mass and momentum equations. In the Appendix A, the details of ions distribution in EDL, the Poisson-Boltzmann equation and three solutions to that are presented. Here, we first show the governing equations and the way potential distribution affects our fluid flow and how it is reflected in body force term in fluid momentum equation.

As shown in Figure 22, a common geometry for separation of DNA or protein sample is the crossing microchannels. The horizontal channel is considered for sample injection and the vertical channel for sample separation. To have an efficient, high resolution separation, a rectangular shape for the sample plug at the intersection of the channels is desired.

The governing equations to be considered are the following:

1. Electric field
2. Flow field including continuity and momentum
3. Concentration field (solved for each species)
4. Energy field

In order to perform numerical simulations for electrophoretic separation, three sets of governing equations must be solved: electric potential equation, flow field equations and concentration equations. In Section 3.3.4, it is shown that energy equation is not solved when Joule heating is negligible.

3.3.1 Electric Field Equation

In problems with a thin electric double layer (EDL), on the order of nanometers, the double layer equations are not solved for ion and potential distribution. However, the effect of the EDL is imposed on the bulk flow as a slip boundary condition, similar to a conveyer layer moving with the electroosmotic velocity. Initially, the microchannels are filled with buffer solution, and then the sample material is injected from R_1 . The sample is a solute within the buffer so the basic fluid properties are those of the buffer. Since the sample concentration is on the order of μmol and the buffer's is on the order of mmol , the electrical

conductivity of the buffer dominates. Diluting the sample with buffer solution, there is no electrical conductivity difference between sample and buffer, and also in the region with zero electric charge density for the bulk flow, i.e., $\rho_e = 0$, the potential equation becomes Laplace's equation, $\nabla^2 \phi = 0$, which, in two dimensional space, is the following:

$$\frac{\partial^2 \phi}{\partial x^2} + \frac{\partial^2 \phi}{\partial y^2} = 0 \quad (11)$$

Potentials are applied at the reservoirs of the injection channel during the injection phase, while the reservoirs of the vertical channel are set to floating or specified voltages, according to the desired configuration to attempt to shape the injected sample. The walls of the channels are electrically insulated. Thus, the boundary conditions to apply to solutions to (11) are: $\phi_{R_1} = \phi_1$, $\phi_{R_3} = \phi_3$ for R_1, R_3 and $\frac{\partial \phi_{R_2}}{\partial y} = \frac{\partial \phi_{R_4}}{\partial y} = 0$ (floating) or $\phi_{R_2} = \phi_2$, $\phi_{R_4} = \phi_4$ (specified) for R_2, R_4 . For the channel walls, we have $\frac{\partial \phi}{\partial n}|_{walls} = 0$.

3.3.2 Flow Field Equations

The continuity equation for an incompressible Newtonian fluid is $\vec{\nabla} \cdot \vec{V} = 0$. For momentum equation we should take electric force into account which is due to net charge density and applied electric field, so electroosmotic body force shows up in general Navier-Stokes equation (12).

$$\rho \left[\frac{\partial \vec{V}}{\partial t} + (\vec{V} \cdot \vec{\nabla}) \vec{V} \right] = -\vec{\nabla} p + \mu \nabla^2 \vec{V} + \rho_e \vec{E} \quad (12)$$

Knowing \vec{V} as the flow velocity, p as pressure, μ the dynamic viscosity, ρ density and ρ_e the charge density, we show how we can neglect some terms based on our so-far understanding of the problem. In Appendix A we show that net charge density, ρ_e , is zero everywhere except in the very thin electric double layer near wall. On the other hand, there would be no body force term for the bulk flow in (12). The gravity force is neglected because of the small height of microchannel being about one fifth of the channel width. Before delving into the flow field boundary conditions, the effect of electrical body force term and EDL on the flow field boundary conditions must be discussed. We discuss the details of EDL and its effect on flow field boundary conditions in Appendix A and showed that for the microscale devices, the EDL is very thin and on the order of nanometers. For such a thin double layer, we do not care about the flow details inside the EDL and solve the problem by using an equivalent asymptotic approach. Therefore, the Coulomb forces are ignored outside the double layer and EDL effect is seen as a slip wall boundary condition, which is defined by electroosmotic mobility. Assuming no EDL in the microchannel, to solve for the fluid flow velocity and pressure, we have to solve the continuity and momentum equations for the incompressible

Newtonian fluid in simplified forms of $\vec{\nabla} \cdot \vec{V} = 0$ and $\left[\frac{\partial \vec{V}}{\partial t} + (\vec{V} \cdot \vec{\nabla}) \vec{V} \right] = -\nabla P + \mu \nabla^2 \vec{V}$, which leads to the following component forms:

$$\frac{\partial u}{\partial x} + \frac{\partial v}{\partial y} = 0 \quad (13)$$

$$\begin{aligned} \rho \left[\frac{\partial u}{\partial t} + \left(u \frac{\partial u}{\partial x} + v \frac{\partial u}{\partial y} \right) \right] &= -\frac{\partial P}{\partial x} + \mu \left(\frac{\partial^2 u}{\partial x^2} + \frac{\partial^2 u}{\partial y^2} \right) \\ \rho \left[\frac{\partial v}{\partial t} + \left(u \frac{\partial v}{\partial x} + v \frac{\partial v}{\partial y} \right) \right] &= -\frac{\partial P}{\partial y} + \mu \left(\frac{\partial^2 v}{\partial x^2} + \frac{\partial^2 v}{\partial y^2} \right) \end{aligned} \quad (14)$$

The reservoirs are set as openings with the flow direction normal to the boundaries and the specified atmospheric pressure $(P - P_a)|_{R_{1-4}} = 0$. The reservoirs are openings because there is no flow driving force at the reservoirs; velocities are the result of the applied electric field on the EDL and the influence of the incompressible continuity equation. In addition, No flow is crossing the channel walls anywhere in the normal direction, so, at R_1 and R_3 , $\frac{\partial u}{\partial x} = \frac{\partial v}{\partial x} = 0$, and at R_2 and R_4 , $\frac{\partial v}{\partial y} = \frac{\partial u}{\partial y} = 0$.

As depicted in Figure 23 electric boundary layers are set to two sides, one is the wall or charged surface and the other one is somewhere far away from wall or say bulk flow along channel center line. On the wall side, we know the surface potential and the no-slip velocity boundary. Whereas along the channel center line we have a zero potential but the velocity is unknown. So to do an equilibrium analysis in EDL, focusing on the direction normal to the wall, we both derive and solve P-B equation. For a negatively charged surface, for ions in EDL there are two forces competing: 1- The electro static forces attracting positive ions to the wall as well as repelling negative ions to the bulk flow and 2- diffusive forces which increase the tendency of the ions to diffuse in the flow like the red dye diffused in water. So, attracting electrostatic force would be balanced with smoothing out diffusive force in equilibrium.

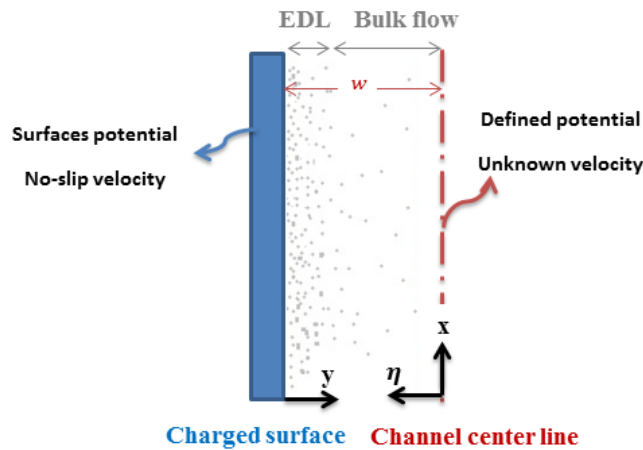


Figure 23: EDL boundary conditions

At the cross sectional ends of the channel, there is no tangential velocity. However, at the walls, tangential velocities deserve more attention because of effect of electric double layer. And this slip-velocity at the wall is indeed due to effect of electric double layer.

$$V_t|_{wall} = -\frac{\epsilon\zeta}{\mu}\vec{E}_{external} \quad (15)$$

Therefore, for the slip walls, the velocity boundary condition at channel walls of injection and separation channels are the electroosmotic velocities along the walls, $V_{\parallel} = \mu_{eo} E_{\parallel}$ and normal to the walls $V_{\perp}=0$. The electric field during the injection phase is $E_x = -\partial\phi/\partial x$ (more details in A). The wall velocities for the separation phase are $v_{walls} = \mu_{eo} E_y$, where $E_y = -\partial\phi/\partial y$ is the electric field during the separation phase. Therefore, the velocity components are $u_{w_{1,3}} = u_{eo}|_{injection/separation}$, $v_{w_{1,3}} = 0$ and $u_{w_{2,4}} = 0$, $v_{w_{2,4}} = v_{eo}|_{injection/separation}$. Initially, there is no fluid motion, i.e. $u, v|_{initial} = 0$.

3.3.3 Concentration Field Equation

For a multi-species sample, the concentration equation for each species is $\frac{\partial c_i}{\partial t} + \vec{V} \cdot \vec{\nabla} c_i = D_i \nabla^2 c_i$, which becomes, for each species:

$$\frac{\partial c_i}{\partial t} + (u + u_{ep,i}) \frac{\partial c_i}{\partial x} + (v + v_{ep,i}) \frac{\partial c_i}{\partial y} = D_i \left(\frac{\partial^2 c_i}{\partial x^2} + \frac{\partial^2 c_i}{\partial y^2} \right) \quad (16)$$

where the electrophoretic velocities are $u_{ep,i} = -\mu_{ep,i} E_x$ and $v_{ep,i} = -\mu_{ep,i} E_y$ and play a key role in the separation of species in a sample. As noted earlier, during the injection phase, the sample is injected from R_1 with a specified concentration, $c_{i,R1} = c_0$ [mol/m³]. R_2 and R_4 are filled with buffer solution with zero concentration, $c_{i,R2,R4} = 0$. R_3 is the waste reservoir for the injection phase into which we keep injecting the buffer and/or sample in the horizontal channel, so the concentration there has a zero gradient, i.e. $\frac{\partial c_i}{\partial x}|_{R_3} = 0$. It is worth mentioning that the condition $c_{i,R2,R4} = 0$ holds for the inflow boundary conditions at $R_{2,4}$ in the case of applying specified voltages. If outflow conditions occur at these reservoirs, the floating condition holds at these boundaries, $\frac{\partial c_i}{\partial y}|_{R_{2,R4}} = 0$. No flow crosses the walls, and the walls are impermeable, i.e., $\frac{\partial c_i}{\partial n} = 0$. Initially, the channels are filled with buffer with zero concentration, i.e., $c_i|_{initial} = 0$

3.3.4 Energy Equation

Energy conservation is not considered in this problem. The reason is that by applying high electrical potential, high dissipation rate is observed due to thermal conductivity of channel walls and high surface-to-volume ratio in microchannels. Therefore, the effect of Joule heating can be neglected and generally we do not consider energy conservation equation except in special situations. Figure 24 shows the heat transfer generated and dissipated in/from fluid element in the microchannel.

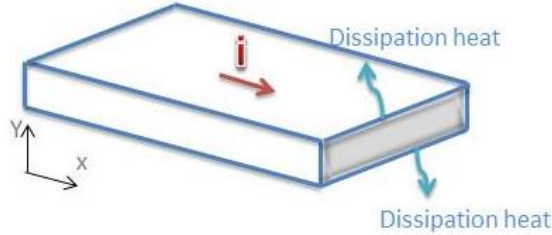


Figure 24: Heat transfer from fluid in microchannel

Having heat transfer equation in (17), and considering temperature gradient along y direction and generated heat due to applied high potential along the channel, then the generated heat would be dissipated to the surrounding area through fluid surface. Assuming insulated wall surfaces for the channel, then:

$$+kA \frac{\partial^2 T}{\partial y^2} + \dot{p}\forall = 0 \quad (17)$$

k is conductive heat transfer coefficient, A and \forall are area and volume respectively and \dot{p} is heat generation which equals to $J\vec{E}$, where J is the current density and \vec{E} is the applied electric field. Convective heat transfer is not considered, since it cools down the fluid and transfers heat out of the system and the transient heat transfer slows down the heating up in the system, therefore:

$$kA \frac{\partial^2 T}{\partial y^2} + JE\forall = 0 \quad (18)$$

Scaling above equation with volume, we get:

$$k \frac{A}{\forall} \frac{\partial^2 T}{\partial y^2} + JE = 0 \quad (19)$$

So, the net heating is dependent on:

- electrical field ($\Delta V/\text{Length}$)
- current ($\Delta V/\text{resistance} = \Delta V * \text{cross sectional area} * \text{electric conductivity of fluid}/\text{Length}$)
- conductivity of chip material (and natural convection if applicable)

- ambient temperature (considered to be constant)
- surface to volume ratio

Taking the non-dimensional form of equation (19), where $T^* = T - T_a$; T_a is ambient temperature, we get:

$$k \frac{A}{V} \frac{\partial^2 T^*}{\partial Y^2} + JE = 0 \quad (20)$$

Integrating above equation with respect to Y , we have:

$$\frac{\partial T^*}{\partial Y} = -\frac{V}{kA} J E Y + C_1 \quad (21)$$

By second integrating, we reach:

$$T^* = -\frac{V}{2kA} J E Y^2 + C_1 Y + C_2 \quad (22)$$

Assuming that the channel material is less conductive than the fluid flow makes the maximum temperature at the center of channel. Moreover, the wall temperature is equal to ambient temperature. So, the boundary conditions are

$$\left. \frac{\partial T^*}{\partial Y} \right|_{Y=0} = 0 \rightarrow C_1 = 0 \quad (23)$$

$$T^*|_{Y=w} = 0 \rightarrow C_2 = \frac{V}{2kA} J E w^2$$

w is the channel width here; therefore,

$$T^* = \frac{V}{2kA} J E w^2 \left(1 - \frac{Y}{w}\right) \quad (24)$$

So at the center of channel, fluid temperature would be

$$T^*|_{Y=0} = \frac{V}{2kA} J E w^2 \quad (25)$$

But due to high ratio of surface to volume, or $\frac{V}{A} = w$. So, the fluid center temperature becomes

$$T^*|_{Y=0} = \frac{1}{2k} J E w^3 \quad (26)$$

So, equation (26) shows that T^* at the center of channel is proportional to the w^3 which is in order of 10^{-18} which even for high electric fields possible is a good proof that the generated heat is dissipated to the surrounding and joule heating effect could be neglected and we do not solve energy equation.

3.4 Conclusions

This chapter provides the problem formulation for the cross-linked channels. The governing equations and boundary conditions are presented for four decoupled fields: electric, flow, concentration and energy fields, in dimensional form. It is briefly explained why the effect of the thin electric double layer on the bulk flow in microchannel is reflected on the slip velocity boundary conditions.

In Appendix A, we provide more details of EDL and ion distribution there. We present the derivation of Poisson-Boltzmann equation from statistical approach to show the electric potential and ion distribution in the electric double layer of microchannels. In Appendix B, we continue with non-dimensionalization of the problem to find the parameters involved and to provide the design for controlling the shape of the sample plug at the cross by the applied electric potentials. The discussion in Appendix B justifies our problem formulation in the current chapter. The details of the distribution of charges in the EDL and bulk flow in microchannels clarifies using the Laplace equation for the zero charge density in the bulk flow for the electric potential distribution and also implementing the slip boundary condition for the flow field. Moreover, at the end of this chapter it is explained why Joule heating effect is neglected and we do not solve the energy equation. Appendix B could be taken as the section following the discussion of problem formulation in third chapter, but in Appendix B, all that problem formulation are discussed in non-dimensional form. We did the non-dimensionalization of the problem to know the parameters involved the problem and to know the length and time scales in the problem. For the cross-shaped microchannel, which is used in this research to control the sample plug shape in the vicinity of the cross, we study the role of the applied voltages and other involved dimensionless parameters, such as Reynolds number, Peclet number, electrokinetic mobilities and velocities. To do a comprehensive non-dimensionalization of the problem, I discussed the possible choices of reference values for length scale, electric potential, velocity, and concentration and, in particular, the use of a convective time scale is compared with that of a diffusive time scale. Finally, the wall electroosmotic velocity, the convective time scale, and the injection/separation channel width are adopted for non-dimensionalization of the problem. In addition to the non-dimensionalization of the problem, I presented some details of the numerical simulation tool and solver, ANSYS CFX. I summarized the main points into the discretization method, implemented solver, the structure of grids, simulation set-up procedure, boundary conditions, and convergence criteria for each field. All the discussions hold true for both injection and separation phases, with minor differences which depend on the flow direction and in particular the choice of a horizontal or vertical injection.

Now that the problem formulation is set and we laid the foundation for better understanding of the problem and parameters involved to control the sample shape at the cross, we start the injection and separation evaluation in the following chapter. We continue this research with the main objective of achieving an ideal rectangular sample plug shape at the cross at injection and quantify the sample plug shape and size and assessment parameters in the next chapter.

Chapter 4

Injection and Separation Evaluation

4.1 Introduction

One key factor that plays a significant role in the efficiency of on-chip electrophoresis separation is the initial shape of the sample plug at injection [23]–[27]. For microchips involved in separation, injection is a key step in efficient analysis. Much research is being carried out on microchip electrophoretic separation, but detailed analysis of the effect of sample plug shape at injection on separation efficiency is still lacking. In literature, it is stated to be difficult to attain a rectangular and narrow sample shape only by adjusting electric voltages. This goal is achieved in this research and this chapter presents the role of sample plug shape thoroughly, and the effective factors in evaluating good injection are addressed quantitatively. Among all different microchip geometries used in electrophoretic separation, cross-linked geometry is very common, for the reasons discussed in section 2.1.3.2. For such a geometry, the chip is first filled with the buffer solution and then the sample is injected from the sample reservoir into the injection channel. In electrokinetic transport, where no external pressure is applied, the sample migrates along the injection channel due to the applied electric field. When a sample approaches the intersection of injection and separation channels, the cross, the electric potentials are switched from injection to separation mode and the sample is pushed into the separation channel. The goal is to have the ideal rectangular sample plug at the cross, with no leakage of the sheath (buffer) flow into the injection channel from side channels. As the sample migrates along the injection channel prior to the separation mode, an interface between pure sample and pure buffer is observed, and causes along-stream diffusion. Once the sample reaches the cross, the cross-stream diffusion starts, and depending on the side-applied electric fields in the separation channel, different shapes of sample plug are achieved. The initial shape of the sample plug prior to separation greatly affects the separation efficiency, as discussed in detail in 4.4. Ideal rectangular injection shapes result in better separation resolution and in order to quantify such a plug shape, a shape factor study is carried out and presented in this chapter. Different parameters needed to be taken into consideration in this study, including the parameters used to quantify the sample plug shape and size by defining a shape factor for shape evaluation. Following the shape factor, the time to stop injection, the definition of separation resolution and the correlation of shape factor and resolution are presented. This chapter addresses the applied electric field configurations at injection and separation.

4.2 Literature Review

Assessment of injection and separation is a key factor in designing microchips in electrophoresis separation. Capillary zone electrophoresis (CZE), compared to traditional liquid chromatography separations, is an analytical technique used to separate samples into their individual components based on their differential migration in a capillary under an applied electric field. In microfluidics, rectangular chips replaced the capillaries which necessitates the sample transport phenomena. Patankar and Hu [9] were pioneers who studied the electroosmotic injection characteristics of a cross-channel device for capillary electrophoresis. They stated that the shape of the inserted sample is an important parameter that influences the resolution of the separated zones during the electrophoresis and depends primarily on the electroosmotic flow pattern at the intersection of the channels. Mohammadi and Santiago [28] presented shape optimization techniques for minimizing dispersion in extraction and separation microfluidic devices using the control parameter. This parameter may be either the potential differences applied during the pinching and pull-back steps, or the turn geometries devoted to keeping the dispersion minimal by reducing the skew of the advected band. The literature also shows that the shape of a sample plug delivered into the separation channel has a great impact on high-quality separation performance, and a distorted sample plug has a negative impact on the quality of separation [29], [25],[24]. Optimal injection depends on the shape and size of the sample plug at the intersection of injection and separation channels during injection [30]. Fu et al. [46] identified severe sample leakage in the floating sample injection method when high voltage gradients were established. They showed how sample leakage effect increased the signal baseline by increasing the number of injection runs, and reduced separation efficiency. They found that the shape of the delivered sample plug depends primarily on the electroosmotic flow pattern at the intersection of the channels and plays an important role in determining the resolution of the electrophoresis analysis.

Despite the notable contributions of the various injection schemes discussed above, few studies have examined sample shape from a theoretical perspective. Research still lacks the development of a sample injection model for on-chip electrophoretic separation. This chapter first focuses on the injection and the shape of the sample at the cross, then presents the effect of that shape on the separation resolution.

4.3 Shape Factor Introduction

Figure 25 shows how the two components of a double-species sample pass by the detector in the separation channel and also presents the possible shapes achieved at the intersection of injection and separation channels. An ideal sample plug is a clear-cut rectangle with only one-dimensional diffusion at the interface of the sample and the buffer solution. Such a shape is not easily achieved due to the diffusion

of the sample at the cross and the applied electric fields. Depending on the electric fields applied in the injection and separation channels, the sample could appear in rectangular or trapezoidal shapes. In Figure 25 a summary of the definition of the sample plug shape and size in correlation with peak concentration and high separation resolution is presented. The optimal injection size should be small enough to avoid wide overlapping bands, yet large enough to provide an adequate detection signal. From those parameters involved in the problem discussed in 0, the goal is to control the sample plug shape by means of the applied electric potentials, to achieve an almost rectangular shape. In this respect, it is worth analyzing the shape of the sample and the plug width at the cross at injection, prior to switching to separation phase. Following that, shape factor parameters are analyzed to quantify sample plug shapes and sizes.

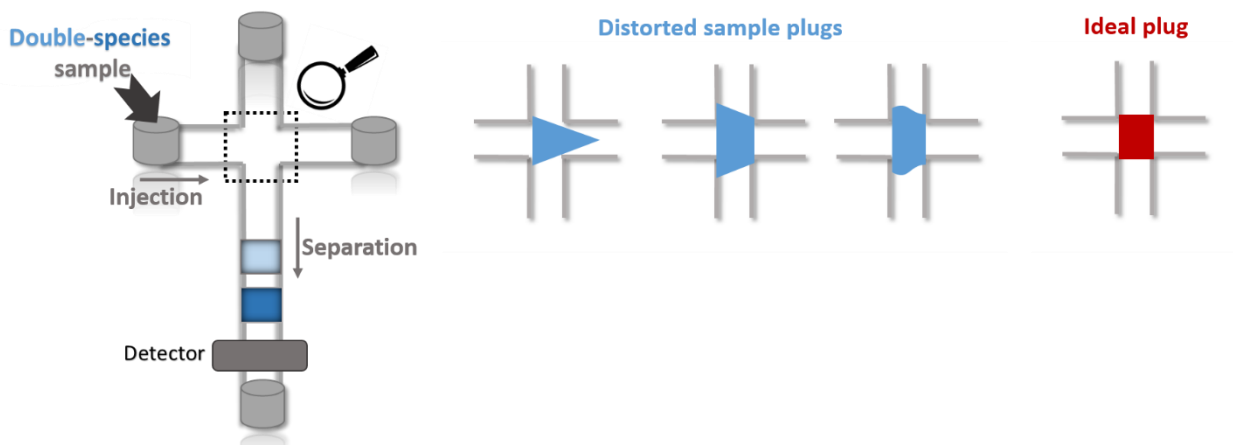


Figure 25: Possible sample plug shapes at the cross

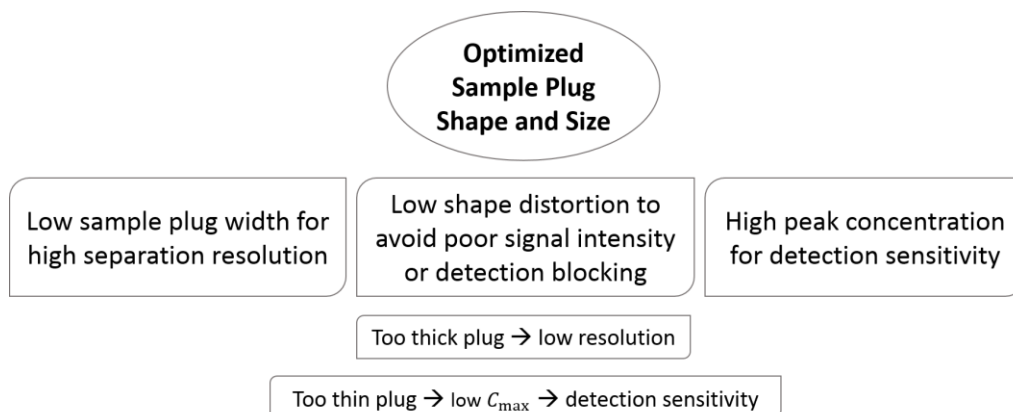


Figure 26: Sample plug shape optimization

4.3.1 Development of a Shape Factor-Guiding Principles

Assuming that injection is carried out in the horizontal channel with symmetric applied electric fields in both sides of the separation channel, we analyze the top half of the sample shown in Figure 27. Since there is no exact edge at the interface of the pure sample and the buffer solution, the analysis is studied for the 50% concentration (Half-Maximum) contour line. This is an arbitrary choice to some extent, but with detection consideration this line is the most stable one and less likely to wander due to diffusion to the buffer solution from both sides. It is thus the best location for analyzing the sample plug shape. Experimentally, it is also easier to measure this line to compare the sample concentration and noise peaks. Considering a symmetric sample at the cross, we evaluate half of the sample either the top or right half depending on whether the injection is performed horizontally or vertically. For the typical plugs shown in Figure 25, the sample plug is characterized with a quadratic function; however, a higher order curve fit results in higher accuracy. We study the quadratic fit on the sample width at 50% concentration contours, normalized by the channel width and defined for the sample plug width as $Y = W_{sp}(X) = A_0 + A_1X + A_2X^2$.

To quantify sample plug shape, characterization parameters are introduced in Table 2 for microchannels with a channel width of W . To be independent of channel dimensions, these parameters are in normalized form, where $X = \frac{x}{W}$; $= \frac{y}{W}$, and the part of the sample to study at the cross is confined to $X[-0.5, 0.5]$ as shown in Figure 27.

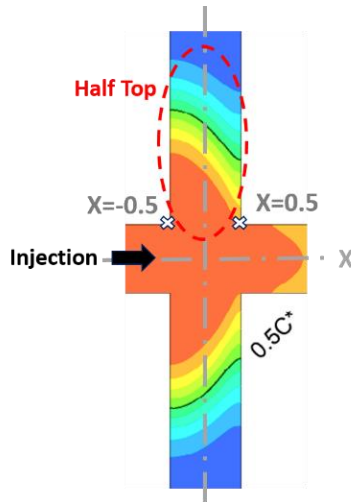


Figure 27: A sample concentration contour for a horizontal injection

Table 2: Shape factors (parameters) used to characterize sample plug shape

| Parameter | Definition |
|--|--|
| \bar{W}_{sp} Mean width of sample plug | $\bar{W}_{sp} = \frac{\int_{-0.5}^{0.5} W_{sp} dX}{\int_{-0.5}^{0.5} dX} = A_0 + \frac{A_2}{12}$ |
| σ Standard deviation | $\sigma = \sqrt{\frac{\int_{-0.5}^{0.5} (W_{sp} - \bar{W}_{sp})^2 dX}{W}} \frac{1}{\bar{W}_{sp}} = \sqrt{\frac{15A_1^2 + A_2^2}{180}} \frac{1}{\bar{W}_{sp}}$ |
| Sy_1 First moment about channel centre line | $Sy_1 = \frac{X_{m_w^{(1)}}}{X_{m_w^{(1)}}} \frac{1}{0.5W} = \frac{A_1}{6\bar{W}_{sp}}$ $m_w^{(1)} = \int_{-0.5}^{0.5} (W_{sp} - \bar{W}_{sp})X dX ; m_w^{(1)} = \int_{-0.5}^{0.5} \bar{W}_{sp} dX$ |
| Sy_2 $\frac{1}{4}$ × Second moment arm about channel centre line | $Sy_2 = \frac{1}{4} \frac{X_{m_w^{(2)}}}{X_{m_w^{(2)}}} = \frac{1}{4} \sqrt{\frac{A_2}{15\bar{W}_{sp}}}$ $m_w^{(2)} = \int_{-0.5}^{0.5} (W_{sp} - \bar{W}_{sp})X^2 dX ; m_w^{(2)} = \int_{-0.5}^{0.5} \bar{W}_{sp}X^2 dX$ |
| Sy : RMS of Sy_1 and Sy_2 | $Sy = \sqrt{Sy_1^2 + Sy_2^2}$ |
| \bar{w}_{sp} : Actual mean width of sample plug | $\bar{w}_{sp} = 2\bar{W}_{sp}W$ |

In the definition of Sy_1 , $X_{m_w^{(1)}}$ and $X_{m_w^{(1)}}$ are the first moment arms about the center line of the channel for a sample plug and a uniform plug, respectively. The normalizing factor $\frac{1}{0.5W}$ assumes that all the sample is located at either edge of the channel. The same holds for Sy_2 as the second moment arm about the center line of the channel. Respectively, $X_{m_w^{(2)}}$ and $X_{m_w^{(2)}}$ are also the second moment arms for a sample plug and a uniform plug. Based on the preliminary results, the second moment arm is divided by a factor of 4 to bring Sy_1 and Sy_2 into the same order of magnitude. It is worth mentioning that all the values for shape factor parameters in Table 2 are in normalized form, except the actual mean width of the sample plug. To get the actual mean width, the normalized mean width of the sample should be multiplied by two times of the channel width, here $50 \mu m$. What we defined for the normalized mean width was for the top half of the sample plug with a symmetric shape; therefore, we double $\bar{W}_{sp}W$ to get the actual sample plug width.

Figure 28 shows some possible shapes for the top-half of the sample plug at the cross during injection in the horizontal channel. Shape factors are in normalized form and based on different values for A_0 , A_1 and A_2 . First, $A_0 = 1$, A_1 and A_2 changing from -2 to 2 . Then more shapes are presented for higher values of these coefficients. To see which parameter is mostly characterizing the shape of the sample, we analyze the values of σ . The smaller the σ , the closer the shape is to the ideal rectangular plug shape. Figure 29 shows different possible shapes presented in Figure 28 but based on ascending σ .

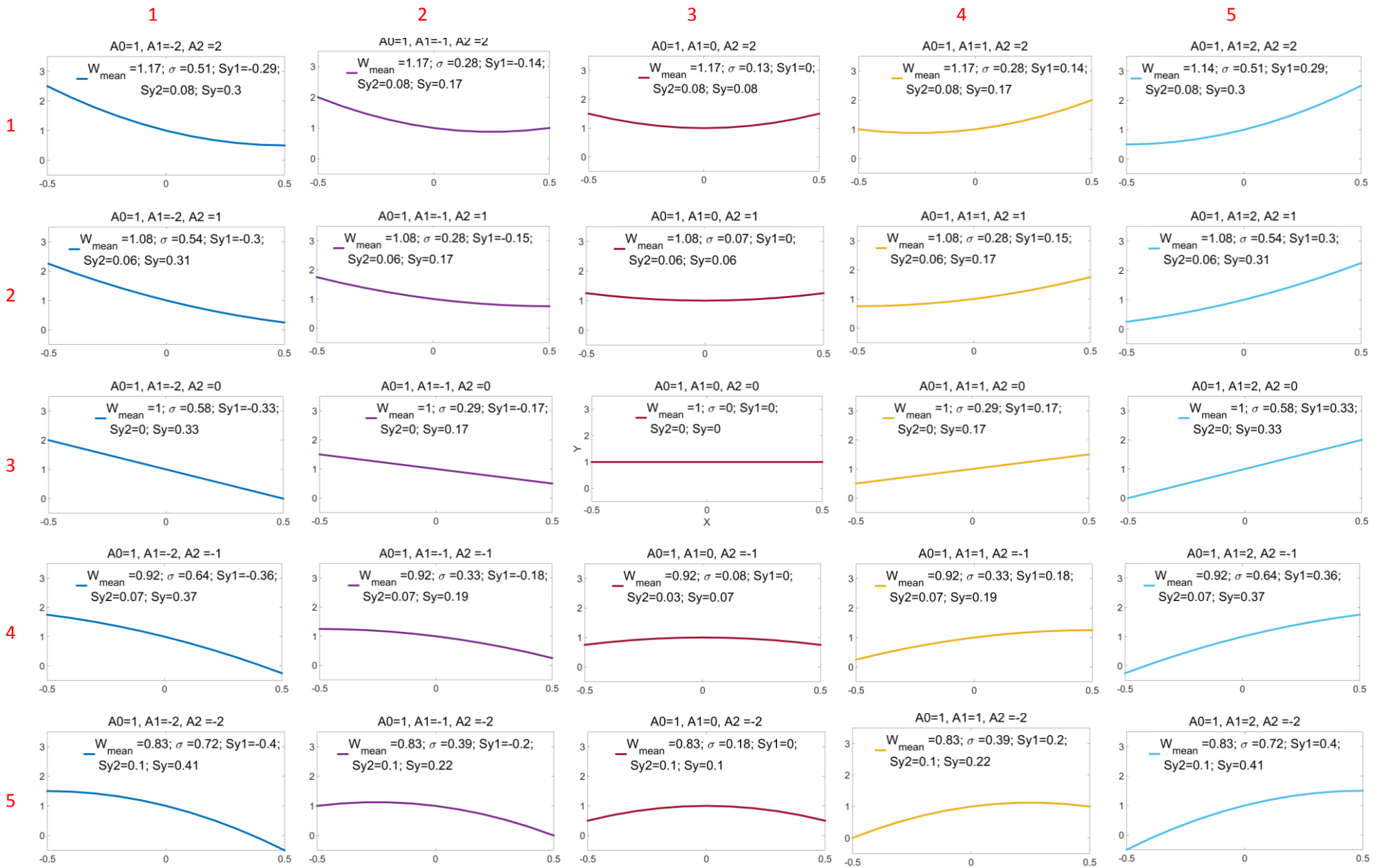


Figure 28 : Different shapes at the top-half of sample plug at the cross ($A_0 = 1$)

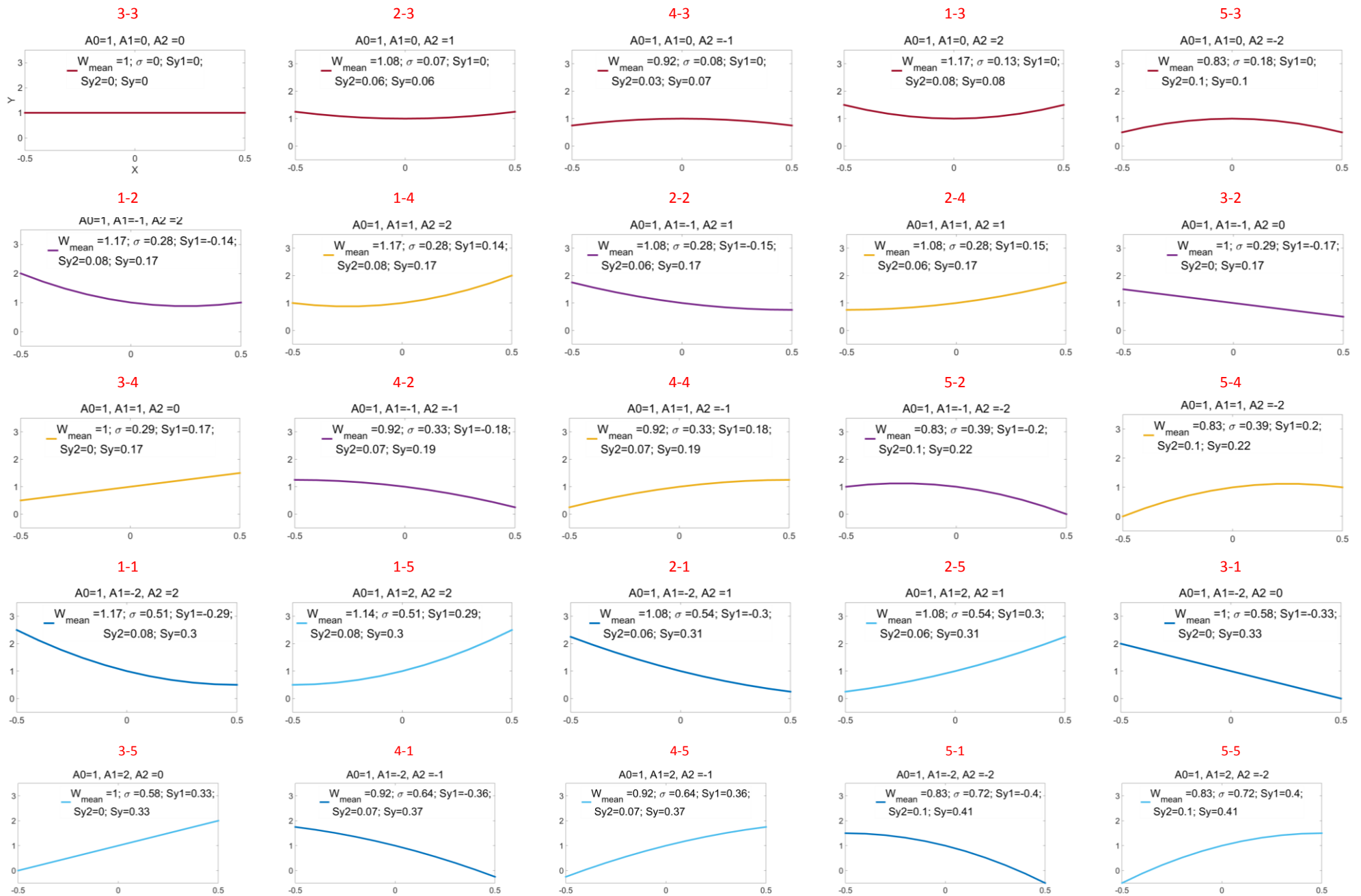


Figure 29 : Different shapes based on ascending σ in rows, row-column box numbers from Figure 28

As mentioned in Table 3 in addition to σ , another parameter, Sy , is defined as $Sy = \sqrt{Sy_1^2 + Sy_2^2}$ to see the effect of both Sy_1 and Sy_2 on the shape of sample plug simultaneously. The results show the values for Sy is on the ascending order while σ is increasing. Only one exception is observed for box 4-3 which Sy is decreasing.

Table 3: Parameters values based on increasing σ

| Box # (Figure 29) | Ascending σ | Sy_1 | Sy_2 | $Sy = \sqrt{Sy_1^2 + Sy_2^2}$ |
|-------------------|--------------------|--------|--------|-------------------------------|
| 3_3 | 0 | 0 | 0 | 0 |
| 2_3 | 0.07 | 0 | 0.06 | 0.06 |
| 4_3 | 0.08 | 0 | 0.03 | 0.03 |
| 1_3 | 0.13 | 0 | 0.08 | 0.08 |
| 5_3 | 0.18 | 0 | 0.1 | 0.10 |
| 1_2 | 0.28 | -0.14 | 0.08 | 0.16 |
| 1_4 | 0.28 | 0.14 | 0.08 | 0.16 |
| 2_2 | 0.28 | -0.15 | 0.06 | 0.16 |
| 2_4 | 0.28 | 0.15 | 0.06 | 0.16 |
| 3_2 | 0.28 | -0.17 | 0 | 0.17 |
| 3_4 | 0.29 | 0.17 | 0 | 0.17 |
| 4_2 | 0.33 | -0.18 | 0.07 | 0.19 |
| 4_4 | 0.33 | 0.18 | 0.07 | 0.19 |
| 5_2 | 0.39 | -0.2 | 0.1 | 0.22 |
| 5_4 | 0.39 | 0.2 | 0.1 | 0.22 |
| 1_1 | 0.51 | -0.29 | 0.08 | 0.30 |
| 1_5 | 0.51 | 0.29 | 0.08 | 0.30 |
| 2_1 | 0.54 | -0.3 | 0.06 | 0.31 |
| 2_5 | 0.54 | 0.3 | 0.06 | 0.31 |
| 3_1 | 0.58 | -0.33 | 0 | 0.33 |
| 3_5 | 0.58 | 0.33 | 0 | 0.33 |
| 4_1 | 0.64 | -0.36 | 0.07 | 0.37 |
| 4_5 | 0.64 | 0.36 | 0.07 | 0.37 |
| 5_1 | 0.72 | -0.4 | 0.1 | 0.41 |
| 5_5 | 0.72 | 0.4 | 0.1 | 0.41 |

Figure 30 provides us with more shapes with a higher resolution on $\sigma \leq 0.2$. Having $\sigma = 0.2$ is arbitrary but it is observed that samples with $\sigma \leq 0.2$ have good shapes. To quantify the optically good shapes, the range of $\sigma \leq 0.2$ looks reasonable. With such a range for standard deviation, Sy as a parameter showing the effect of both Sy_1 and Sy_2 is smaller than 0.13.

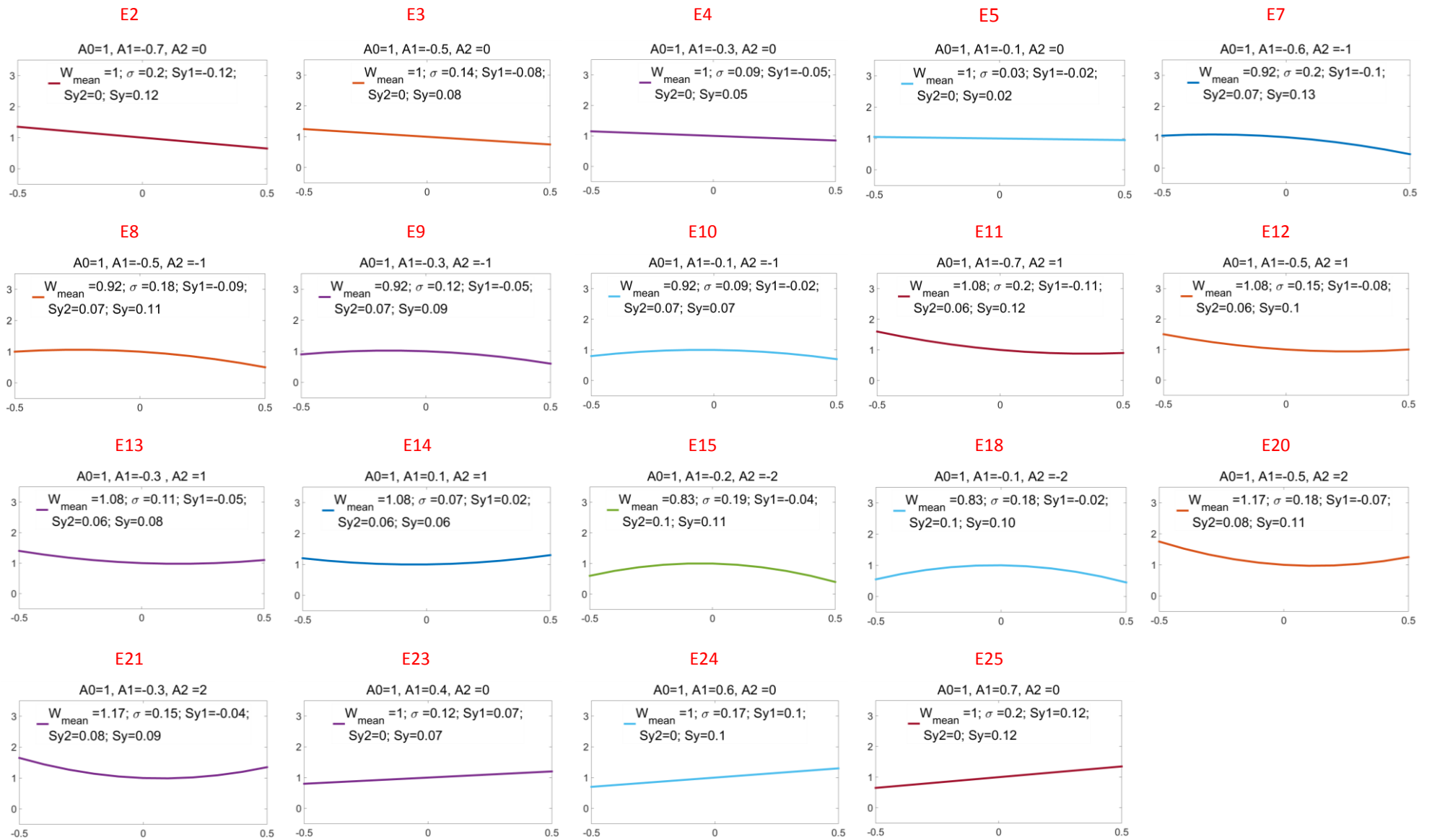


Figure 30 : More shapes with $0 \leq \sigma \leq 0.2$

For a better resolution of σ , some extra shapes are provided with smaller steps for the coefficient of linear term, i.e. A_1 and based on an ascending order of standard deviation σ the results are shown in Figure 31. The results show that σ and Sy are following the same trend with more significant difference at more deviated shapes, i.e. larger σ 's. To find the ratio of σ/Sy two methods of averaging or least square fitting by setting the y intercept to a zero or non-zero value are applied. The former provides us with a ratio of 1.65 and the latter with 1.73 (in case of a zero y-interception); therefore, for the sake of an easier evolution for the sample plug, we take a value of 1.7 as a number in between the above mentioned results. Figure 32 shows the trends of σ and the overlapping values for $1.7 Sy$. This means in order to quantify the sample shape, it is sufficient to characterize the shape of the sample with one parameter, σ and all other three parameters of Sy_1, Sy_2 and Sy are taken into account in the evaluation.

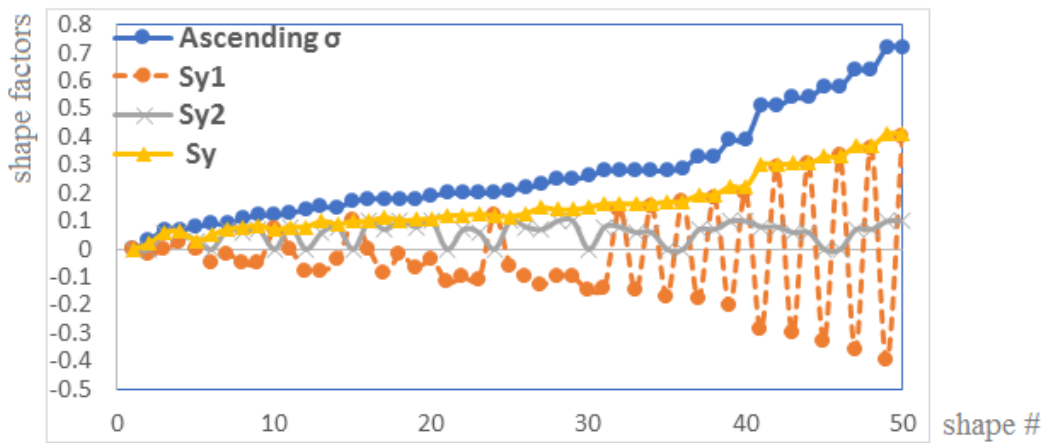


Figure 31: Trends of ascending σ, Sy_1, Sy_2 and Sy for 50 different shapes

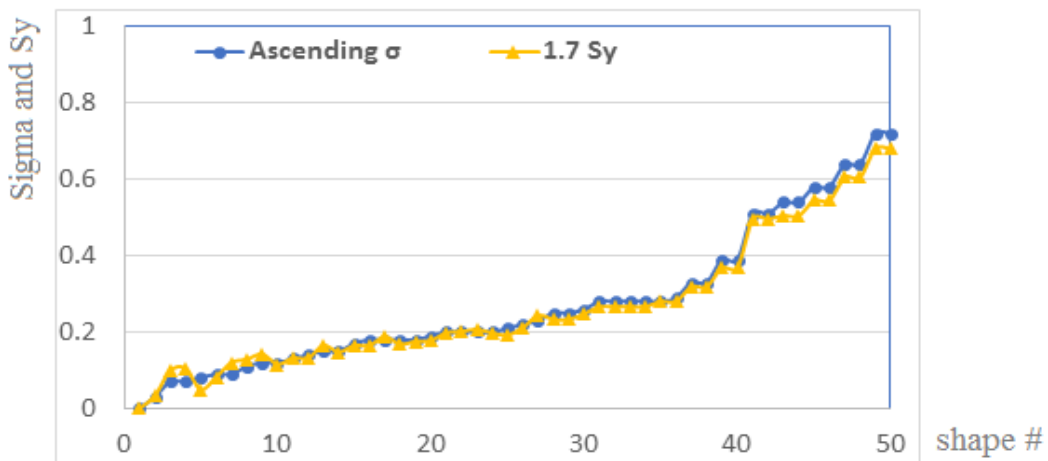


Figure 32: Trends of ascending σ and $Sy = 1.7 \sigma$ for 50 different shapes

Figure 33 shows how the shape of the sample looks when $\sigma \leq 0.2$.

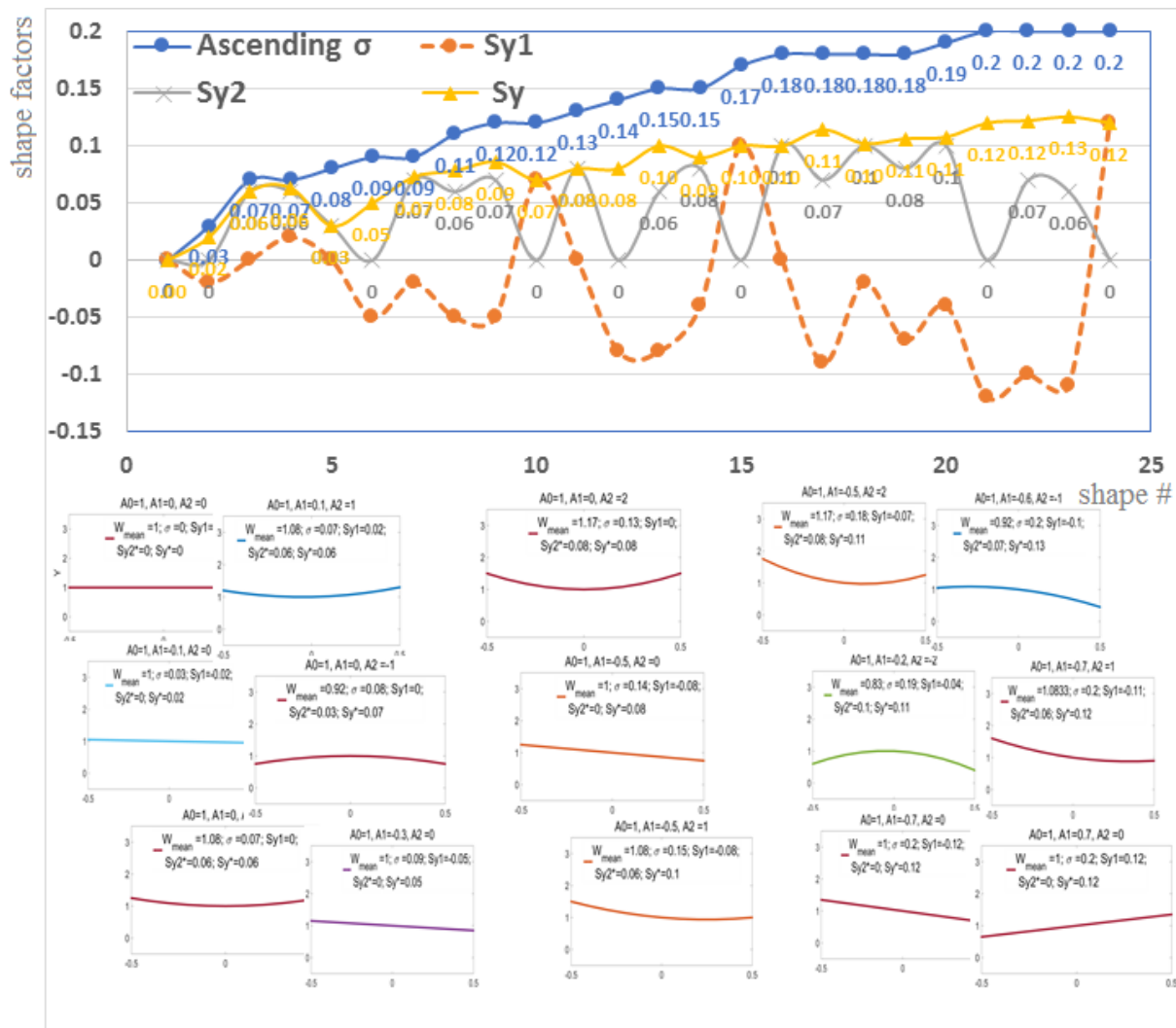


Figure 33: Zoom of Trends for ascending σ [$0 \leq \sigma \leq 0.2$], Sy_1 , Sy_2 and Sy

So far the shapes of sample were presented for $A_0 = 1$ and more shapes are shown in Figure 34 for higher A_0 . Increasing A_0 results in higher values of sample mean width; therefore the values of σ and Sy decrease. Figure 35 shows three more shapes with increased A_2 to four resulting in increasing σ and Sy .

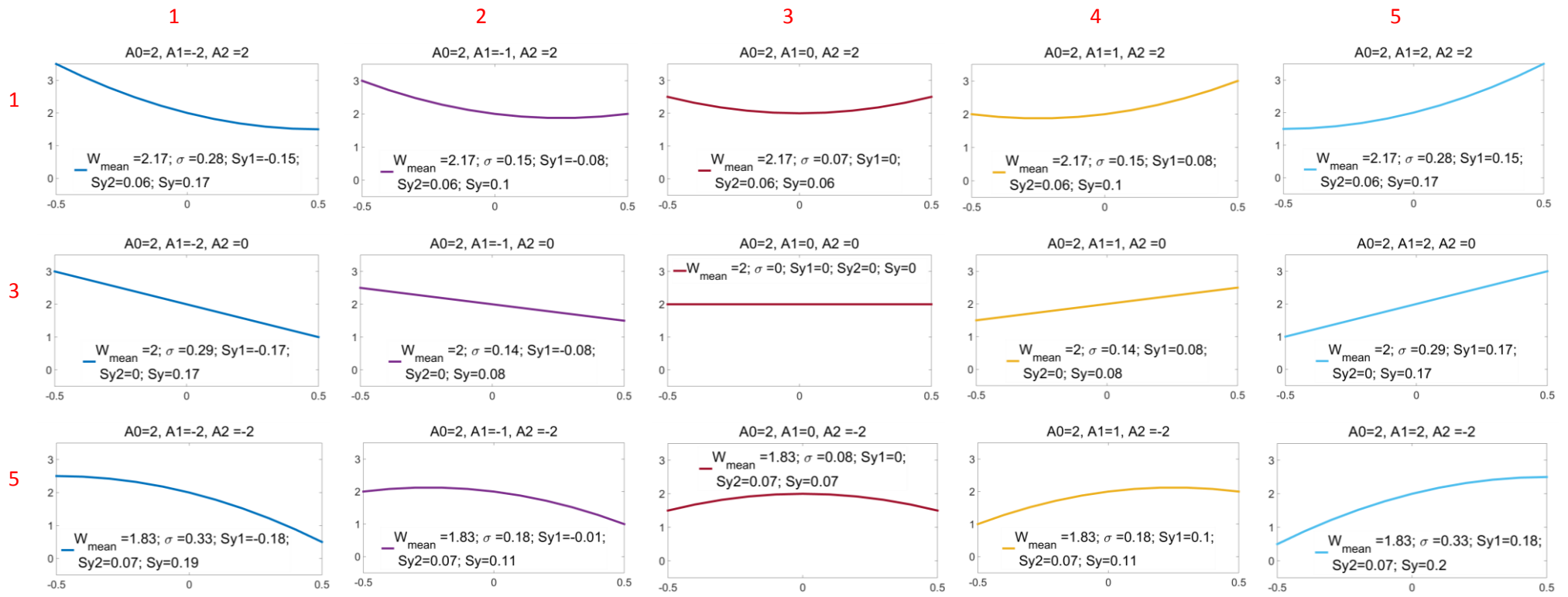


Figure 34 : More sample shapes of Figure 28 with $A_0 = 2$

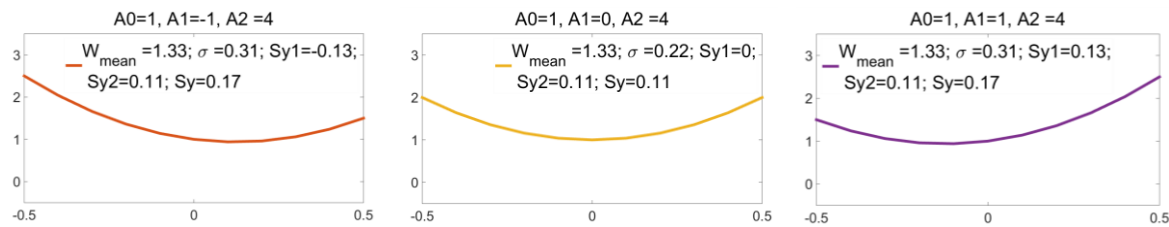


Figure 35 : Extra sample shapes for $A_2 = 4$

Figure 36 shows a comparison of four cases by making A_0 double. All shows that $\sigma \leq 0.2$ and $Sy \leq 0.13$ is valid for good shapes.

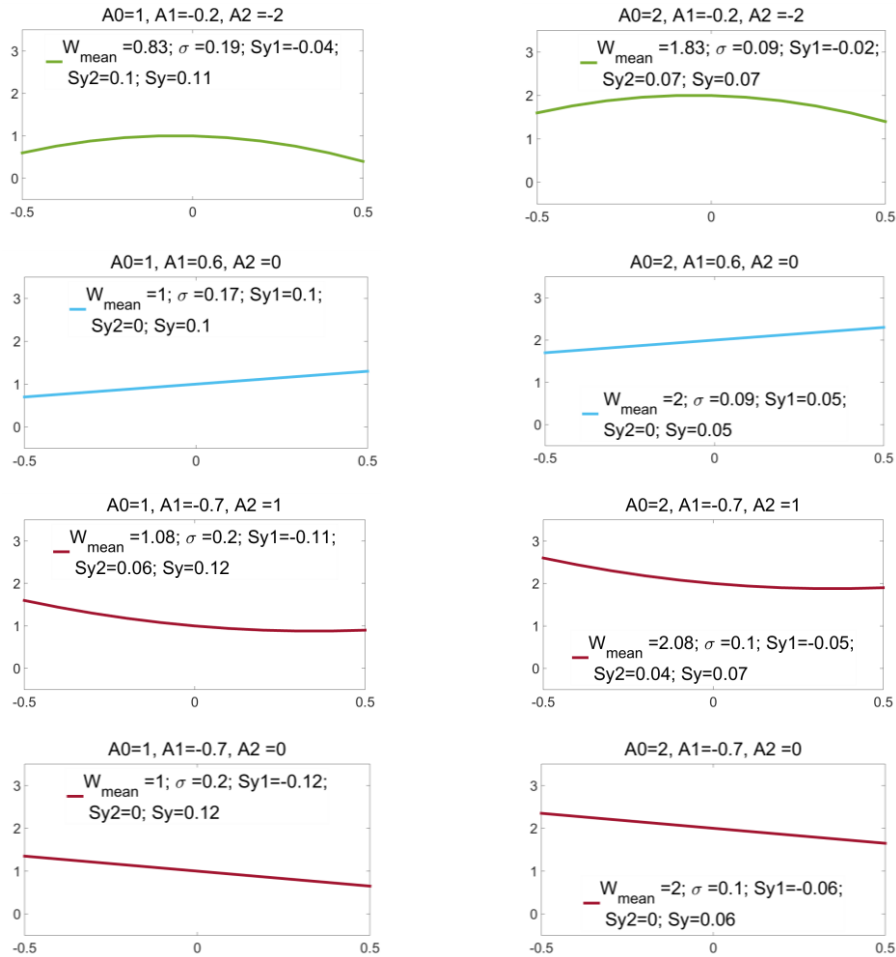


Figure 36 : Left to right comparison of four random cases for $A_0 = 1$ vs $A_0 = 2$

4.3.2 Conclusion for the Shape Factor Value

The study of the shape factor for analyzing sample plug shape and size shows that among different shape evaluation factors, the standard deviation σ is a reasonable factor for such purpose. It shows us how much a sample plug is deviated from the mean width supposed as a rectangular plug. So, by fitting a quadratic function of $Y = W_{sp}(X) = A_0 + A_1X + A_2X^2$, $\sigma \leq 0.2$ provides good shapes when $A_0 = 1$. As shown in parameters of Table 2, changing A_0 only changes the size of the sample, not its deviation form from the mean width plug.

4.3.3 Assessment of Shape Factor Model with Experiments in Literature

In order to verify the value of the shape factor for evaluating good shapes at injection, several injected shapes from experimental results reported in the literature are analyzed. Figure 37 shows the results of research by Fu et al. in 2003 on electrokinetic focusing injection on microfluidic devices. They compared concentration profiles for different focusing ratios in a double-cross injection system with 80 μm -wide microchannels.

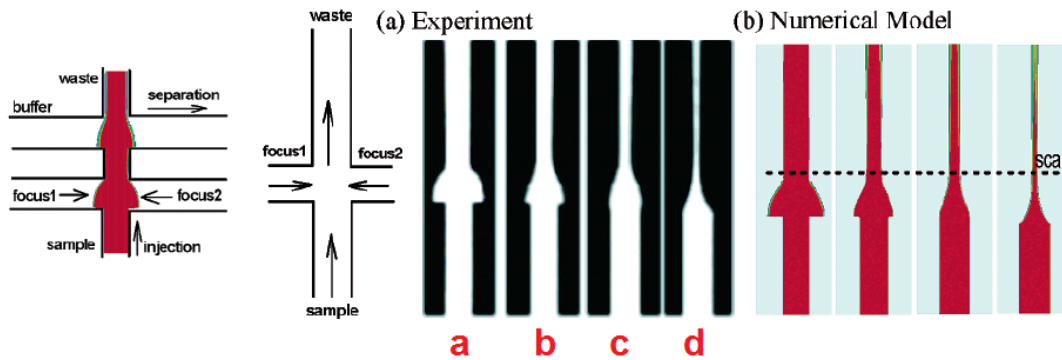


Figure 37 : Experimental results of Fu et al. [61] for verification of shape factor model

Figure 38 shows the curve fitting results and shape factor σ for the shapes “a” to “d” in Figure 37 and shows how shapes “a” and “c” which are less deviated from the sample mean width provide smaller shape factors below 0.2.

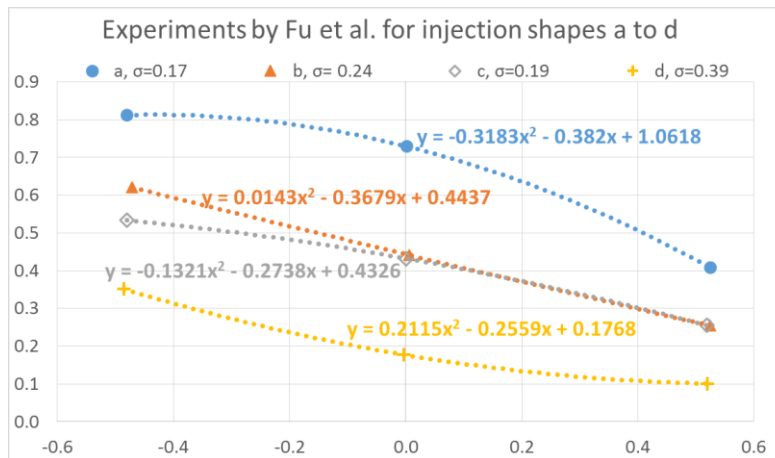


Figure 38 : Experimental results of Fu et al. [61] for verification of shape factor model

In Figure 39 to Figure 42 we applied the shape factor model to more experimental results to verify the good shapes have $\sigma \leq 0.2$. Taking the injection in X direction, the results show smaller σ for the shapes which are less deviated from their mean width plug.

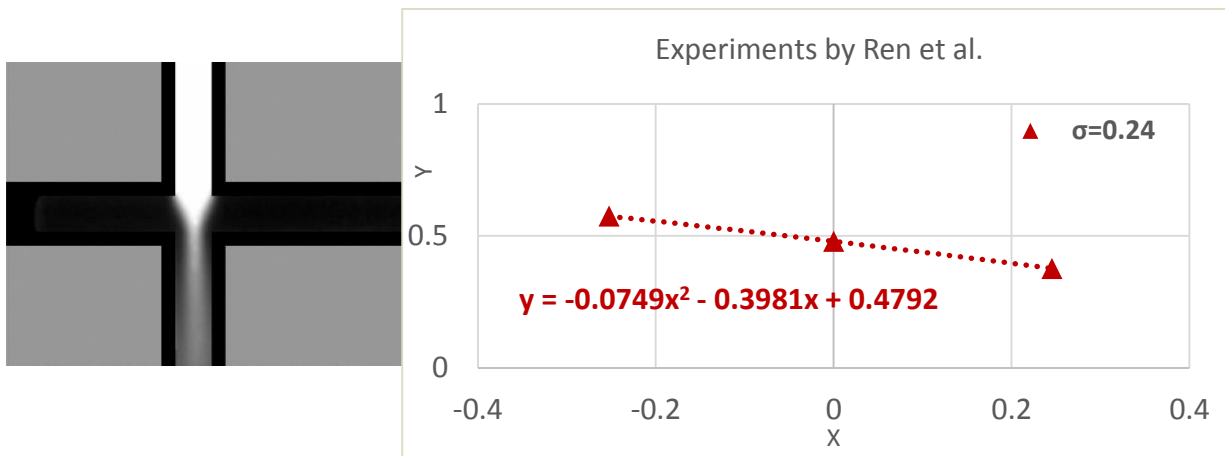


Figure 39 : Shape factor model on experimental results of Ren et al. [111]

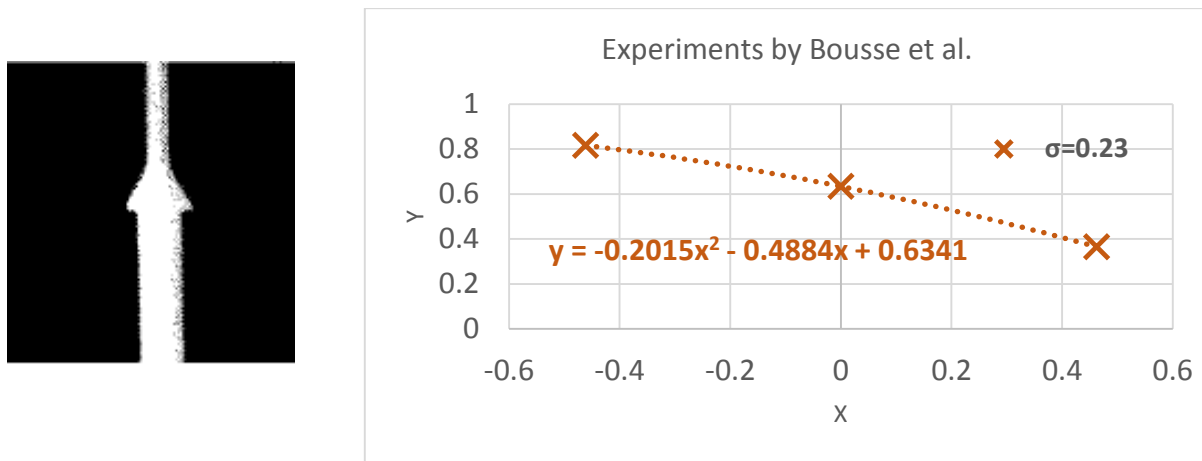


Figure 40 : Shape factor model on experimental results of Bousse et al. [30]

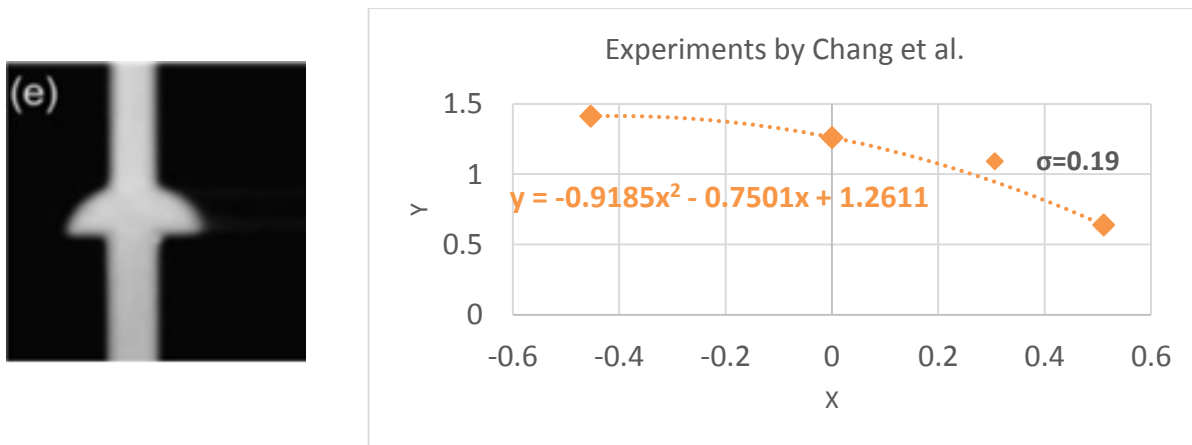


Figure 41 : Shape factor model on experimental results of Chang et al. [112]

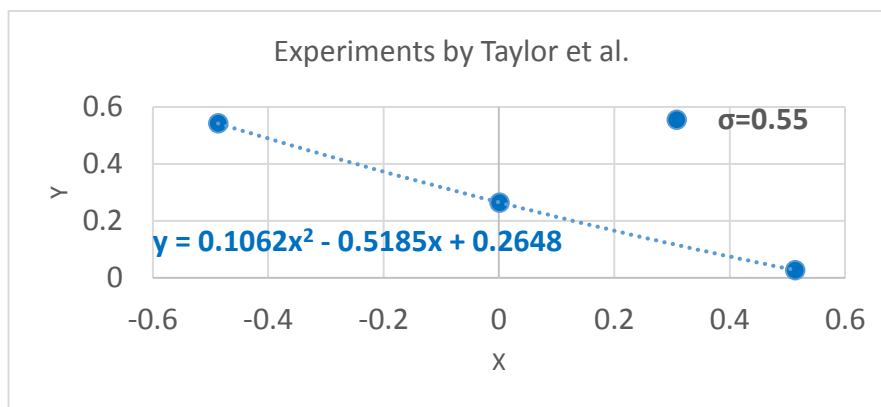
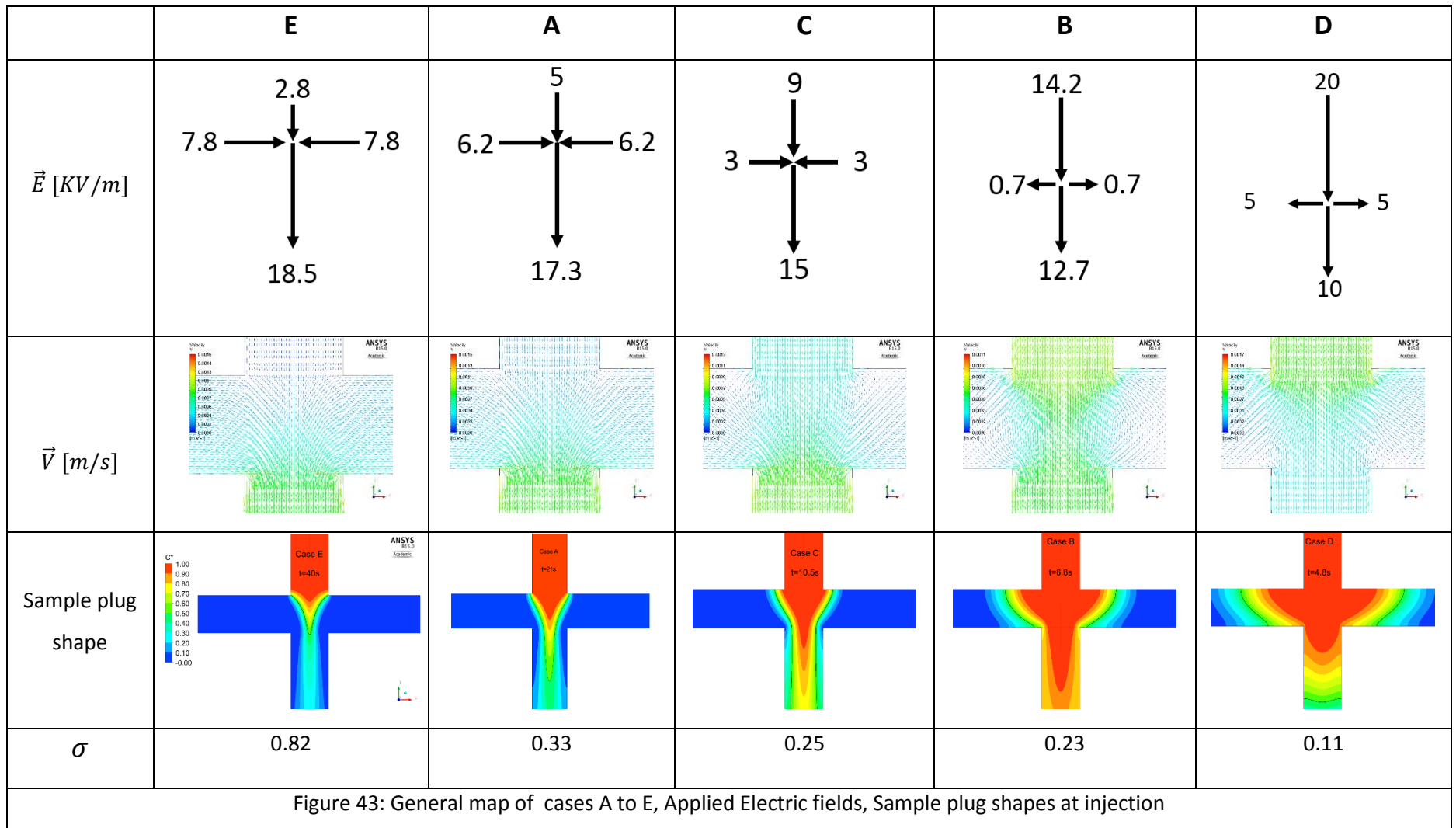


Figure 42 : Shape factor model on experimental results of Taylor et al.[25]

4.3.4 Injection and Separation of 5 Cases

From this section to the end of the thesis, the injection is carried out in vertical channel. This is for the purpose of a symmetric control on the sample plug shape at the cross. To see the effect of shape factor on separation efficiency, five cases, A to E, with triangular (pinched) or trapezoidal (dispersed) shapes at the cross are studied. Two outcomes of this study are finding the correlation between the shape factor and separation resolution and also the identification of the configuration of applied electric fields leading to good shapes.

For the purpose of finding the correlation between shape factor and resolution, the double-species sample is first loaded at injection channel. The earliest time when the high-concentration part of the sample covers the majority of the cross is taken as the stop-injection time. Then the electric fields are switched to the separation mode and by setting the detection spots in three points along the separation channel, the separation resolution is calculated for the two species. This study shows the better sample shape at injection, the better resolve the sample components. The five cases A to E as shown in Figure 43 are studied. For each case, the electric field configuration, velocity fields, the sample plug shape at the cross and the shape factor σ as an indicator of the electrophoretic injection are presented. To provide more clarity, the results of case B are discussed in more details and in the following the comparison of the cases will be addressed. All the simulation results are based on the time step of 0.001s and 40×40 grids at the cross as shown in the grid independency discussed in 5.2. More details of numerical simulation is discussed in Appendix B.



4.3.5 Time to stop injection

For the non-steady shapes at the cross, as time goes by, more sample disperses into the separation channel, therefore, the time to stop the injection affects the shape of the sample and consequently the separation resolution. In this section, we did a study on this issue for one of the five cases presented in Figure 43. In Figure 44, different time frames of the migration of sample along the injection channel are presented for case B. With the applied electric field shown in Figure 43 and the electroosmotic mobility of $4.5e - 8 [m^2/Vs]$, it takes 6.6s that enough amount of high concentration sample covers the cross. Stopping injection sooner than this time and switching to separation results in sensitivity problem due to the lack of high concentration part of the sample at the cross. On the other hand, delaying in switching to separation gives the sample more time for diffusion, which results in poor resolution. In Figure 44, From the shape of the sample plug at $t = 6.4$ to $7s$, $t = 6.6s$ is the best time to stop the injection. First, the high concentration part of the sample entered the cross and second, it is not dispersed much into the separation channel. Therefore, the concentration results at this time are implemented as the initial condition for the separation simulations.

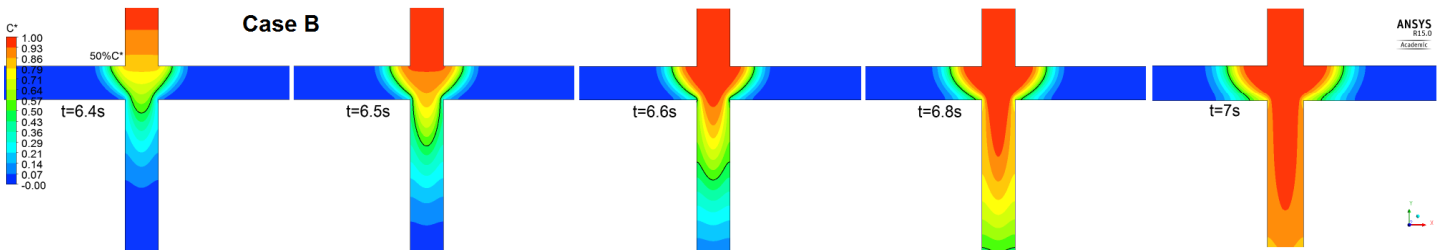


Figure 44: Case B , time frames when the sample approaches the cross

For the cases with triangular (pinched) sample shape at the cross, the electric fields in the separation channel during injection is so high that the high concentration part of the sample is stopped at the cross. For such cases with stabilized flow at the cross, the time when enough amount of high-concentration sample is at the cross considered as an appropriate time to stop injection. For the other cases, with trapezoidal (dispersed) shape, a similar observation as mentioned above is necessary for the sample approaching the cross to stop injection sooner than diffusion disperses the sample into the separation channel wings. Once the injection is stopped, the applied electric potentials at the reservoirs of the injection channel are switched to those of the separation channel. Doing so pushes the sample plug into the separation channel and the sample components start resolving due to their different electrophoretic mobilities. With the goal of a high separation resolution, the effect of shape factor on resolution is studied. After stopping the injection, the electrical potentials are switched to the separation mode, and for all the cases studied here the electric potential and field configuration at separation are as shown in Figure 45. The applied potentials are based on experiments of Sinton et al. [113], for the uniform conductivity and non-dynamic loading case, which were adjusted by Kirchhoff's law for the current chip.

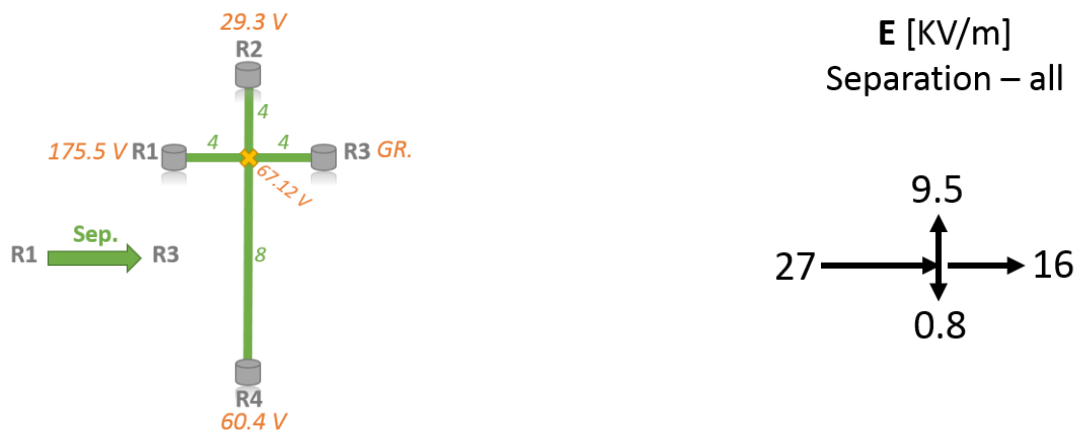


Figure 45 Configurations of electric potential and field applied to five cases A to E

For a double-species sample which are labelled with Rhodamine B and Fluorescein for the purpose of detection, the result of such applied electric field in separation appears as shown in the Figure 46 for case B from $t = 0.5$ to $4s$. Due to showing the contours in one figure, Rhodamine B is presented with only the contour lines. Both components migrate along the separation channel under the applied electric field, and due to the difference in their electrophoretic mobilities they migrate with different pace which leads to their separation.

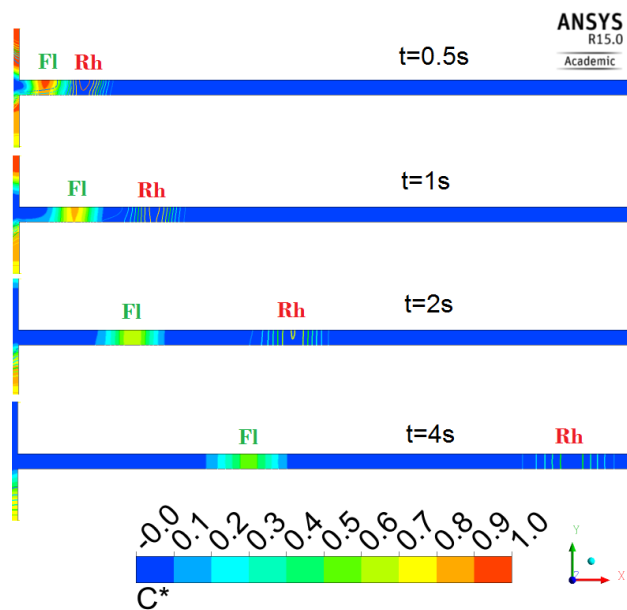


Figure 46: Concentration contours for the separation of fluorescein and rhodamine in case B

In order to calculate the separation resolution for a two-component sample (here Rhodamine B and Fluorescein) different detection spots along the separation channel were taken and the dimensionless concentration for each component, normalized by sample initial concentration, were measured at three points across the stream: top wall, center line and bottom wall where the origin is located at center of the cross and the microchannel width is $50 \mu m$.

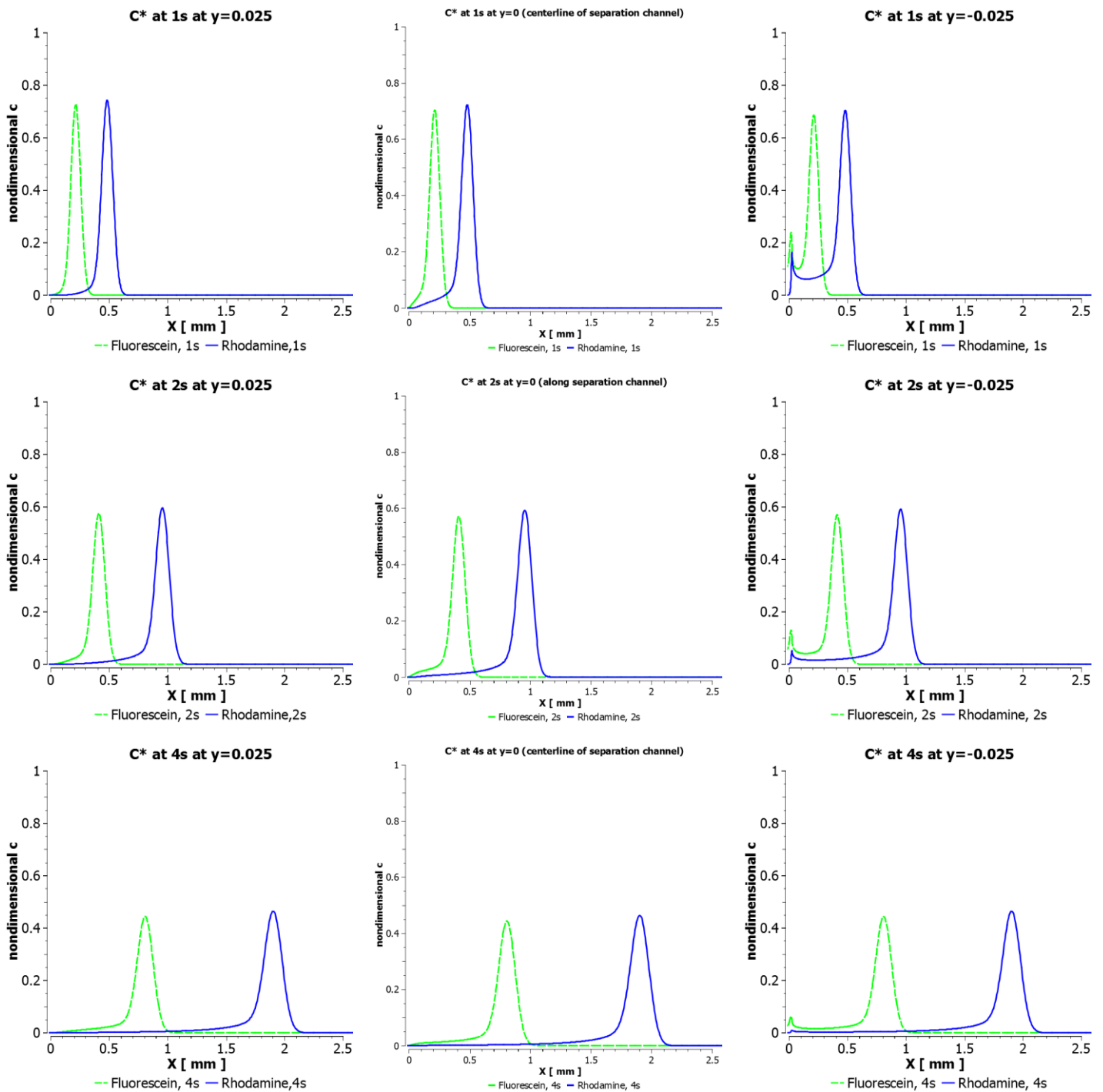


Figure 47: Case B- Spatial separation graphs for c^* at $t = 1, 2$ and $4s$ for fluorescein and rhodamine along separation channel at $y = 0.025, 0, -0.025 \text{ mm}$, stopped injection time: $6.6s$

To calculate the resolution, two approaches for the concentration of the cross-stream locations of the sample components along the separation channel were taken: 1-calculating the average of the resolution for three points on top and bottom walls and center line; 2- calculating the resolution of averaged concentration for those points. Both approaches were tried for different detection spots along the separation channel. Figure 48 shows that except in the vicinity of the cross or very close

to it, the concentration graphs are overlapping in both methods, and we take the second approach of averaged concentration as the base of our calculations for resolution. This is in accordance with the input of the detector as well.

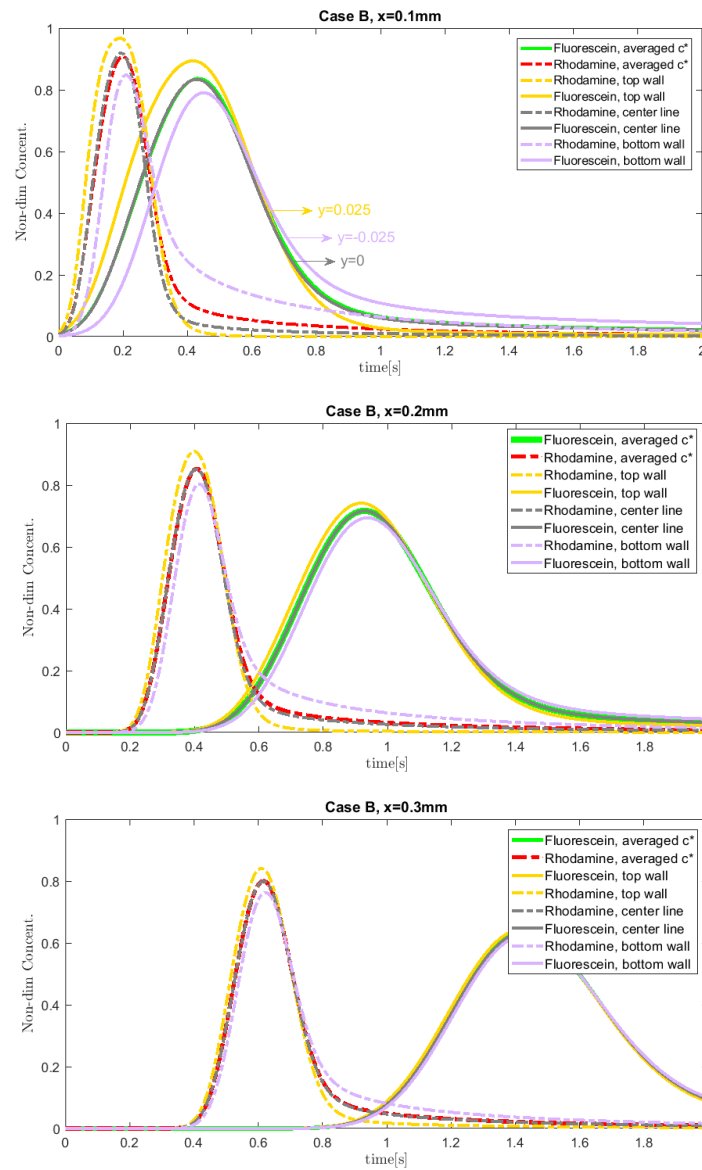
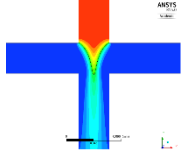
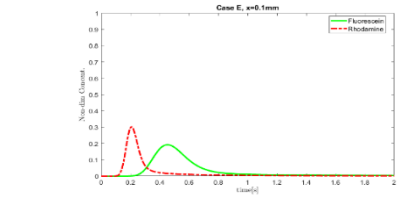
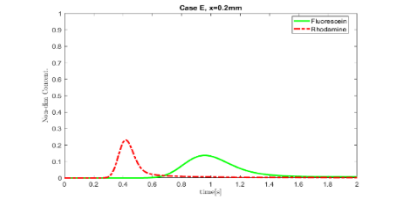
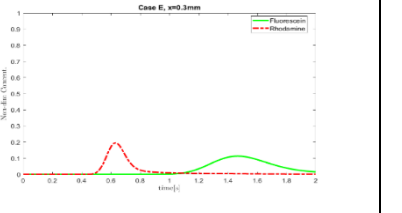
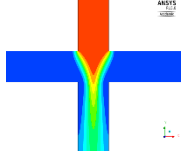
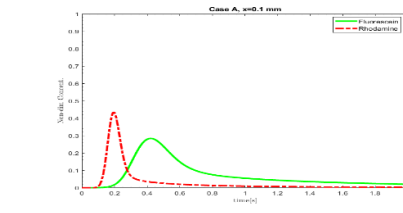
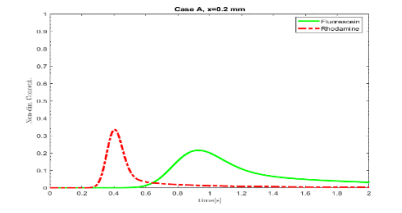
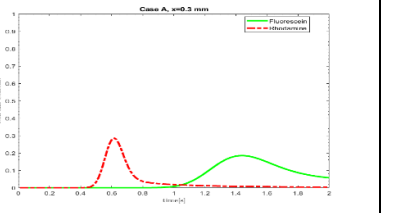
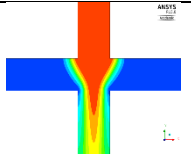
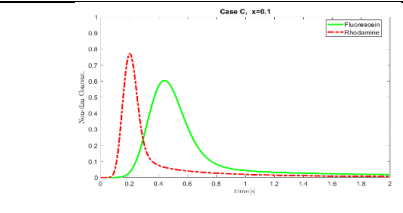
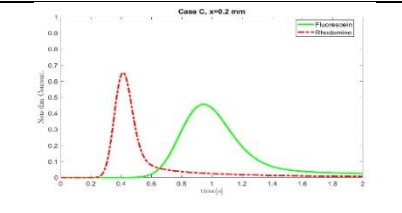
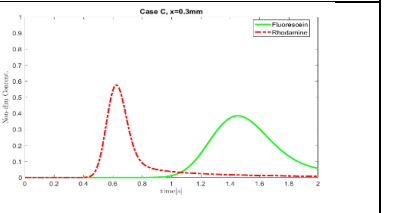
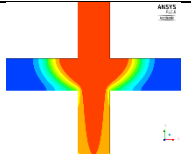
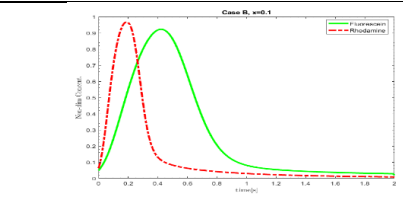
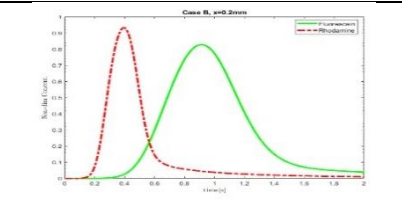
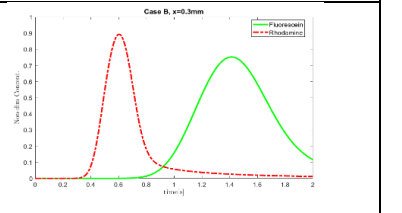
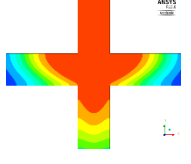
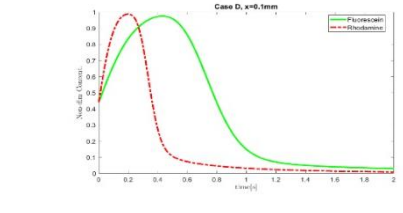
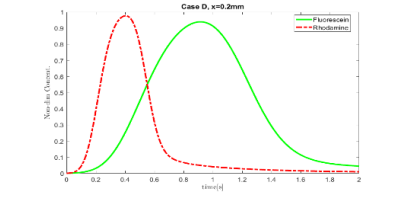
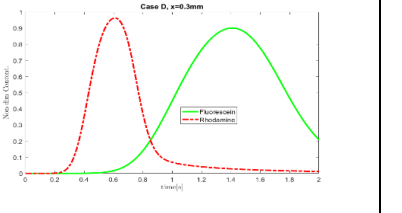


Figure 48: Case B- temporal separation graphs for averaged c^* vs. c^* at $y = 0.025, 0, -0.025\text{ mm}$ at detection spots of $x = 0.1, 0.2$ and 0.3 mm

Based on having the same resolution in the two approaches mentioned above, all the resolution values discussed in this chapter are calculated for the averaged non-dimensional concentration. So, for cases A to E studied in 4.3.4 for the shape factor, the results of separation are presented in Table 4. Non-dimensional concentration is plotted for all the cases along the separation channel at three detection spots which location on the center line is normalized by the channel width of 50. After analyzing the separation graphs of Table 4, and before delving into the details of improvements in the geometry, the injection and separation procedures, we assess the traditional definition of assessment in the following section.

Table 4: Comparison of fl (green) and Rh (red) separation for cases A- E along separation channel

| | Sample plug | σ | $t_{stop\ injection}$ (s) | $X = 2$ ($x = 100\ \mu m$) | $X = 4$ ($x = 200\ \mu m$) | $X = 6$ ($x = 300\ \mu m$) |
|----------|---|----------|---------------------------|--|---|---|
| E |  | 0.82 | 40 |  |  |  |
| A |  | 0.33 | 21 |  |  |  |
| C |  | 0.25 | 10.5 |  |  |  |
| B |  | 0.23 | 6.6 |  |  |  |
| D |  | 0.12 | 4.8 |  |  |  |

4.4 Assessment of Resolution

In 2.4, the conventional definition of separation resolution is presented. However, this definition lacks the factor of detection sensitivity. In the detection of the resolved sample components, the fact that how far the components are migrating apart plays an important role in separation efficiency.

4.4.1 Solution to Concentration Equation for a Finite Body

In the conventional definition of resolution of $R_s = \Delta x/4\sigma$, the diffusion distance reported in the literature is $\sigma^2 = 2Dt$, which comes from the solution of concentration equation for a semi-infinite problem. (Appendix B)

The current problem, with the interface of the sample and the buffer from two sides is an infinite problem. To see how much the peak of the sample concentration is dropped during migration along the separation channel, the concentration – temperature analogy could be applied. For this purpose, Heisler charts show the temperature drop from the center of different bodies in a transient heat transfer, which could be applied to our concentration problem. Knowing the concentration of the center, ideally the original concentration, the concentration drop and diffusion distance could be calculated. Indeed, we want to get the diffusion distance along the migration of the sample components in the separation channel.

Heisler Charts do the same thing for finding the center temperature of a slab, sphere or cylinder when $Fo > 0.2$.

As shown in Figure 49, in heat transfer, we have Fourier number and Biot numbers in these charts. Fourier number could be translated to mass transfer by Dt/L^2 and Bi number could be assumed as one. Basically, Bi number is the ratio of internal heat resistance to the surface heat resistance as $(L/KA)/(1/hA)$ which in our mass diffusion problem is almost one because of equal diffusion resistance at both sides of the interface.

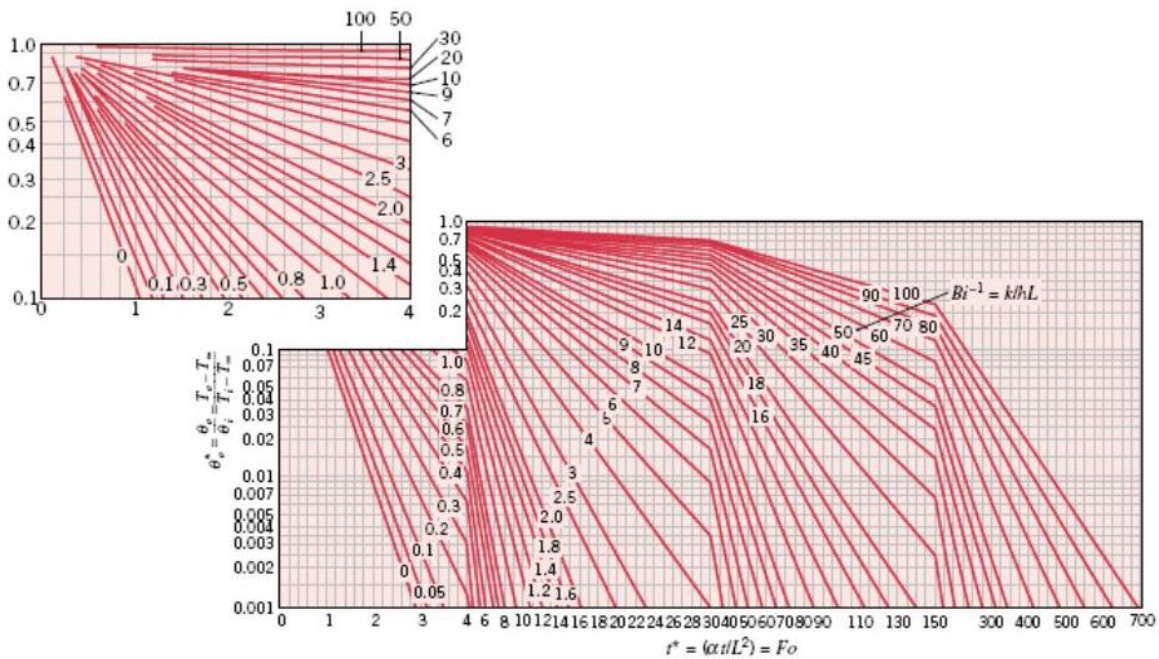


Figure 49: Heisler Charts for mid-plane temperature of a slab

So initially, as much as the peak drops the 50% points drops too. Making the analogy between the temperature and concentration is $\theta = \frac{T-T_{\infty}}{T_{cr}-T_{\infty}}$, T_{cr} is the central temperature and T is the atmosphere temperature. Similarly, $c^* = \frac{c-c_{surface}}{c_0-c_{surface}}$, where initially $c_{surface}$ is the concentration at the interface of sample and buffer and could be assumed as 50% of the initial sample concentration. Over time, this concentration starts falling. c_0 is the initial sample concentration. Having the Heisler charts based on c^* over $Fo = Dt/L^2$ and reading from $Bi = 1$, gives us the exact relation between L^2 and Dt . The problem for using these charts to get this exact solution is the unknown concentration at 50% point.

4.4.2 Detection Sensitivity, Peak to Valley factor

An important factor, which makes the detection and identification of peaks conceivable, is the difference between the amplitudes of the peaks. This has not been considered in conventional definition of the resolution, where only the horizontal distance between the peaks mattered. We introduce a new definition of resolution (Figure 50) that equals to the difference between the amplitude of the lesser of the peaks and the intersection of peak graphs, ideally the base line, normalized by the detectability threshold of the detector. This indeed is a sensitivity issue which depends on the threshold of the detector sensitivity as well as the original sample concentration in experimental measurements. Therefore, the conventional definition of separation resolution is modified by considering this peak-to-valley difference in a normalized form as expressed in (27) and the modified definition of resolution in (28).

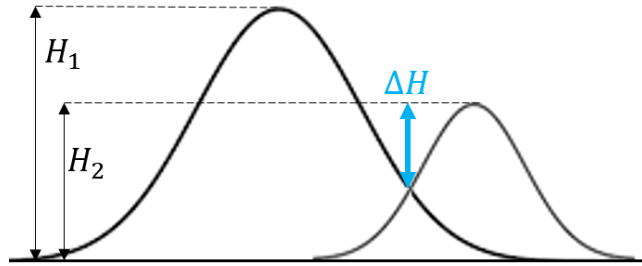


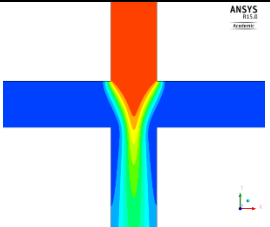
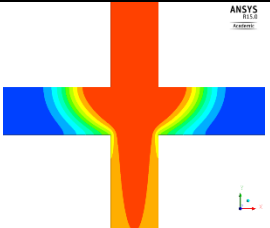
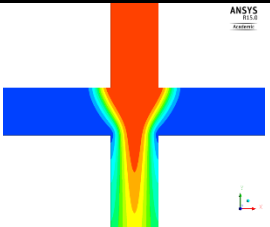
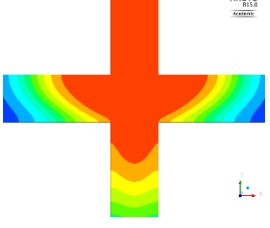
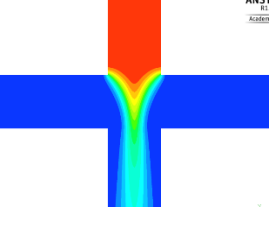
Figure 50: Peak to valley difference

$$F = \frac{\Delta H}{\text{Detectability threshold}} \quad (27)$$

$$R_{s,mod} = F \times R_{s,con.} \quad (28)$$

The results of the peak-to-valley factor assuming the detectability threshold of 0.1 for the modified resolution are presented in Table 5. Figure 51 and Figure 52 also show the trend of conventional and modified resolution for each configuration. These figures show that at the conventional definition of resolution, cases E, C and A provide higher resolutions. These cases are all in steady-state shapes which do not necessitate the observation for the time-to-stop injection.

Table 5: Modified resolution for cases A to E

| Case | Injection Shape | Shape factor | | | $R_{s,con.}$ | F | $R_{s,mod.}$ |
|------|---|-----------------|---|------|--------------|------|--------------|
| A |  | $\sigma = 0.34$ | detection spot from the center of cross , normalized by channel width | 2 | 0.62 | 1.7 | 1.8 |
| | | | | 4 | 1.01 | 1.8 | 1.81 |
| | | | | 6 | 1.31 | 1.8 | 2.35 |
| B |  | $\sigma = 0.19$ | | 2 | 0.37 | 2 | 0.74 |
| | | | | 4 | 0.77 | 6 | 4.62 |
| | | | | 6 | 1.13 | 6.8 | 7.7 |
| C |  | $\sigma = 0.24$ | | 2 | 0.64 | 3.5 | 2.24 |
| | | | | 4 | 1.09 | 4 | 4.36 |
| | | | | 6 | 1.38 | 3.5 | 4.83 |
| D |  | $\sigma = 0.12$ | 2 | 0.23 | 0.7 | 0.16 | |
| | | | 4 | 0.51 | 3.8 | 1.93 | |
| | | | 6 | 0.75 | 6.9 | 5.17 | |
| E |  | $\sigma = 0.82$ | 2 | 0.35 | 1.4 | 0.49 | |
| | | | 4 | 1.19 | 1.2 | 1.43 | |
| | | | 6 | 1.50 | 1 | 1.5 | |

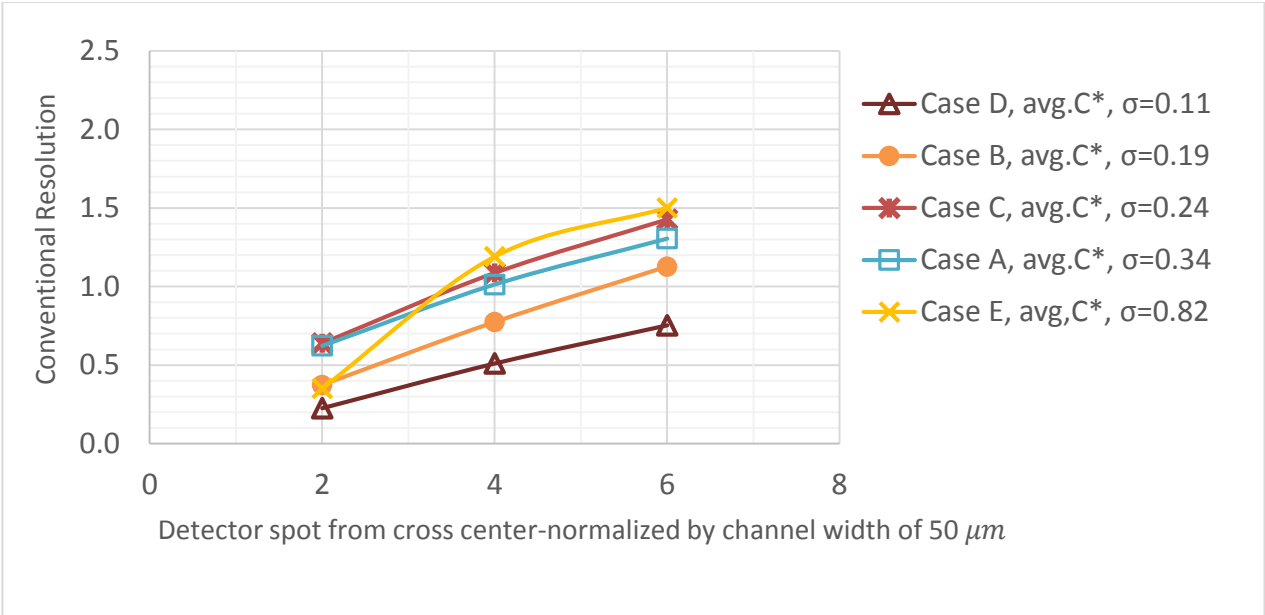


Figure 51: Conventional resolution

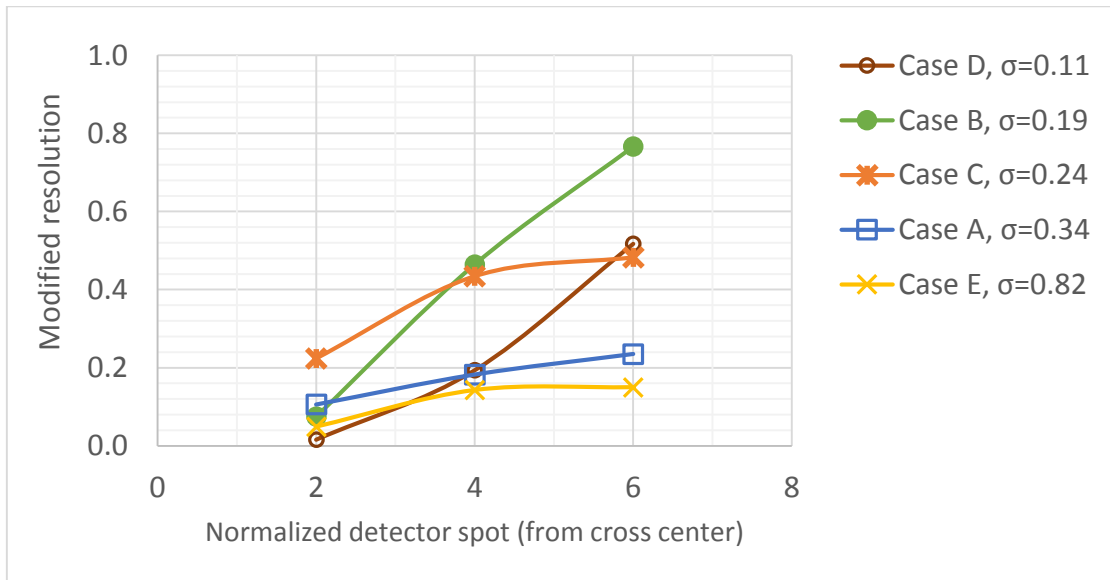


Figure 52: Modified resolution based on no threshold for detectability and normalized detector spot by channel width (50 μm)

4.5 Conclusions

In this chapter we evaluated the injection and separation with two parameters respectively: Injection is assessed by the shape factor and separation by resolution. We introduced the shape-factor model to assess the sample plug shape at injection at the (cross) intersection of the injection and separation channels. After introducing the four parameters for analyzing the shape of the sample, i.e., sample plug mean width, standard deviation from the mean width, first and second moments, standard deviation σ was introduced as the sole parameter as a benchmark to assess the shape of the sample plug. To find out the acceptable range for this shape-factor, we presented various possible shapes at the cross and concluded $\sigma \leq 0.2$ provides good shapes which are close to ideal rectangular shape.

To do the sample shape analysis with this model, and for further validation of the results with the experiments in literature, we started with the microchip design, where sample was injected vertically, for a symmetric control of the sample plug shape as the purpose of this research. The applied electric potentials were in accordance with the referred experiment in literature, adjusted for the current chip geometry. In the preliminary study of the sample plug shape, we did the numerical simulations for five different cases and presented the results of the shape-factor for each case by curve fitting to the 50% line at the concentration contours and plugging the coefficients of the curve fitted function into our shape factor model. For those five different achieved shapes, we provided the injection results, the shape factor σ , spatial and temporal separation results, and the separation resolution R_s , both in conventional and modified definitions. It is briefly explained that how diffusion of the sample into the buffer, vice versa, causes the peak concentration drop during separation and why the peak heights play a role in detecting the sample constituents. Addressing these issues, we modified the conventional definition of the resolution by adding a peak-to-valley factor for the concentration peaks which should be normalized by the detectability threshold, which indeed is a characteristic of the detector. We also studied the time-to-stop injection for the plugs which do not reach a pinched steady-state shape at the cross. The results show, the steady-state plugs maintain an unchanged shape factor after reaching the steady-state at the cross, which is an advantage in skipping the observation for time-to-stop injection.

In the next chapter, first I show the convergence study of the single-constituent sample injection and validate the numerical simulation results with experiments available in literature, then I do further analysis for improving σ by modifying the geometry, injection and separation procedures.

Chapter 5

Validation and Analysis

5.1 Introduction

In this chapter, I show the independency of the results from the grids in the numerical simulations. In addition to the grid independency, the results of the injection of a single-constituent sample is validated with experiments available in literature. Then Injection and separation analysis for the modified chip geometry and different configurations of applied electric potentials is provided.

5.2 Convergence Study

To examine the grid convergence for the solution, we show spatial (grid size) for electric and flow fields and both spatial and temporal (time-step) convergence for concentration field. This has to be proved in any computational problem to eliminate or reduce the influence of the number (size) of the grid on the computational results. Since the main objective of this thesis is the study of the shape of the sample at injection, or at the cross, so the mesh is generated by paying more attention to the $50 \times 50 \mu m^2$ region of the cross. To show the grid independency for discretization of the problem, this region was studied in six different structured meshes by starting from a coarse grid of 10×10 to the fine grid of 60×60 cells by adding 10 cells to each side for each case Figure 53, Table 6. To avoid large aspect ratios between the neighboring cells at the cross, the total number of grids increased as well. As shown in this figure, for the spatial grid at the region of interest in the problem, i.e. the cross, we started from a coarse mesh of 10×10 cells at the cross to a finer mesh of 60×60 cells, each time by adding ten cells to each side. For the time step, we started from a large time step of 0.1s and refined it to 0.01, 0.001, and finally 0.0005s.

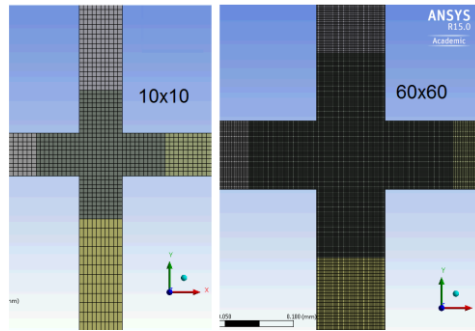


Figure 53: Making the mesh finer from 10×10 to 60×60 at the cross

Table 6: Spatial grid refinement information

| No. of grids at the cross | No. of Nodes | No. of Cells | Comment |
|---------------------------|--------------|--------------|---------------------------------------|
| 10x10 | 26730 | 12,140 | Steady state Electric and flow fields |
| 20x20 | 64218 | 30,560 | |
| 30x30 | 123,566 | 59,760 | |
| 40x40 | 201,146 | 98,080 | Transient concentration field |
| 50x50 | 392,802 | 192,500 | |
| 60x60 | 573,522 | 282,000 | |

To study the independency of the solution, the time step was fixed and the grid was refined and then the grid was fixed and time-step was refined. Figure 54 shows that all the refining the mesh has no effect on the electric field, however, Figure 55 shows the effect of refining the grid on the flow field. For the centerline velocity along the injection channel at the vicinity of the cross, with a slight discrepancy the corners, the results of 50x50 and 60x60 are overlapping.

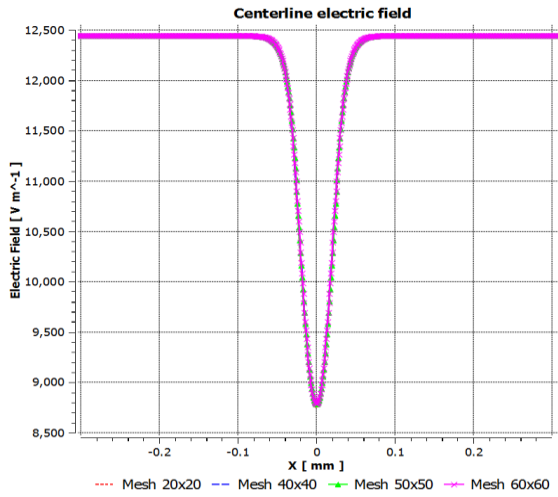


Figure 54: Grid independency for centerline electric field along injection channel

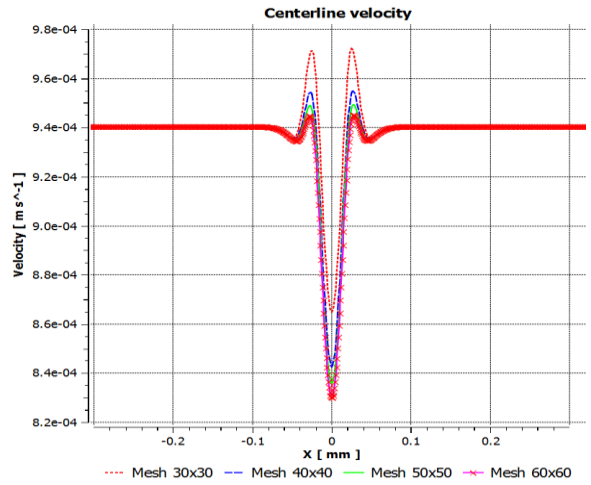


Figure 55: Grid independency for centerline velocity along injection channel

To show the grid independency for the electric field, the peak of \vec{E} is examined at the center of the cross as shown in Table 7. It shows steady and continuous growth with mesh refinement for peak of the electric field and the difference is approaching zero from 40x40 grid to 60x60.

Table 7: Electric Field and grid independency

| Mesh | Peak of E [KV/m] | Delta Peak of E [kV/m] | E(0,0) [KV/m] | Delta E(0,0) [KV/m] | Nominal Electric Field [KV/m] |
|-------|------------------|------------------------|---------------|---------------------|-------------------------------|
| 10x10 | 16 | | 8.66313 | | 12.422 |
| 20x20 | 18.5 | 2.5 | 8.74526 | 0.08213 | |
| 30x30 | 20.5 | 2 | 8.76783 | 0.02257 | |
| 40x40 | 22 | 1.5 | 8.77784 | 0.01001 | |
| 50x50 | 23.5 | 1.5 | 8.78335 | 0.00551 | |
| 60x60 | 25 | 1.5 | 8.78678 | 0.00343 | |

To refine the time step, the concentration solution along the centerline of the injection channel (horizontal injection) and with 0.1 mol/m^3 original sample concentration is examined. Figure 56 shows the independency of the problem to the time-step by refining it to 0.005s, 0.001 and 0.0005s. For the two grids shown in this figure, 20x20 and 60x60, it is observed that the results are overlapping for time steps 0.001 and 0.0005s; therefore, time step 0.001s is chosen.

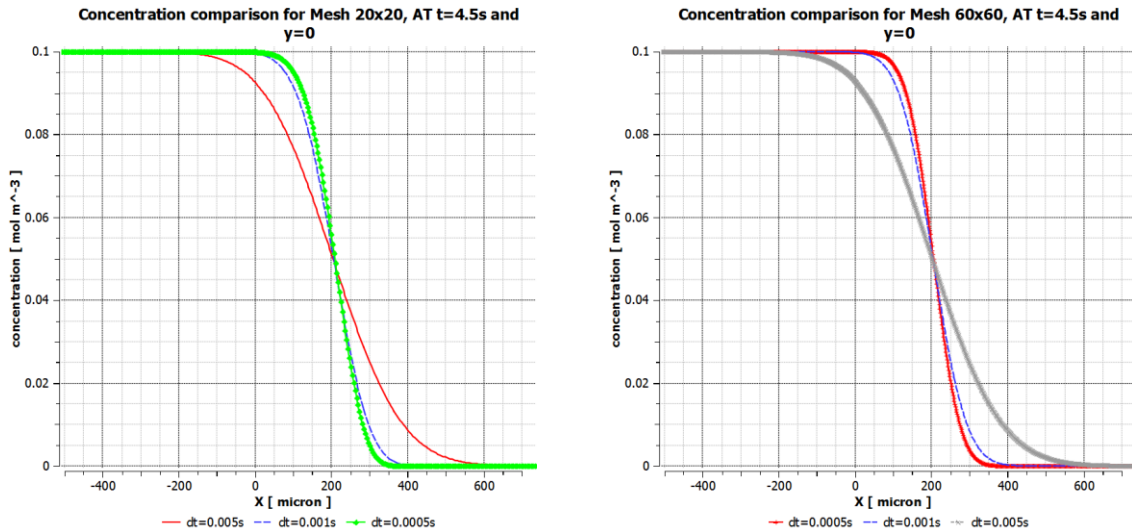


Figure 56: Time-step independency for medium and fine grid sizes 20x20 (left) and 60x60 (right)

Figure 57 shows the sample in white for the region with concentration equal/greater than 50% of that of the original sample at time step 0.001s when the sample reached the cross (here at $t = 4.5s$). At the interface of the sample and buffer, $50\%C$ is the most stable and reliable location for concentration analysis. At 20x20 grids, the location for the tip of $50\%C$ is $(206\mu m, 0)$ and for 30x30grid is $(204.7\mu m, 0)$. The results of the location of $X_{0.5C}$ are presented in Figure 58 and Figure 59 for the first and second order of accuracy when N is the number of cells at each side of the cross.

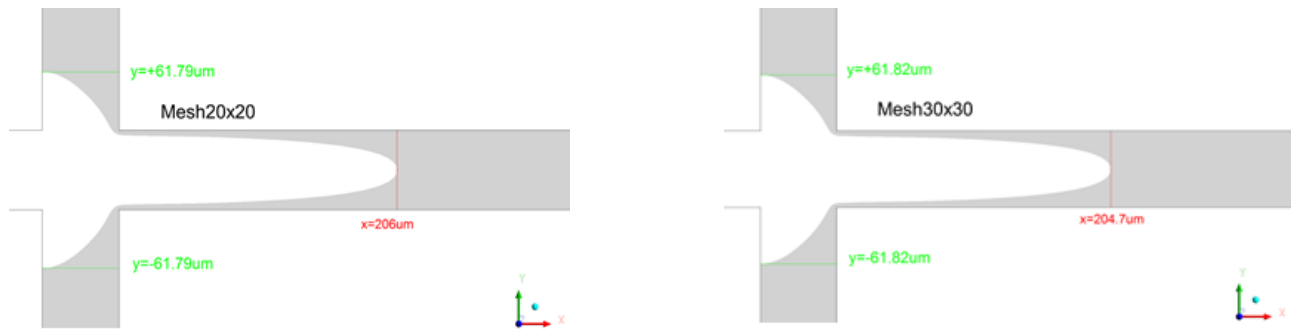


Figure 57: Sample concentration region $C^* \geq 0.5$ (white), $dt=0.001s$ for two different grids

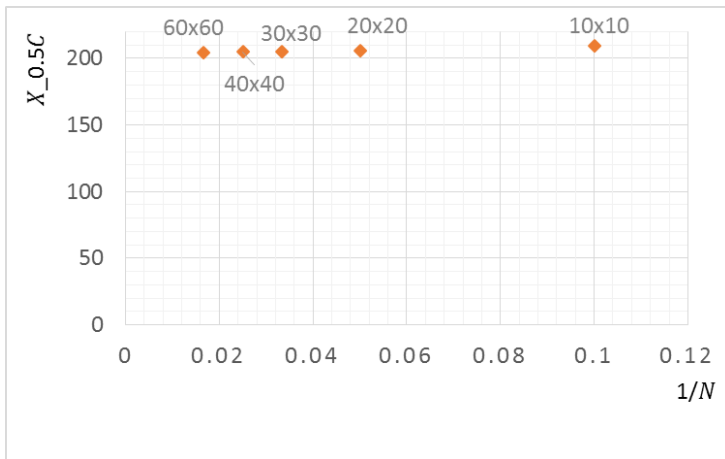


Figure 58: $x_{0.5c}-1/N$, $dt = 0.001s$

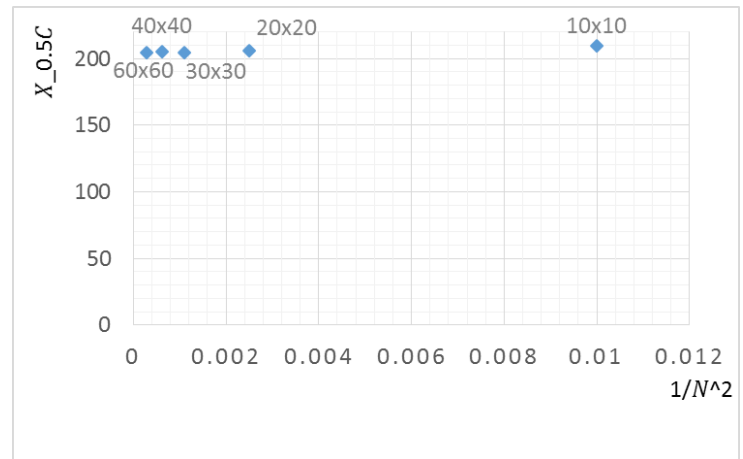


Figure 59: $x_{0.5c}-1/N^2$, and $dt = 0.001s$

Figure 60 and Figure 61 show the second order of accuracy for the spatial grid by refining the mesh from 10×10 to 60×60 cells at the $50 \times 50 \mu m^2$ cross. $1/N$ and $1/N^2$ are used for the first and second order of accuracy of spatial grids when N is number of cells at each side of the cross. A quadratic fit on the $1/N$ results in Figure 60 shows 0.26 % error and a linear fit to the results of Figure 61 comes with an error of 0.5%. To see more details of these figures, Figure 62 and Figure 63 are presented.

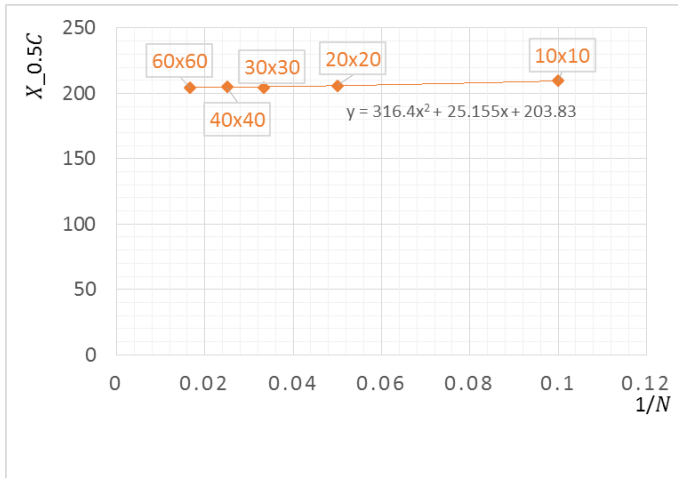


Figure 60: $x_{0.5c}-1/N$, and $dt = 0.001s$

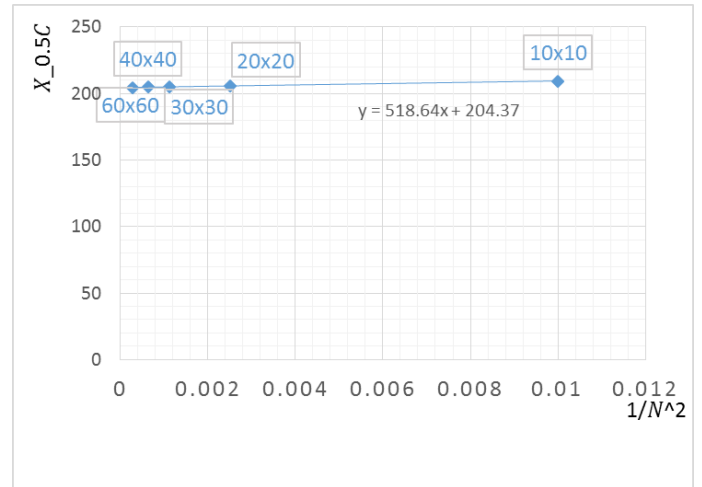


Figure 61: $x_{0.5c}-1/N^2$, and $dt = 0.001s$

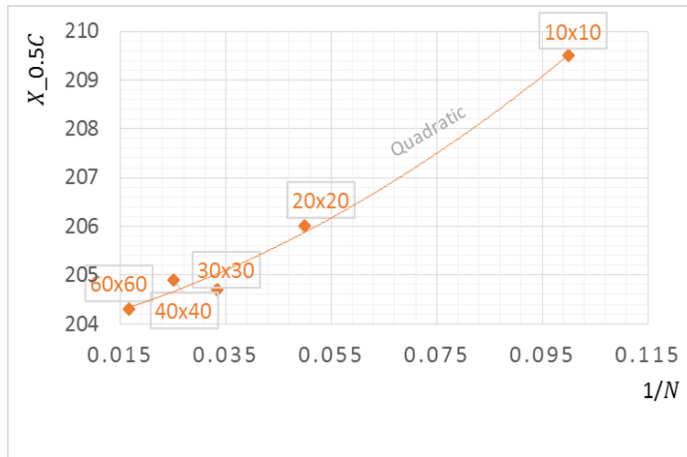


Figure 62: Zoom of $x_{0.5c}-1/N$, and $dt = 0.001s$

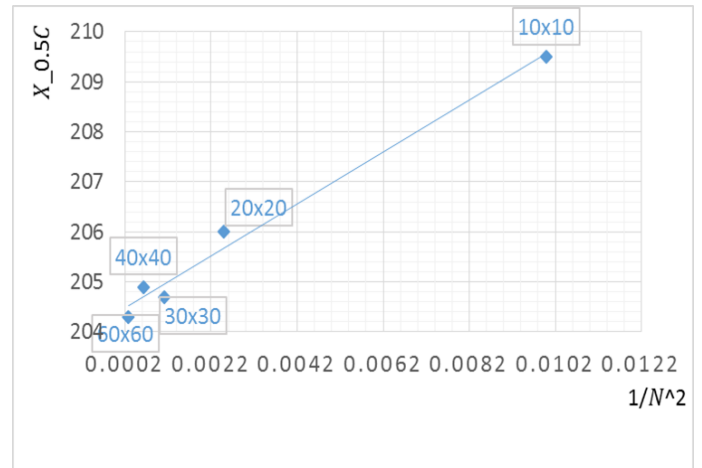


Figure 63: Zoom of $x_{0.5c}-1/N^2$, and $dt = 0.001s$

Table 8 shows the results of the location of the 50%C location along the injection channel for different time steps, compared for a coarse and fine spatial grid at the cross.

Table 8: Time-step grid independency of 50%C location for fine and coarse grids

| Time step (s) | $X_{0.5c}(\mu m)$ at 4.5s (at cross) | |
|---------------|--------------------------------------|---------|
| | 20x20 | 60x60 |
| 0.01 | 200 | 200.951 |
| 0.005 | 204.698 | 202.006 |
| 0.001 | 206.572 | 204.373 |
| 0.0005 | 209.382 | 205.557 |

The location of the front edge of the 50% C^* contour on the centerline of the injection channel is examined for the small and large time steps for the finest grid at the cross (60x60). The results are plotted in Figure 64 for first order accuracy of time step Δt and the error becomes 0.35% .

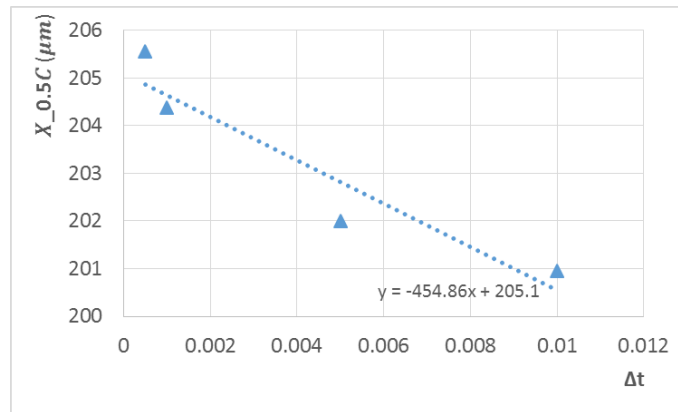


Figure 64: Time step convergence, $\Delta t = 0.001s$ for the finest grid at the cross (60x60)

The results of the grid independency studies presented above proves that we can stop refining the mesh at the uniform mesh 40×40 cells at the cross and also use the time step 0.001s . Figure 65 also shows the convergence history of $1e - 8$ for RMS of electric potential by refining the grids at the cross from 10x10 to 60x60.

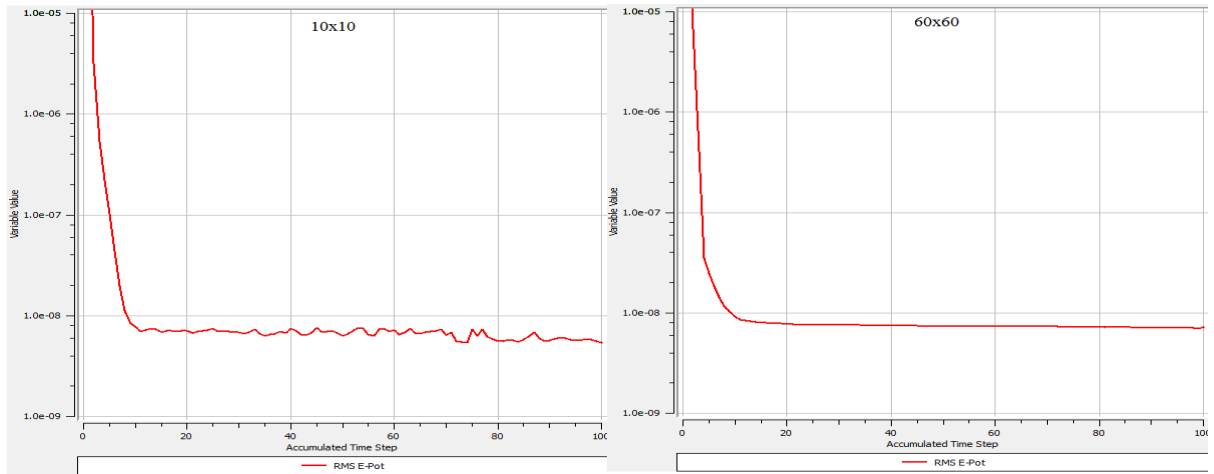


Figure 65: Electric potential RMS convergence for grids 10x10 to 60x60 at the cross

Figure 66 shows the electric potential convergence error for refining the grids at the cross from 10x10 to 50x50.

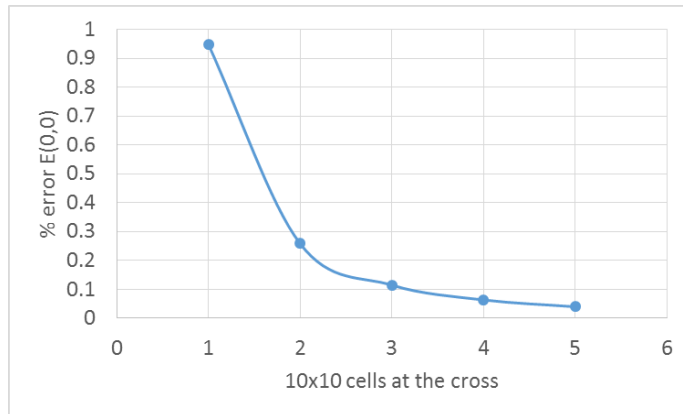


Figure 66: Electric potential convergence error for grids 10x10 to 50x50 at the cross

Based on the above convergence studies, the spatial grid at the cross is 40x40 and the time step is 1ms.

5.3 Validation

To validate the injection model for a single-species sample, the numerical results are compared to the experimental results of Ren et al. [111]. They used a glass chip with the shown geometry in Figure 67 and potentials were applied at the reservoirs to load and dispense the sample and buffer solutions. In their experiments, the sample was injected from R_1 and after being loaded at the intersection of the channels, the separation performed in the channel between R_2 and R_4 reservoirs. $\phi_{1,2,4} = 1369V$ and $\phi_3 = 0V$. The electroosmotic and electrophoretic mobilities of the used sample were $\mu_{eo} = 4.5 \times 10^{-8} \frac{m^2}{Vs}$, $\mu_{ep} = -1.65 \times 10^{-8} \frac{m^2}{Vs}$ and the diffusivity was $D = 4.37 \times 10^{-10}$.

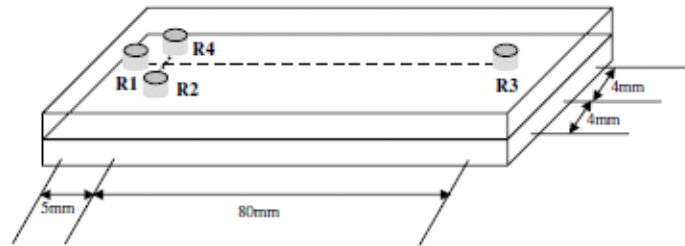


Figure 67: Chip configuration in experiments of Ren et al. for verification of injection model

Figure 68 shows the experimental image of concentration field in grey scale, where white is the sample and black is the buffer solution. (Except the black lines for channel walls)

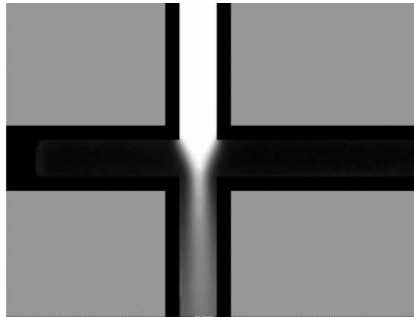


Figure 68: Direct experimental image of concentration field in grey scale copied from Fig.7a by Ren et al. [111]

Figure 69 shows a good agreement of the current numerical model at injection with the experimental results for such steady-state plug at the cross. The earliest time sample reached the cross was $t = 21s$.

The normalized concentration along the injection channel is zero in the buffer region and at center of the cross reaches to the peak of the original sample concentration.

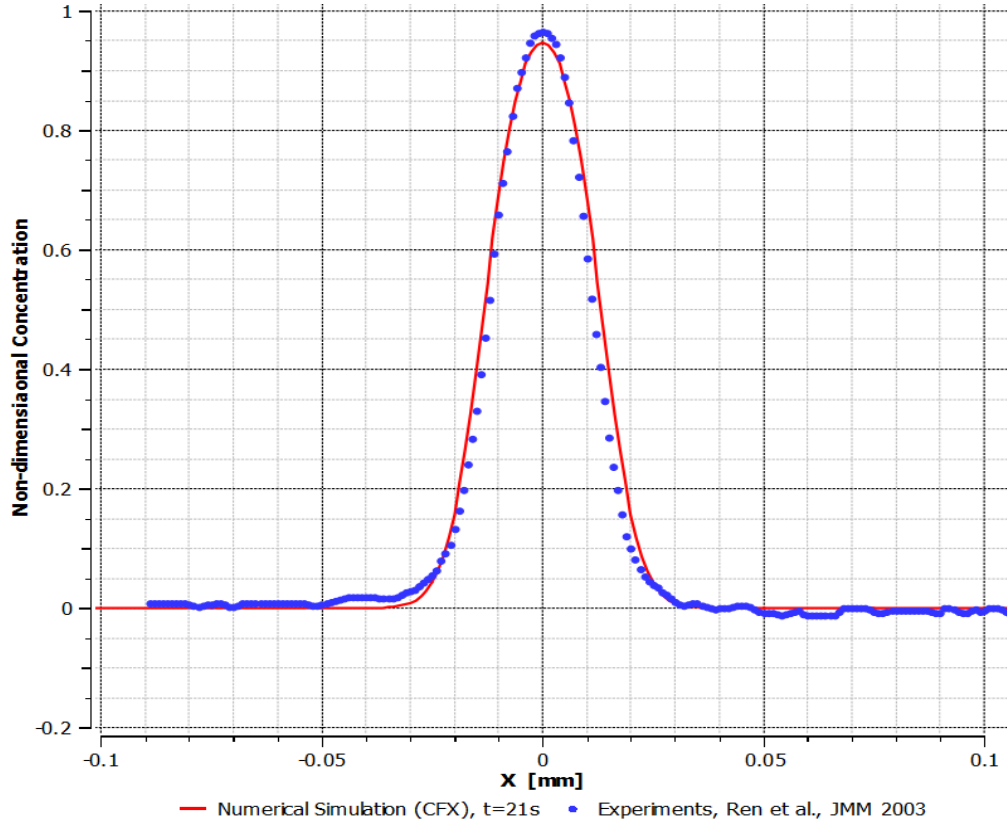


Figure 69: Verification of injection simulation of a single-component sample with experiments

5.4 Injection and Separation Analysis

In this section, first the modifications on geometry are addressed. Then, for the final geometry, different configurations for the applied electric potentials at injection are presented. Following the injection configurations, the same procedure is taken for the separation. Finally, the results of the best injection procedure and separation configuration are presented.

5.4.1 Modified Geometry

Figure 71 shows how we modified the geometry of channels during this research. The first geometry was based on a horizontal injection and also with a separation channel longer than the injection one. This geometry was selected based on the common long separation channel and also for

the purpose of verification with the experimental results in the literature. The second geometry has similar dimensions to the first one, but the sample is injected vertically. Such rotation for the sample injection direction provides a symmetric sample plug shape with the side-applied electric potentials. The results of the second geometry showed the separation of the sample constituents prior to the middle of the separation channel; therefore the third geometry is based on reducing the separation channel length. Moreover, all the channel legs have equal length. Finally, to limit the sample deviation, the separation channel width is reduced to half.

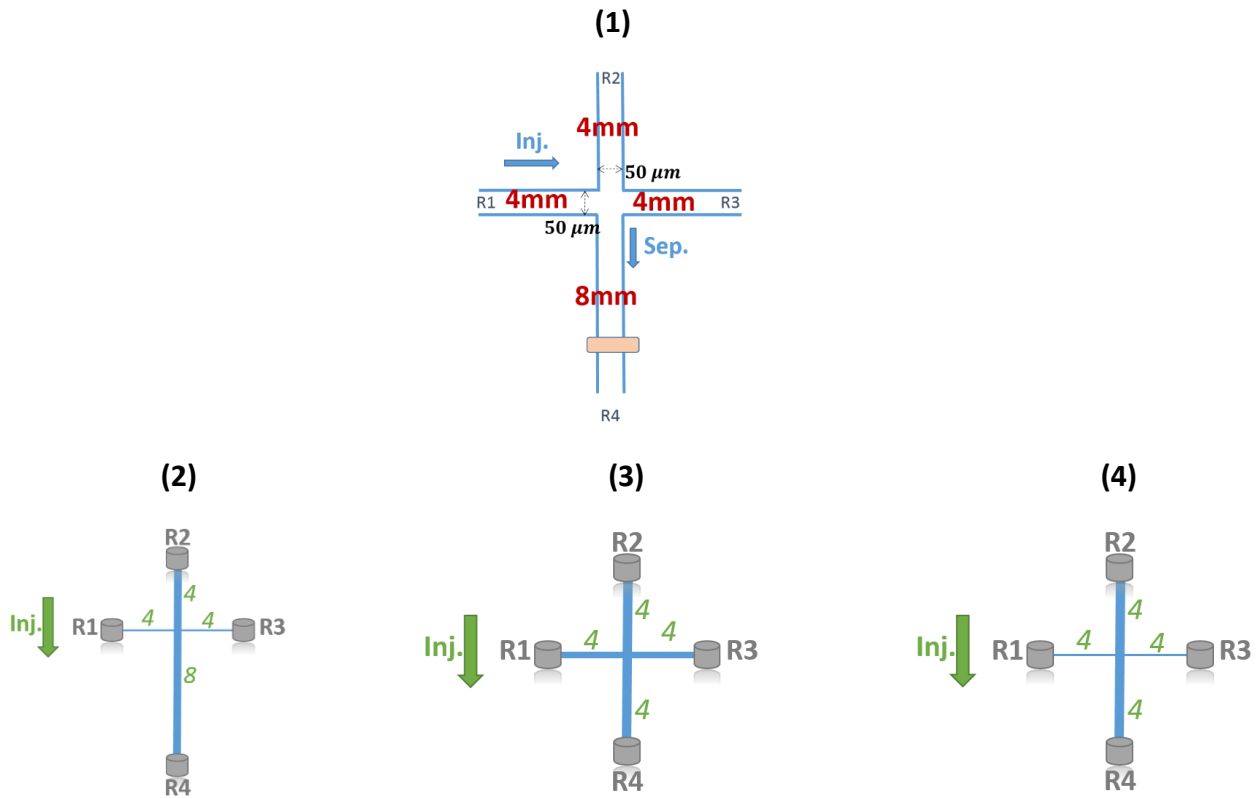


Figure 70: Modifications on chip geometry

The following results are all based on the final geometry as shown in Figure 71.

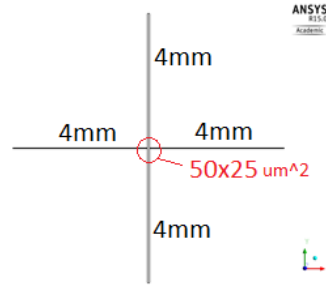


Figure 71: New geometry of channels with equal length and narrow separation channel

5.4.2 Injection Configurations for the Final Geometry

As discussed in Appendix B, the non-dimensional applied potential at reservoir “i”, $\phi_{Ri}^* = \frac{\phi_{Ri} - \phi_r}{\Delta\phi_r}$, is an important controlling parameter for the shape of the sample plug at injection.

Further studies show that at separation it also affects the achieved resolution.

For a vertical injection from R_2 to R_4 , the controlling parameters for the shape of the sample plug are $\phi_{R1}^* = \frac{\phi_{R1} - \phi_r}{\Delta\phi_r}$ and $\phi_{R3}^* = \frac{\phi_{R3} - \phi_r}{\Delta\phi_r}$, where $\Delta\phi_r = \phi_2 - \phi_4$ and ϕ_4 is set to ground. The controlling potential at injection is called ϕ_{inj}^* and we studied different configuration of $\phi_{inj}^* = 1, 0.75, 0.6, 0.5, 0.4, 0.25$ and floating in the following sections. The results of injection, sample plug shape and shape factor analysis for each configuration are presented.

5.4.2.1 $\phi_{inj}^* = 1$ and 0.75

Figure 72 shows the applied electric potentials/fields for $\phi_{inj}^* = 1$, when $\phi_2 = 100V$.

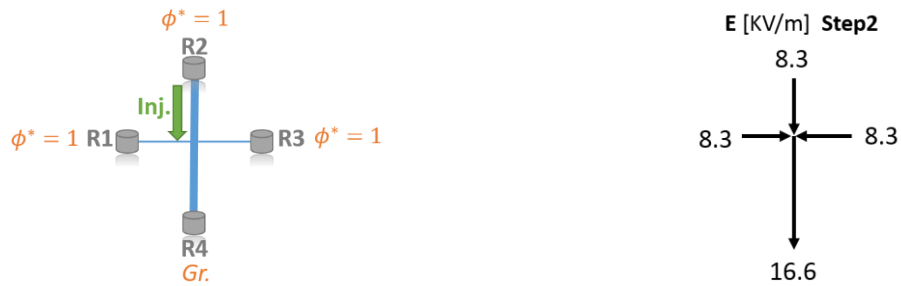


Figure 72: Configuration $\phi_{inj}^* = 1$ ($\phi_2 = 100V$)

For such configuration, the electric field and flow streamlines are as presented in Figure 73, which result in a pinched injection as shown in the two left columns of Figure 74.

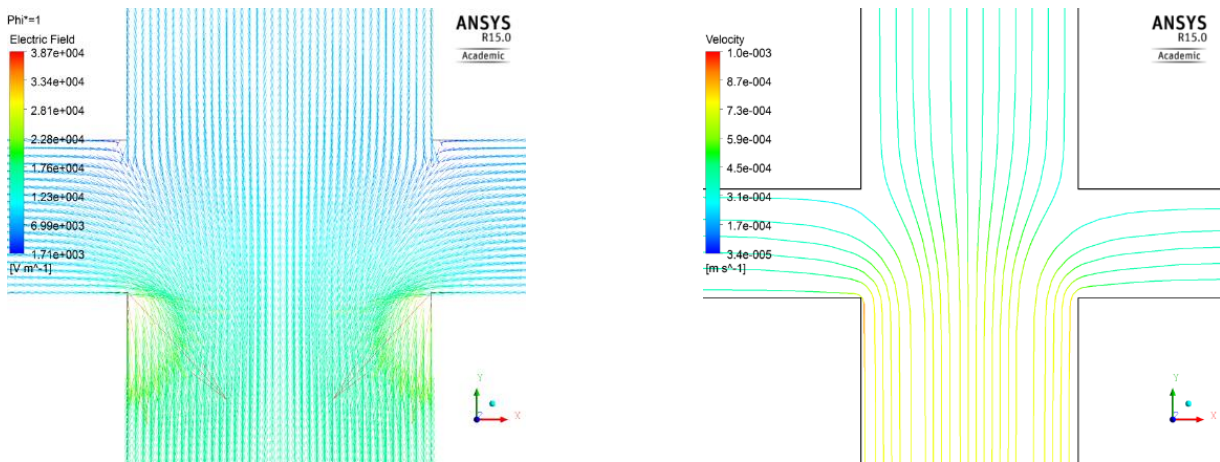


Figure 73: Electric field vectors and flow field stream lines ($\phi^* = 1$)

Figure 74 shows the concentration contours for the two configurations $\phi_{inj}^* = 1$ and $\phi_{inj}^* = 0.75$ for both Rhodamine and Fluorescein, each at four different time slots before the cross, at the cross and past the cross. The black line at each contour shows the 50% concentration line, which is analyzed for the shape factor to evaluate the sample plug shape. It is worth mentioning that the injection stops when the slower constituent reaches the cross. When the high concentration part of the sample (here red) covers the cross, then we switch to separation.

The concentration contours for fluorescein at $\phi_{inj}^* = 1$ show that fluorescein doesn't penetrate the cross sufficiently, therefore, it is not worth trying the separation at this stage. It reaches the steady-state

pinched injection and in the following section, we show that by adding a second injection step to this configuration, we achieve much better results. The same problem holds for $\phi_{inj}^* = 0.75$, however with more penetration of the high concentration part for fluorescein but not sufficient yet.

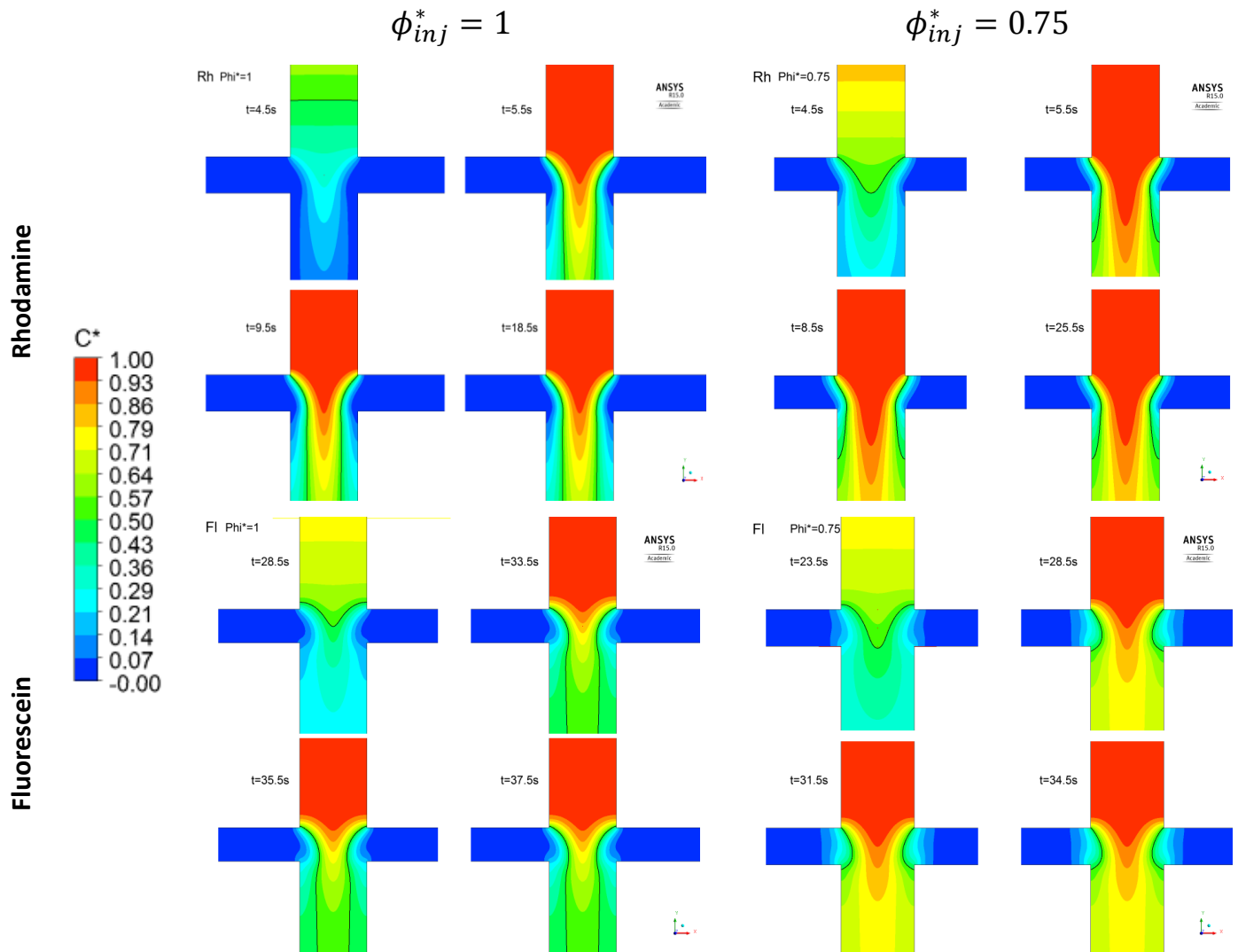


Figure 74: Sample plug shapes for Rhodamine (1st and 2nd rows) and Fluorescein (3rd and 4th rows) at different times for two configurations $\phi_{inj}^* = 1$ and 0.75

Although, configurations $\phi_{inj}^* = 1$ is not good for switching to separation, the sample shape analysis is shown in Figure 75.

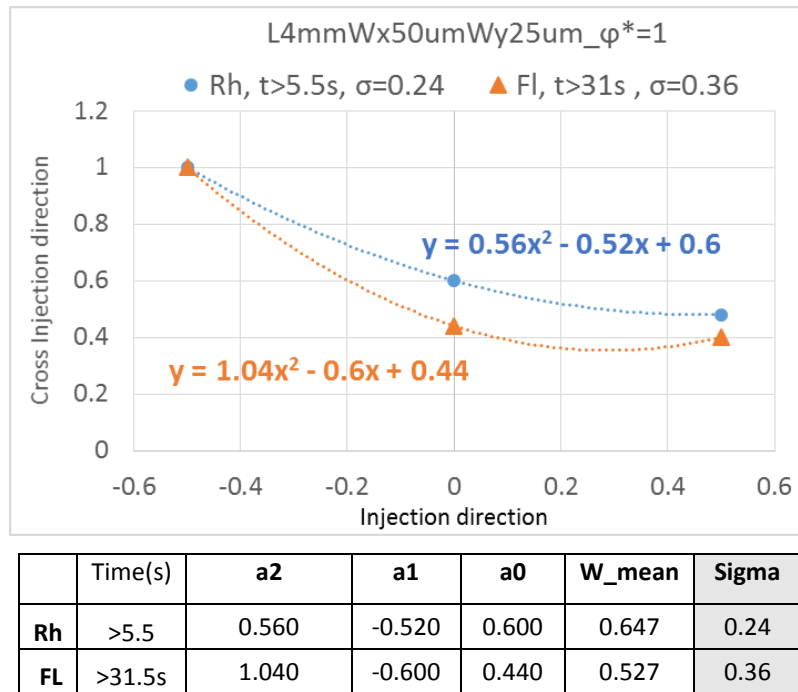


Figure 75: Shape factors for both constituents at $\phi^* = 1$

For both configurations of $\phi_{inj}^* = 1$ and 0.75, the slower constituent does not penetrate the cross sufficiently; therefore this configuration is not worth switching to separation either!

5.4.2.2 $\phi_{inj}^* = 0.5$ and 0.25

To give the slower constituent, here fluorescein, more chance of penetrating the cross, the side potentials are reduced to configurations of $\phi_{inj}^* = 0.5$ and 0.25 as shown in Figure 76. The results show that no steady-state is achieved, therefore, the stop-injection time must be observed thoroughly. Remarkably, it is observed that $\phi_{inj}^* = 0.5$ provide an almost rectangular plug.

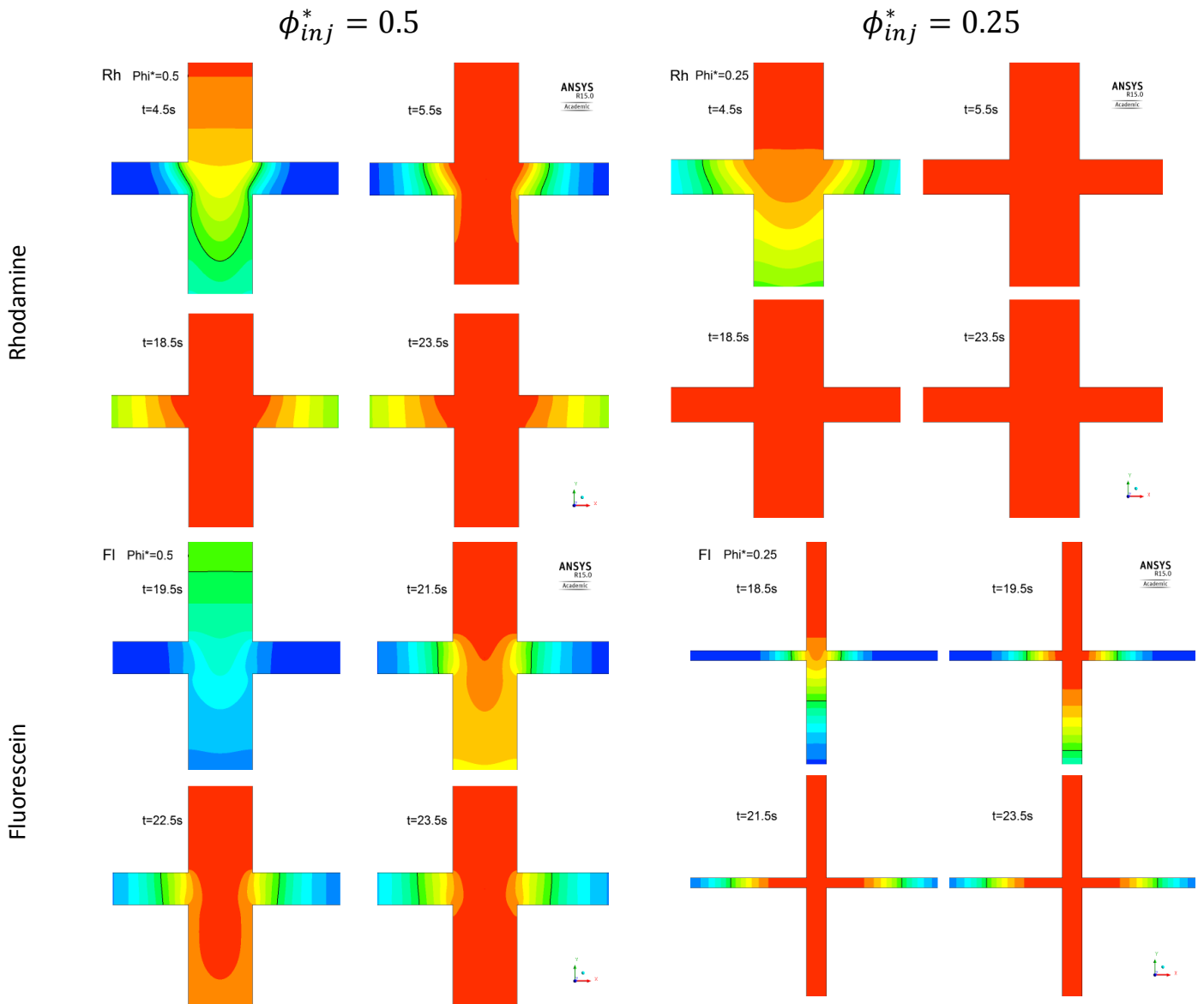


Figure 76: Sample plug shapes for Rh (1st and 2nd rows) and Fl (3rd and 4th rows) at different times for two configurations $\phi_{inj}^* = 0.5$ and 0.25

In $\phi_{inj}^* = 0.25$, for the same reason of not having a pinched and steady-state configuration, the sample plug is wide, which takes more time for the constituents to be separated from each other. As shown in Figure 78, by the time the slower constituent reaches the cross, the faster one is pretty much dispersed,

up to the middle of the separation channel. Such a wide sample plug results in a poor separation resolution and is not worth trying the separation.

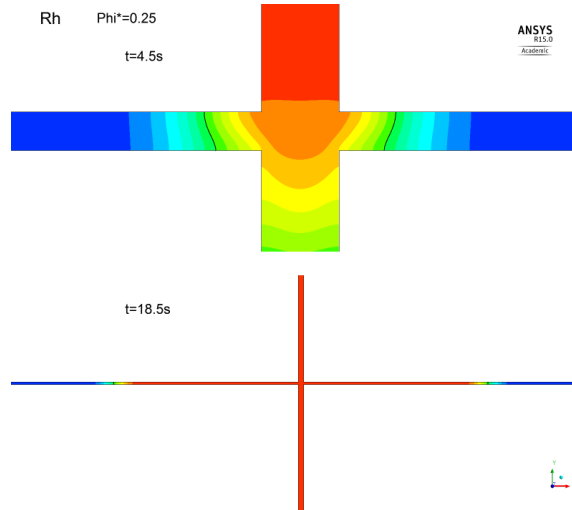
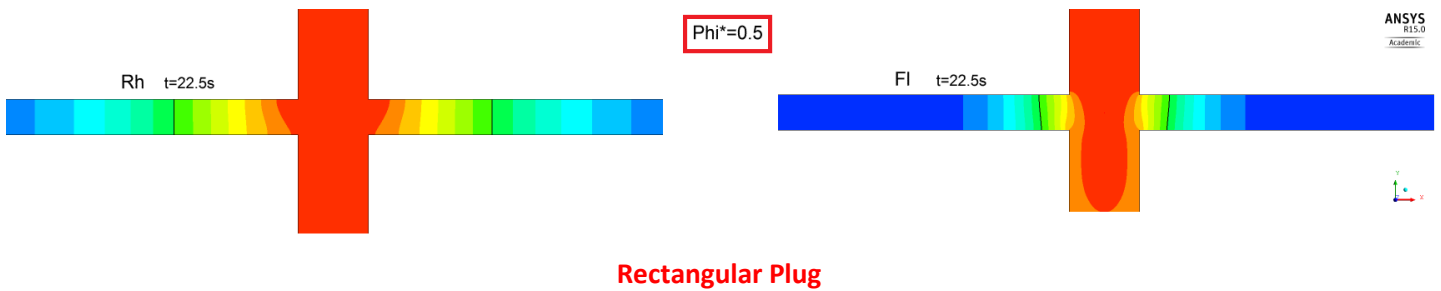


Figure 77: Wide Rhodamine sample plug at $\phi_{inj}^* = 0.25$

For $\phi_{inj}^* = 0.5$, at the earliest time, when both Rhodamine and Fluorescein arrive at the cross, the sample plug shapes are illustrated in Figure 78. The results show a rectangular plug, with wider actual width for the faster constituent, Rhodamine. This shows maintaining one of the main objectives in this thesis, to achieve the ideal plug only by controlling the applied potentials and chip geometry modifications.



Rectangular Plug

Figure 78: Rectangular plug (at 50% contour line) for $\phi_{inj}^* = 0.5$ configuration

For this configuration ($\phi_{inj}^* = 0.5$), more detailed temporal results of concentration is shown in Figure 79, $t = 21.9s$ is selected as the stop-injection time. At $t = 21.9s$ both sample constituents are available at the cross with high non-dimensional concentration. Indeed, by the time the slower constituent reaches the cross, the faster one arrived at the end of the injection channel, but injection is stopped when both constituents are at the cross. This assures the purpose of separation starting from the cross.

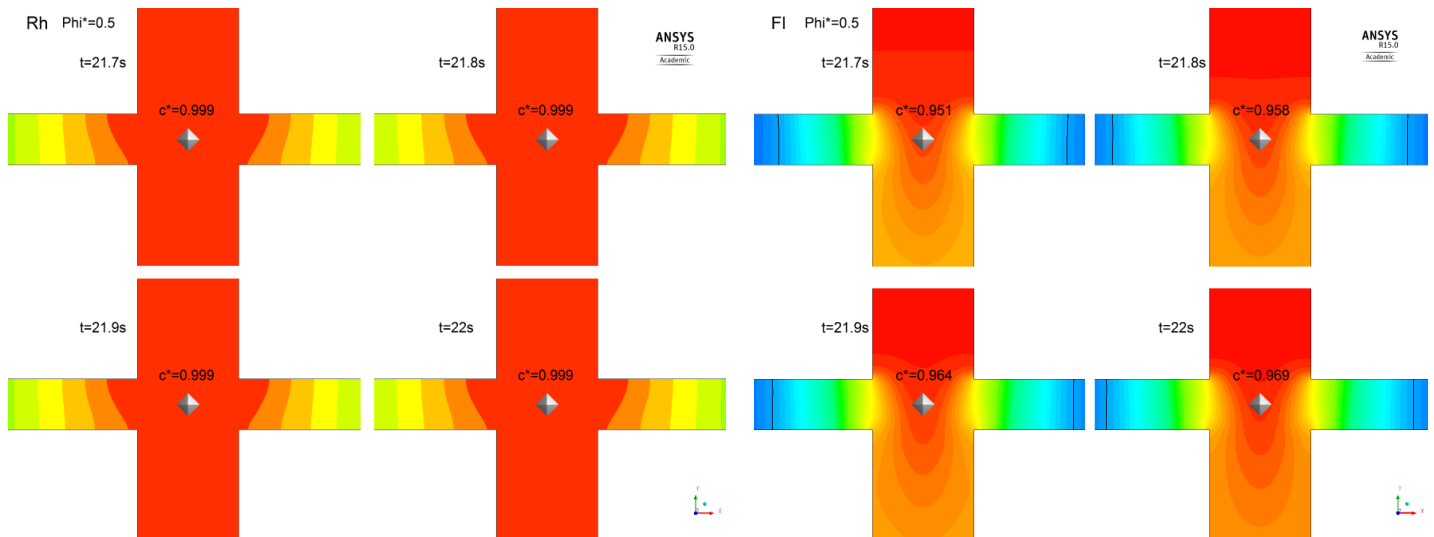


Figure 79: Stop-injection time, max c^* at the cross, Rh (Left), FI (Right), $\phi_{inj}^* = 0.5$

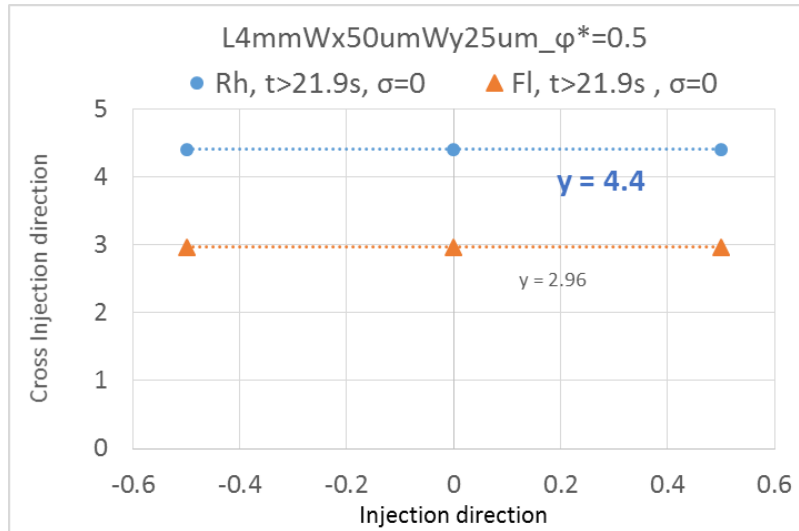


Figure 80: Rectangular plug and zero shape factor

The results of injection at $t = 21.9s$ are used as the initial concentration condition for separation.

5.4.2.3 ϕ_{inj}^* : floating

In addition to above configurations, floating configuration (zero potential gradient) between the reservoirs of separation channel is also studied which also provides rectangular plug.

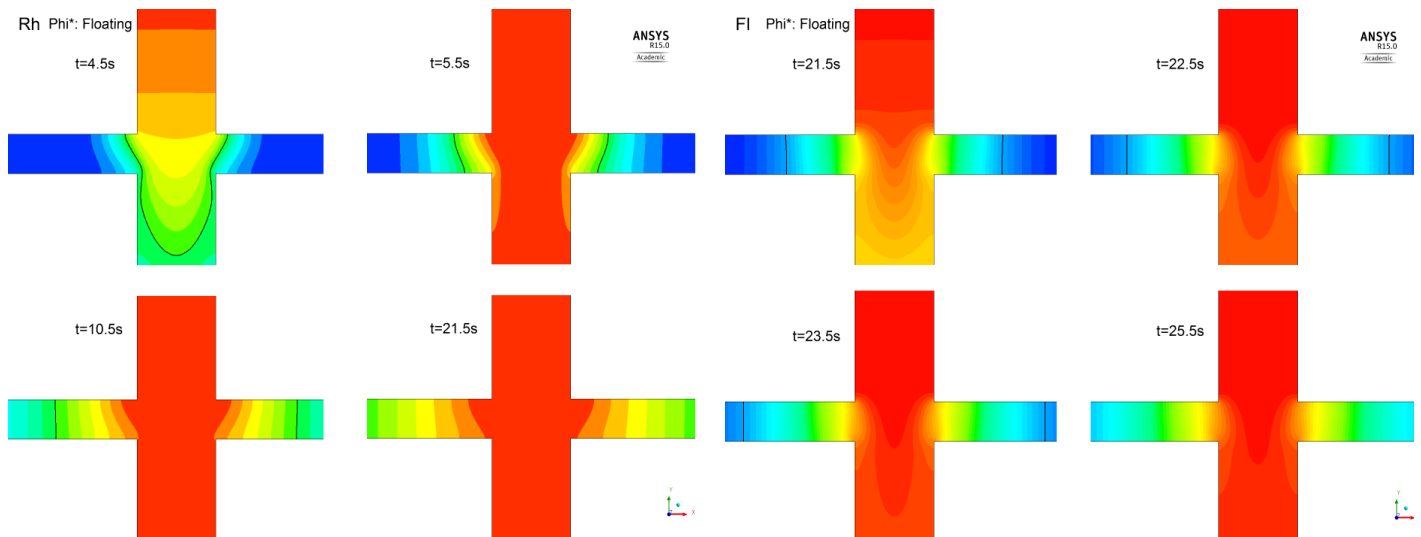


Figure 81: Sample plug shapes for Rhodamine (Left) and Fluorescein (Right) at different times, ϕ_{inj}^* : floating

Similar to the $\phi_{inj}^* = 0.5$ configuration, the sample plug shape is rectangular at floating injection. Both constituents penetrate the cross and keep migrating along the injection channel, while dispersed into the separation channel as long as the sample is kept injected.

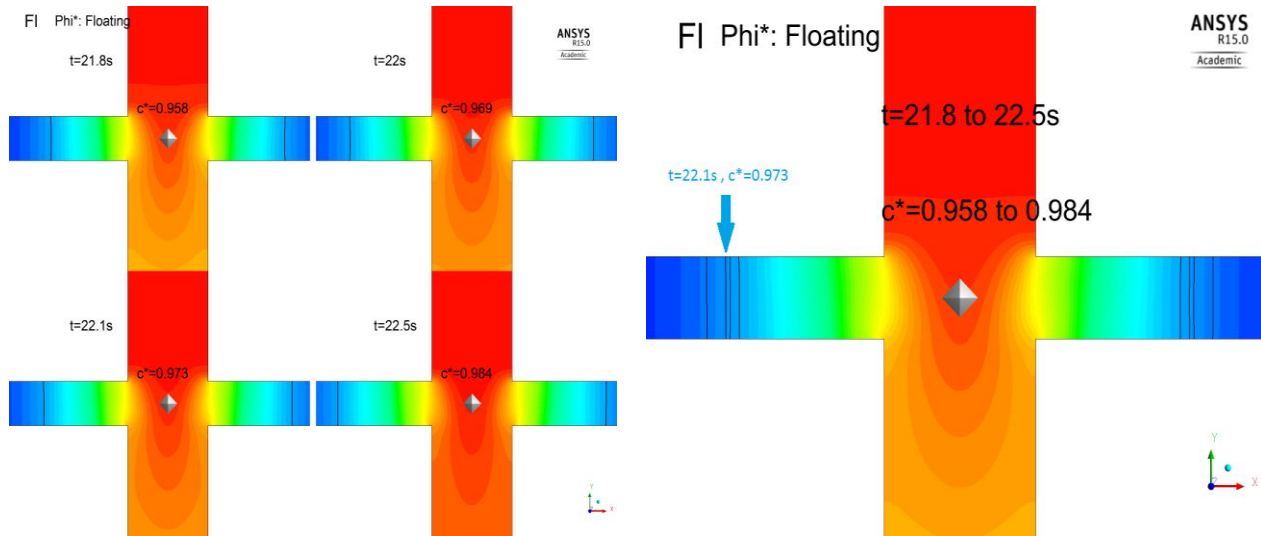


Figure 82: Stop-injection time ($t = 22.1s$) and max c^* at the cross for ϕ_{inj}^* : floating

A comparison between the floating injection and $\phi_{inj}^* = 0.5$ configuration shows identical sample plug shape as shown in Figure 83.

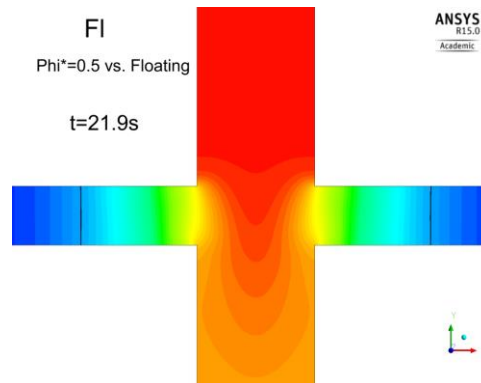


Figure 83: A comparison between $\phi^* = 0.5$ and f floating injection configurations for Fluorescein sample plug shapes at $t = 21.9s$

From all above mentioned configurations, first we run the separation for $\phi_{inj}^* = 0.5$ configuration. Similar to injection configurations, separation potential configurations are also in 5 forms of $\phi^* = 1, 0.75, 0.5, 0.25$ and floating. First, we studied floating configuration.

5.4.2.4 $\phi_{inj}^* = 0.4$

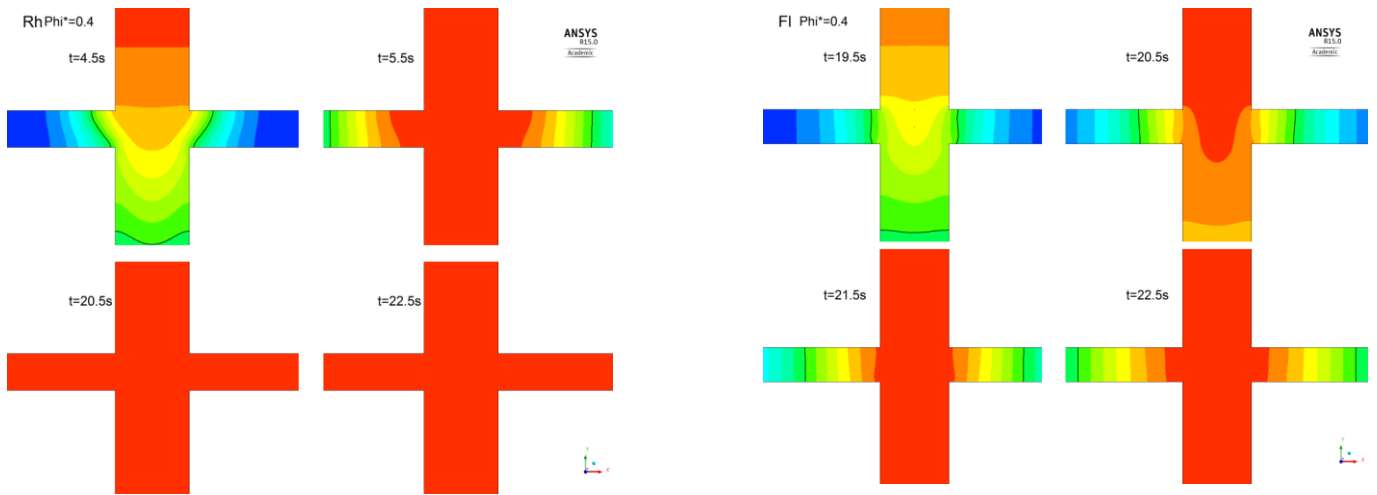


Figure 84: Concentration contours, injection $\phi_{inj}^* = 0.4$

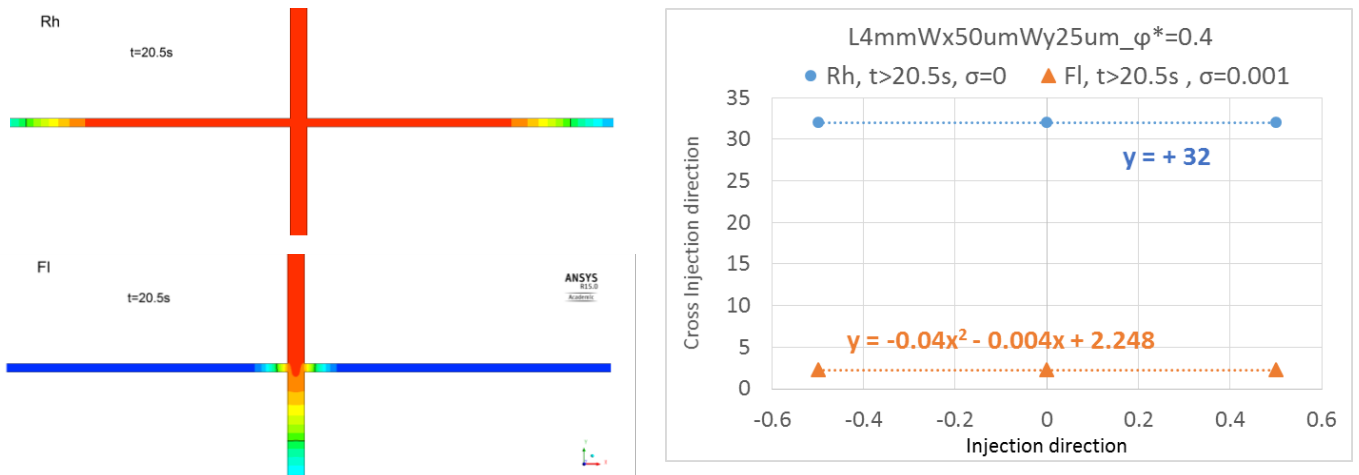


Figure 85: Concentration contours and shape factor at $t = 20.5s$ for injection $\phi_{inj}^* = 0.4$

5.4.2.5 $\phi_{inj}^* = 0.6$

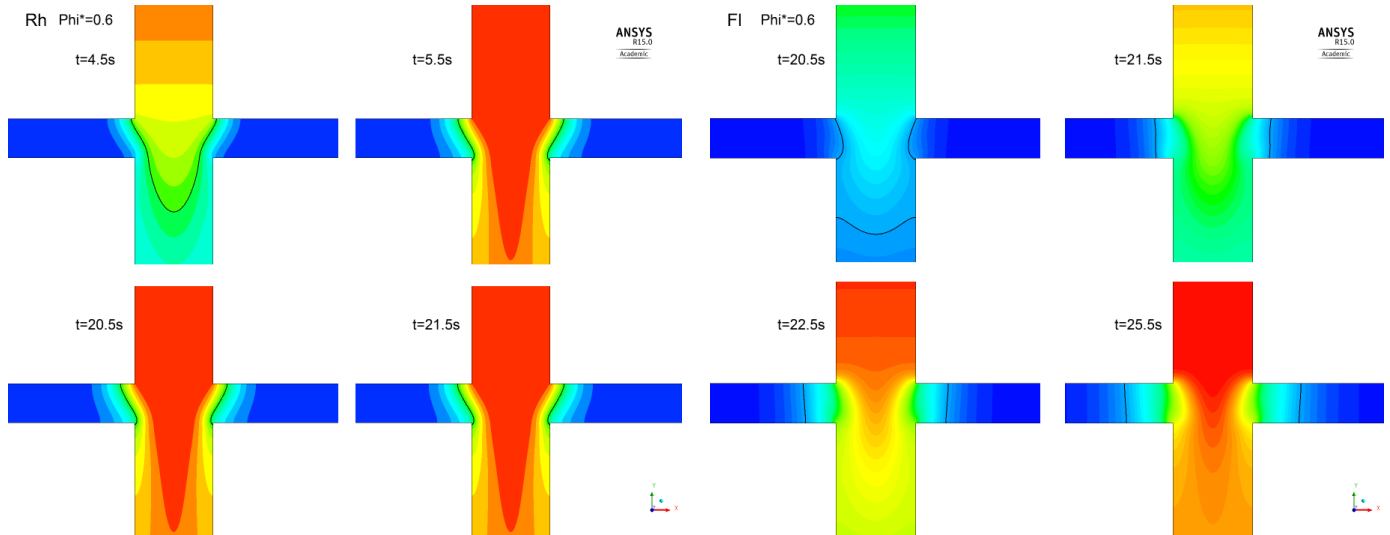


Figure 86: Concentration contours, injection $\phi_{inj}^* = 0.6$

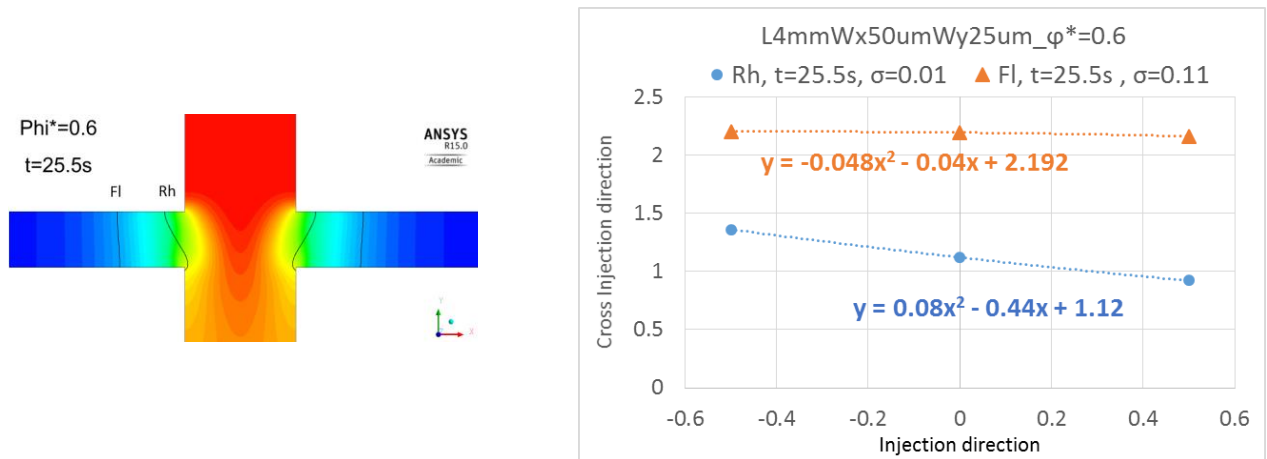


Figure 87: Concentration contours and shape factor at $t = 25.5s$ for injection $\phi_{inj}^* = 0.6$

5.4.3 Comparison among Different ϕ_{inj}^* Configurations

Table 9 and Figure 88 show the comparison of four different configurations at injection for shape factor and actual mean width of the sample plug. The results show that considering these two factors, $\phi_{inj}^* = 0.5$ provides the rectangular sample plug. In terms of sample actual mean width, $\phi_{inj}^* = 0.4$ configuration provides a very wide plug for Rhodamine which results in a poor resolution.

Table 9: A comparison of shape factor and sample plug width for different ϕ_{inj}^*

| ϕ_{inj}^* | | 1 | 0.6 | 0.5 | 0.4 |
|----------------------------------|----|------|-------|-----|-------|
| Shape factor σ | Rh | 0.24 | 0.01 | 0 | 0 |
| | Fl | 0.36 | 0.11 | 0 | 0.001 |
| Actual mean width (μm) | Rh | 32.3 | 109.6 | 220 | 1600 |
| | Fl | 26.3 | 55.7 | 148 | 112.2 |

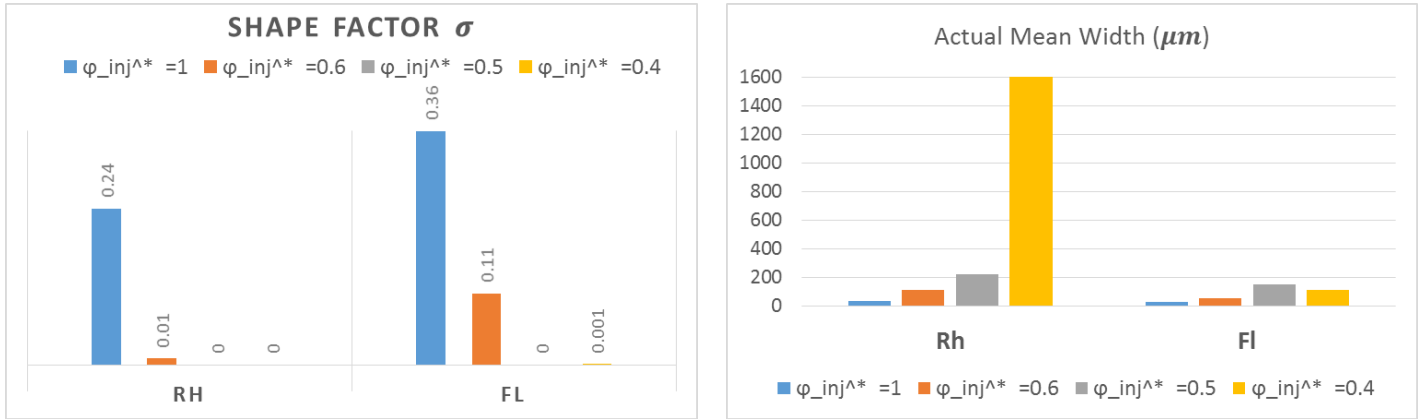


Figure 88: A comparison of shape factor and sample plug width for different ϕ_{inj}^* configurations

5.4.4 Separation Configurations

Similar to injection configurations, we have $\phi_{Ri}^* = \frac{\phi_{Ri} - \phi_r}{\Delta\phi_r}$, as an important controlling parameter at separation. Further studies show that in addition to the shape of the plug, separation

configuration affects the separation resolution. For a vertical injection from R_2 to R_4 , the controlling parameters at separation along the channel from R_1 to R_3 , are $\phi_{R2}^* = \frac{\phi_{R2} - \phi_r}{\Delta\phi_r}$ and $\phi_{R4}^* = \frac{\phi_{R4} - \phi_r}{\Delta\phi_r}$, where $\Delta\phi_r = \phi_1 - \phi_3$ and ϕ_3 is set to ground. The controlling potential at separation is called ϕ_{sep}^* and we studied different configuration of $\phi_{sep}^* = 0, 0.25, 0.4, \text{floating}, 0.6$ and 1 . From the previous injection results, configuration $\phi_{inj}^* = 0.5$ is taken as the best injected plug so far. Similar to injection, different configurations are studied for separation as shown in Figure 89.

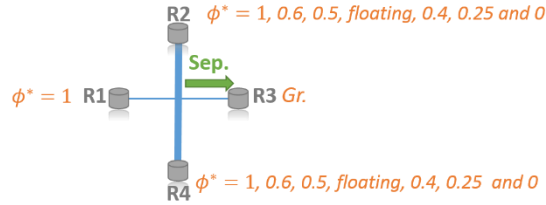


Figure 89: Separation Configurations

5.4.4.1 ϕ_{sep}^* : Floating

Injection is stopped at $t = 21.9s$ for $\phi_{inj}^* = 0.5$ (Figure 79) and the floating separation is applied. The results of the concentration contours, shown in Figure 90, show that after $t = 6.1s$ the constituents are resolved. Figure 91 also shows the separation graphs at four different detection spots along the separation channel for the first 4s after separation process starts. After a longer time, the two constituents resolve better for sure, but their peak concentration will also drop. This brings up the sensitivity issue for the detection threshold.

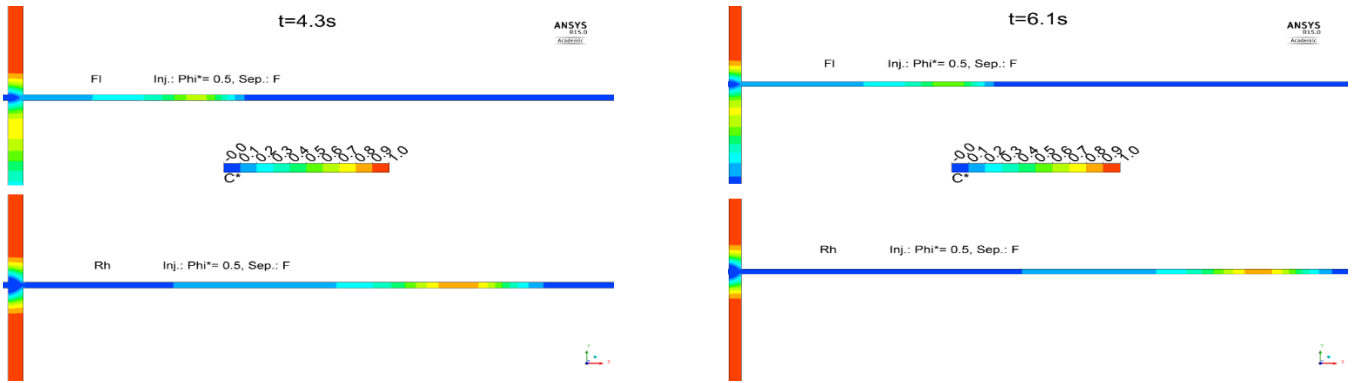


Figure 90: Concentration contours of separation for $\phi_{inj}^* = 0.5$ and $\phi_{sep}^* = Floating$

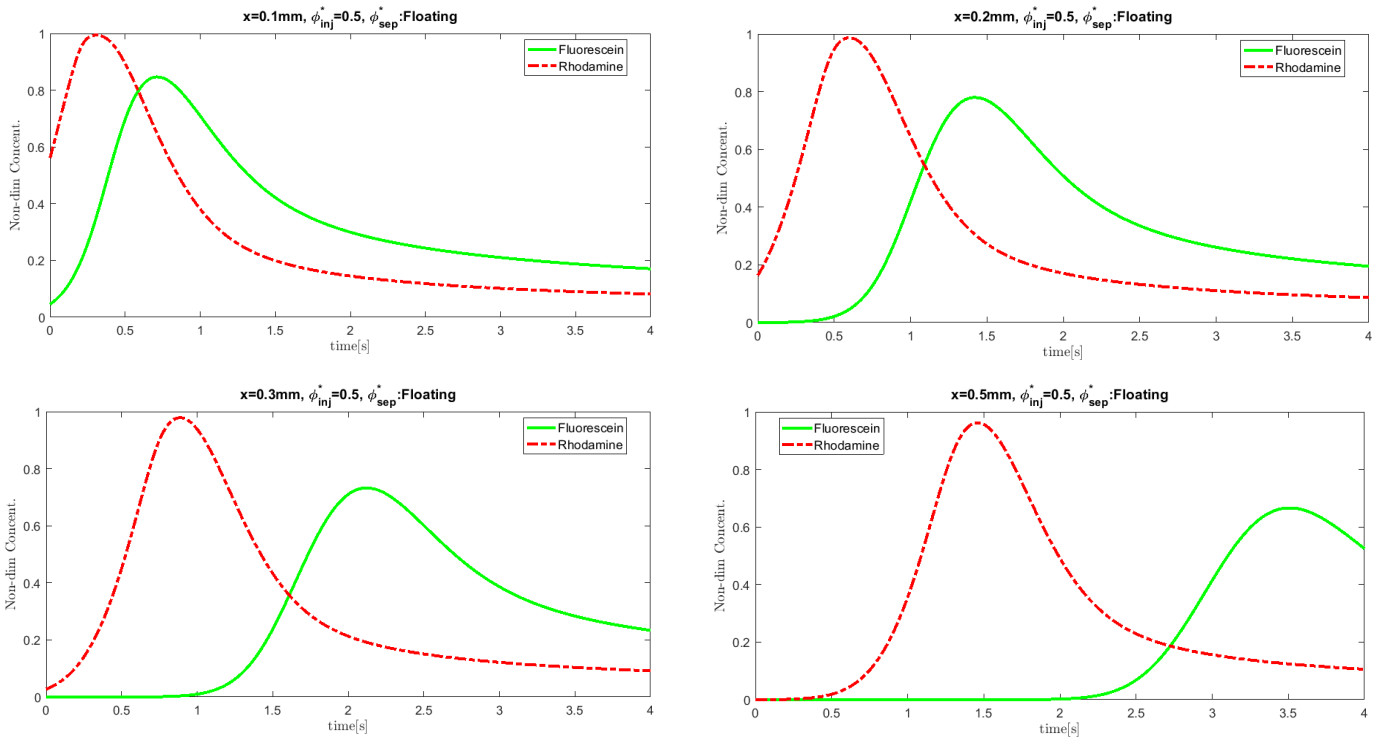


Figure 91: Separation graphs at different detection spots $x = 0.1, 0.2, 0.3$ and 0.5 mm for $\phi_{inj}^* = 0.5$ and $\phi_{sep}^* = F$

5.4.4.2 $\phi_{sep}^* = 0.25$ vs. ϕ_{sep}^* : *Floating*

To see the effect of separation electric potential configuration on the resolution, we start with two configurations: *Floating* and $\phi_{sep}^* = 0.25$. As presented in Table 9, we study the injection configuration $\phi_{inj}^* = 0.5$, which σ is zero, and has smaller width comparing to $\phi_{inj}^* = 0.4$. Figure 92 shows the comparison of concentration contours shortly after starting the separation process. It is observed that the maximum concentration for the slower constituent, FI, drops at $\phi_{sep}^* = 0.25$, which causes detectability problems after a few seconds. Figure 93 shows that at about 3s the peak concentration of Fluorescein drops to almost 50% of its original concentration when detector is located at $0.3mm$ distance from the center of the cross. This figure shows the comparison of these two separation configurations at different detection spots in 4s. The grey graphs represent the floating separation configuration.

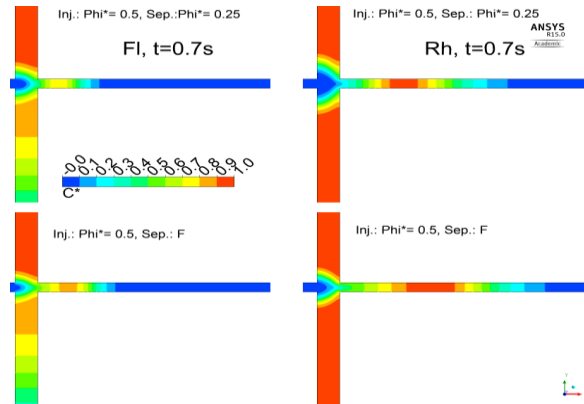


Figure 92: Concentration contours, injection $\phi_{inj}^* = 0.5$ and separation $\phi_{sep}^* = Floating$ vs $\phi_{sep}^* = 0.25$, $t = 0.7s$

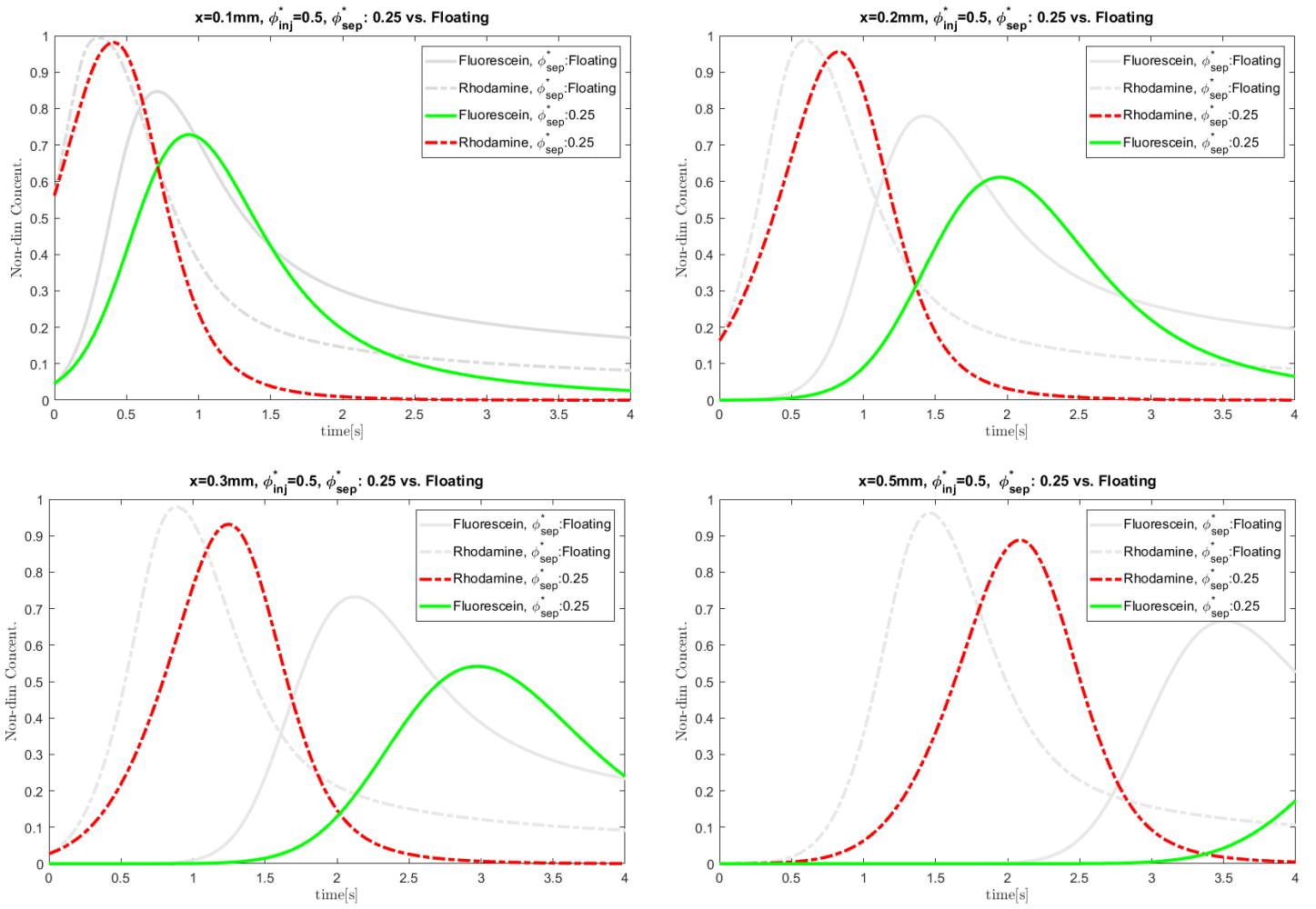


Figure 93: Separation graphs at different detection spots $x = 0.1, 0.2, 0.3$ and 0.5 mm for $\phi_{inj}^* = 0.5$ and $\phi_{sep}^* = 0.25$ vs. Floating

Figure 94 shows the conventional and modified resolutions for two separation configurations $\phi_{sep}^* = 0.25$ and floating. It is observed that $\phi_{sep}^* = 0.25$ results in higher resolutions in both definitions.

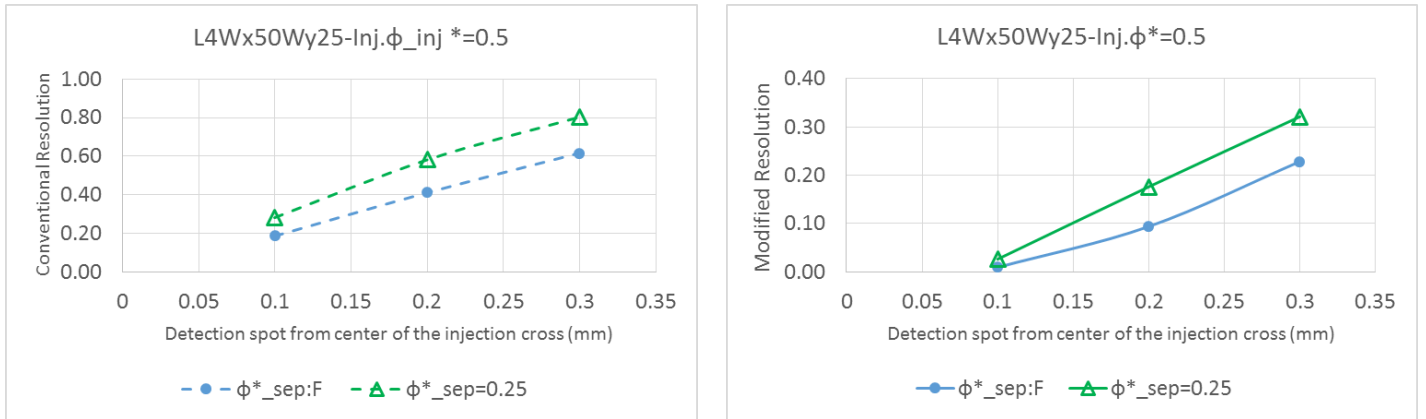


Figure 94: Separation resolution (Left: conventional, Right: modified) for Rhodamine and Fluorescein at different detection spots; $\phi_{inj}^* = 0.5$; $\phi_{sep}^* = 0.25$ vs. Floating

With the preliminary results of the separation configurations for two cases of floating and $\phi_{sep}^* = 0.25$, we study the modification of the injection procedure in the following section.

5.4.5 Modified Injection Procedure

The analysis of the injection results shows that for a steady-state plug at the cross, we can take an additional step by shifting the plug slightly down the injection channel to achieve a better shape, closer to rectangular. In the following section, we show how a two-step injection configuration results in much improved shapes.

5.4.5.1 Two-step Injection for Steady-State Configuration

As discussed, another approach to provide a better plug shape sample at the cross is applying a two-step injection configuration. Looking at the results presented in Figure 74, Figure 86, and Table 9, we choose $\phi_{inj}^* = 1$ configuration, which provides a narrower steady-state plug. Applying a second step injection with $\phi_{inj}^* = 0.5$, and for 0.5s, results in a much better shape, shown in the next section (Figure 95).

5.4.5.2 $\Phi_{inj_1}^* = 1, \Phi_{inj_2}^* = 0.5$

Looking at the two left columns of Figure 74, shows that is we stop configuration $\phi_{inj}^* = 1$ at a time when sample is close to the cross, but not there yet (here at $t = 31.5s$), and apply a new

configuration of $\phi_{inj}^* = 0.5$, then we see that in 0.5s we get an ideal plug which is mostly rectangular and nearly limited to the cross width for the high concentration part of the sample. (Figure 95)

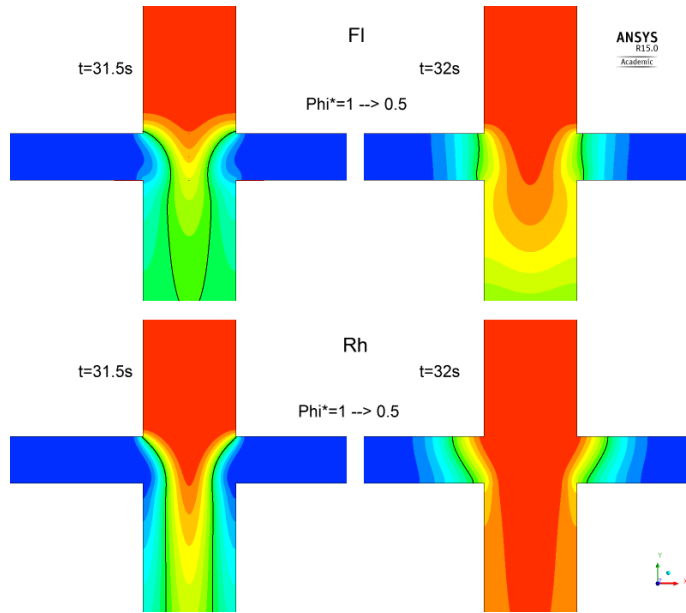


Figure 95: Concentration contours for two-step injection with configurations of $\phi_{inj_1}^* = 1$ and $\phi_{inj_2}^* = 0.5$

Figure 96 shows the shape factor analysis for 50% contour lines of Rhodamine and Fluorescein at $t = 32s$. The quadratic fits show a very small σ for both constituents.

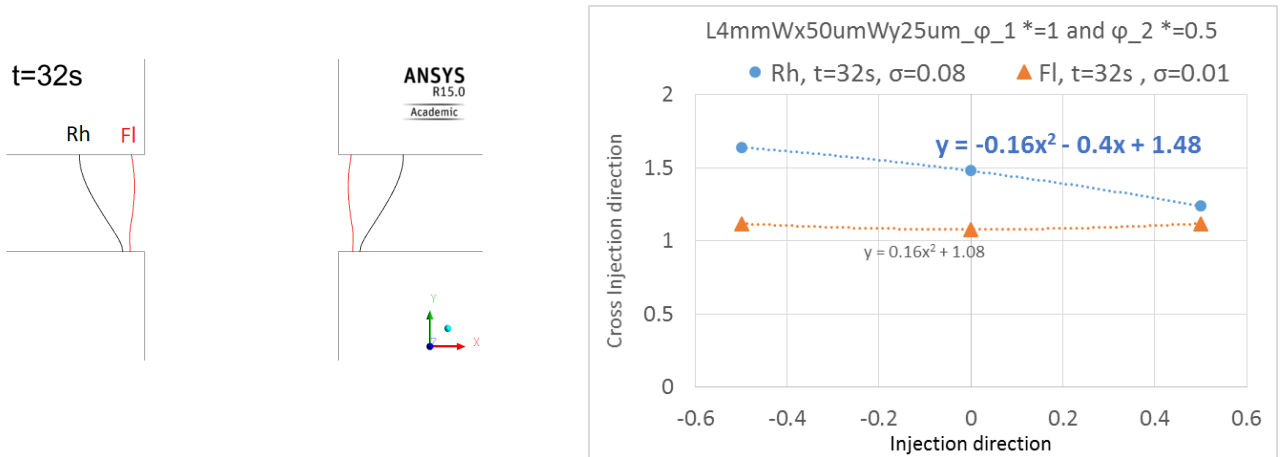


Figure 96: σ at $t=32s$ for two-step injection with configuration $\phi_{inj_1}^* = 1$ and $\phi_{inj_2}^* = 0.5$

A comparison of shape factor and sample plug actual mean width is reported in Table 10 for such a two-step injection with the best results of the previous one-step injection.

Table 10: A comparison of shape factor for best results of one step and two step injection

| Φ_{inj}^* | | 0.6 | 0.5 | $(\Phi_{inj_1}^* = 1, \Phi_{inj_2}^* = 0.5)$ |
|----------------------------------|----|-------|-----|--|
| Shape factor σ | Rh | 0.01 | 0 | 0.08 |
| | Fl | 0.11 | 0 | 0.01 |
| Actual mean width (μm) | Rh | 109.6 | 220 | 73.3 |
| | Fl | 55.7 | 148 | 54.7 |

5.4.6 Separation of the modified injection ($\Phi_{inj_1}^* = 1, \Phi_{inj_2}^* = 0.5$)

Different separation configurations are investigated for the two-step injection to see the effect of applied potentials on the separation resolution.

Figure 97 shows schematically how the flow and electric fields increase with increasing the applied electric potentials at the top and bottom reservoirs at separation. In 5.4.6.3, we provide the numerical results of the electric and flow fields for different configurations of applied electric potentials at separation.

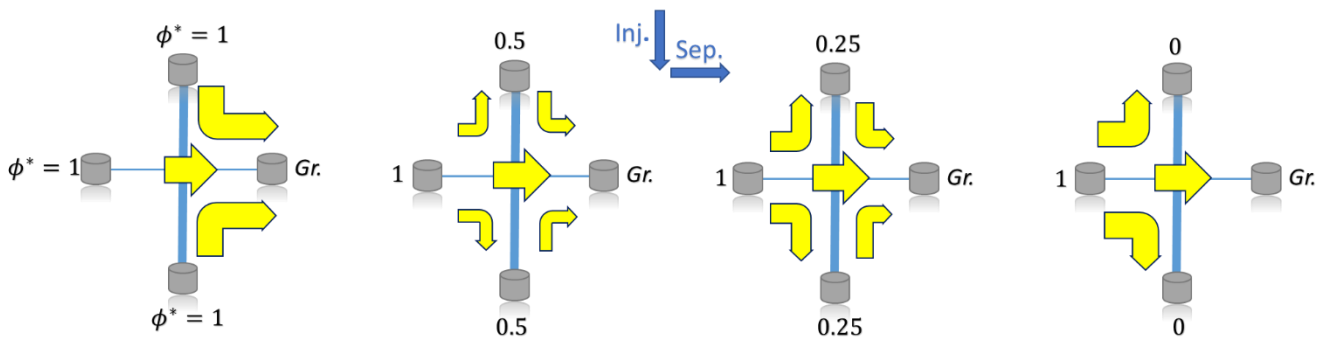


Figure 97: Separation configurations; yellow arrows show flow/electric field intensity

5.4.6.1 ϕ_{sep}^* : Floating

Figure 98 shows the separation graphs for the two-step injection by changing the electric potential configurations from 1 to 0.5 when sample reaches a steady-state at the cross. The grey lines also show the separation results for direct (one-step) injection configuration. As observed in Table 10, the sample plug width, and consequently the peak widths are narrower in the two-step injection.

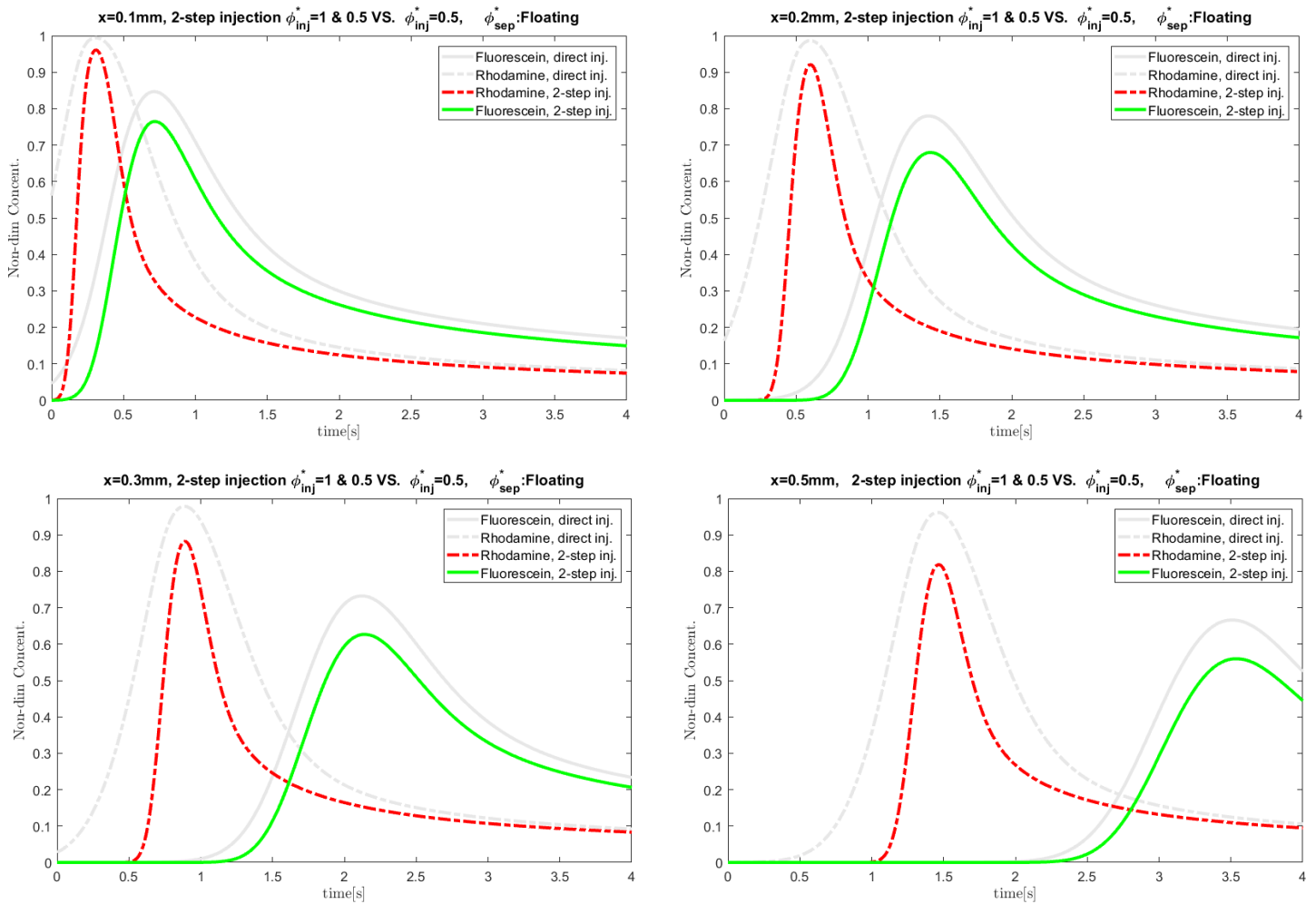


Figure 98: Separation graphs at different detection spots $x = 0.1, 0.2, 0.3$ and 0.5 mm for two-step injection ($\phi_{inj_1}^* = 1$ and $\phi_{inj_2}^* = 0.5$) and $\phi_{sep}^* = \text{Floating}$ (grey lines represent one-step injection)

Figure 99 shows the comparison of separation resolution between the two-step and direct injection methods, when floating separation configuration is applied. The results represent an increased separation efficiency in both conventional and modified definitions.

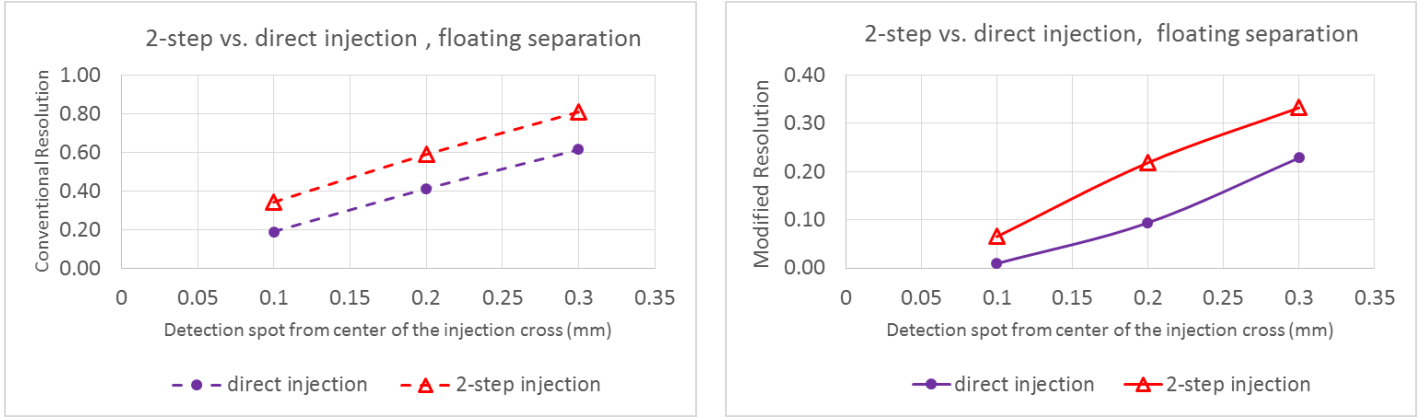


Figure 99: Separation resolution (Left: conventional, Right: modified) for Rh and Fl at different detection locations; two-step ($\phi_{inj_1}^* = 1$ and $\phi_{inj_2}^* = 0.5$) vs. direct injection ; ϕ_{sep}^* : Floating

5.4.6.2 $\phi_{sep}^* = 0.25$

Figure 100 and Figure 101 show a comparison of two separation configurations for applied potentials at two different times when sample is migrating along the separation channel. The concentration contours for two constituents of Fluorescein and Rhodamine are presented for both $\phi_{sep}^* = 0.25$ and ϕ_{sep}^* : floating at $t = 2$ and 4s. The results show that $\phi_{sep}^* = 0.25$ provides narrower plugs, with slightly lower peaks. The overall resolution in both conventional and revised definitions are improved in applying $\phi_{sep}^* = 0.25$ for separation applied potentials.

The problem is that however the results are captured at the same time in both separation configurations, but they are not at the same stage of evolution. Due to different electric fields resulting from the floating configuration or the one with the applied side potentials, $\phi_{sep}^* = 0.25$, the convection and diffusion will be different. The peaks of the constituents are not at the same location at the same time.

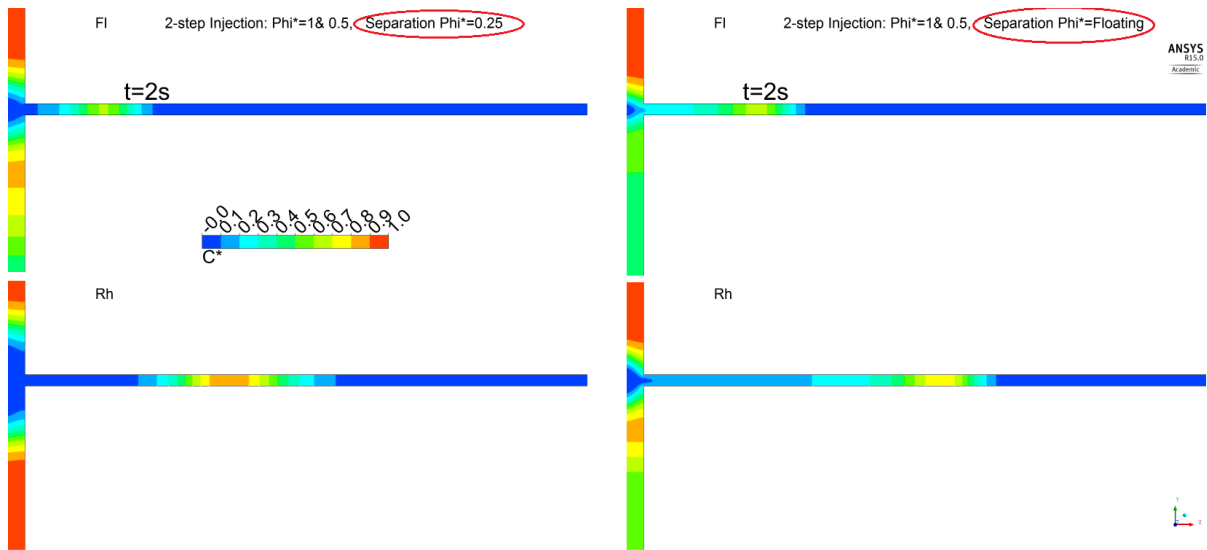


Figure 100: Comparison of separation contours at $t = 2s$ ($\phi_{sep}^* = 0.25$ vs. ϕ_{sep}^* : floating)

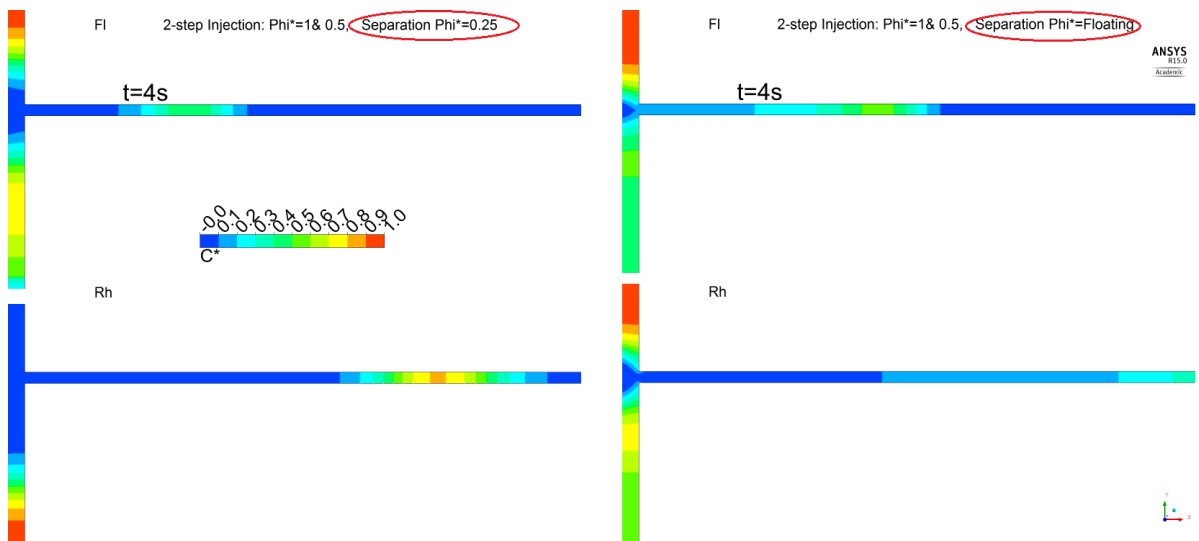


Figure 101: Comparison of separation contours at $t = 4s$ ($\phi_{sep}^* = 0.25$ vs. ϕ_{sep}^* : floating)

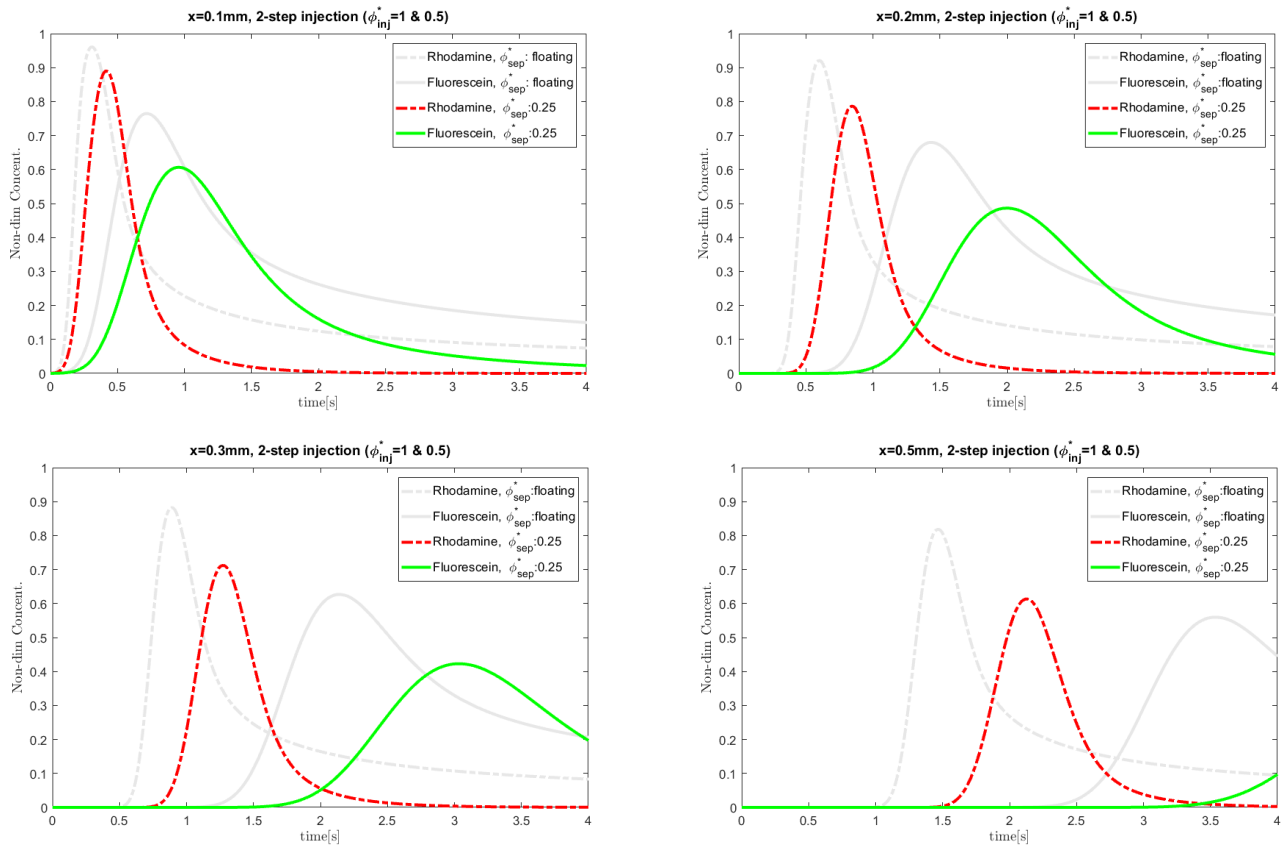


Figure 102: Separation graphs at different detection spots $x = 0.1, 0.2, 0.3$ and 0.5 mm for two-step injection ($\phi_{inj_1}^* = 1$ and $\phi_{inj_2}^* = 0.5$) and comparison of $\phi_{sep}^* = \text{Floating}$ (grey lines) vs. $\phi_{sep}^* = 0.25$ (red and green)

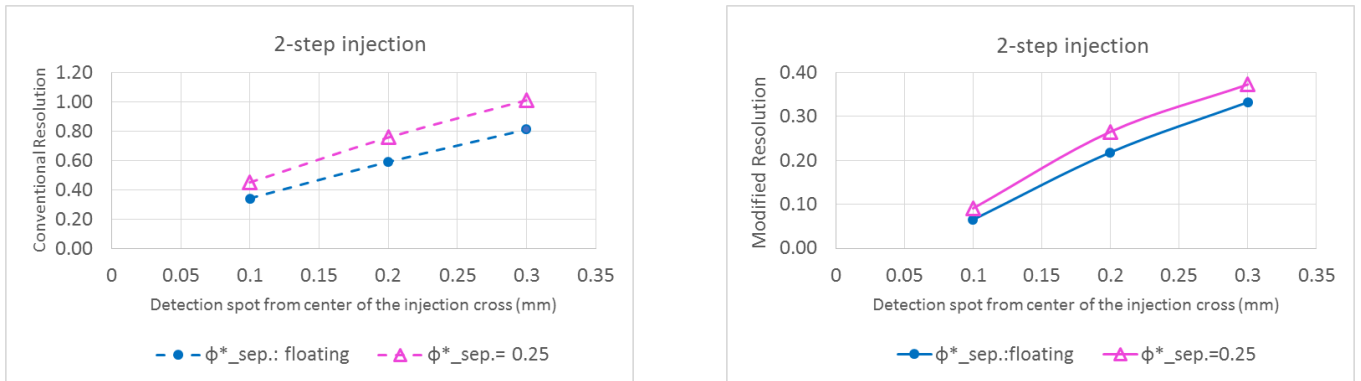


Figure 103: Separation resolution (Left: conventional, Right: modified) for Rhodamine and Fluorescein at different detection spots; two-step injection ($\phi_{inj_1}^* = 1$ and $\phi_{inj_2}^* = 0.5$); ϕ_{sep}^* : Floating vs. 0.25

5.4.6.3 All separation configurations ($\phi_{sep}^* = 0, 0.25, 0.4$, floating and 0.6)

Initially, right after switching from injection to separation, irrespective of the applied separation configurations for electric potentials the peaks are overlapping. Figure 104 shows the sample peaks from the ideal 2-step injection at initial time of separation.

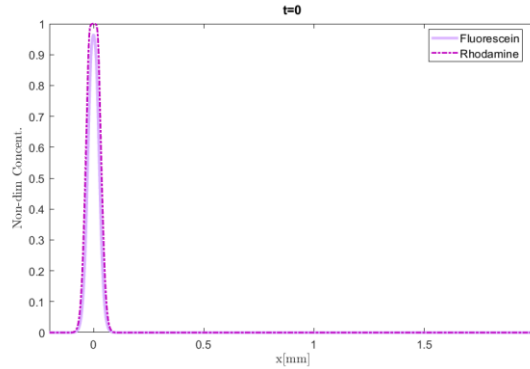


Figure 104: Initial non-dimensional concentration, $t = 0s$, for all separation configurations ($\phi_{sep}^* = 0, 0.25, 0.4$, floating and 0.6)

Figure 105 and Figure 106 show the effect of separation configuration for applied potentials on the separation of constituents, conventional and modified resolution. It is observed that increasing ϕ_{sep}^* results in a slight drop of the peaks. The electric field streamlines in Figure 105 for different separation configurations show how the sample at the cross moves towards the up/down reservoirs when lower side potentials i.e., $\phi_{sep}^* = 0.25$, are applied. Indeed increasing the side potentials causes the separation of the high-concentrated part of the sample plug from its upper and lower sides, therefore, a part of the sample plug at the cross is pulled back to the reservoirs of the injection channel (side reservoirs at separation) at the onset of separation. This means that the concentration of the sides of the plug is diminished, which results in more lateral diffusion. Moreover, from the electric field streamlines and it is observed that higher voltages at the side reservoirs of the separation channel, with less pull-back effect towards those reservoirs, result in higher electric fields in the separation channel. Considering the negative electrophoretic mobilities, we show further in Figure 113 that the red and green graphs, representing $\phi_{sep}^* = 0.4$ move with a slower pace than $\phi_{sep}^* = 0.25$ and faster than floating separation configuration. Figure 106 shows the velocity field at the cross for different separation configurations.

It is observed that at higher ϕ_{sep}^* , more sample is squeezed into the separation channel and a severe change in the flow direction at the corner of the cross occurs.

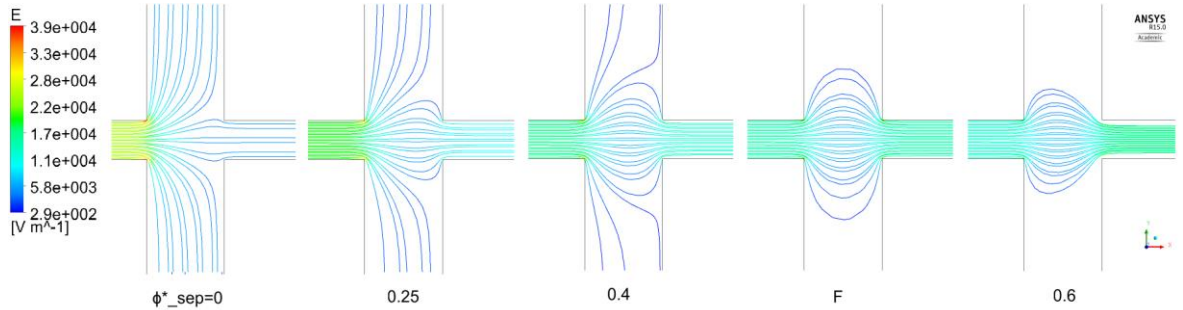


Figure 105: Electric field streamlines for different separation configurations

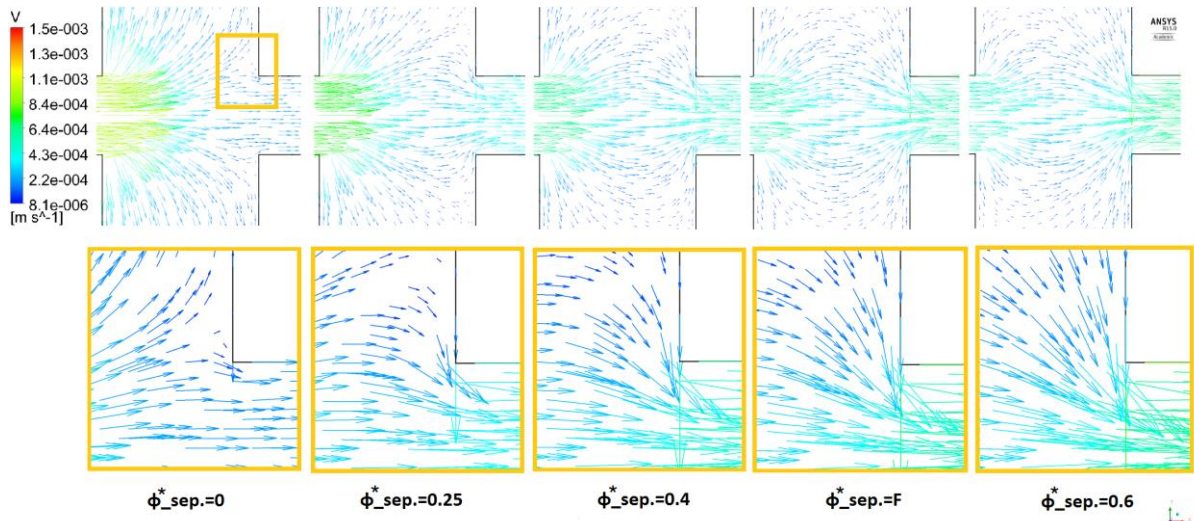


Figure 106: Flow field for different separation configurations

Figure 107 shows the spatial separation of the same plug, shown in Figure 104, at $t = 2$ and $4s$. From these graphs it is not clear why the peaks for $\phi_{sep}^* = 0.25$ are lower or why $\phi_{sep}^* = 0.6$ has longer tails. At this stage, we are not sure if the lower peaks happens due to the stronger pull-back effect. Although part of the sample is separated from the plug, the concentration at the center of the plug could be unaffected, however, when the upper and lower side of the plug is separated from the main plug at the cross, the side concentration is diminished, which results in more lateral diffusion. For more clarification, Figure 108 provides results of the concentration contours at the evolution stages of each

separation configuration. For a better observation, Figure 109 shows the 50% c^* lines for the different separation configurations at two time frames of $t = 0.1$ and $0.5s$ at separation. It is observed that the effect of separation configurations on sample plug separation is minimal at initial times, but as time evolves, it changes. However, none of these figures justifies having longer tails and higher peaks at $\phi_{sep}^* = 0.6$. Therefore, we further investigate the concentration contours at $t = 2$ and $4s$ in Figure 110 to Figure 112.

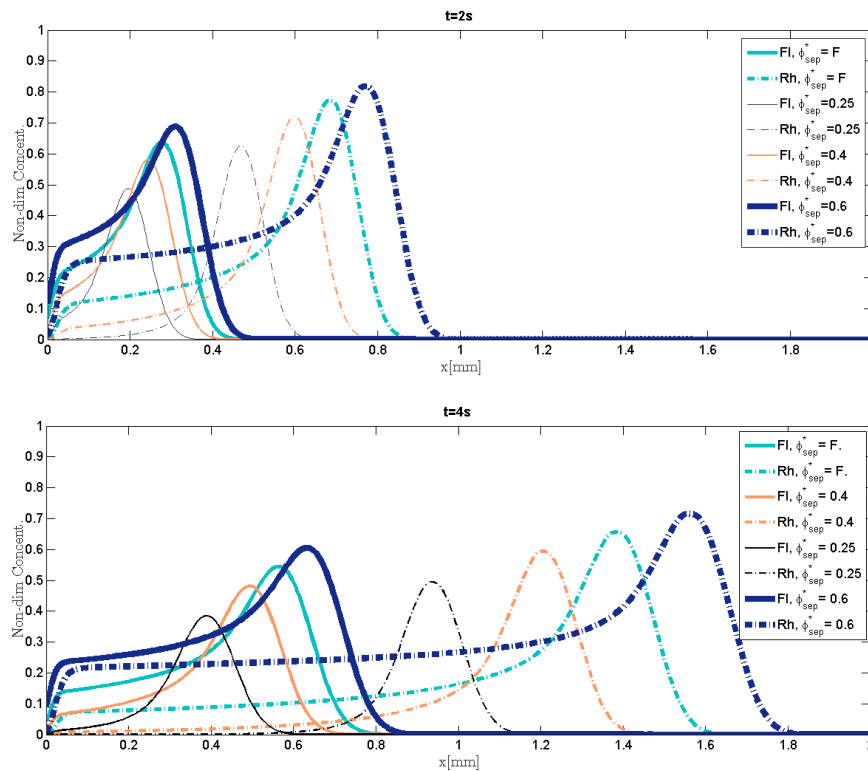


Figure 107: Spatial separation peaks at $t = 2$ and $4s$ ($\phi_{sep}^* = 0.25, 0.4, \text{floating and } 0.6$)

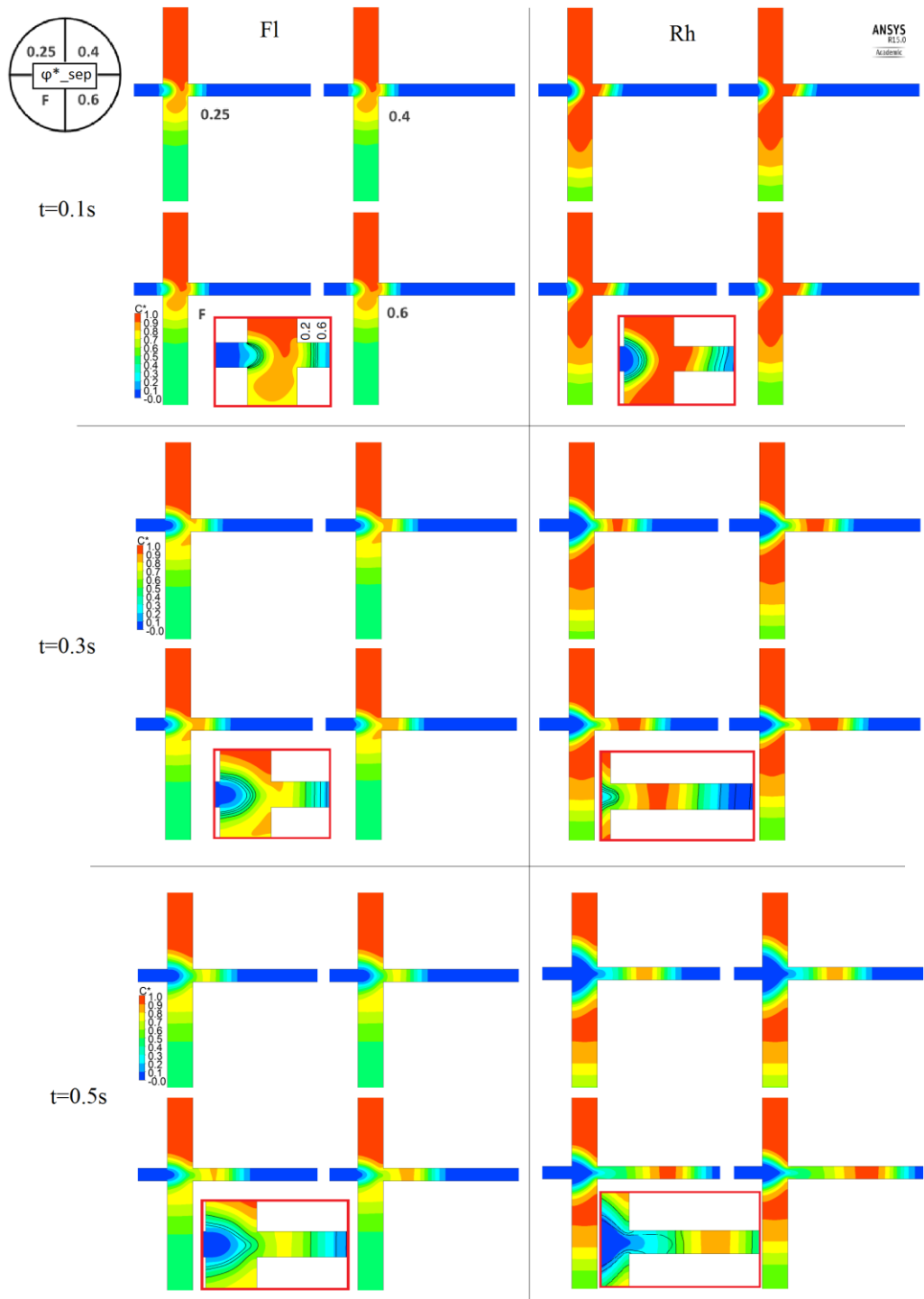


Figure 108: C^* contours at $t = 0.1, 0.3$ and $0.5s$ for $\phi_{sep}^* = 0.25, 0.4, \text{floating}$ and 0.6

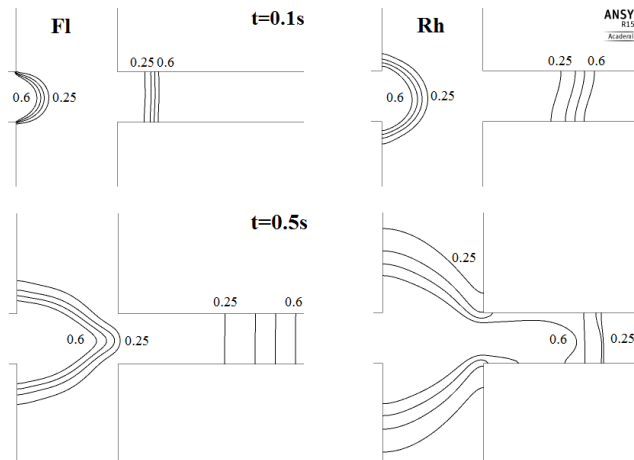


Figure 109: Zoom of 50% C^* contour lines at $t = 0.1$ and $0.5s$ for $\phi_{sep}^* = 0.25, 0.4, \text{floating}$ and 0.6

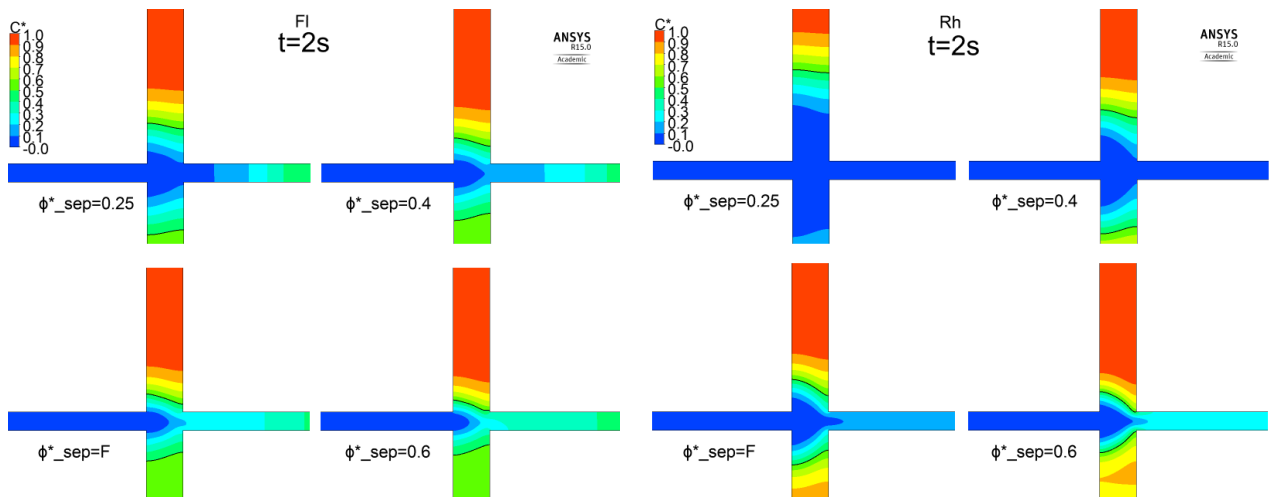


Figure 110: C^* contours at the cross at $t = 2s$; $\phi_{sep}^* = 0.25, 0.4, \text{floating}$ and 0.6
Left: Fl; Right: Rh

Figure 111 and Figure 112 show closer inspections of the concentration contours for each separation configuration at two time frames, $t = 2$ and $4s$, zoomed at the cross and along the separation channel.

t=2s

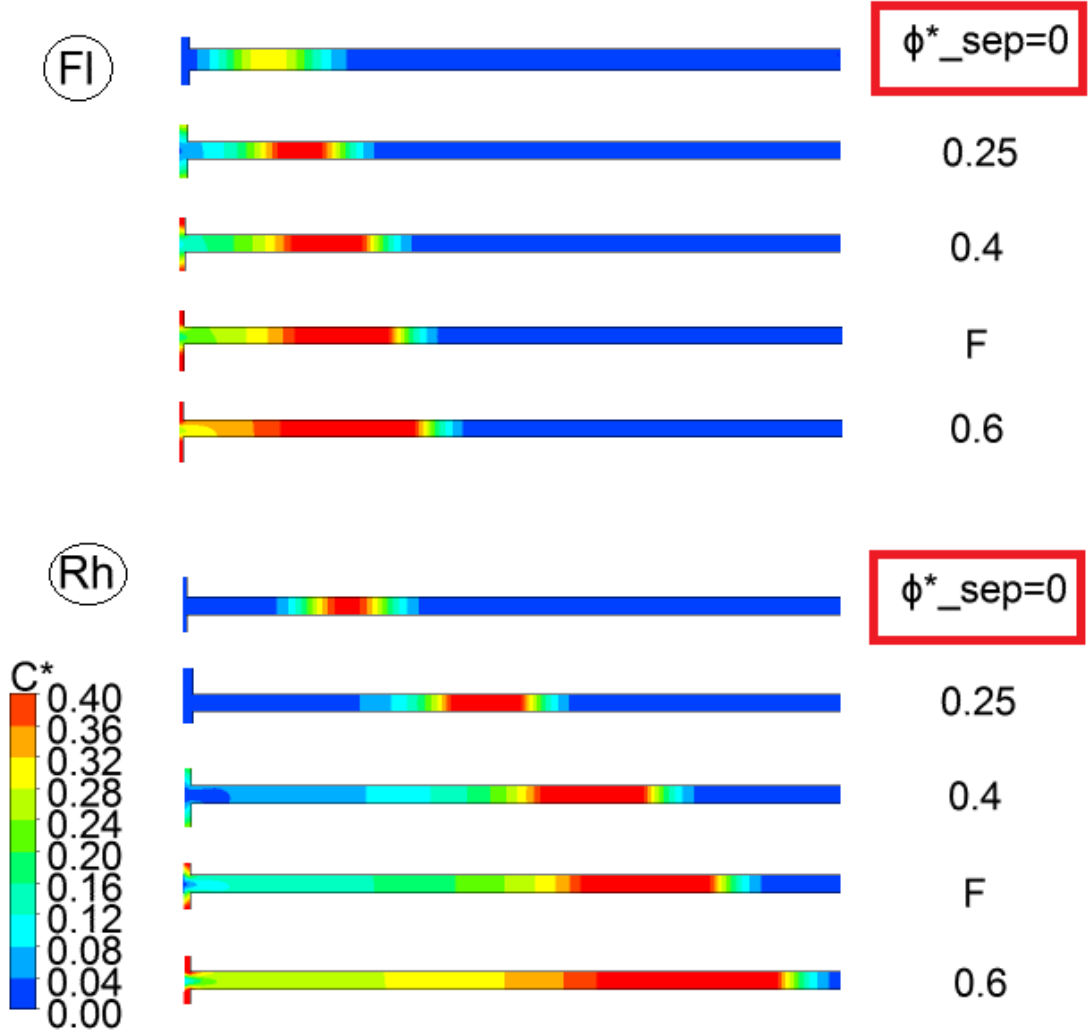


Figure 111: C^* contours at $t = 2s$ for $\phi^*_{sep} = 0, 0.25, 0.4, \text{floating}$ and 0.6

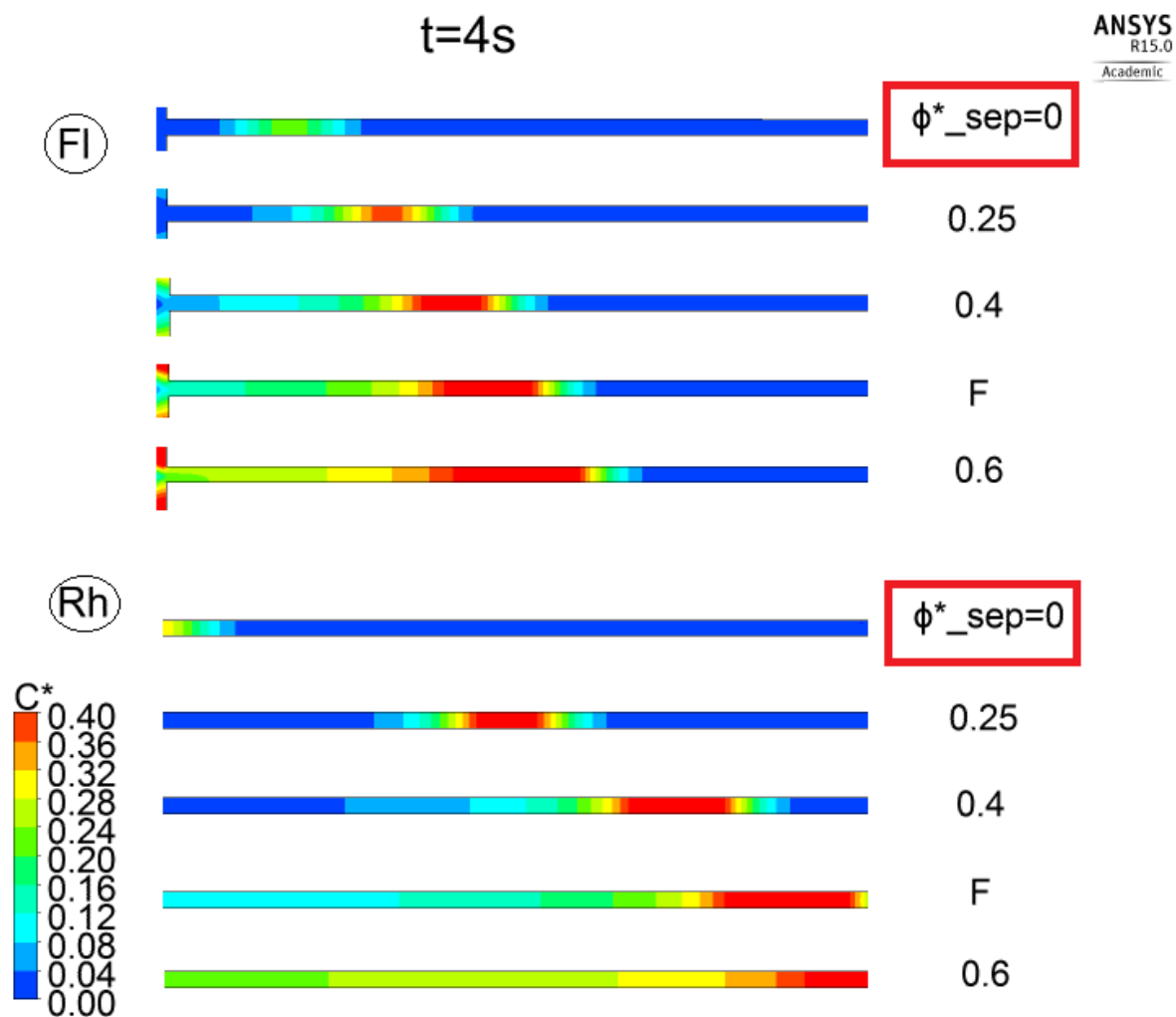


Figure 112: C^* contours at $t = 4s$ for $\phi^*_{sep} = 0, 0.25, 0.4$, floating and 0.6

Figure 113 shows the temporal separation graphs at different separation configurations $\phi^*_{sep} = 0, 0.25, 0.4$, floating and 0.6 . It is observed that, increasing the controlling potentials at separation, i.e. ϕ^*_{sep} , results in stronger electric field in the separation channel after the cross, shown in Figure 105, which supports the opposite migration of charged particles with negative electrophoretic mobilities. This is in accordance with the results presented in Figure 113, which represents shorter time for sample constituents at $\phi^*_{sep} = 0.25$ to pass by the detector.

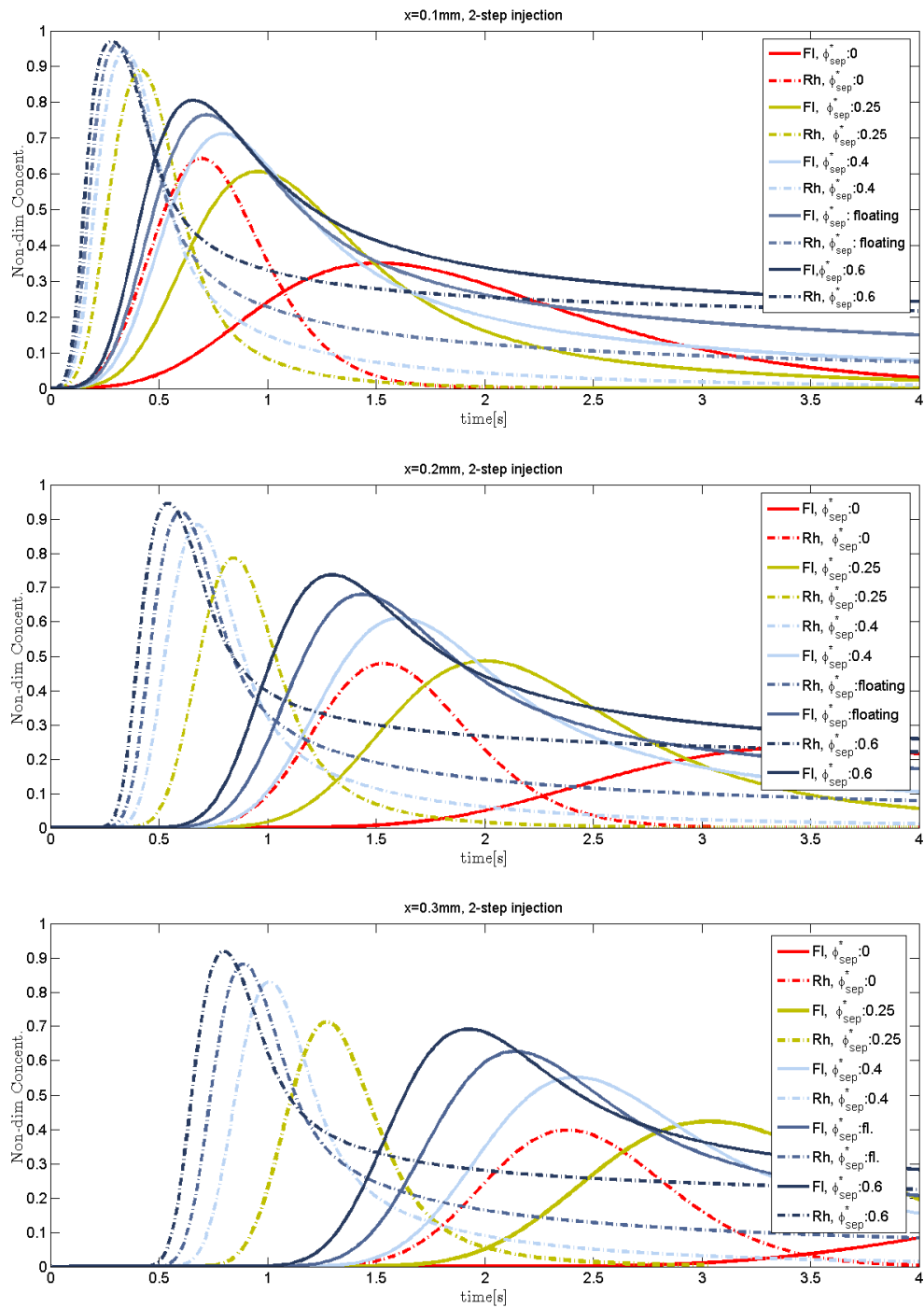


Figure 113: Separation graphs at different detection spots $x = 0.1, 0.2, 0.3mm$ for two-step injection ($\phi_{inj_1}^* = 1$ and $\phi_{inj_2}^* = 0.5$) and comparison of $\phi_{sep}^* = 0, 0.25, 0.4, Floating$ and 0.6

Figure 114 (left) shows $\phi_{sep}^* = 0.25$ has higher conventional resolution, which represents higher distance between the peaks along the separation channel. However the modified resolution in this figure (right), shows that $\phi_{sep}^* = 0.4$ and 0.25 provide the same modified resolutions. This means there is a trade-off between the height of the peaks and the horizontal distance between two constituents. In $\phi_{sep}^* = 0.4$, the peak concentrations are lower while the distance between the peaks is more.

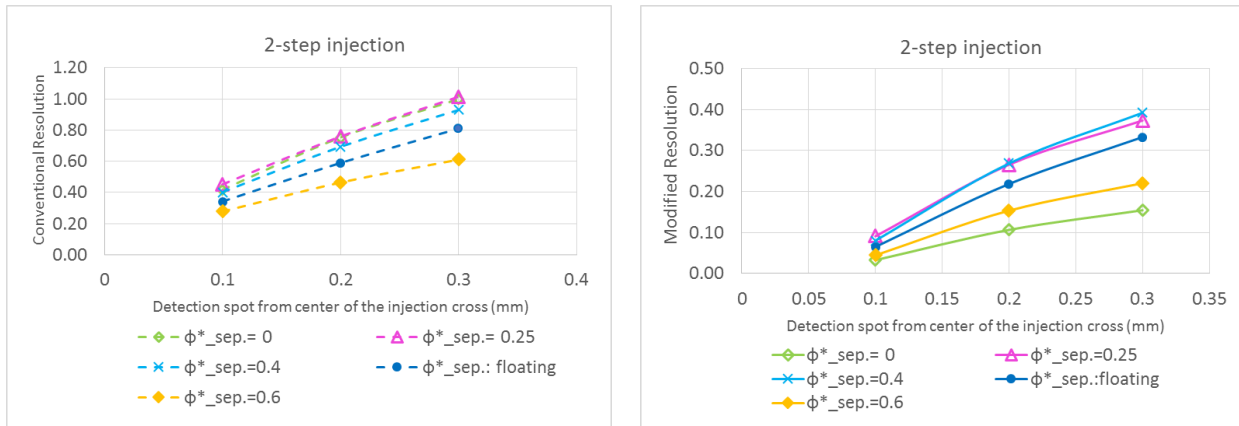


Figure 114: Effect of separation configuration on separation resolution for two-step injection (Left: conventional, Right: modified); $\phi_{sep}^* = 0, 0.25, 0.4, \text{Floating}$ and 0.6

Moreover, Figure 115 is presented to delve into more details of the conventional resolution. It is observed that both the distance between the peaks (numerator) and the summation of half-maximum (HM) widths (denominator) increase as the detection location increases, but the rate of change in HM widths is slower, therefore, the rate of change of resolution increases. This is in accordance with the competition of convection and diffusion. In the former $\Delta x = V \cdot t$, whereas in the latter $\Delta x = D\sqrt{t}$ the square root of time has a key role, therefore separation distance happens faster.

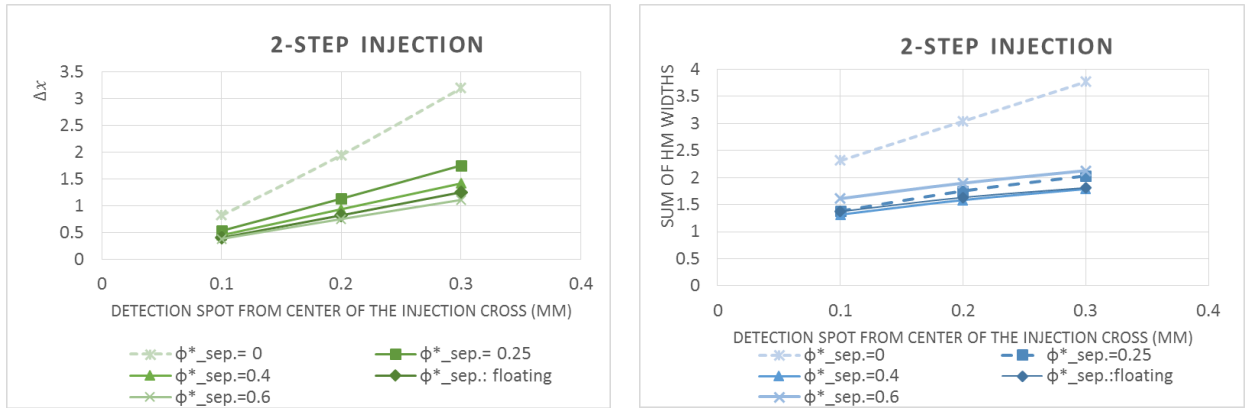


Figure 115: Comparing peak distances (Left) and sum of half-width maximums (Right) at different separation configurations $\phi^*_{sep} = 0, 0.25, 0.4, 0.6$ and floating

The above results, all confirm that a $\phi^*_{sep} = 0.25$ separation configuration for the applied potentials at separation provide the best resolution in both definitions, conventional or modified.

5.5 Conclusions

The seventh chapter of this thesis starts with the grid independency of the solution. I show the injection of a single-constituent sample is independent of the number of grids and the time step, when the grids at the $50 \times 50 \mu\text{m}^2$ -cross are as fine as 40×40 cells and the time step is 1ms . The results show that the steady solution of the electric and flow fields are independent of the grid at the cross. Moreover, the solution of the concentration field presents both the spatial and temporal independency. The location of the front edge on the centerline of the injection channel is examined for the coarse and fine grids for the 50% concentration line, where all the shape factor analysis is performed.

To validate the injection model for a single-constituent sample, the numerical results are compared to the experimental results presented in literature and showed overlapped concentration non-dimensional graphs at the cross.

After the discussion of grid independency and validation of numerical results, I started a thorough analysis for both injection and separation to achieve an ideal rectangular plug shape at the cross, improve the shape factor σ , and increase the separation efficiency and resolution. To do so, I modified the geometry of the channels, which primarily was selected based on the experimental results for the validation purposes. The first modification was reducing the width of separation channel which resulted

in an improvement in shape factor. Then, to better control the injection and separation applied potential configurations, the design was improved to channels of equal length. Finally, both of these modifications combined and the final design included cross-linked channels of equal length with the 0.5 aspect ratio of the channel widths, i.e., a narrower separation channel.

After modifying the geometry of the channels, and analyzing the preliminary injection results, I studied six configurations for the applied potentials at injection as $\phi_{inj}^* = 1, 0.75, 0.6, 0.5, 0.4, 0.25$. The results showed that for higher ϕ_{inj}^* , the high concentration part of the sample does not penetrate the cross. Therefore, we improved the injection procedure to a two-step injection, where at the first step $\phi_{inj}^* = 1$ and at second step $\phi_{inj}^* = 0.5$. This two-step injection procedure resulted in achieving a rectangular plug at the cross, which was not possible at different designs and according to the literature was difficult to achieve. For such a minimum shape factor at a two-step injection, I carried out a comparison among different configurations of applied potential at separation. The first goal was to show that a good plug, assessed with the proposed shape factor model, results in a good resolution. This holds true for the conventional definition of resolution but not for the modified one. Results show that a good plug provides high conventional resolution when no (or low) potential is applied at the side reservoirs of the separation channel at separation stage. However, the modified resolution address the low peak issue when no potential is applied at those side reservoirs. To tackle this issue, which indeed is the sensitivity issue, the applied potentials at the side reservoirs of the separation channels slightly increased to $\phi_{sep}^* = 0.25$, which provided the highest resolution in both conventional and modified definitions and is the best separation configuration.

Chapter 6

Conclusions and Recommendations

6.1 Contributions of This Thesis

Electrophoresis separation is a rapid and sensitive analytical technique with many applications in different areas such as Biology, clinical diagnostics, nutrition and water treatment, forensic investigations, and energy. With the trending miniaturization of point-of-care devices and Lab-On-Chip (LOC) systems, microchip electrophoresis has attracted attention as a promising analytical technique. Through such physical downsizing, analysis time and sample consumption decrease significantly; portable chips provide the advantages of personalized medical devices. Parallelization is another advantage, which makes high-throughput tests and automation of individual steps possible. To perform the electrophoretic separation of DNA and protein samples in microchannels, injection and separation were studied in detail, focused on a simple cross-linked microchannel consisting of an injection and a separation channel and the cross at the intersection of those channels. One of the contributions of this thesis is to present a novel method to assess the shape of the sample at injection, prior to separation.

A method was introduced for evaluating the shape and size of the sample at the intersection of a cross-linked microchannel. One of the issues that the experimental work in the literature revealed was the significant role that the sample plug shape and size play in separation performance. The more deviated the sample plug is from an ideal rectangular shape, the lower is the separation resolution.

Although it is generally very difficult to provide a rectangular injection plug, it is essential that the shape and size of the plug be quantified. The shape factor is introduced to assess the sample plug shape and size and the results show increased separation resolution when a rectangular plug, with minimal distortion, is achieved during injection. Five parameters are introduced to analyze the shape of the sample including the sample plug mean width, standard deviation, σ , from the mean width, first and second moments, and the RMS of the moments, S_y . Evaluating the plug shapes by these parameters, we concluded that either σ or the RMS of the first and second moments can be used to assess the shape of the sample plug individually. Using $1.7S_y$ provides the same results as assessed by σ . To find out

the acceptable range for this shape-factor, we presented various possible shapes at the cross and concluded that $\sigma \leq 0.2$ provides quite acceptable shapes that are close to the ideal rectangular shape.

To assess the separation, a modified resolution was introduced after investigating the conventional resolution. Both the conventional and modified definitions assume a Gaussian distribution for sample concentration for each species. For the adjacent peaks, a high value for the conventional resolution is indicative of identifiable and distinct peaks. However, such definition lacks consideration of the sensitivity of the detector and provides no indication of the ability to discriminate between peaks. To solve this issue, a modified resolution was introduced which is the ratio of peak-to-valley magnitude, for the lesser of the peaks, to the detector sensitivity. The modified resolution provides a better indicator of the sample separation, especially in the cases for which the sample-buffer diffusion causes considerable drop in concentration peaks. Multiplying the conventional resolution by this factor reflects the importance of the peak heights in detecting the sample constituents and provides an improved indicator of the separation resolution.

The microchip design was modified to achieve minimum σ . The channels were changed to having equal lengths and the separation channel was narrowed to 50% of the injection channel width. This design led to less deviation of the sample from the mean width in the narrower separation channel. Most importantly, the equal length of channels, reducing the length of the separation channel, provided an easier geometry for studying different configurations of the applied electric potentials. Injection and separation analysis were carried out on this modified geometry.

At injection, to achieve the ideal rectangular plug, we studied the effect of applied potentials on the sample plug at the cross. A ϕ_{inj}^* was introduced as the ratio of the applied potential of the side reservoirs (R_1, R_3) of the injection channel, to the difference of potentials at the reservoirs of the injection channel itself, (R_2, R_4); R_4 is set to ground. Studying a range of ϕ_{inj}^* , we achieved different sample plug shapes and analyzed the injection plugs with the proposed shape factor model.

From the injection configuration study, it was revealed that under certain configurations a steady-state plug is formed at the cross as a result of competing physics in the problem. First of all the shape and

size of the sample plug at the cross do not change over time. Secondly, a time-to-stop-injection is not important for those plugs which reach a steady-state shape. When this occurs, there is a balance between the buffer and sample flows at the cross, which prevents buffer leakage into the sample plug domain. The steady-state plug was achieved for the sample at the cross when $\phi_{inj}^* = 1$. However, due to the lack of penetration of either species into the cross or the separation channel, an opportunity presented itself. The injection procedure was modified into a two-step injection, $\phi_{inj}^* = 1$ and 0.5, with the second step starting from the steady-state configuration. In this way, both species are transported across the relatively short channel distance and less diffusion occurs during the second step of the injection. Employing this procedure not only resulted in having more of the high-concentration part of the sample at the cross, but it also led to achieving the ideal rectangular plug. Therefore, we did the separation analysis on the two-step injection plug.

Having achieved a high quality sample plug shape and size, a study was conducted to ascertain the effects of potentials at the side reservoirs of the separation channel (R_2, R_4). For the steady-state sample plug shape at the cross, and the two-step injection configuration, providing the best plug shape, different separation configurations were studied for a range of ϕ_{sep}^* . The ϕ_{sep}^* was introduced as the ratio of the applied potential of the side reservoirs (R_2, R_4) of the separation channel to the difference of potentials at the reservoirs of the separation channel itself, (R_1, R_3); R_3 is set to Ground. Results showed an improved separation resolution, for both conventional and modified definitions, for the two-step injection, and the separation configuration with lower potentials at (R_2, R_4) at separation. It was observed that separation of the species injected as the rectangular plug, results in a high conventional resolution, but a poor modified one when no potentials are applied at (R_2, R_4) during separation. However, when these potentials are slightly increased to $\phi_{sep}^* = 0.25$, both the conventional and modified resolutions increase and provide the most efficient separation for the best shape plug. The details of the electric and flow fields are presented which show lower flow of parasitic sample to the separation channel during separation. Applying such a configuration helps avoid wide plugs and that results in better resolution.

The derivation of the Poisson-Boltzmann equation is provided in Appendix A to find the distribution of electric potential and charge density distribution in the EDL. The approximations and simplifications

to solve this equation provided the justifications for neglecting the electric body force in the Navier-Stokes equation as well as neglecting solving the problem in the EDL. This validates reflecting the effect of the thin electric double layer, for a symmetric electrolyte, with the slip boundary condition in the flow field. Incorporating these conclusions, helped us make the appropriate choice of decoupling the electric, flow and concentration fields, which significantly saves computation time. A thorough study was performed on the problem formulation for both injection and separation, in non-dimensional forms.

Appendix B provides more insight by identifying the parameters in the problem in the form of dimensionless parameters and numbers like Reynolds and Peclet numbers. In the physically meaningful dimensionless problem, we justified the decisions over neglecting some terms like the inertial term in the momentum equation, because of the very low Reynolds number. Non-dimensionalization reduced the complexity of the problem and provided us with insight into the time and length scales, and the dominant transport phenomena of convection and diffusion.

6.2 Recommendations for Extension of Work

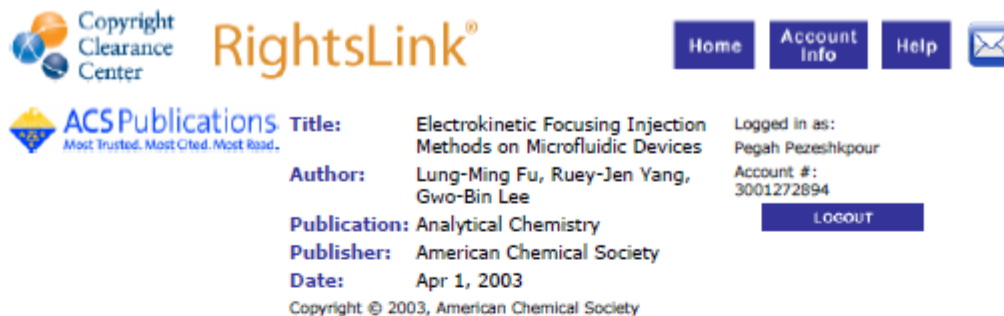
A few suggestions are made in this section for future work to enhance the research done in this thesis.

- More detailed study of the chip geometry: In modifying the geometry, we did reduce the width of the separation channel to half of the injection channel width. However, a more detailed study on the separation channel width in terms of a non-dimensional width could be undertaken.
- Location of the detector: In order to design a reliable separation microchip, the separation resolution and location of the detector play significant roles. In the present separation results, we measured the resolutions at three arbitrary points and concluded that the conventional resolution increases when the cross-to-detector distance increases. On the other hand, the more the sample migrates along the separation channel, more diffusion occurs and the peak concentrations drop which result in poor modified resolution. An optimized location of the detector in particular in conjunction with the separation channel width, requires extended research.

- Effect of 3D simulations: All the numerical simulation results presented in this thesis are two-dimensional. To investigate the phenomena happening in the third dimension along the depth of the microchannel, it is suggested to run fully three-dimensional simulations to see the effect of the third dimension on the electroosmotic velocities of the flow, on the shape of the sample at the cross, and on the separation.
- The effects of absolute value of potentials: Numerically, there is no limitation on the absolute values of the applied potentials, although those values affect the computation time and migration pace of the sample. However, on the experimental side, there are some practical concerns in high electric fields. High potentials could denature the biological sample, damage the chip or form gas bubbles due to electrolysis at the electrodes. At what potentials such damage becomes significant should be studied.
- Integrating microchip electrophoresis with other separation techniques: Depending on the sample constituents and their electrophoretic mobilities and initial concentration, two-dimensional separation methods could be implemented. Other techniques such as free flow electrophoresis (FFE), Iso-electric focusing (IEF) or Iso-tachopheresis (ITP) could be integrated with the current electrophoresis separation.

Letters of Copyright Permissions'

Below is the permissions obtained from the copyright holder of the images used in this dissertation.



The screenshot shows the Copyright Clearance Center RightsLink interface. At the top left is the Copyright Clearance Center logo. To its right is the RightsLink logo. Further right are navigation buttons for Home, Account Info, Help, and an email icon. Below the Copyright Clearance Center logo is the ACS Publications logo with the tagline "Most Trusted. Most Cited. Most Read." The main content area displays the following information:

| | | | |
|---------------------|---|------------------------|-------------------|
| Title: | Electrokinetic Focusing Injection Methods on Microfluidic Devices | Logged in as: | Pegah Pezeshkpour |
| Author: | Lung-Ming Fu, Ruey-Jen Yang, Gwo-Bin Lee | Account #: | 3001272894 |
| Publication: | Analytical Chemistry | LOGOUT | |
| Publisher: | American Chemical Society | | |
| Date: | Apr 1, 2003 | | |

Copyright © 2003, American Chemical Society

PERMISSION/LICENSE IS GRANTED FOR YOUR ORDER AT NO CHARGE

This type of permission/license, instead of the standard Terms & Conditions, is sent to you because no fee is being charged for your order. Please note the following:

- Permission is granted for your request in both print and electronic formats, and translations.
- If figures and/or tables were requested, they may be adapted or used in part.
- Please print this page for your records and send a copy of it to your publisher/graduate school.
- Appropriate credit for the requested material should be given as follows: "Reprinted (adapted) with permission from (COMPLETE REFERENCE CITATION). Copyright (YEAR) American Chemical Society." Insert appropriate information in place of the capitalized words.
- One-time permission is granted only for the use specified in your request. No additional uses are granted (such as derivative works or other editions). For any other uses, please submit a new request.

If credit is given to another source for the material you requested, permission must be obtained from that source.

[BACK](#)

[CLOSE WINDOW](#)

Copyright © 2018 Copyright Clearance Center, Inc. All Rights Reserved. [Privacy statement](#), [Terms and Conditions](#). Comments? We would like to hear from you. E-mail us at customercare@copyright.com

**JOHN WILEY AND SONS LICENSE
TERMS AND CONDITIONS**

Apr 11, 2018

This Agreement between Pegah Pezeshkpour ("You") and John Wiley and Sons ("John Wiley and Sons") consists of your license details and the terms and conditions provided by John Wiley and Sons and Copyright Clearance Center.

| | |
|---------------------------------------|---|
| License Number | 4325961399348 |
| License date | Apr 11, 2018 |
| Licensed Content Publisher | John Wiley and Sons |
| Licensed Content Publication | Electrophoresis |
| Licensed Content Title | A low-leakage sample plug injection scheme for crossform microfluidic capillary electrophoresis devices incorporating a restricted cross-channel intersection |
| Licensed Content Author | Chin-Lung Chang, Hui-Hsiung Hou, Lung-Ming Fu, et al |
| Licensed Content Date | Jul 24, 2008 |
| Licensed Content Volume | 29 |
| Licensed Content Issue | 15 |
| Licensed Content Pages | 10 |
| Type of use | Dissertation/Thesis |
| Requestor type | University/Academic |
| Format | Print and electronic |
| Portion | Figure/table |
| Number of figures/tables | 1 |
| Original Wiley figure/table number(s) | Figure 4 |
| Will you be translating? | No |
| Title of your thesis / dissertation | PhD Thesis |
| Expected completion date | May 2018 |
| Expected size (number of pages) | 1 |
| Requestor Location | Pegah Pezeshkpour MME Department 200 University Avenue West Waterloo, ON N2L 3G1 Canada Attn: |
| Publisher Tax ID | EU826007151 |
| Total | 0.00 CAD |
| Terms and Conditions | |

JOHN WILEY AND SONS LICENSE
TERMS AND CONDITIONS

Apr 11, 2018

This Agreement between Pegah Pezeshkpour ("You") and John Wiley and Sons ("John Wiley and Sons") consists of your license details and the terms and conditions provided by John Wiley and Sons and Copyright Clearance Center.

| | |
|---------------------------------------|--|
| License Number | 4325970129274 |
| License date | Apr 11, 2018 |
| Licensed Content Publisher | John Wiley and Sons |
| Licensed Content Publication | Electrophoresis |
| Licensed Content Title | Experimental determination of sample stream focusing with fluorescent dye |
| Licensed Content Author | Jay Taylor, G. D. Stubbley, Carolyn L. Ren |
| Licensed Content Date | Jul 23, 2008 |
| Licensed Content Volume | 29 |
| Licensed Content Issue | 14 |
| Licensed Content Pages | 7 |
| Type of use | Dissertation/Thesis |
| Requestor type | University/Academic |
| Format | Print and electronic |
| Portion | Figure/table |
| Number of figures/tables | 1 |
| Original Wiley figure/table number(s) | Figure 2 |
| Will you be translating? | No |
| Title of your thesis / dissertation | PhD Thesis |
| Expected completion date | May 2018 |
| Expected size (number of pages) | 1 |
| Requestor Location | Pegah Pezeshkpour MME Department 200 University Avenue West Waterloo, ON N2L 3G1 Canada Attn: |
| Publisher Tax ID | EU826007151 |
| Total | 0.00 CAD |
| Terms and Conditions | |



Note: Copyright.com supplies permissions but not the copyrighted content itself.

1
PAYMENT

2
REVIEW

3
CONFIRMATION

Step 3: Order Confirmation

Thank you for your order! A confirmation for your order will be sent to your account email address. If you have questions about your order, you can call us 24 hrs/day, M-F at +1.855.239.3415 Toll Free, or write to us at info@copyright.com. This is not an invoice.

Confirmation Number: 11710629
Order Date: 04/11/2018

If you paid by credit card, your order will be finalized and your card will be charged within 24 hours. If you choose to be invoiced, you can change or cancel your order until the invoice is generated.

Payment Information

Pegah Pezeshkpour
p2pezesh@uwaterloo.ca
+1 (519) 502-5034
Payment Method: n/a

Order Details

Journal of micromechanics and microengineering : structures, devices, and systems

| | |
|--|--|
| Order detail ID: 71119315 | Permission Status: Granted |
| Order License Id: 4325960604609 | Permission type: Republish or display content |
| ISSN: 0960-1317 | Type of use: Thesis/Dissertation |
| Publication Type: Journal | |
| Volume: | Requestor type: Academic institution |
| Issue: | |
| Start page: | Format: Print, Electronic |
| Publisher: INSTITUTE OF PHYSICS PUBLISHING | |
| Author/Editor: Institute of Physics (Great Britain) ; American Institute of Physics | Portion: image/photo |
| | Number of images/photos requested: 1 |
| | The requesting person/organization: Pegah Pezeshkpour |
| | Title or numeric reference of the portion(s): Figure 7a |
| | Title of the article or chapter the portion is from: Numerical simulation of microfluidic injection processes in crossing microchannels |
| | Editor of portion(s): N/A |
| | Author of portion(s): Ren Liqing, Sinton David, Li Dongqing |
| | Volume of serial or monograph: 13 |
| | Page range of portion: 739-747 |

References

- [1] F. F. Reuss, “Sur un nouvel effet de l’électricité galvanique,” *Mem. la Soc. Imp. Nat. Moscou*, vol. Vol. 2, p. 327, 1809.
- [2] S. Ghosal, “Fluid mechanics of electroosmotic flow and its effect on band broadening in capillary electrophoresis,” *Electrophoresis*, vol. 25, no. 2, pp. 214–228, 2004.
- [3] H. Helmholtz, “The Study of electrical boundary layers (translated title of Studien über elektrische Grenzschichten),” *Ann. Phys.*, 1879.
- [4] A. Tiselius, “CLXXXII. ELECTROPHORESIS OF SERUM GLOBULIN II. ELECTROPHORETIC ANALYSIS OF NORMAL AND IMMUNE SERA.”
- [5] F. R. Nakache and D. Burgreen, “Capillary Slits’,” no. 1, pp. 1084–1091, 1963.
- [6] C. L. Rice and R. Whitehead, “Electrokinetic Flow in a Narrow Cylindrical Capillary,” *J. Phys. Chem.*, vol. 69, no. 11, 1965.
- [7] R. O. Neukirchen, B. Schlosshauer, S. Baars, H. Jäckle, and U. Schwarz, “Two-dimensional protein analysis at high resolution on a microscale.,” *J. Biol. Chem.*, vol. 257, no. 24, pp. 15229–34, Dec. 1982.
- [8] a. V. Finkelstein, a. Y. Badretdinov, and a. M. Gutin, “Why do protein architectures have Boltzmann-like statistics?,” *Proteins Struct. Funct. Genet.*, vol. 23, no. 2, pp. 142–150, 1995.
- [9] N. a Patankar and H. H. Hu, “Numerical simulation of electroosmotic flow.,” *Anal. Chem.*, vol. 70, no. 9, pp. 1870–1881, 1998.
- [10] B. J. Kirby, *Micro- and Nanoscale Fluid Mechanics: Transport in Microfluidic Devices*. Cambridge University Press, 2010.
- [11] H. Bruus, *Theoretical microfluidics*. Oxford University Press, 2007.
- [12] L. Y. Yeo, H. C. Chang, P. P. Y. Chan, and J. R. Friend, “Microfluidic devices for

- bioapplications,” *Small*, vol. 7, no. 1, pp. 12–48, 2011.
- [13] E. K. Sackmann, A. L. Fulton, and D. J. Beebe, “The present and future role of microfluidics in biomedical research.,” *Nature*, vol. 507, no. 7491, pp. 181–9, 2014.
- [14] E. R. Castro and A. Manz, “Present state of microchip electrophoresis: State of the art and routine applications,” *Journal of Chromatography A*. 2015.
- [15] M. Trojanowicz and K. Kołacińska, “Recent advances in flow injection analysis,” *Analyst*, 2016.
- [16] S. M. Kim, M. A. Burns, and E. F. Hasselbrink, “Electrokinetic Protein Preconcentration Using a Simple Glass/Poly(dimethylsiloxane) Microfluidic Chip,” *Anal. Chem.*, vol. 78 (14), pp. 4779–4785, 2006.
- [17] J. Ha and J. Hahn, “Acupuncture sample injection for microchip capillary electrophoresis and electrokinetic chromatography,” *Anal. Chem.*, 2016.
- [18] L. Zaino, W. Wichert, and G. Crouch, “Microchannel Voltammetry in the Presence of Large External Voltages and Electric Fields,” *Anal. Chem.*, vol. 88, p. 4200.
- [19] J. S. Rossier, A. Schwarz, F. Reymond, R. Ferrigno, F. Bianchi, and H. H. Girault, “Microchannel networks for electrophoretic separations,” in *From Genome to Proteome: Advances in the Practice & Application of Proteomics*, 2007.
- [20] “2002_Fu_Numerical simulation of electrokinetic focusing in microfluidic chips_J. Micromech. Microeng.”
- [21] W. Thormann, J. Caslavská, and R. A. Mosher, “Computer simulation of electrophoretic aspects of enantiomer migration and separation in capillary electrochromatography with a neutral selector,” *Electrophoresis*, vol. 36, no. 5, pp. 773–783, 2015.
- [22] Y. Wang, Q. Lin, and T. Mukherjee, “A model for Joule heating-induced dispersion in microchip electrophoresis.,” *Lab Chip*, vol. 4, pp. 625–631, 2004.

- [23] L.-M. Fu, R.-J. Yang, and G.-B. Lee, "Electrokinetic focusing injection methods on microfluidic devices," *Anal. Chem.*, vol. 75, no. 8, pp. 1905–10, Apr. 2003.
- [24] M. Blas, N. Delaunay, and J. L. Rocca, "Electrokinetic-based injection modes for separative microsystems," *Electrophoresis*. 2008.
- [25] J. Taylor, G. D. Stubbley, and C. L. Ren, "Experimental determination of sample stream focusing with fluorescent dye," *Electrophoresis*, vol. 29, no. 14, pp. 2953–2959, 2008.
- [26] T. Yasui, N. Kaji, Y. Okamoto, M. Tokeshi, Y. Horiike, and Y. Baba, "Nanopillar array chip integrated with on-line stacking for fast DNA separation with high sensitivity and high resolution," *Microfluid. Nanofluidics*, vol. 14, no. 6, pp. 961–967, 2013.
- [27] J. T. Del Bonis-O'Donnell, D. K. Fyngenson, and S. Pennathur, "Fluorescent silver nanocluster DNA probes for multiplexed detection using microfluidic capillary electrophoresis," *Analyst*, 2015.
- [28] B. Mohammadi and J. G. Santiago, "SIMULATION AND DESIGN OF EXTRACTION AND SEPARATION FLUIDIC DEVICES Mathematics Subject Classification," *Math. Model. Numer. Anal. Mod' elisation Math' ematique Anal. Num' erique*, vol. 35, no. 3, pp. 513–523, 2001.
- [29] G.-S. Zhuang, G. Li, Q.-H. Jin, J.-L. Zhao, and M.-S. Yang, "Numerical analysis of an electrokinetic double-focusing injection technique for microchip CE," *Electrophoresis*, vol. 27, no. 24, pp. 5009–19, Dec. 2006.
- [30] L. Bousse', A. Minalla, M. Deshpande, K. B. Greiner, and J. R. Gilbert, "OPTIMIZATION OF SAMPLE INJECTION COMPONENTS IN ELECTROKINETIC MICROFLUIDIC SYSTEMS."
- [31] B. J. Kirby and E. F. Hasselbrink, "Zeta potential of microfluidic substrates: 1. Theory, experimental techniques, and effects on separations," *Electrophoresis*. 2004.
- [32] E. A. S. Doherty, R. J. Meagher, M. N. Albarghouthi, and A. E. Barron, "Microchannel wall

- coatings for protein separations by capillary and chip electrophoresis,” *Electrophoresis*, vol. 24, no. 12, pp. 34–54, 2003.
- [33] I.-I. J. Issaq, I. Z. Atamna, / G M Muschik, and / G M Janini, “The Effect of Electric Field Strength, Buffer Type and Concentration on Separation Parameters in Capillary Zone Electrophoresis.”
- [34] A. E. Herr, J. I. Molho, K. A. Drouvalakis, J. C. Mikkelsen, P. J. Utz, J. G. Santiago, and T. W. Kenny, “On-chip coupling of isoelectric focusing and free solution electrophoresis for multidimensional separations,” *Anal. Chem.*, vol. 75, no. 5, pp. 1180–1187, 2003.
- [35] J. G. Shackman and D. Ross, “Counter-flow gradient electrofocusing,” *Electrophoresis*, vol. 28, no. 4, pp. 556–571, 2007.
- [36] S. S. Bahga and J. G. Santiago, “Coupling isotachopheresis and capillary electrophoresis: a review and comparison of methods.”
- [37] L. L. Shultz-Lockyear, C. L. Colyer, Z. Hugh Fan, K. I. Roy, and D. J. Harrison, “Effects of injector geometry and sample matrix on injection and sample loading in integrated capillary electrophoresis devices,” *Electrophoresis*, 1999.
- [38] C. T. Culbertson, S. C. Jacobson, and J. M. Ramsey, “Microchip devices for high-efficiency separations,” *Anal. Chem.*, vol. 72, no. 23, pp. 5814–5819, 2000.
- [39] V. Dolník, “Capillary electrophoresis on microchip CE and CEC,” *Electrophoresis*, vol. 21, pp. 41–54, 2000.
- [40] J. I. Molho, A. E. Herr, B. P. Mosier, J. G. Santiago, T. W. Kenny, R. A. Brennen, G. B. Gordon, and B. Mohammadi, “Optimization of turn geometries for microchip electrophoresis,” *Anal. Chem.*, 2001.
- [41] L. M. Fu, R. J. Yang, and G. B. Lee, “Analysis of geometry effects on band spreading of microchip electrophoresis,” *Electrophoresis*, 2002.
- [42] D. Ross, C. F. Ivory, L. E. Locascio, and K. E. Van Cott, “Peak compression and resolution

- for electrophoretic separations in diverging microchannels,” *Electrophoresis*, vol. 25, no. 21–22, pp. 3694–3704, 2004.
- [43] N. a Patankar and H. H. Hu, “Numerical simulation of electroosmotic flow.,” *Anal. Chem.*, vol. 70, no. 9, pp. 1870–81, May 1998.
- [44] S. C. Jacobson, S. V. Ermakov, and J. M. Ramsey, “Minimizing the number of voltage sources and fluid reservoirs for electrokinetic valving in microfluidic devices,” *Anal. Chem.*, vol. 71, no. 15, pp. 3273–3276, 1999.
- [45] M. Blas, E. L. Asselin, T. Liu, C. Rodriguez, R. R. Panepucci, and B. R. McCord, “Minimizing the number of voltage sources for pinched injection on a microfluidic device.,” *Lab Chip*, vol. 10, no. 10, pp. 1319–23, May 2010.
- [46] L.-M. Fu and C.-H. Lin, “Numerical Analysis and Experimental Estimation of a Low-Leakage Injection Technique for Capillary Electrophoresis,” *Anal. Chem.*, vol. 75, pp. 5790–5796, 2003.
- [47] K. D. Jo, J. E. Schiffbauer, B. E. Edwards, R. Lloyd Carroll, and A. T. Timperman, “Fabrication and performance of a microfluidic traveling-wave electrophoresis system.,” *Analyst*, vol. 137, no. 4, pp. 875–883, 2012.
- [48] C. S. Effenhauser, G. J. M. Bruin, A. Paulus, and M. Ehrat, “Integrated Capillary Electrophoresis on Flexible Silicone Microdevices: Analysis of DNA Restriction Fragments and Detection of Single DNA Molecules on Microchips,” *Anal. Chem.*, vol. 69, no. 17, pp. 3451–3457, 1997.
- [49] A. T. Woolley, K. Lao, A. N. Glazer, and R. A. Mathies, “Capillary Electrophoresis Chips with Integrated Electrochemical Detection,” *Anal. Chem.*, vol. 70, no. 4, pp. 684–688, 1998.
- [50] M. L. Chabinyc, D. T. Chiu, J. C. McDonald, A. D. Stroock, J. F. Christian, A. M. Karger, and G. M. Whitesides, “An integrated fluorescence detection system in poly(dimethylsiloxane) for microfluidic applications,” *Anal. Chem.*, vol. 73, no. 18, pp. 4491–4498, 2001.

- [51] C. Dongre, J. van Weerd, G. A. J. Besselink, R. M. Vazquez, R. Osellame, G. Cerullo, R. van Weeghel, H. H. van den Vlekkert, H. J. W. M. Hoekstra, and M. Pollnau, “Modulation-frequency encoded multi-color fluorescent DNA analysis in an optofluidic chip,” *Lab Chip*, vol. 11, no. 4, pp. 679–683, 2011.
- [52] S. Fekete, D. Guillarme, P. Sandra, and K. Sandra, “Chromatographic, Electrophoretic, and Mass Spectrometric Methods for the Analytical Characterization of Protein Biopharmaceuticals,” *Analytical Chemistry*. 2016.
- [53] J. P. Landers, *Handbook of Capillary Electrophoresis*. FL: CRC Press: Boca Raton, 1994.
- [54] G. Karniadakis, A. Beskok, and N. Aluru, *Microflows and Nanoflows: Fundamentals and Simulation*. Springer Science+Business Media, LLC, 2005.
- [55] D. Gillespie and S. Pennathur, “Separation of ions in nanofluidic channels with combined pressure-driven and electro-osmotic flow,” *Anal. Chem.*, vol. 85, no. 5, pp. 2991–2998, 2013.
- [56] N. M. Laurendeau, *2 Part One, FUNDAMENTALS OF STATISTICAL THERMODYNAMICS 2 Probability and Statistics*. .
- [57] D. Sinton, L. Ren, and D. Li, “Visualization and numerical modelling of microfluidic on-chip injection processes,” *J. Colloid Interface Sci.*, 2003.
- [58] X. Xuan and D. Li, “Focused electrophoretic motion and selected electrokinetic dispensing of particles and cells in cross-microchannels,” *Electrophoresis*, vol. 26, no. 18, pp. 3552–3560, 2005.
- [59] C. S. Effenhauser, A. Paulus, A. Manz, and H. M. Widmer, “High-speed separation of antisense oligonucleotides on a micromachined capillary electrophoresis device,” *Anal. Chem.*, 1994.
- [60] B. Jung, R. Bharadwaj, and J. G. Santiago, “Thousandfold signal increase using field-amplified sample stacking for on-chip electrophoresis,” *Electrophoresis*, vol. 24, no. 19–20, pp. 3476–83, 2003.

- [61] L. M. Fu, R. J. Yang, and G. Bin Lee, "Electrokinetic focusing injection methods on microfluidic devices," *Anal. Chem.*, 2003.
- [62] C.-H. Tsai, M. F. Hung, C.-L. Chang, L.-W. Chen, and L.-M. Fu, "Optimal configuration of capillary electrophoresis microchip with expansion chamber in separation channel.," *J. Chromatogr. A*, vol. 1121, no. 1, pp. 120–8, Jul. 2006.
- [63] L. M. Fu, J. C. Leong, C. F. Lin, C. H. Tai, and C. H. Tsai, "High performance microfluidic capillary electrophoresis devices," *Biomed. Microdevices*, 2007.
- [64] S. C. Jacobson, R. Hergenroder, L. B. Koutny, / R J Warmack, and J. M. Ramsey, "Effects of Injection Schemes and Column Geometry on the Performance of Microchip Electrophoresis Devices," *Anal. Chem. Heal. Sci. Res. Div. ACS Symp. Ser. J. M. Anal. Chem. J. Trends Anal. Chem. IEEE Trans. Electron Devices*, vol. 66, no. 104, pp. 1107–1113, 1994.
- [65] D. J. Harrison, K. Fluri, K. Seiler, Z. Fan, C. S. Effenhauser, and a Manz, "Micromachining a miniaturized capillary electrophoresis-based chemical analysis system on a chip.," *Science*, vol. 261, no. 5123, pp. 895–7, Aug. 1993.
- [66] K. Seiler, Z. H. H. Fan, K. Fluri, and D. J. Harrison, "Electroosmotic Pumping and Valveless Control of Fluid-Flow Within a Manifold of Capillaries on a Glass Chip," *Anal. Chem.*, vol. 66, no. 20, pp. 3485–3491, 1994.
- [67] G. S. Zhuang, G. Li-, Q. H. Jin, J. L. Zhao, and M. S. Yang, "Numerical analysis of an electrokinetic double-focusing injection technique for microchip CE," *Electrophoresis*, 2006.
- [68] A. J. Wang, J. J. Xu, and H. Y. Chen, "Proteins modification of poly(dimethylsiloxane) microfluidic channels for the enhanced microchip electrophoresis," *J. Chromatogr. A*, vol. 1107, no. 1–2, pp. 257–264, 2006.
- [69] S. V. Ermakov, S. C. Jacobson, and J. M. Ramsey, "Computer simulations of electrokinetic injection techniques in microfluidic devices," *Anal. Chem.*, vol. 72, no. 15, pp. 3512–7, 2000.
- [70] J. P. Kutter, R. S. Ramsey, S. C. Jacobson, and J. M. Ramse, "Determination of Metal Cations

in Microchip Electrophoresis Using On-Chip Complexation and Sample Stacking,” *J Micro Sep*, vol. 10, pp. 313–319, 1998.

- [71] G. Atkinson, *Electrochemical information*. Institute of Physics Handbook, 1972.
- [72] J. W. Jorgenson and K. DeArman Lukacs, “Zone electrophoresis in open-tubular glass capillaries: Preliminary data on performance,” *J. High Resolut. Chromatogr.*, vol. 4, no. 5, pp. 230–231, 1981.
- [73] X. Huang, W. F. Coleman, and R. N. Zare, “ANALYSIS OF FACTORS CAUSING PEAK BROADENING IN CAPILLARY ZONE ELECTROPHORESIS,” *Elsevier Sci. Publ. B.V.*, vol. 480, no. 21, pp. 95–110, 1989.
- [74] L. E. Locascio, C. E. Perso, and C. S. Lee, “Measurement of electroosmotic flow in plastic imprinted microfluid devices and the effect of protein adsorption on flow rate,” *J. Chromatogr. A*, 1999.
- [75] X. Huang, M. J. Gordon, and R. N. Zare, “Current-Monitoring Method for Measuring the Electroosmotic Flow Rate in Capillary Zone Electrophoresis,” *Anal. Chem.*, vol. 60, pp. 1837–1838, 1988.
- [76] J. C. Giddings, “Generation of Variance, ‘Theoretical Plates,’ Resolution, and Peak Capacity in Electrophoresis and Sedimentation,” *Sep. Sci.*, vol. 4, no. 3, pp. 181–189, 1969.
- [77] J. W. Jorgenson and K. D. Lukacs, “Zone electrophoresis in open-tubular glass capillaries,” *Anal. Chem.*, vol. 53, pp. 1298–1302, 1981.
- [78] J. a Luckey, T. B. Norris, and L. M. Smitb, “Analysis of Resolution in DNA Sequencing by Capillary Gel Electrophoresis,” *J. Phys. Chem.*, vol. 97, pp. 3067–3075, 1993.
- [79] R. Bharadwaj, J. G. Santiago, and B. Mohammadi, “Design and optimization of on-chip capillary electrophoresis,” *Electrophoresis*, vol. 23, pp. 2729–2744, 2002.
- [80] D. Ross, “Step width, spacing, and resolution in gradient elution moving boundary electrophoresis. Part 1. Theory and comparison with zone electrophoresis,” *Electrophoresis*,

vol. 31, 2010.

- [81] M. Viefhues, J. Regtmeier, and D. Anselmetti, "Fast and continuous-flow detection and separation of DNA complexes and DNA in nanofluidic chip format," *Methods Mol. Biol.*, vol. 1274, pp. 99–110, 2013.
- [82] J. J. Simhadri, H. A. Stretz, M. A. Oyanader, and P. E. Arce, "Assessing Performance of Irregular Microvoids in Electrophoresis Separations," *Ind. Eng. Chem. Res.*, vol. 54, no. 42, pp. 10434–10441, 2015.
- [83] Q. Mao and J. Pawliszyn, "Demonstration of isoelectric focusing on an etched quartz chip with UV absorption imaging detection."
- [84] A. S. Zarabadi and J. Pawliszyn, "Accurate determination of the diffusion coefficient of proteins by fourier analysis with whole column imaging detection," *Anal. Chem.*, 2015.
- [85] T. K. Khurana and J. G. Santiago, "Preconcentration, separation, and indirect detection of nonfluorescent analytes using fluorescent mobility markers," *Anal. Chem.*, 2008.
- [86] B. Gaš and E. Kenndler, "System zones in capillary zone electrophoresis," *Electrophoresis*, vol. 25, no. 23–24, pp. 3901–3912, 2004.
- [87] F. Lisdat, W. O. Ho, U. Wollenberger, F. W. Scheller, T. Richter, and U. Bilitewski, "Recycling Systems Based on Screen-Printed Electrodes."
- [88] O. D. Leite, O. Fatibello-Filho, and A. D. M. Barbosa, "Determination of catecholamines in pharmaceutical formulations using a biosensor modified with a crude extract of fungi laccase (*Pleurotus ostreatus*)," *J. Braz. Chem. Soc.*, 2003.
- [89] S. R. Wallenborg, L. Nyholm, and C. E. Lunte, "End-column amperometric detection in capillary electrophoresis: Influence of separation-related parameters on the observed half-wave potential for dopamine and catechol," *Anal. Chem.*, 1999.
- [90] C. D. Meinhart, S. T. Wereley, and J. G. Santiago, "PIV measurements of a microchannel flow," *Exp. Fluids*, 1999.

- [91] H. C. Yeh, J. Sharma, J. J. Han, J. S. Martinez, and J. H. Werner, "A DNA-silver nanocluster probe that fluoresces upon hybridization," *Nano Lett.*, 2010.
- [92] S. W. Yang and T. Vosch, "Rapid detection of microRNA by a silver nanocluster DNA probe," *Anal. Chem.*, 2011.
- [93] B. Mosier, J. Molho, and J. Santiago, "Photobleached-fluorescence imaging of microflows," *Exp. Fluids*, 2002.
- [94] D. Sinton, "FLOW VISUALIZATION IN MICROCHANNELS."
- [95] J. P. Landers, R. P. Oda, B. J. Madden, and T. C. Spelsberg, "High-performance capillary electrophoresis of glycoproteins: The use of modifiers of electroosmotic flow for analysis of microheterogeneity," *Anal. Biochem.*, 1992.
- [96] G. J. M. Bruin, J. P. Chang, R. H. Kuhlman, K. Zegers, J. C. Kraak, and H. Poppe, "Capillary zone electrophoretic separations of proteins in polyethylene glycol-modified capillaries," *J. Chromatogr. A*, 1989.
- [97] W. Nashabeh and Z. El Rassi, "Capillary zone electrophoresis of pyridylamino derivatives of maltooligosaccharides," *J. Chromatogr. A*, 1990.
- [98] M. C. Roman and P. R. Brown, "Free-Flow Electrophoresis: As a Preparative Separation Technique," *Anal. Chem.*, vol. 66, no. 2, 1994.
- [99] R. T. Turgeon and M. T. Bowser, "Micro free-flow electrophoresis: Theory and applications," *Anal. Bioanal. Chem.*, vol. 394, no. 1, pp. 187–198, 2009.
- [100] F. E. P. Mikkers, F. M. Everaerts, and T. P. E. M. Verheggen, "High-performance zone electrophoresis," *J. Chromatogr. A*, 1979.
- [101] B. Jung, R. Bharadwaj, and J. G. Santiago, "Thousandfold signal increase using field-amplified sample stacking for on-chip electrophoresis," *Electrophoresis*, 2003.
- [102] B. Jung, R. Bharadwaj, and J. G. Santiago, "On-chip millionfold sample stacking using

- transient isotachopheresis,” *Anal. Chem.*, vol. 78, no. 7, pp. 2319–27, Apr. 2006.
- [103] T. K. Khurana and J. G. Santiago, “Sample zone dynamics in peak mode isotachopheresis,” *Anal. Chem.*, 2008.
- [104] P. Smejkal, D. Bottenus, M. C. Breadmore, R. M. Guijt, C. F. Ivory, F. Foret, and M. Macka, “Microfluidic isotachopheresis: A review,” *Electrophoresis*, vol. 34, no. 11, pp. 1493–1509, 2013.
- [105] S. S. Bahga and J. G. Santiago, “Coupling isotachopheresis and capillary electrophoresis: a review and comparison of methods,” *Analyst*, 2013.
- [106] A. Rogacs, L. A. Marshall, and J. G. Santiago, “Purification of nucleic acids using isotachopheresis,” *Journal of Chromatography A*. 2014.
- [107] M. Gad-el-Hak, K. V Sharp, and R. J. Adrian, *MEMS Handbook-Liquid Flows in Microchannels 10.1*, 2nd ed. 2005.
- [108] D. Ross and L. E. Locascio, “Microfluidic temperature gradient focusing,” *Anal. Chem.*, vol. 74, no. 11, pp. 2556–2564, 2002.
- [109] S. M. Shameli, T. Glawdel, and C. L. Ren, “Model of separation performance of bilinear gradients in scanning format counter-flow gradient electrofocusing techniques,” *Electrophoresis*, 2015.
- [110] S. M. Shameli and C. L. Ren, “Microfluidic Two-Dimensional Separation of Proteins Combining Temperature Gradient Focusing and Sodium Dodecyl Sulfate-Polyacrylamide Gel Electrophoresis,” *Anal. Chem.*, 2015.
- [111] L. Ren, D. Sinton, and D. Li, “Numerical simulation of microfluidic injection processes in crossing microchannels,” *J. Micromechanics Microengineering*, vol. 13, no. 5, pp. 739–747, Sep. 2003.
- [112] C. L. Chang, H. H. Hou, L. M. Fu, and C. H. Tsai, “A low-leakage sample plug injection scheme for crossform microfluidic capillary electrophoresis devices incorporating a restricted

- cross-channel intersection,” *Electrophoresis*, vol. 29, no. 15, pp. 3135–3144, 2008.
- [113] D. Sinton, L. Ren, and D. Li, “A dynamic loading method for controlling on-chip microfluidic sample injection,” *J. Colloid Interface Sci.*, 2003.
- [114] I. Borukhov, D. Andelman, and H. Orland, “Adsorption of large ions from an electrolyte solution: A modified Poisson-Boltzmann equation,” *Electrochim. Acta*, vol. 46, no. 2–3, pp. 221–229, 2000.
- [115] M. E. Fisher, “The story of coulombic criticality,” *J. Stat. Phys.*, vol. 75, no. 1, pp. 1–36, 1994.
- [116] N. Cu villier and F. Rondelez, “Breakdown of the Poisson-Boltzmann description for electrical double layers involving large multivalent ions,” *Thin Solid Films*, vol. 327, pp. 19–23, 1998.
- [117] R. Kjellander, S. Marčelja, R. M. Pashley, and J. P. Quirk, “A theoretical and experimental study of forces between charged mica surfaces in aqueous CaCl₂ solutions,” *J. Chem. Phys.*, vol. 92, no. 7, pp. 4399–4407, 1990.
- [118] I. Borukhov, D. Andelman, and H. Orland, “Steric Effects in Electrolytes: A Modified Poisson-Boltzmann Equation,” *Phys. Rev. Lett.*, vol. 79, no. 3, pp. 435–438, 1997.
- [119] M. S. Kilic, M. Z. Bazant, and A. Ajdari, “Steric effects in the dynamics of electrolytes at large applied voltages. II. Modified Poisson-Nernst-Planck equations,” *Phys. Rev. E - Stat. Nonlinear, Soft Matter Phys.*, 2007.
- [120] M. S. Kilic, M. Z. Bazant, and A. Ajdari, “Steric effects in the dynamics of electrolytes at large applied voltages. I. Double-layer charging,” *Phys. Rev. E - Stat. Nonlinear, Soft Matter Phys.*, 2007.
- [121] D. Li, *Electrokinetics in Microfluidics*. Academic Press, 2004.
- [122] N. M. Laurendeau, *10 Statistical Thermodynamics, Distribution, Equilibrium Particle Mixture, Ideal Gas. .*
- [123] M. Bowley, R. and Sanchez, *Introductory Statistical Mechanics*. Clarendon Press, Oxford,

2000.

- [124] F. Mandl, *Statistical Physics*. John Wiley, 1988.
- [125] P. Dutta and A. Beskok, “Analytical Solution of Combined Electroosmotic/Pressure Driven Flows in Two-Dimensional Straight Channels: Finite Debye Layer Effects,” *Anal. Chem.*, vol. 73, no. 9, pp. 1979–1986, May 2001.
- [126] P. Dutta, A. Beskok, and T. C. Warburton, “Electroosmotic flow control in complex microgeometries,” *J. Microelectromechanical Syst.*, vol. 11, no. 1, pp. 36–44, 2002.
- [127] C. L. Ren and D. Li, “Electrokinetic sample transport in a microchannel with spatial electrical conductivity gradients,” *J. Colloid Interface Sci.*, vol. 294, no. 2, pp. 482–491, 2006.
- [128] D. Erickson and D. Li, “Influence of surface heterogeneity on electrokinetically driven microfluidic mixing,” *Langmuir*, vol. 18, no. 5, pp. 1883–1892, 2002.
- [129] R. Yang, L. Fu, and Y. Lin, “Electroosmotic Flow in Microchannels,” *J. Colloid Interface Sci.*, vol. 105, no. October 2015, pp. 98–105, 2001.
- [130] B. D. Storey, B. S. Tilley, H. Lin, and J. G. Santiago, “Electrokinetic instabilities in thin microchannels,” *Phys. Fluids*, vol. 17, no. 1, pp. 10–13, 2005.
- [131] S. Arulanandam and D. Li, “Liquid transport in rectangular microchannels by electroosmotic pumping,” *Colloids Surfaces A Physicochem. Eng. Asp.*, vol. 161, no. 1, pp. 89–102, 2000.
- [132] J. Feng, Z. Chuncheng, Z. Peng, and Z. Deyi, “Analysis of Electroosmotic Flow with Linear Variable Zeta Potential,” *2005 Int. Conf. MEMS, NANO Smart Syst.*, pp. 319–326, 2005.
- [133] “Ansys Fluent Theory Guide.” 2015.
- [134] “CFX Solver Theory Guide.” 2015.
- [135] T. BARTH and D. Jespersen, “The design and application of upwind schemes on unstructured meshes,” *27th Aerosp. Sci. Meet.*, 1989.

- [136] M. Raw, "Robustness of coupled Algebraic Multigrid for the Navier-Stokes equations," in *34th Aerospace Sciences Meeting and Exhibit, Aerospace Sciences Meetings*, 1996.
- [137] "ANSYS Meshing User's Guide," 2015.
- [138] Z. Shao, C. L. Ren, and G. E. Schneider, "A complete numerical model for electrokinetic flow and species transport in microchannels," *Eur. Phys. J. Spec. Top.*, vol. 171, no. 1, pp. 189–194, May 2009.

Appendices

Appendix A- EDL and Poisson-Boltzmann Equation in Microfluidics

Statistical Thermodynamics and Entropy Consideration

In this appendix we fulfill the literature gap in microfluidics for the derivation of Poisson-Boltzmann equation as a governing equation for the distribution of charges and electric potential in EDL. For Lab-on-chip systems, DNA and protein separation technologies, we require numerical models for sample transport. In this chapter, a thorough investigation of electrokinetics and microfluidics transport phenomena reviews the background of the Poisson-Boltzmann equation with the view to providing a more consolidated and comprehensive understanding of it. We present a detailed derivation of the equation, which is not available in the microfluidic literature at one place. This equation is then applied to find the electric potential and charge density distributions in the electric double layer (EDL). The present study provides a detailed derivation of the Boltzmann distribution by first providing insight into the physics behind it. Principles of probability are used to identify the most probable ion distribution. This distribution is subject to constraints of constant number of particles and total energy of the system; Lagrangian Multipliers are used to solve the resulting constrained optimization problem. Classical thermodynamics is shown to be consistent with the distribution of ions: the Boltzmann distribution. Then, based on Coulomb's law, the derivation of Poisson's equation, and its special form of Laplace's equation, the electric potential distribution in the EDL and in the bulk flow is derived and presented. By applying classical thermodynamics and integrating the Boltzmann distribution and Poisson equation together, the Poisson-Boltzmann equation is achieved. Figure A- 1 shows a summary of the derivation of this equation. Different solutions to this equation and approximations are all provided at the end of this chapter.

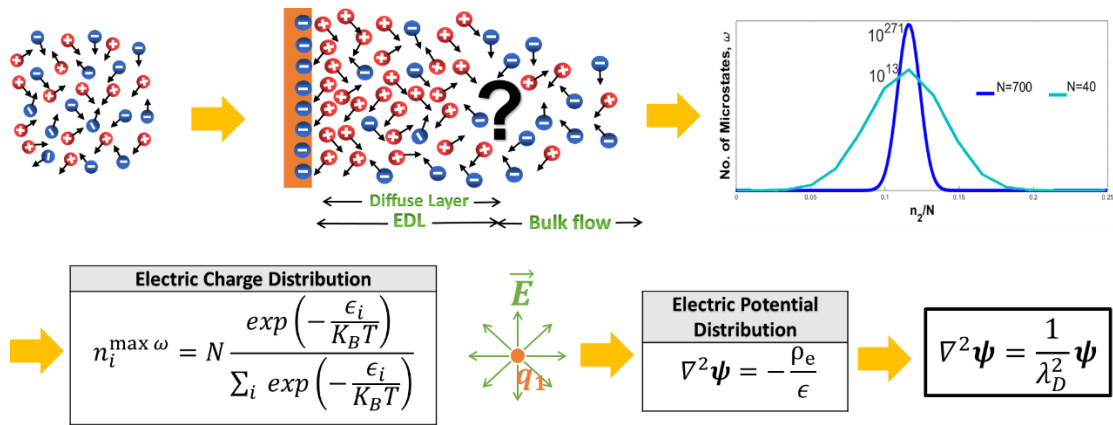


Figure A- 1: Summary of Poisson-Boltzmann equation derivation

According to Borukhov et al. in 2000 [114], the main advantage of P-B equation is its simplicity, which allows for analytical solutions in simple cases, and its surprisingly good agreement with experiments. It was applied to many situations including ion distribution around a charged cylinder or sphere, adsorption of ions to flat surfaces and in biological systems like DNA and charged membranes. The authors state that it is a successful equation in view of the various approximations resulting in a mean field approach that totally neglects correlations and all specific (non-electrostatic) interactions between the ions including the ionic finite size. Nevertheless, despite the success of this approach in describing a wide range of systems, it has limitations in several cases: (i) the phase transition of electrolyte solutions [115], (ii) the adsorption of charged ions to highly charged surfaces [114] -[116], and (iii) the attractive interactions that can be observed between equally charged surfaces in the presence of multivalent counter ions [117] [118]. Kilic et al. , in their two-part series research [119][120], also applied Poisson-Boltzmann equation and its modified form as Poisson-Nernst-Planck equation for dilute electrolytes under large applied potentials. They reviewed the interaction of ions but mainly focused on comparing these two models regardless of the derivation of P-B equation. On derivation aspect, Li and Kirby [121] [10] provided more details in their books, particularly on the Poisson equation and electrostatic force among charges. However, providing the application of this distribution, many steps are skipped in their derivations. Bruus [11], working in theoretical microfluidics, provided a derivation of the Poisson-Boltzmann equation with the greatest detail available in the microfluidic literature. He presented the thermodynamics part of the Boltzmann equation, but yet there remains an information gap related to the details of the Boltzmann distribution derivation.

The focus of this appendix is on derivation of Poisson-Boltzmann equation as a fundamental governing equation in microfluidics and nanofluidics, with non-overlapping EDL's, even though not solved directly in many applications. This study presents a detailed derivation on the P-B equation in two parts: the first is the derivation of the Boltzmann distribution in the electric double layer, using a probability and statistical thermodynamics approach; and the second is the derivation of Poisson's equation. Consistent with a classical thermodynamics approach, these two are then merged together. For clarification, a summary map of the derivation is illustrated in Figure A- 2.

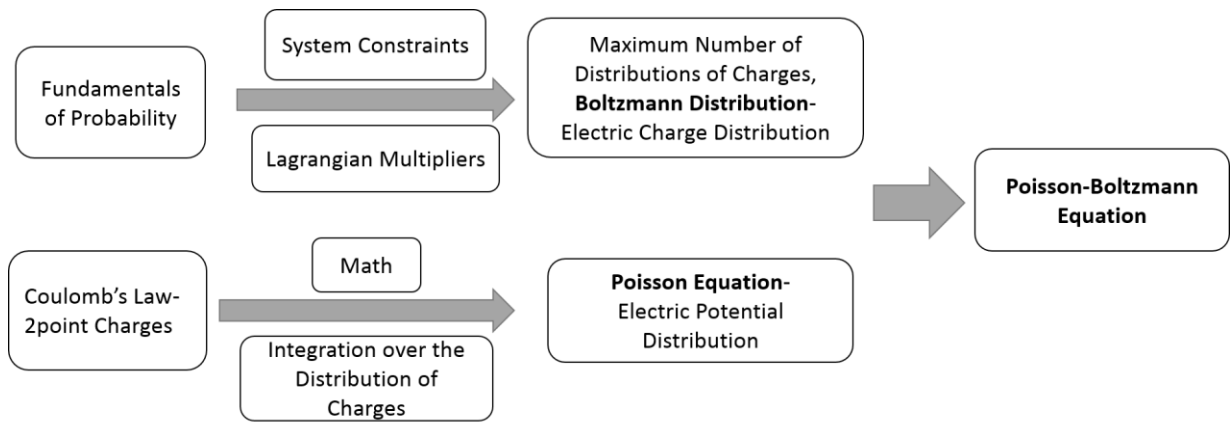


Figure A- 2: Summary map of the derivation of Poisson-Boltzmann Equation

Fundamentals of Probability

To gain a thorough understanding of the electric charge distribution in the electric double layer in microchannels, the Boltzmann distribution is derived. Based on statistical and classical thermodynamics and the Boltzmann equation, a clear understanding of ion distribution is provided. In statistical thermodynamics, we have to keep in mind that atoms are considered as independent particles. According to Laurendeau [122], the entropy of an isolated system increases because of increased molecular probabilities. First, the fundamentals of probability are briefly explained, and then, based on probability rules, the distribution of ions in the EDL is developed. As we know from the system energy viewpoint, a molecular system in quantum mechanics has discrete energy levels, whereas each energy level is composed of energy states. The number of independent energy states per energy level is called its degeneracy. As an analogy, energy levels are like book shelves, and energy states are like baskets

on each shelf. In classical mechanics the state of a particle is defined by its position and energy as a continuous variable, but, in quantum mechanics, each distribution of discrete quantum states that provides for a total number, volume, and energy, is called a microstate and it shows that state's distribution of particles. Microstates, and their numbers, provide a measure of the disorder in the system as a way to measure entropy. An isolated system with the largest number of microstates, subject to constraints of fixed N , V and E , respectively, the number of particles, system volume and energy of the system, provides an equilibrium whose distribution maximizes entropy.

According to a definition of probability, in a sample space of N_s mutually exclusive, equally likely possible outcomes and N_A outcome points in "A" event; the probability of event "A" would be $P(A) = N_A/N_s$. As an example, the probability of drawing a single ace from a well-mixed card deck is $P(A) = \frac{4}{52} = \frac{1}{13}$. It should be noted that $N_A \leq N_s$ and "Mutually Exclusive" means that no two outcomes can occur simultaneously in a single sample space. The other concept to discuss in probability is the number of *permutations* and *combinations*. A simple example of a combination would be selecting marbles from a marble bag randomly in an independent sequential manner. Identifying all possible labeled marbles from the bag as A, B, C, etc. (as distinguishable particles), and each different sequence being a *permutation*, which for " N " particles provides for $N!$ permutations. But for unlabeled marbles, there would be only one *combination* obtainable. If the order does not matter, it is a *combination* and if the order does matter it is a *permutation*. So, the possible permutations of choosing M cards out of N cards would be $P(N, M) = \frac{N!}{(N-M)!}$ and the combination of having M cards out of N cards at a time, i.e., $C(N, M)$ or ${}_N C_M$, equals to $C(N, M) = \frac{P(N, M)}{M!} = \frac{N!}{(N-M)! M!}$. In general, where n_i indicates the number of atoms in the i^{th} state, the number of distinguishable configurations of a distribution is

$$\omega = \frac{N!}{\prod_1^M n_i!} \quad (\text{A- 1})$$

To have a better understanding of equation (A- 1), for distribution k , (i.e. $\omega_k = \frac{N!}{\prod_1^M n_i!}$), we start with a two-state problem, where we have n_1 and n_2 particles in two states, 1 & 2. Picking n_1 particles to be in state 1 means $(N - n_1)$ particles have to be in state 2. The first particle can be picked in N ways and the second one in $(N - 1)$ ways. The third particle can be picked in $(N - 2)$ different ways. So, the number of ways to pick different particles is $N \times (N - 1) \times (N - 2) \times \dots \times (N - n_1 + 1) = \frac{N!}{(N-n_1)!}$

and dividing it by the number of permutations of the n_1 particles, i.e., $n_1!$, we get $\omega = \frac{N!}{n_1!(N-n_1)!}$. Generalizing this example to a many-state particle problem, we would say the number of ways to put n_1 particles in box 1 and the other $(N - n_1)$ in other boxes is given, and the number of ways to put n_2 particles in box 2 is given by a similar formula with $N - n_1$ (there are only $N - n_1$ particles after n_1 particles have been put in box 1 and) and $n_1 \rightarrow n_2$. These numbers of ways multiply. Then it comes to box 3, until the last box n . Therefore, $\omega = \frac{N!}{n_1!(N-n_1)!} \times \frac{(N-n_1)!}{n_2!(N-n_1-n_2)!} \times \dots \times \frac{n_n!}{n_n!0!}$ which was previously introduced as (A- 1) above. From a probability point of view, ω_k shows us the number of ways N identical, distinguishable objects may be placed in M different containers (here energy levels) such that the j^{th} container holds n_j objects (here particles/ions). The probability of the macrostate is then equal to $P_k = \frac{\omega_k}{\sum_k \omega_k}$. ω_k is the thermodynamic probability, which is not a true probability since it can be equal to one or even much higher. In contrast, P_k is called the true probability and is always less than one. To further clarify, an isolated system with N particles of 10 atoms with a total energy of 10ϵ is considered. For such a system, the *macrostate* exhibits the thermodynamics variables of the system such as pressure, volume, temperature, energy, entropy, etc. and here is defined by $N = 10$ and $E = 10\epsilon$. The *microstates* are defined by those distributions that provide for $N = \sum_i n_i = 10$ and $E = \sum_i n_i \epsilon_i = 10\epsilon$. Here, n_i indicates the number of atoms in the i^{th} state of energy of ϵ_i . Increasing the number of particles to 10 in a system with 10ϵ energy, the number of distributions jumps to 12,600. Similarly, in a 12 particle system with the same energy of 10ϵ , this number rises to 55,440. It is important to note that we have examined many more distributions with higher numbers of particles and higher system energy levels. In general, a system of N particles and a total energy of E will be subject to two constraints: first, the total number of particles in the system is constant, and second, the total energy of the system is constant, while the system temperature is kept constant and no work is done by/on the system. Therefore, $N = \sum_i n_i = \text{const.}$ and $E = \sum_i n_i \epsilon_i = \text{const.}$

Boltzmann Distribution – Electric Charge Distribution

To find the most probable state, i.e. the most probable distribution of particles among energy levels that with the highest number of microstates, ω should be a maximum with respect to the total number of microstates. Our code results and the number of distributions both change with increasing

number of particles and consequent increase in system energy as the system has an energy of $E = \frac{N\epsilon}{2}$. The number of distributions in the most populated level, non-dimensionalized by the total number of particles, i.e., $\frac{n_2}{N}$ is compared for different systems varying in N and E . The plots, shown in Figure A- 3 narrow considerably around the peak and the ω distribution approaches a Dirac delta function for a large number of particles (e.g. a mole of material). These plots confirm our expectations for the most probable state. The trend of changing ω is evidence of the tendency towards a preferred distribution of particles as the number of particles, distributions, microstates, becomes significant.

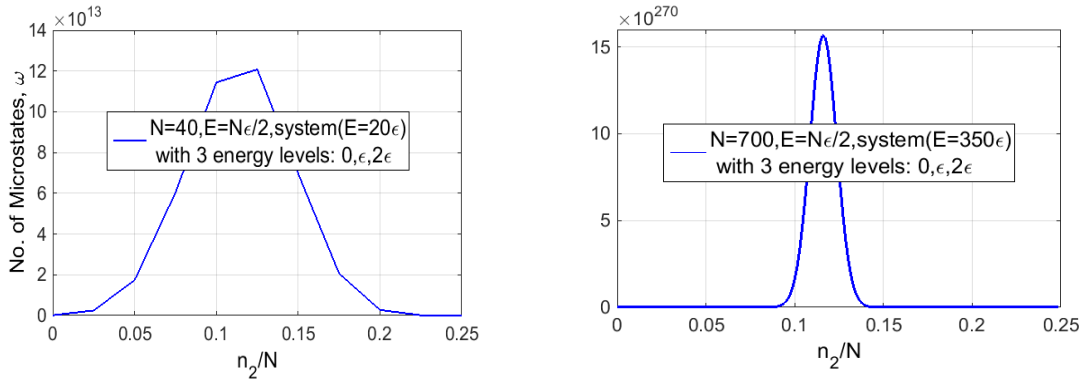


Figure A- 3: Dependence of the number of distributions on the number of particles

Considering all possible microstates for the above distributions and noting that atoms interact up to 10^{35} (times/second), any averaging method would produce a distribution close to the most probable state and provide a more solid conclusion [123] [124]. Two averaging approaches can be considered: time averaging and distribution averaging or ensemble average. With the high interaction among atoms, the former cannot be a good approach in practice; however, the latter can be implemented. As shown in the tables of distributions, there are many possible microstates showing the specific occurrence probability for each macrostate. By letting n_i be the i^{th} microstate number of particles with occurrence probability P_i , the ensemble average would be $\langle n_i \rangle = \sum_i P_i n_i$. Taking an isolated system into consideration, for a macroscopic state with 10^{23} atoms, two statistical assumptions are made:

1. Using the Principle of Equal Equilibrium Probabilities (PEEP) for an isolated system in equilibrium, all microstates consistent with a given macrostate of an isolated system (i.e., given E, V, N) have equal a priori probability. i.e., $P_k = \frac{\omega_k}{\sum_k \omega_k}$, where ω_k is the number of microstates for each k-labelled macrostate.

2. The Ergodic Hypothesis Time averages are equivalent to ensemble averages. Equivalently, left to its own devices, a system will explore all possible members of the ensemble $\sum_k P_k = 1$.

Therefore, assuming PEEP condition, the most likely distribution would have an average occupancy known from the ensemble average of $\langle n_i \rangle = \frac{\sum_k n_i(k) \omega_k}{\sum_k \omega_k}$.

Table A- 1 shows all the possible distributions for a system with $N = 4, E = 10\epsilon$. For each macrostate (k -labelled rows), the number of particles at each energy level (ϵ_i -labelled columns) are shown and for each macrostate the number of microstates and the ratio of the number of microstates to the highest probable number of microstates are given as ω_k and $\frac{\omega_k}{\omega_{max}}$. We are looking for the most probable state and the distribution of particles in that state. With that respect we calculate the ensemble average of the distribution of particles. For example, in a system with $N = 4, E = 10\epsilon$, ensemble average for the ground level of energy is $\langle n_0 \rangle = 0.92$. To get this ensemble average, we get $n_0 * \omega_k$ for each row, with k from 1 to 23, then get the summation of them for ground level of all the macrostates and divide the summation value by the total summation of ω_k for the table of distributions. With this ensemble averaging method, we can find out the average number of particles at each energy level ϵ_i , if only we had one macrostate holding the highest number of microstates in the system. An interesting finding regarding the above ensemble average is that, for smaller numbers of particles there are many distributions having comparable probabilities, whereas as the number of particles increases, the most probable distributions becomes more concentrated. For example, there are 5 states with equal and maximum probabilities for the above mentioned system with $N = 4, E = 10\epsilon$, whereas the other two systems with a higher number of particles, $N = 10$ and 12 , also for $E = 10\epsilon$, indicate only one state as the most probable. Note a whole table is presented only for $N = 4, E = 10\epsilon$; and the other two tables show just the most probable macrostates. For $N=10$ and $E=10\epsilon$ there are 12,600 distributions and for $N=12$ and $E=10\epsilon$ there are 55,440 distributions. Thus, with few particles, many states have equal probability, whereas as the number of particles increases, there becomes a single most-probable state. If we denote the probability of the most-probable state, for a system with N particles and energy E and $P^{max}_{N,E} = \frac{\omega_{k,max}}{\sum_k \omega_k}$, and for the systems shown in Table A- 1, we will have $P^{max}_{4,10} = 0.08392$, $P^{max}_{10,10} = 0.1364$, and $P^{max}_{12,10} = 0.1572$. This clearly indicates a higher probability for the most-probable state(s) for systems with higher numbers of particles; as the number of particles becomes very large, $O(10^{23})$, there becomes a single state with the very highest probability.

Table A- 1: Ensemble average tables for 3 different systems

N=4, E=10ε

| ϵ_i (energy level) | | 0 | ϵ | 2ϵ | 3ϵ | 4ϵ | 5ϵ | 6ϵ | 7ϵ | 8ϵ | 9ϵ | 10ϵ | ω_k | ω_k / ω_{max} |
|------------------------------------|-----------------|-------|------------|-------------|-------------|-------------|-------------|-------------|-------------|-------------|-------------|--------------|---|---------------------------|
| k μ states | n_i particles | n_0 | n_1 | n_2 | n_3 | n_4 | n_5 | n_6 | n_7 | n_8 | n_9 | n_{10} | | |
| 1 | | 0 | 0 | 2 | 2 | 0 | 0 | 0 | 0 | 0 | 0 | 0 | 6 | 0.3 |
| 2 | | 0 | 0 | 3 | 0 | 1 | 0 | 0 | 0 | 0 | 0 | 0 | 4 | 0.2 |
| 3 | | 0 | 1 | 0 | 3 | 0 | 0 | 0 | 0 | 0 | 0 | 0 | 4 | 0.2 |
| 4 | | 0 | 1 | 1 | 1 | 1 | 0 | 0 | 0 | 0 | 0 | 0 | 24 | 1 |
| 5 | | 0 | 1 | 2 | 0 | 0 | 1 | 0 | 0 | 0 | 0 | 0 | 12 | 0.5 |
| 6 | | 0 | 2 | 0 | 0 | 2 | 0 | 0 | 0 | 0 | 0 | 0 | 6 | 0.3 |
| 7 | | 0 | 2 | 0 | 1 | 0 | 1 | 0 | 0 | 0 | 0 | 0 | 12 | 0.5 |
| 8 | | 0 | 2 | 1 | 0 | 0 | 0 | 1 | 0 | 0 | 0 | 0 | 12 | 0.5 |
| 9 | | 0 | 3 | 0 | 0 | 0 | 0 | 0 | 1 | 0 | 0 | 0 | 4 | 0.2 |
| 10 | | 1 | 0 | 0 | 2 | 1 | 0 | 0 | 0 | 0 | 0 | 0 | 12 | 0.5 |
| 11 | | 1 | 0 | 1 | 0 | 2 | 0 | 0 | 0 | 0 | 0 | 0 | 12 | 0.5 |
| 12 | | 1 | 0 | 1 | 1 | 0 | 1 | 0 | 0 | 0 | 0 | 0 | 24 | 1 |
| 13 | | 1 | 0 | 2 | 0 | 0 | 0 | 1 | 0 | 0 | 0 | 0 | 12 | 0.5 |
| 14 | | 1 | 1 | 0 | 0 | 1 | 1 | 0 | 0 | 0 | 0 | 0 | 24 | 1 |
| 15 | | 1 | 1 | 0 | 1 | 0 | 0 | 1 | 0 | 0 | 0 | 0 | 24 | 1 |
| 16 | | 1 | 1 | 1 | 0 | 0 | 0 | 0 | 1 | 0 | 0 | 0 | 24 | 1 |
| 17 | | 1 | 2 | 0 | 0 | 0 | 0 | 0 | 0 | 1 | 0 | 0 | 12 | 0.5 |
| 18 | | 2 | 0 | 0 | 0 | 0 | 2 | 0 | 0 | 0 | 0 | 0 | 6 | 0.3 |
| 19 | | 2 | 0 | 0 | 0 | 1 | 0 | 1 | 0 | 0 | 0 | 0 | 12 | 0.5 |
| 20 | | 2 | 0 | 0 | 1 | 0 | 0 | 0 | 1 | 0 | 0 | 0 | 12 | 0.5 |
| 21 | | 2 | 0 | 1 | 0 | 0 | 0 | 0 | 0 | 1 | 0 | 0 | 12 | 0.5 |
| 22 | | 2 | 1 | 0 | 0 | 0 | 0 | 0 | 0 | 0 | 1 | 0 | 12 | 0.5 |
| 23 | | 3 | 0 | 0 | 0 | 0 | 0 | 0 | 0 | 0 | 0 | 1 | 4 | 0.2 |
| $\langle n_i \rangle$ (Ens. avg.) | | 0.92 | 0.77 | 0.63 | 0.50 | 0.39 | 0.29 | 0.21 | 0.14 | 0.08 | 0.04 | 0.01 | 286 $\Sigma \omega_k$ | |
| $\langle n_i \rangle * \epsilon_i$ | | 0 | 0.77 | 1.26 | 1.51 | 1.57 | 1.47 | 1.26 | 0.98 | 0.67 | 0.38 | 0.14 | 10 $\Sigma \langle n_i \rangle * \epsilon_i$ | |

N=10, E=10ε

| | | | | | | | | | | | | | | |
|------------------------------------|---|-----|-----|-----|-----|-----|-----|-----|---|---|----|---|---|---|
| $k_{\omega_{max}}$ | 4 | 3 | 2 | 1 | 0 | 0 | 0 | 0 | 0 | 0 | 0 | 0 | 12,600 | 1 |
| $\langle n_i \rangle$ (Ens. avg.) | 0 | 1 | 2 | 3 | 4 | 5 | 6 | 7 | 8 | 9 | 10 | | 92378 $\Sigma \omega_k$ | |
| $\langle n_i \rangle * \epsilon_i$ | 0 | 2.6 | 2.8 | 2.1 | 1.3 | 0.7 | 0.3 | 0.1 | 0 | 0 | 0 | | 10 $\Sigma \langle n_i \rangle * \epsilon_i$ | |

N=12, E=10ε

| | | | | | | | | | | | | | | |
|------------------------------------|------|------|------|------|------|------|------|------|------|---|---|---|---|---|
| $k_{\omega_{max}}$ | 6 | 3 | 2 | 1 | 0 | 0 | 0 | 0 | 0 | 0 | 0 | 0 | 55,440 | 1 |
| $\langle n_i \rangle$ (Ens. avg.) | 6.29 | 3.14 | 1.49 | 0.66 | 0.27 | 0.10 | 0.03 | 0.01 | 0 | 0 | 0 | | 352716 $\Sigma \omega_k$ | |
| $\langle n_i \rangle * \epsilon_i$ | 0 | 3.14 | 2.98 | 1.98 | 1.09 | 0.51 | 0.20 | 0.07 | 0.02 | 0 | 0 | | 10 $\Sigma \langle n_i \rangle * \epsilon_i$ | |

It is also concluded that by the PEEP assumption, the sum of the products of the ensemble average and corresponding energy levels add up to the total energy of the system as follows

$$\sum_{i=0}^{n_\epsilon} \langle n_i \rangle * \epsilon_i = E \quad (\text{A- 2})$$

Figure A- 4 shows the trend of ensemble average of the number of particles with respect to their energy levels. It is observed that for a system with fixed total energy like $E = 10\epsilon$, increasing the number of particles forces a higher tendency for particles to sit in the ground state, with fewer particles at higher excited energy levels. With more particles in the system with fixed energy, the distributions approach each other asymptotically and show a most-probable state. There is also a crossover in the following graphs. Increasing the number of particles in a system with constant energy means that the particles have a higher tendency to fill the lower energy levels. This crossover in the graphs demonstrates the exponential trend corresponding to a large number of particles on the scale of Avogadro’s number, order 10^{23} atoms in one mole.

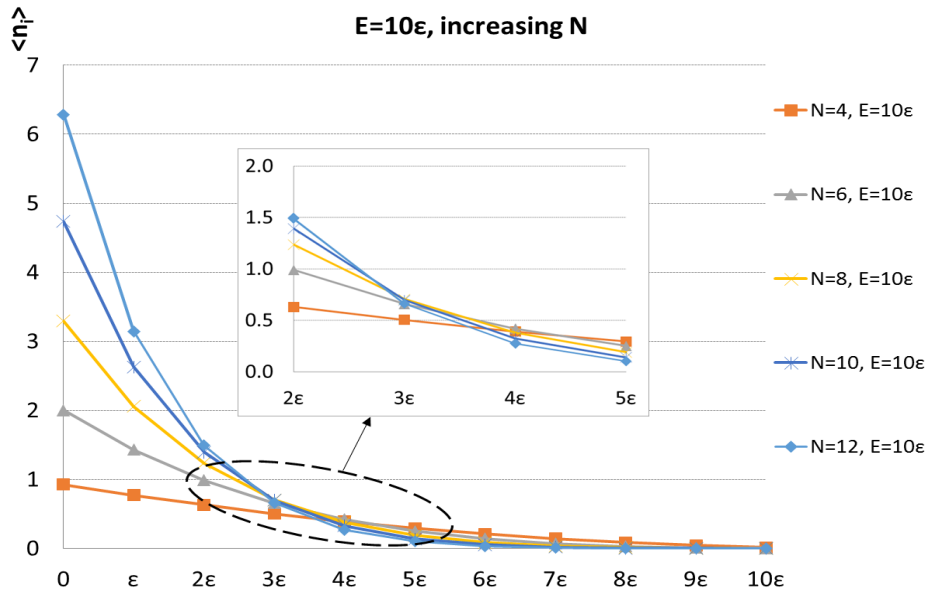


Figure A- 4: Ensemble avg. of particles distribution over energy levels, changing N for $E = 10\epsilon$

Similarly, as depicted in Figure A- 5, fixing the number of particles in the system to $N = 10$ and increasing the energy of the system, the ensemble average distribution shows a decaying exponential trend with respect to energy levels. Increasing the average energy in the system shows a subtle crossover of the distributions. For a fixed N , the higher the energy level, the more room there is for particles to

be at more-excited energy levels. As a result, they migrate to higher energy levels, and the number of states populated at ϵ_0 decreases.

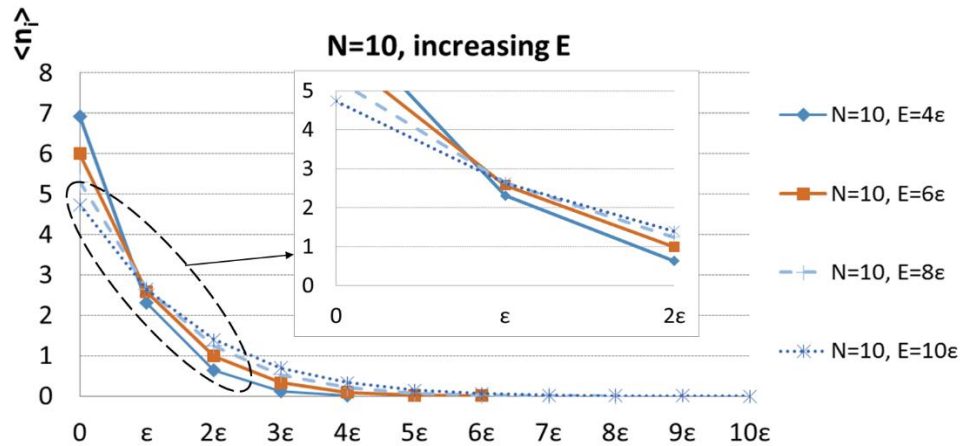


Figure A- 5: Ensemble average of particles distribution over energy levels, $N=10$, changing E

Figure A- 6 presents the trends of ω vs. $\ln\left(\frac{\omega_{max}}{\omega}\right)$ for systems with $E = 11\epsilon$ and varying in the number of particles. By increasing the number of particles, N , the most probable state becomes notably more probable and ω_{max} increases remarkably. The abscissa is condensed with a natural logarithmic function and is non-dimensionalized with respect to the most probable number of microstates. Therefore, ω of the most probable state peaks at $\ln\left(\frac{\omega_{max}}{\omega}\right) = 0$. Increasing the number of particles from $N = 4$ to 11 makes a huge difference in the number of microstates, ω , for the most probable distribution, and this tail of higher particle number systems skyrockets. In contrast, for states other than the most probable, this difference becomes insignificant.

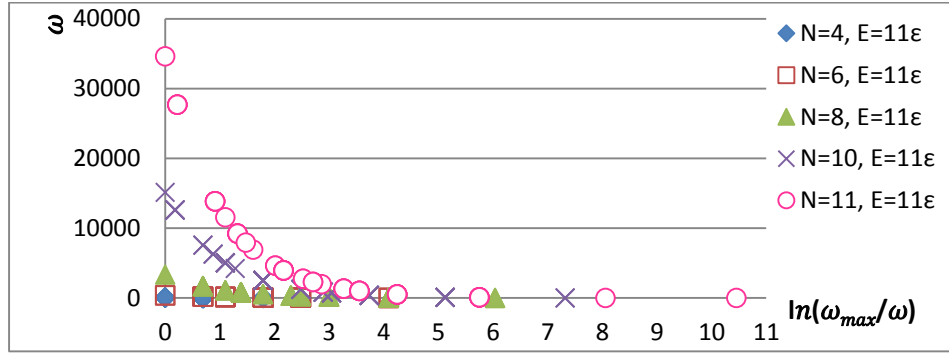


Figure A- 6: ω vs. $\ln(\frac{\omega_{max}}{\omega})$ for $N = 4$ to 11 and $E = 11\epsilon$

From the above tables and plots, it is observed that there is a most probable state which has the highest number of microstates and which represents the equilibrium state. To find the most probable state and maximize the number of microstates, the mathematical approach of Lagrangian Multipliers [21] is applied. In order to maximize ω to find the most probable state, we have to consider macroscopic order. Since the number of atoms (particles) in the system is very large, it is mathematically easier to maximize $\ln \omega$. The method used to find the maximum of a function, subjected to two homogeneous constraints, is the method of “Lagrangian Multipliers” with two homogenous constraints, which here are expressed as $N - \sum_i n_i = 0$ and $E - \sum_i n_i \epsilon_i = 0$. Having the total number of particles and the total energy of the system as two fixed constraints, the Lagrangian function is defined as

$$f(n_i, \alpha, \beta) = \ln \omega + \alpha(N - \sum_i n_i) + \beta(E - \sum_i n_i \epsilon_i) \quad (\text{A- 3})$$

Taking the homogeneous constraints as g and h , to maximize f subject to these constraints we would have $\vec{\nabla} f + \alpha \vec{\nabla} g + \beta \vec{\nabla} h = \vec{0}$, where $\nabla f = \frac{\partial f}{\partial n_i} + \frac{\partial f}{\partial \alpha} + \frac{\partial f}{\partial \beta}$, etc. In other words, in the first instance, for n_i , we have

$$\frac{\partial (\ln \omega + \alpha(N - \sum_i n_i) + \beta(E - \sum_i n_i \epsilon_i))}{\partial n_i} = 0 \quad (\text{A- 4})$$

Recalling from (A- 1) and using Stirling’s theorem [22] that, for a large N , $\ln N! \approx N \ln N - N$, which is then on the order of $e^{10^{23}} \ln(10^{23}) - 10^{23}$, the natural logarithm of the number of microstates ω becomes

$$\ln\omega = N\ln N - N - \ln\left[\prod_i n_i!\right] = N\ln N - N - \sum_i \ln n_i! \quad (\text{A- 5})$$

Substituting $\ln n!$, from Stirling's theorem, (A- 5) becomes

$$\ln\omega = N\ln N - N - \sum_i (n_i \ln n_i - n_i) \quad (\text{A- 6})$$

Using this result, (A- 4) becomes

$$\frac{\partial [N\ln N - N - \sum_i (n_i \ln n_i - n_i)]}{\partial n_i} + \frac{\partial [\alpha(N - \sum_i n_i)]}{\partial n_i} + \frac{\partial [\beta(E - \sum_i n_i \epsilon_i)]}{\partial n_i} = 0 \quad (\text{A- 7})$$

Knowing that N and E are constant due to system constraints, making their derivatives zero, and noting that summation and differentiation are interchangeable in (A- 7) one gets $\sum_i \left[\frac{\partial (n_i \ln n_i - n_i)}{\partial n_i} - \alpha - \beta \epsilon_i \right] = 0$. Finally, and taking the derivative of $n_i \ln n_i - n_i$ with respect to n_i , results in $\ln n_i + \alpha + \beta \epsilon_i = 0$, that leads to

$$n_i^{\max \omega} = \exp(-\alpha - \beta \epsilon_i) = \exp(-\alpha) \cdot \exp(-\beta \epsilon_i) \quad (\text{A- 8})$$

The number of particles for each energy level with the most-probable distribution is denoted by $n_i^{\max \omega}$; this distribution is the ‘‘Boltzmann distribution’’, with the exponential unknowns α and β . As noted relative to Table 1 above, the overall distribution is a set of n_i 's, where $n_i^{\max \omega}$ provides the state with maximum ω . Taking $A = \exp(-\alpha)$, (A- 8) becomes $n_i^{\max \omega} = A \exp(-\beta \epsilon_i)$, and considering the constraint of a constant number of particles, we get

$$N = \sum_i n_i = \sum_i A \exp(-\beta \epsilon_i) \quad (\text{A- 9})$$

Therefore by substituting $A = \exp(-\alpha)$ in (A- 9), $\exp(-\alpha) = \frac{N}{\sum_i \exp(-\beta \epsilon_i)}$, and using this result in (A- 8), $n_i^{\max \omega}$ can be expressed as

$$n_i^{\max \omega} = \frac{N \exp(-\beta \epsilon_i)}{\sum_i \exp(-\beta \epsilon_i)}, \quad (\text{A- 10})$$

which is Boltzmann distribution including the as yet unknown Lagrangian multiplier β . Defining $\sum_i \exp(-\beta \epsilon_i)$ as the partition function Z , which is a probability normalizer, the particle distribution becomes

$$n_i^{\max \omega} = \frac{N}{Z} \exp(-\beta \epsilon_i), \quad (\text{A- 11})$$

Knowing $N = \sum_i n_i$, we can rewrite (A- 6) as $\ln\omega = N\ln N - \sum_i n_i - [\sum_i n_i \ln n_i - \sum_i n_i]$, or simply as $\ln\omega = N\ln N - \sum_i n_i \ln n_i$. Then, substituting n_i from (A- 11), we get a more simplified form for $\ln\omega$:

$$\begin{aligned} \ln\omega &= N\ln N - \sum_i \left[\frac{N}{Z} \exp(-\beta\epsilon_i) \ln \frac{N}{Z} + \frac{N}{Z} \beta\epsilon_i \exp(-\beta\epsilon_i) \right] \\ &= N\ln N - \sum_i \frac{N}{Z} \exp(-\beta\epsilon_i) \ln \frac{N}{Z} + \beta \sum_i \frac{N}{Z} \epsilon_i \exp(-\beta\epsilon_i) \end{aligned} \quad (\text{A- 12})$$

Similarly, taking the second constraint for E into account and replacing n_i , we would have

$$E = \sum_i n_i \epsilon_i = \sum_i \epsilon_i \frac{N}{Z} \exp(-\beta\epsilon_i) \quad (\text{A- 13})$$

which can be recognized as being multiplied by β in the last term of (A- 12). Therefore, $\ln\omega = N\ln N - \left[\ln N - \ln Z \right] \sum_i \left[\frac{N}{Z} \exp(-\beta\epsilon_i) \right] + \beta E$. The term $\frac{N}{Z} \exp(-\beta\epsilon_i)$ is just n_i so the sum is just N . Thus,

$\ln\omega = N\ln N - N\ln N + N \ln Z + \beta E$, which simplifies to (A- 14):

$$\ln\omega = N \ln Z + \beta E \quad (\text{A- 14})$$

To solve equation (A- 8) for $n_i^{\max\omega}$, α and β are required with α given in terms of β . To find β , we use the parallel with classical Thermodynamics for our system from a macroscopic view with a differential change in energy through energy transfer as heat. Based on what was stated in section 2.1 for the system conditions, and from the first law of thermodynamics for our system with heat transfer and no work, $dE = dQ$, When the system is in mechanical and thermal equilibrium with the surrounding, any reversible heat transfer is given by $dQ = Tds$; thus, the change in entropy is $dS = dQ/T$ which, for our system, also translates to $ds = dE/T$. If we associate $\ln\omega$ with entropy, i.e. $S = k\ln\omega$, since the premise of Eqn. (A- 7) was that to maximize $\ln\omega$ to find the equilibrium state was equivalent to maximizing entropy, then

$$dS = kd(\ln\omega) = k\beta dE = \frac{dE}{T} \quad (\text{A- 15})$$

From this, $\beta = \frac{1}{kT}$, and where k is a constant whose value should be defined and β , our Lagrangian multiplier for the energy constraint, becomes $\beta = \frac{1}{kT}$. The constant k is the Boltzmann constant K_B and

is equal to $1.38 * 10^{-23}$ [J/molecule.K]. Solving for β and going back to (A- 10), we achieve the Boltzmann Distribution

$$n_i^{\max \omega} = N \frac{\exp\left(-\frac{\epsilon_i}{K_B T}\right)}{\sum_i \exp\left(-\frac{\epsilon_i}{K_B T}\right)} \quad (\text{A- 16})$$

s discussed, the ion distribution in the electric double layer is given by the Boltzmann distribution. With the presence of the co-/counter ions in EDL and by applying the fundamentals of probability, this distribution was achieved.

Further, to find the electric potential distribution, Poisson's equation should be solved in two regions, the EDL and the bulk flow. This equation comes from fundamental Physics: Coulomb's law, and is developed in the following.

Poisson Equation - Electric Potential Distribution

According to Coulomb, one can measure the electric force between two point charges, q_1 and q_2 , which are located at \vec{r}_1 and \vec{r}_2 from the origin respectively with a displacement of $(\vec{r}_2 - \vec{r}_1)$ between each other. The electric force between two point charges can be expressed as $\vec{f}_2 = -\vec{f}_1 = \frac{q_1 q_2}{4\pi\epsilon_0} \frac{(\vec{r}_2 - \vec{r}_1)}{|\vec{r}_2 - \vec{r}_1|^3}$. Based on the electric force of Coulomb's law, the electric field at q_2 is defined as $\vec{E} = \frac{\vec{f}}{q_2}$.

. For a single point charge, q_1 , the electric field $\vec{E}_q(r) = \frac{q_1}{4\pi\epsilon_0 r^2} \frac{\vec{r}}{|\vec{r}|}$ would be radial with outwards direction for a positive charge. Coulomb's law also substantiates that there is no tangential force between a point-charge and surrounding test charges, i.e., the electric force between every two single charges is in the direction of $\vec{r} = \vec{r}_2 - \vec{r}_1$. Moreover, no circulation is observed in the electric field. Therefore, the curl of the electric field is equal to zero; $\vec{\nabla} \times \vec{E} = 0$. Mathematically, it is shown that in spherical coordinates, the curl of an electric field of a point charge equals zero

$$\vec{\nabla} \times \vec{E} = \begin{vmatrix} \hat{e}_r & \hat{e}_\theta & \hat{e}_\varphi \\ r^2 \sin \theta & r \sin \theta & r \\ \frac{\partial}{\partial r} & \frac{\partial}{\partial \theta} & \frac{\partial}{\partial \varphi} \\ \vec{E}_r & r \vec{E}_\theta & r \sin \theta \vec{E}_\varphi \end{vmatrix} = \begin{vmatrix} \hat{e}_r & \hat{e}_\theta & \hat{e}_\varphi \\ r^2 \sin \theta & r \sin \theta & r \\ \frac{\partial}{\partial r} & \frac{\partial}{\partial \theta} & \frac{\partial}{\partial \varphi} \\ \frac{q_1}{4\pi\epsilon_0 r^2} & 0 & 0 \end{vmatrix} = 0 \quad (\text{A- 17})$$

As a vector property, it is known that the curl of the gradient of any function, ϕ , is zero, i.e., $\vec{\nabla} \times (\vec{\nabla}\phi) = 0$. Thus, the electric field can be described as the gradient of a scalar function with an associated and arbitrary negative sign as $\vec{E} = -\vec{\nabla}\phi$. Also, Stokes' theorem, a fundamental vector calculus theorem, states that the integral of the curl of a vector field over a surface is equal to the cyclic (line) integral of that vector field over the surface boundaries, $\iint_A \vec{\nabla} \times \vec{E} \, dA = \oint \vec{E} \cdot \vec{dl}$. Since the curl of any electric field equals zero, we have $\vec{\nabla} \times \vec{E} = 0$, and thus $\oint \vec{E} \cdot \vec{dl} = 0$ which leads to $\oint \vec{\nabla}\phi \cdot \vec{dl} = 0$. This contour integral is independent of the path, so the integral between any two points A and B yields $\int_A^B \vec{\nabla}\phi \cdot \vec{dl} = \phi(B) - \phi(A)$. ϕ is the electric potential which is proportional to the electric potential energy for moving a point charge from point A to B and has the units of "Joules per coulomb" or "Volt". Therefore, the electric field is known as the negative of the gradient of the electric potential.

According to Gauss's law, the integral of an electric field over a closed surface is proportional to the total charge within that surface and it shows the electric field flux. The integral $\oint \vec{E} \cdot \vec{ds}_r$ is examined for a single point charge dq (not the total charge), in a region with permittivity ϵ at any distance from the charge and on an element with an area normal vector of \vec{ds}_r along \vec{r} .

Substituting the left hand side of Gauss's law by the definition of \vec{E} based on Coulomb's law, we get

$$\oint \vec{E}_{dq} \cdot \vec{ds}_r = \oint \frac{dq}{4\pi\epsilon r^2} \hat{r} \cdot \vec{ds}_r \quad (\text{A- 18})$$

For spherical coordinates, (A- 18) can be rewritten as $\oint \vec{E}_{dq} \cdot \vec{ds}_r = \iint_V \vec{\nabla} \cdot \vec{E}_{dq} dv$ using $\vec{ds}_r = ds \hat{r}$ which leads to $\iint_V \vec{\nabla} \cdot \vec{E}_{dq} dv = \frac{dq}{\epsilon}$, that is indeed another form of Gauss's law. Implementing the distribution of charges with a total Charge Q , where $Q = \iint_V dq_i$ with dq_i representing a point charge dq_i , Gauss's law becomes $\iint_V \vec{\nabla} \cdot \vec{E}_{dq} dv = \frac{dq_i}{\epsilon}$. To attain the electric field for the total charge Q , by integrating over all charges, we get

$$\iint_Q \left(\iint_V \vec{\nabla} \cdot \vec{E}_{dq} dv \right) dq_i = \iint_Q \frac{1}{\epsilon} dq_i \quad (\text{A- 19})$$

Since dv and dq_i are mutually independent, the order of integrations with respect to dv and dq_i are interchangeable; further, the divergence operation is independent of the integration with respect to

charge. Finally, the electric field for the collection of charges is expressed as the sum of those, resulting from point charges, i.e. $\vec{E}_Q = \iint_Q \vec{E}_{dq} dq_i$; therefore

$$\iint_V \vec{\nabla} \cdot \vec{E}_Q dv = \iint_Q \frac{1}{\epsilon} dq_i \quad (\text{A- 20})$$

Using the electric charge density, $\rho_e = \frac{dq_i}{dv}$ in (A- 20) yields

$$\iint_V \vec{\nabla} \cdot \vec{E}_Q dv = \iint_V \frac{\rho_e}{\epsilon} dv \quad (\text{A- 21})$$

Equation (A- 21) is applicable to any arbitrary volume, V , including a differential volume dv , thus, the integrands must be equal, i.e. $\vec{\nabla} \cdot \vec{E}_Q = \frac{\rho_e}{\epsilon}$. Implementing $\vec{E} = -\vec{\nabla}\psi$, leads to **Poisson's equation**: $\nabla^2\psi = -\frac{\rho_e}{\epsilon}$ in electric double layer. It is very important to differentiate between the applied potential ϕ and the potential among ions in EDL. Patankar and Hu [9], explained very well when the EDL thickness is small and the charge at the walls is not large, the distribution of ions is governed mainly by the surface potential at the wall and is affected very little by the external electric field. Thus, the charge distribution near the walls can be determined independent of the external electric field. The charge distribution may be affected by fluid motion since the charged species convect with the flow. However, the effect of fluid motion on the charge redistribution can be neglected when the fluid velocity is small. That's why the electric field equations and the fluid flow equations can be decoupled, and the total potential can be decomposed into a potential due to the external electric field, ϕ , and a potential due to the charge at the walls, ψ . For the special case, where the charge density ρ_e is zero, this gives Laplace's equation, $\nabla^2\phi = 0$. This occurs over most of the domain in a microchannel because the electric double layer is so thin and confined to the surface.

As provided before, the Boltzmann distribution for ions in the electric double layer is presented in (A- 16). The Boltzmann distribution and Poisson's equation are combined together to achieve the Poisson-Boltzmann equation as will be described in the following section.

Poisson Boltzmann Equation

One part of the Poisson-Boltzmann equation is Poisson's equation as derived in the foregoing and the other part is the Boltzmann distribution, derived earlier, above, to provide the electric charge and ion distribution in the electric double layer in microchannels. A clear understanding of the ion distribution was provided in section 2.3. It was clearly discussed that for a system subjected to two

constraints of $N - \sum_i n_i = 0$ and $E - \sum_i n_i \epsilon_i = 0$, the particle distribution was found in terms of β , ($\beta = \frac{1}{K_B T}$), by implementing the Lagrange multiplier approach, as $\frac{n_i^{\max \omega}}{N} = \frac{\exp(-\beta \epsilon_i)}{\sum_i \exp(-\beta \epsilon_i)}$.

According to the “Callen” postulates, (1985) [23], for a system with internal energy U , volume V and n_i number of species or ions, a function called entropy S , exists in terms of extensive parameters U, V and n_i , and is defined for all equilibrium states. The values assumed by the extensive parameters are those which maximize the entropy for the composite isolated system. Therefore, the internal energy of the system is $U = U(S, V, N_i)$. From the first law of thermodynamics, $dU = dQ + dW$, for a system with chemical components and charged particles, we have chemical and electrical energies and the work done $dW = -PdV$, therefore

$$dU = dQ + \underbrace{\{\sum_i \mu_i dn_i\}}_{\text{Chem.Pot.E}} + \underbrace{\{\sum_i \psi z_i e dn_i\}}_{\text{Elec.Pot.E}} - \underbrace{\{PdV\}}_{\text{Mech.work}} = dQ + \underbrace{\{\sum_i (\mu_i + \phi z_i e) dn_i\}}_{\text{Electrochemical.Pot.E}} - \underbrace{\{PdV\}}_{\text{Mech.work}} \quad (\text{A- 22})$$

From the second law of thermodynamics for a reversible process, $dQ = Tds$. At equilibrium no chemical reaction happens, and no mass or heat transfer occurs through the system boundaries; no work is done and no entropy is produced in the system. By combining the chemical and electric energies in (A- 22), as shown, the electro-chemical potential for the i^{th} species emerges as $\tilde{\mu}_i = \mu_i + z_i e \psi$. In equilibrium, the electrochemical potential must be uniform everywhere; therefore, the electrostatic forces which move the charges by electric field forces balance the energy changes by diffusion. In other words, in equilibrium, the gradient of the electro-chemical potential for each species is zero, i.e. $d\tilde{\mu}_i = 0$ or

$$d\mu_i = -Z_i e d\psi \quad (\text{A- 23})$$

The chemical potential is defined as $\mu_i = dU/dn_i$, and according to the first law of thermodynamics for a reversible process with no work, $du = Tds$, therefore $\mu_i = T \frac{ds}{dn_i}$. From our discussions on the Boltzmann distribution, $s = K_B \ln \omega$ and also from (A- 6), $ds_i = -K_B d(\ln n_i)$, thus

$$d \ln n_i = -\frac{Z_i e}{K_B T} d\psi \quad (\text{A- 24})$$

By integrating over the region, $\int_{n_i(x)}^{n_{i,mean}} d(\ln n_i) = -\frac{Z_i e}{K_B T} \int_{\psi(x)}^{\psi_{mean}} d\psi$, therefore, $\frac{n_{i,x}}{n_{i,mean}} = \exp[-\frac{Z_i e}{K_B T} (\psi(x) - \psi_{mean})]$. Assuming $\psi_{mean} = 0$ in the absence of an applied electric field, and $(x) = \psi$, then $n_i = n_{i,mean} \exp(\frac{-Z_i e \psi}{K_B T})$. In practice though, ionic concentration is

considered rather than the number of particles. Therefore, introducing the solution molar concentration $C_i = \frac{n_i}{V}$, results in $c_i(z) = c_i^0 \exp(-\frac{ze\psi}{K_B T})$. The anions and cations are respectively derived as

$$c^- = c_0 \exp\left(\frac{ze\psi}{K_B T}\right), \quad c^+ = c_0 \exp\left(-\frac{ze\psi}{K_B T}\right) \quad (\text{A- 25})$$

where c_0 and z are the mean ionic number concentration in the bulk flow and the ion valence, respectively. The electron charge is denoted by e , the absolute temperature is T , and K_B is the Boltzmann constant. Assuming a two-species symmetric electrolyte solution with two oppositely charged ions like Na^+ and Cl^- in a $NaCl$ solution, $z^+ = z^- = z$ and $c^+ = c^- = c_0$, the net charge density from the Boltzmann distribution becomes $\rho_e = ze(c^+ - c^-) = -2zec_0 \sinh\left(\frac{ze\psi}{K_B T}\right)$.

Substituting ρ_e from the Poisson's equation we have $\nabla^2\psi = -\frac{\rho_e}{\epsilon}$ and this leads to the Poisson-Boltzmann equation

$$\nabla^2\psi = \frac{2zec_0}{\epsilon} \sinh\left(\frac{ze\psi}{K_B T}\right) \quad (\text{A- 26})$$

In a more general case of having more than two oppositely charged ions in a symmetric electrolyte, we have: $\nabla^2\psi = \frac{-1}{\epsilon} \sum_{i=1}^N c_i^0 z_i e \exp\left(-\frac{z_i e\psi}{K_B T}\right)$, where c_i^0 is the mean concentration of charges. Using a Taylor series expansion for the exponential term and assuming the system's electrical energy is much less than its thermal energy, i.e., $e\psi \ll K_B T$, one can approximate

$$\exp\left(-\frac{z_i e\psi}{K_B T}\right) \approx 1 - \frac{z_i e\psi}{K_B T} \quad (\text{A- 27})$$

This linear approximation linearizes the Poisson-Boltzmann equation in the form of

$$\nabla^2\psi = \sum_{i=1}^N \frac{c_i^0 z_i^2 e^2}{\epsilon K_B T} \psi - \frac{1}{\epsilon} \sum_{i=1}^N c_i^0 z_i e \quad (\text{A- 28})$$

For electrically neutral systems, the second term on the right hand side of (A- 28) vanishes and the coefficient of the electric potential in the first term becomes the inverse of the length scale known as

the Debye-Hückel Length, $\lambda_D = \left(\frac{\sum_{i=1}^N c_i^0 z_i^2 e^2}{\epsilon K_B T}\right)^{-0.5}$. Implementing the definition of λ_D , the linearized form of the Poisson-Boltzmann equation becomes

$$\nabla^2\psi = \frac{1}{\lambda_D^2}\psi \quad (\text{A- 29})$$

The Poisson-Boltzmann equation must be solved to determine the electric potential ψ and the net charge density ρ_e . Solutions of the Poisson-Boltzmann equation are available in the literature, based on different approximations. For a symmetric electrolyte and a sample concentration in the order of $10^{-6}\sim 10^{-2}$ [$\frac{mol}{L}$], λ_D becomes on the order of $300\sim 3$ [nm]. Indeed, $\lambda_D \propto (\Sigma c_i)^{-0.5}$ and plays an important role in the thickness of the EDL. The distribution of ions in the EDL, is dependent on $c_i^0, z_i e, \epsilon, K_B$ and T , and is independent of any electric field applied parallel to the EDL. This derivation, valid for any situation without an externally applied electric field, leads us to find ion distribution for many cases. The present derivation presents a fundamental Boltzmann distribution derivation and is valid for ion distribution in the EDL; it also enhances our understanding of the Boltzmann distribution and assists in furthering microfluidic electroosmotic and electrophoretic research, understanding, and progress. It also provides a guide future research on how to proceed to clarify problems, solve the Poisson-Boltzmann equation, and apply this understanding for different boundary conditions, including overlapping EDL's.

So far, we showed that the distribution of the ions in the electric double layer in a microchannel is provided through the derivation of the Boltzmann distribution. Considering ions as point charges, and using probability concepts for a system subject to constraints of constant number of particles, and constant energy, the distribution of charges is determined as the Boltzmann distribution. For a detailed derivation of the ion distribution in the EDL, a statistical thermodynamics approach is used for implementing the mathematical method of Lagrangian multipliers. It is clearly shown that for systems subject to two constraints of constant number of particles and constant total system energy, there is one most probable state having the highest probability, corresponding to the highest number of microstates. The relevance of the most probable state, with the highest number of microstates, and the system being in an equilibrium state is thoroughly studied, and our findings regarding the number of microstates for systems with various specific numbers of particles and energy are illustrated graphically. Further, it is shown that, for a system with a fixed total energy, adding more particles to the system brings a tendency for higher particle distribution in the ground state and fewer particles distributed in the higher excited energy levels. These results have been graphically illustrated, showing a cross-over in the graphs for the ensemble average. Moreover, it is shown that the ensemble average is very close, quantitatively, to the most probable distribution of the number of particles in each energy level. For the most probable

states, the number of microstates asymptotically increases as the number of particles in the system increases; for molar scales of solution on the order of Avogadro's number, 10^{23} atoms, the most probable state becomes an almost certainty. Systems with fixed numbers of particles and changing total energies are studied. In addition to the overall distribution of particles, it is observed that particles migrate to higher energy levels when the total energy of the system is increased. The most probable state is that for which the ensemble average and the number of microstates asymptotically increases, and the associated probability is remarkably higher than the other states which are much less probable. Since not much research has been done on theoretical microfluidics, especially on the ion distribution, the current chapter provides a thorough understanding and comprehensive derivation of the Boltzmann distribution; this is not available in the microfluidic literature at one place. By using Coulomb's law, further studies are done on the potential distribution in microchannels. Through classical thermodynamics, in addition to statistical thermodynamics, the entropy of an isolated system in equilibrium is maximized. For a symmetric electrolyte solution with oppositely charged ions, the Boltzmann distribution provides the net charge density. The roles of the solution concentration and electrochemical-potential are both addressed in this article. By combining the Boltzmann distribution derivation and the Poisson equation derivation, together, a comprehensive understanding of the Poisson-Boltzmann equation, and its influence, is achieved. It is worth mentioning the assumptions and approximations implemented in Poisson-Boltzmann equation such as considering ions as point charges or neglecting the electric energy of the system which is much less than its thermal energy. The electrolyte is also assumed to be a symmetric solution and the non-electrostatic interactions between the ions are neglected as well. Because of its good agreement with experiments, Poisson-Boltzmann equation is yet applied as a key governing equation in many situations.

Solutions to Poisson-Boltzmann equation

In previous sections we showed the derivation of the Poisson-Boltzmann equation. Our objective in this section is to solve this equation, in order to find the electric potential distribution in an electric double layer as well as bulk flow region in the microchannel. Knowing electric potential distribution, then according to Poisson's equation, we would find geometric distribution of ions. Then we can move on to fluid mechanics and implement both ρ_e and \vec{E} terms into our body force term in Navier-Stokes

equation, which will be discussed in the next chapter. Solutions of the Poisson-Boltzmann equation started from analytical solutions in complete form or simplified forms based on approximations and more complete solutions have been done by the help of numerical methods. It is good to mention that for a general electrolyte (not a symmetric one); Poisson-Boltzmann equation has no analytical solution and has to be solved numerically.

In the Poisson equation mentioned, i.e., $\nabla^2\psi = -\frac{\rho_e}{\epsilon}$, where by assuming a symmetric electrolyte of equal valence, our net charge density was substituted and resulted in the Poisson-Boltzmann equation as $\nabla^2\psi = \frac{2zec_0}{\epsilon} \sinh\left(\frac{ze\psi}{K_B T}\right)$ which is rewritten as:

$$\nabla^2\psi^* = \beta \sinh(\alpha\psi^*) \quad (\text{A- 30})$$

Where, $\psi^* = \frac{\psi}{\zeta}$ and α is the ionic energy parameter given by:

$$\alpha = \frac{ez\zeta}{K_B T} \quad (\text{A- 31})$$

Having zeta potential of 25.4 mV at 20°C , gives us $\alpha = 1$, and β is defined as:

$$\beta = \frac{(w/\lambda_D)^2}{\alpha} \quad (\text{A- 32})$$

Where, λ_D refers to the Debye-Hückel length and w is the half-channel width. Therefore by non-dimensionalizing as $y^* = \frac{y}{w}$, (A- 30) becomes:

$$\frac{d^2\psi^*}{dy^{*2}} = \beta \sinh(\alpha\psi^*) \quad (\text{A- 33})$$

Multiplying both sides of (A- 33) by $2 \frac{d\psi^*}{dy^*}$, results in:

$$\frac{d}{dy^*} \left[\left(\frac{d\psi^*}{dy^*} \right)^2 \right] = 2\beta \frac{d\psi^*}{dy^*} \sinh(\alpha\psi^*) \frac{d\psi^*}{dy^*} \quad (\text{A- 34})$$

Integrating two sides of (A- 34) w.r.t y^* , we obtain:

$$\left(\frac{d\psi^*}{dy^*} \right)^2 = \frac{2\beta}{\alpha} \cosh(\alpha\psi^*) + C'_1 \quad (\text{A- 35})$$

where C'_1 is the integration constant.

Knowing ψ_c^* from boundary conditions that at the center of channel, i.e., $y^* = 1$, $\frac{d\psi^*}{dy^*} = 0$, then constant C'_1 becomes $C'_1 = \frac{-2\beta}{\alpha} \cosh(\alpha\psi_c^*)$ and (A- 35) becomes

$$\frac{d\psi^*}{dy^*} = \sqrt{\frac{2\beta}{\alpha}} (\cosh(\alpha\psi^*) - \cosh(\alpha\psi_c^*))^{0.5} \quad (\text{A- 36})$$

Rewriting (A- 36)

(A- 36) based on separation of variables we get:

$$\frac{d\psi^*}{(\cosh(\alpha\psi^*) - \cosh(\alpha\psi_c^*))^{0.5}} = \sqrt{\frac{2\beta}{\alpha}} dy^* \quad (\text{A- 37})$$

Applying half-angle argument, we get:

$$\frac{d(\alpha\psi^*/2)}{(\cosh^2(\frac{\alpha\psi^*}{2}) - \cosh^2(\frac{\alpha\psi_c^*}{2}))^{0.5}} = \sqrt{2} (\mathbf{w}/\lambda_D) dy^* \quad (\text{A- 38})$$

As Burgreen and Nakache showed in [5], integrating left hand side of (A- 38) would result in an analytical solution in form of an incomplete elliptic integral of first kind and Non-dimensionalized electric potential distribution becomes $\psi^*(y^*) = F(\theta, k)$, where F is defined mathematically. Using this solution is kind of cumbersome because it is only available in tabular form. Moreover, they provided both variables of integration ϕ^* and parameters θ, k dependent on variable of integration, which is not clear. Therefore, simplified solutions were required to solve Poisson-Boltzmann equation.

Simplified Approximate Solution to Poisson-Boltzmann equation

As expressed above, instead of finding the incomplete elliptic integral of first kind for analytical solution two more simplified solutions to P-B equation are available:

- Dutta-Beskok solution
- Debye-Hückel approximation

The assumptions and approximations for each solution are explained in detail below.

Dutta-Beskok simplification

To simplify the complicated analytical solution by Burgreen et al. [5], Dutta and Beskok [125] showed a simpler solution for electric potential distribution. They assumed for $\alpha \geq 1$ and $\lambda_D \ll w$, the electric potential at the center of the channel is practically zero; $\psi_c^* \rightarrow 0$, by integrating (A- 37), then

$$\int_{\psi^*=1}^{\psi^*=0} \frac{d\psi^*}{[\cosh(\alpha\psi^*) - \cosh(\alpha\psi_c^*)]^{0.5}} = \sqrt{\frac{2\beta}{\alpha}} \int_0^1 dy^* \quad (\text{A- 39})$$

Assuming zero potential at the center of channel, i.e., $\psi_c^* = 0$, and by applying the trigonometric identity of $\cosh(t) = 2 \sinh^2\left(\frac{t}{2}\right) + 1$, the denominator turns into $(2\sinh^2\left(\frac{\alpha\psi^*}{2}\right) + 1 - 1)^{0.5}$, then

$$\int_{\psi^*=1}^{\psi^*=0} \frac{d\psi^*}{(2\sinh^2\left(\frac{\alpha\psi^*}{2}\right))^{0.5}} = \sqrt{\frac{2\beta}{\alpha}} \int_0^1 dy^* \quad (\text{A- 40})$$

which is rewritten as

$$\int_{\psi^*=1}^{\psi^*=0} \frac{d\psi^*}{\sinh\left(\frac{\alpha\psi^*}{2}\right)} = 2 \sqrt{\frac{\beta}{\alpha}} \int_0^1 dy^* \quad (\text{A- 41})$$

and by knowing $\int \frac{dt}{\sinh(t)} = \ln\left(\tanh\left(\frac{t}{2}\right)\right) + \text{constant}$, then

$$\ln\left(\tanh\left(\frac{\alpha}{4}\psi^*\right)\right) = -\sqrt{\alpha\beta}y^* + C_1 \quad (\text{A- 42})$$

Or:

$$\tanh\left(\frac{\alpha}{4}\psi^*\right) = \exp(-\sqrt{\alpha\beta}y^* + C_1) \quad (\text{A- 43})$$

Applying the boundary condition at the wall, $y^* = 0$ where $\psi^* = 1$, then $C_1 = \log\left(\tanh\left(\frac{\alpha}{4}\right)\right)$, so we

would have $\tanh\left(\frac{\alpha}{4}\psi^*\right) = \exp(-\sqrt{\alpha\beta}y^* + \log\left(\tanh\left(\frac{\alpha}{4}\right)\right))$ or

$\tanh\left(\frac{\alpha}{4}\psi^*\right) = \tanh\left(\frac{\alpha}{4}\right) \exp(-\sqrt{\alpha\beta}y^*)$; Therefore

$$\psi^*(y^*) = \frac{4}{\alpha} \tanh^{-1}\left(\tanh\left(\frac{\alpha}{4}\right) \exp(-\sqrt{\alpha\beta}y^*)\right) \quad (\text{A- 44})$$

Moreover in near wall region, knowing $\sqrt{\alpha\beta} = \frac{w}{\lambda_D}$ and applying a new variable $\chi = \sqrt{\alpha\beta}y^*$ as a near-wall scaling parameter named inner-layer scale potential distribution turns into

$$\psi^*(y^*) = \frac{4}{\alpha} \tanh^{-1} \left[\tanh \left(\frac{\alpha}{4} \right) \exp(-\chi) \right] \quad (\text{A- 45})$$

when we have $\tanh \left(\frac{\alpha}{4} \right) \leq 1$ and $\exp(-\chi) \ll 1$, then (A- 45) would turn to

$$\psi^*(y^*) \approx \frac{4}{\alpha} \tanh \left(\frac{\alpha}{4} \right) \exp(-\chi) \quad (\text{A- 46})$$

Debye-Hückel Approximation

As previously shown, analytical solution to Poisson-Boltzmann equation is so complicated. The second approach was based on Dutta and Beskok assumptions for the zeta potential and EDL thickness. The third approach for simplifying the solution to the nonlinear Poisson-Boltzmann equation is using linearized Debye-Hückel approximation. Solving P-B equation for a symmetric electrolyte, $\nabla^2 \psi = \frac{z z e c_0}{\epsilon} \sinh \left(\frac{z e \psi}{K_B T} \right)$, is not convenient because of its nonlinear term. So, for small potentials which make electric potential term much smaller than thermal term at $\sinh \left(\frac{z e \psi}{K_B T} \right)$, then there would be a linear approximation of Poisson-Boltzmann equation assuming $\sinh \left(\frac{z e \psi}{K_B T} \right) = \frac{z e \psi}{K_B T}$. Debye-Hückel length λ_D as problem length scale is $\lambda_D = \left(\frac{\sum_i e^2 z_i^2 n_i}{\epsilon K_B T} \right)^{-1/2}$ and comes from equal electrokinetic energy and thermal energy. By applying this approximation, P-B equation becomes

$$\nabla^2 \psi = \lambda_D^{-2} \psi \quad (\text{A- 47})$$

Considering 1-D case, $\frac{d^2 \psi}{dy^2} - \frac{1}{\lambda_D^2} \psi = 0$ results in

$$\psi(y) = A \exp \left(\frac{y}{\lambda_D} \right) + B \exp \left(-\frac{y}{\lambda_D} \right) \quad (\text{A- 48})$$

And by applying the boundary conditions of zeta potential at wall surfaces for η coordinate system which is at the center of channel as $\psi(\pm w) = \zeta$, we get $A = B = \frac{\zeta}{2 \cosh \left(\frac{w}{\lambda_D} \right)}$. Accordingly by knowing

exponential identities of $\sinh \left(\frac{w}{\lambda_D} \right)$ and $\cosh \left(\frac{w}{\lambda_D} \right)$ finally:

$$\psi(\eta) = A \exp \left(\frac{\eta}{\lambda_D} \right) + B \exp \left(-\frac{\eta}{\lambda_D} \right) \quad (\text{A- 49})$$

which finally results in:

$$\psi(\eta) = \zeta \frac{\cosh\left(\frac{\eta}{\lambda_D}\right)}{\cosh\left(\frac{w}{\lambda_D}\right)} \quad (\text{A- 50})$$

Assuming ζ potential @ $y = 0$ and $\phi \rightarrow 0$ @ $y \rightarrow \infty$, then by knowing $y = w - \eta$ we would have

$$\psi(y) = \zeta \frac{\cosh\left(\frac{w-y}{\lambda_D}\right)}{\cosh\left(\frac{w}{\lambda_D}\right)}$$

and by cosh identities of $\cosh(a - b) = \cosh a \cosh b - \sinh a \sinh b$, we get:

$$\psi(y) = \zeta \frac{\cosh \frac{w}{\lambda_D} \cosh \frac{y}{\lambda_D} - \sinh \frac{w}{\lambda_D} \sinh \frac{y}{\lambda_D}}{\cosh\left(\frac{w}{\lambda_D}\right)} \quad (\text{A- 51})$$

As shown in Table A- 2, for $\frac{w}{\lambda_D} \gg 1$, $\cosh \frac{w}{\lambda_D} = \sinh \frac{w}{\lambda_D}$, but still we are very close to the wall in order of $10^{-6} \sim 10^{-8} m$.

Table A- 2: Example of showing values for cosh(x) and sinh(x)

| $x = y/\lambda_D$ | Approx. y (m) | cosh(x) | sinh(x) | cosh(x)-sinh(x) | $d^2(\cosh(x)-\sinh(x))/d^2x$ |
|-------------------|--------------------|-----------|-----------|-----------------|-------------------------------|
| 0 | 0 | 1 | 0 | 1 | 0.3995764 |
| 1 | 1.00E-08 | 1.5430806 | 1.1752012 | 0.3678794 | 0.1740343 |
| 2 | 2.00E-08 | 3.7621957 | 3.6268604 | 0.1353353 | 0.0252957 |
| 4 | 4.00E-08 | 27.308233 | 27.289917 | 0.0183156 | 0.0036551 |
| 6 | 6.00E-08 | 201.71564 | 201.71316 | 0.0024788 | 0.0001498 |
| 10 | 1.00E-07 | 11013.233 | 11013.233 | 4.54E-05 | 1.79E-06 |
| 15 | 1.50E-07 | 1634508.7 | 1634508.7 | 3.06E-07 | 1.22E-08 |
| 20 | 2.00E-07 | 242582598 | 242582598 | 0 | 0 |
| 50 | 5.00E-07 | 2.59E+21 | 2.59E+21 | 0 | 0 |
| 100 | 1.00E-06 | 1.34E+43 | 1.34E+43 | 0 | 0 |
| 500 | 5.00E-06 | 7.02E+216 | 7.02E+216 | 0 | 0 |

The last column of above table shows us the pace of change in potential and to solve the governing

equations, we will use this column for scaling $\nabla^2 \psi$. Therefore, $\psi(y) = \zeta (\cosh \frac{y}{\lambda_D} - \sinh \frac{y}{\lambda_D})$.

If we want to use exponential form as an easier form, this equation would be rewritten as

$$\psi(y) = \zeta e^{-\frac{y}{\lambda_D}} \quad (\text{A- 52})$$

The three different approaches to solve Poisson-Boltzmann equation are shown in Table A- 3.

Table A- 3: Analytical and simplified solutions of Poisson-Boltzmann equation

| P-B equation solutions | Assumption | Solution |
|--------------------------|---|--|
| Burgreen and Nakache [5] | @ $y^* = 1$, $\frac{d\psi^*}{dy^*} = 0$ | incomplete elliptic integral of first kind $\frac{d(\alpha\psi^*/2)}{(\cosh^2(\frac{\alpha\psi^*}{2}) - \cosh^2(\frac{\alpha\psi^*}{2}))^{0.5}}$ $= \sqrt{2} (w/\lambda_D) dy^*$ |
| Dutta and Beskok [126] | @ $y^* = 1$, $\psi_c^* \rightarrow 0$ $\exp(-\sqrt{\alpha\beta}y^*) \ll 1$ $\tanh\left(\frac{\alpha}{4}\right) \leq 1$ $\sqrt{\alpha\beta} = \frac{w}{\lambda_D}$, $\frac{w}{\lambda_D} \gg 1$ | $\psi^*(y^*)$ $= \frac{4}{\alpha} \tanh^{-1} \left(\tanh\left(\frac{\alpha}{4}\right) \exp(-\sqrt{\alpha\beta}y^*) \right)$ $\psi^*(y^*) \approx \frac{4}{\alpha} \tanh\left(\frac{\alpha}{4}\right) \exp(-\sqrt{\alpha\beta}y^*)$ $(\psi^*(y^*) \approx e^{-\frac{w}{\lambda_D}y^*})$ |
| Debye-Hückel | $\sinh\left(\frac{ze\psi}{K_B T}\right) \cong \frac{ze\psi}{K_B T}$ $\frac{w}{\lambda_D} \gg 1$ $\cosh\frac{w}{\lambda_D} = \sinh\frac{w}{\lambda_D}$ $\frac{w}{\lambda_D} \gg 1$ | $\psi(y) = \zeta e^{-\frac{y}{\lambda_D}}$ |

So, from above three solutions to P-B equation providing same results, we take the exponential form, based on Debye-Hückel approximation, which is much easier to deal with. To quantify where the edge of electric double layer is located, we make an analogy with fluid boundary layer. Recalling from fluid mechanics, based on 99% boundary layer thickness, we know that at a normal distance y from the wall in a flow over the flat plate with free stream flow velocity u_0 , $u(y) = 0.99 u_0$, then boundary layer thickness would be:

$$\delta_{Laminar} \approx \frac{4.91x}{\sqrt{Re_x}} \tag{A- 53}$$

Similarly, the electric double layer thickness could be defined as a vertical distance from wall up to where the potential decreases to 1% of its original value [126]. If we call $\chi_{0.99}$ the location at which the potential decreases to its 99% of its value at the wall. As it is shown in (A- 46), Dutta and Beskok

illustrated how electroosmotic potential is decaying as a function of χ , it would be a very very thin layer to reach 99% of potential value at the wall. So, that's why we show how the effect of this pretty thin electric double layer could be reflected in velocity boundary condition and is neglected in terms of body force term along the flow in microchannel. It is also good to mention that from $\sqrt{\alpha\beta} = \frac{w}{\lambda_D}$ and $\chi = \sqrt{\alpha\beta}y^*$ it is observed that for $\lambda_D \ll w$, when $\alpha \geq 1$, χ would be independent of β which is shown in Figure A- 7 for the pretty thin electric double layer.

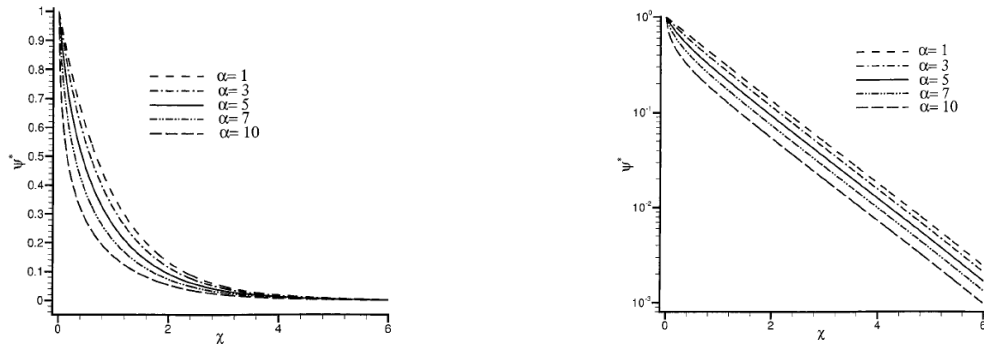


Figure A- 7: Electroosmotic potential distribution within EDL as a function of the inner-layer scale χ (left)in normal and (right) logarithmic scaling [125]

Having a better insight to different models applied to electric double layer as mentioned above, and the solutions to Poisson-Boltzmann equation, we found electric potential and net charge density distributions. Now, we are ready to end up with body force term which would be implemented in Navier-Stokes equation. In appendix B, it is shown that how this body force term could be reflected into slip velocity boundary conditions of bulk flow. Thus, we do not solve the Poisson-Boltzmann equation in the electric double layer, but the effect of the EDL is reflected as the slip velocity boundary conditions of the microchannel walls.

Electric Double Layer and Slip Boundary Condition

In this section we continue our discussion in flow field formulation. Electric double layer simplest description is the very thin layer of ions near a solid surface adjacent to an aqueous solution, which in a microchannel has a nanometer thickness. It is shown that, the velocity at the edge of EDL meets the bulk flow and it is known from Helmholtz-Smoluchowski equation, which is one of the most

common simplifications in electroosmotic flows. This velocity is reflected in boundary conditions for the bulk flow. As pointed out in assumption of very small $\frac{\lambda_D}{w}$ is a good assumption, therefore derived potentials and ions density are good solutions particularly for Dutta-Beskok and Debye-Hückel.

To get the velocity at the edge of EDL and bulk flow, we go back to Navier-Stokes equation shown in (12). Within EDL, the stream-wise momentum equation for a pure electroosmotic flow assumed to be steady-state (the system reaches steady-state instantaneously), fully developed, 1-D flow with no pressure gradient and very small Reynolds number (discussed in detail in Appendix B). So, Navier-Stokes equation (12) simplifies to:

$$\mu \frac{d^2 u}{dy^2} + \rho_e \vec{E}_x = 0 \quad (\text{A- 54})$$

From the Poisson's equation, ρ_e , electrical charge density $\rho_e = -\epsilon \nabla^2 \psi$, which due to a potential difference in a normal direction to the wall in EDL region would result in:

$$\rho_e = -\epsilon \frac{d^2 \psi}{dy^2} \quad (\text{A- 55})$$

Therefore, by plugging ρ_e into (12), we would have:

$$\mu \frac{d^2 u}{dy^2} + \epsilon \frac{d^2 \psi}{dy^2} \vec{E}_x = 0 \quad (\text{A- 56})$$

Taking the integral of $\mu \frac{d^2 u}{dy^2} + \epsilon \frac{d^2 \psi}{dy^2} \vec{E}_x = 0$, with respect to y , results in:

$$\frac{d u}{d y} = -\frac{\epsilon}{\mu} \frac{d \psi}{d y} \vec{E}_x + c_1 \quad (\text{A- 57})$$

And by integrating once more, we get:

$$u(y) = -\frac{\epsilon}{\mu} \psi(y) \vec{E}_x + c_1 y + c_2 \quad (\text{A- 58})$$

Which by applying following boundary conditions results in slip velocity at wall. We know that on the wall we have no-slip boundary equation and the potential is almost zeta potential, so:

$$y = 0: u = 0 \quad \& \quad \phi = \zeta \quad (\text{A- 59})$$

So, $c_2 = \epsilon \zeta / \mu \vec{E}_x$, and far from the wall $\frac{d u}{d y} \rightarrow 0$, $\frac{d \psi}{d y} \rightarrow 0$ for $y \rightarrow \infty$, which leads us to zero c_1 , so:

$$u_x|_{wall} = \vec{u}_{eo} = -\frac{\epsilon \zeta}{\mu} E_x \quad (\text{A- 60})$$

This shows us a plug like velocity profile outside electric double layer, or in other words in the region starting from edge of EDL towards bulk flow. Equation (A- 60) shows that fluid velocity at EDL edge is linearly proportional to external electric field. The proportionality coefficient is electroosmotic mobility as $\mu_{eo} = -\frac{\epsilon\zeta}{\mu}$, so in other words $\vec{u}_{eo} = \mu_{eo}\vec{E}$. Moreover, by solving $\mu \frac{d^2u}{dy^2} + \epsilon \frac{d^2\psi}{dy^2} \vec{E}_x = 0$ in EDL and considering Debye-Hückel approximation for potential distribution, $\phi(y) = \zeta e^{-y/\lambda_D}$, we apply velocity boundary conditions @ $y = 0$, $u = 0$ and $\frac{du}{dy} \rightarrow 0$ @ $y \rightarrow \infty$, therefore:

$$u(y) = \mu_{eo}\vec{E}_x(1 - e^{-y/\lambda_D}) \quad (\text{A- 61})$$

So, in the vicinity of wall, in very thin electric double layer, where we have charge density how electric potential and its second derivative is changing with y/λ_D . So, since the majority of flow in bulk region is not subject to body force term in pure electroosmotic flow the effect of EDL on the bulk flow is seen in slip boundary condition on the walls. This slip-wall velocity acts like a conveyer pushing the bulk flow forward and is used for non-dimensionalization of velocity.

In this appendix we mainly discussed the Poisson-Boltzmann equation, its derivation and the methods to solve it. This equation is one of the key governing equations in electrokinetic microfluidics and it has been applied in many references to find the distribution of electric potential. We presented a detailed derivation of this equation from statistical approach. First, we presented the fundamentals of probability for the distribution of ions, the Boltzmann distribution. The maximum number of microstates at each macrostate for a system with fixed number of particles and fixed energy is well explained. Lagrangian multipliers are implemented to find the most probable state with the maximum number of microstates, and through classical thermodynamics it is shown that this distribution is the Boltzmann distribution. Revisiting the classical physics, electric potential distribution and the derivation of Poisson's equation are addressed. Putting these two together, we show the derivation of the Poisson-Boltzmann equation at one place. Then, different approaches to solve this equation are addressed and simplifications and approximations for solving this equation are provided. Finally, it is shown why we reflect the effect of EDL as a slip boundary condition on the bulk flow.

Appendix B-Non-Dimensionalization of Problem and Numerical Model Formulation

In this appendix, the non-dimensionalization of the problem governing equations and boundary conditions, Chapter 3, is presented as preliminary preparation for performing computational and physical experiments. With the objective of designing an optimized sample-separation microchip, non-dimensionalization plays a key role in guiding this design and avoiding redundant efforts, whether they be computational or experimental. This chapter presents a comprehensive approach to the non-dimensionalization of the electric potential field, flow field, and concentration field, including both governing equations and boundary conditions. For the case of a cross-shaped microchannel used to control the sample shape in the vicinity of the injection site, we detail role of the applied voltages and other involved dimensionless parameters, such as Reynolds number, Peclet number, electrokinetic mobilities and velocities. The possible choices of reference values for length scale, electric potential, velocity, and concentration are studied in detail and, in particular, the use of a convective time scale is compared with that of a diffusive time scale. In the end, the wall electroosmotic velocity, the convective time scale, and the injection/separation channel width are adopted for non-dimensionalization of the problem. For a methodical study and to avoid studying redundant cases, either numerically or experimentally, knowledge of the governing dimensionless parameters is crucial. A numerical study allows one to vary the governing parameters individually such that each numerical simulation can be considered a ‘numerical experiment’. The governing dimensionless groups guide us to perform relevant studies and to draw meaningful conclusions. The net result is a savings of both time and cost by minimizing the number of studies required. In this chapter, the problem governing equations and boundary conditions are non-dimensionalized. The selection of alternative reference quantities is considered and the rationale for the final choices is presented. The result is a complete non-dimensional problem formulation (geometry, governing equations, and boundary conditions) for the cross-channel microchip configuration with a complete compilation of the governing dimensionless parameters.

Non-dimensionalization Procedure for Injection Phase

In order to non-dimensionalize our problem, both the equations and boundary conditions must be non-dimensionalized. The sets of equations and boundary conditions will be explored in this section to

determine the reference parameters. When choosing relevant scales to use in non-dimensionalizing the problem, the considerations include:

- The choices should make for a simpler mathematical problem to solve
- The choices should best reflect the governing characteristics of the problem

In the electrophoresis separation of a sample on a microchip, there are two phases: injection and separation. In this section, the non-dimensionalization of the injection phase will be explored.

Having an ideal rectangular shape for the injected sample at the cross-channel intersection, a higher resolution in the separation channel is expected. Length scales, time scales, reference velocity scales, and electric potential scales are examined in the non-dimensionalization of the equations and boundary conditions. There are some obvious choices for dimensional scales, but some choices are not so obvious. The latter will be considered, together with the consequences, and an assessment made of the appropriate choices that should be made. In the following section, the non-dimensionalization is presented for the geometry, potential equation, Navier-Stokes equations, concentration equations, as well as their boundary conditions. All for a two-dimensional cross-channel configuration.

Definition of Non-dimensional Parameters

In the cross-channel shown in Figure 22, there are three independent variables including coordinates x, y , and time, t , and 9 dependent variables: $\phi, u, v, P, u_{eo}^*, v_{eo}^*, u_{ep,i}, v_{ep,i}, c$. Of course, there will be one c for each 'i'. Non-dimensionalizing the variables, then, we have:

$$\begin{aligned}
 x^* &= \frac{x-x_r}{\Delta x_r} & \phi^* &= \frac{\phi-\phi_r}{\Delta\phi_r} & P^* &= \frac{P-P_a}{\Delta p_r} & u_{ep,i}^* &= \frac{u_{ep,i}-u_r}{\Delta u_r} \\
 y^* &= \frac{y-y_r}{\Delta y_r} & u^* &= \frac{u-u_r}{\Delta u_r} & u_{eo}^* &= \frac{u_{eo}-u_r}{\Delta u_r} & v_{ep,i}^* &= \frac{v_{ep,i}-v_r}{\Delta v_r} \\
 t^* &= \frac{t-t_r}{\Delta t_r} & v^* &= \frac{v-v_r}{\Delta v_r} & v_{eo}^* &= \frac{v_{eo}-v_r}{\Delta v_r} & c^* &= \frac{c-c_r}{\Delta c_r}
 \end{aligned} \tag{B- 1}$$

where ϕ^*, u^*, v^*, P^* are all dimensionless variables, being respectively the electric potential, velocity components in the x and y directions, and pressure. The non-dimensional components of electroosmotic and electrophoretic velocities are denoted by $u_{eo}^*, v_{eo}^*, u_{ep,i}^*, v_{ep,i}^*$, and c^* is the dimensionless concentration.

Geometric Boundaries based on a Length Scale l_r

In the absence of compelling arguments to the contrary, it seems reasonable to take the reference origins for x , y , u , v and t to be $x_r, y_r, u_r, v_r, t_r = 0$. Table B- 1 shows the geometric boundaries of the problem based on length scale l_r .

Table B- 1 : Geometric boundaries based on length scale l_r

| | | |
|------------|---|--|
| Reservoirs | $R_1 : x^* = -\frac{L_1}{l_r}, -\frac{W_h}{2l_r} \leq y^* \leq \frac{W_h}{2l_r};$ $R_3 : x^* = \frac{L_3}{l_r}, -\frac{W_h}{2l_r} \leq y^* \leq \frac{W_h}{2l_r};$ | $R_2 : -\frac{W_v}{2l_r} \leq x^* \leq \frac{W_v}{2l_r}, y^* = \frac{L_2}{l_r}$ $R_4 : -\frac{W_v}{2l_r} \leq x^* \leq \frac{W_v}{2l_r}, y^* = \frac{-L_4}{l_r}$ |
| Walls | $W_1 : -\frac{L_1}{l_r} \leq x^* \leq -\frac{W_v}{2l_r}, y^* = \pm \frac{W_h}{2l_r};$ $W_3 : +\frac{W_v}{2l_r} \leq x^* \leq \frac{L_3}{l_r}, y^* = \pm \frac{W_h}{2l_r};$ | $W_2 : x^* = \pm \frac{W_v}{2l_r}, \frac{W_h}{2l_r} \leq y^* \leq \frac{L_2}{l_r}$ $W_4 : x^* = \pm \frac{W_v}{2l_r}, -\frac{W_h}{2l_r} \leq y^* \leq \frac{-L_4}{l_r}$ |
| Channels | $Ch_1 : -\frac{L_1}{l_r} \leq x^* \leq -\frac{W_v}{2l_r}, -\frac{W_h}{2l_r} < y^* < \frac{W_h}{2l_r};$ $Ch_3 : +\frac{W_v}{2l_r} \leq x^* \leq \frac{L_3}{l_r}, -\frac{W_h}{2l_r} < y^* < \frac{W_h}{2l_r};$ | $Ch_2 : -\frac{W_v}{2l_r} \leq x^* \leq \frac{W_v}{2l_r}, \frac{W_h}{2l_r} < y^* < \frac{L_2}{l_r}$ $Ch_4 : -\frac{W_v}{2l_r} \leq x^* \leq \frac{W_v}{2l_r}, -\frac{W_h}{2l_r} < y^* < \frac{-L_4}{l_r}$ |
| Cross | $-\frac{W_v}{2l_r} \leq x^* \leq \frac{W_v}{2l_r}, -\frac{W_h}{2l_r} < y^* < \frac{W_h}{2l_r}$ | |

If $\Delta x_r = \Delta y_r = l_r$, the same scaling will be applied to both horizontal and vertical dimensions. With this choice, the ratio $\Delta x_r / \Delta y_r$ will not appear in the equations, as would otherwise be the case.

Non-Dimensionalization of Potential Equation and Boundary conditions

Non-dimensionalization of (11) with respect to the reference length scales $\Delta x_r = \Delta y_r = l_r$, and irrespective of the choice for $\Delta \phi_r$, results in $\frac{\Delta \phi_r}{\Delta x_r^2} \frac{\partial^2 \phi^*}{\partial x^{*2}} + \frac{\Delta \phi_r}{\Delta y_r^2} \frac{\partial^2 \phi^*}{\partial y^{*2}} = 0$, or

$$\frac{\partial^2 \phi^*}{\partial x^{*2}} + \frac{\partial^2 \phi^*}{\partial y^{*2}} = 0 \quad (\text{B- 2})$$

he non-dimensional boundary conditions applied to the electric field are $\phi_{R1}^* = \frac{\phi_{R1} - \phi_r}{\Delta\phi_r}$ and $\phi_{R3}^* = \frac{\phi_{R3} - \phi_r}{\Delta\phi_r}$. Dimensionless floating or specified voltages at R_2 and R_4 are defined as $\frac{\partial\phi_{R2}^*}{\partial y^*} = \frac{\partial\phi_{R4}^*}{\partial y^*} = 0$ and $\phi_{R2}^* = \frac{\phi_{R2} - \phi_r}{\Delta\phi_r}$, and $\phi_{R4}^* = \frac{\phi_{R4} - \phi_r}{\Delta\phi_r}$, respectively. The walls are insulated, so $\frac{\partial\phi^*}{\partial n}\Big|_{walls} = 0$.

Non-Dimensionalization of Flow Field Equations and Boundary conditions

Implementing the non-dimensional variables of (B- 1) for flow field equations, and by choosing $\Delta u_r = \Delta v_r = \Delta V_r$, one can rewrite the continuity equation (13) as

$$\frac{\Delta u_r}{\Delta x_r} \frac{\partial u^*}{\partial x^*} + \frac{\Delta u_r}{\Delta y_r} \frac{\partial v^*}{\partial y^*} = 0, \text{ or}$$

$$\frac{\partial u^*}{\partial x^*} + \frac{\partial v^*}{\partial y^*} = 0 \quad (\text{B- 3})$$

The momentum equations, (14), become the following non-dimensional form

$$\rho \left(\frac{\Delta V_r}{\Delta t_r} \frac{\partial u^*}{\partial t^*} + \frac{\Delta V_r^2}{l_r} u^* \frac{\partial u^*}{\partial x^*} + \frac{\Delta V_r^2}{l_r} v^* \frac{\partial u^*}{\partial y^*} \right) = - \frac{\Delta p_r}{l_r} \frac{\partial P^*}{\partial x^*} + \frac{\mu \Delta V_r}{l_r^2} \left(\frac{\partial^2 u^*}{\partial x^{*2}} + \frac{\partial^2 u^*}{\partial y^{*2}} \right),$$

$$\rho \left(\frac{\Delta V_r}{\Delta t_r} \frac{\partial v^*}{\partial t^*} + \frac{\Delta V_r^2}{l_r} u^* \frac{\partial v^*}{\partial x^*} + \frac{\Delta V_r^2}{l_r} v^* \frac{\partial v^*}{\partial y^*} \right) = - \frac{\Delta p_r}{l_r} \frac{\partial P^*}{\partial y^*} + \frac{\mu \Delta V_r}{l_r^2} \left(\frac{\partial^2 v^*}{\partial x^{*2}} + \frac{\partial^2 v^*}{\partial y^{*2}} \right) \quad (\text{B- 4})$$

Dividing equations (B- 4) by $\frac{\mu \Delta V_r}{l_r^2}$ provides a unit coefficient for the viscous term, and one obtains

$$\frac{\rho l_r^2}{\mu \Delta t_r} \frac{\partial u^*}{\partial t^*} + \frac{\rho l_r \Delta V_r}{\mu} \left(u^* \frac{\partial u^*}{\partial x^*} + v^* \frac{\partial u^*}{\partial y^*} \right) = - \frac{l_r \Delta p_r}{\mu \Delta V_r} \frac{\partial P^*}{\partial x^*} + \left(\frac{\partial^2 u^*}{\partial x^{*2}} + \frac{\partial^2 u^*}{\partial y^{*2}} \right),$$

$$\frac{\rho l_r^2}{\mu \Delta t_r} \frac{\partial v^*}{\partial t^*} + \frac{\rho l_r \Delta V_r}{\mu} \left(u^* \frac{\partial v^*}{\partial x^*} + v^* \frac{\partial v^*}{\partial y^*} \right) = - \frac{l_r \Delta p_r}{\mu \Delta V_r} \frac{\partial P^*}{\partial y^*} + \left(\frac{\partial^2 v^*}{\partial x^{*2}} + \frac{\partial^2 v^*}{\partial y^{*2}} \right) \quad (\text{B- 5})$$

Substituting $\frac{\rho \Delta V_r l_r}{\mu}$ as the Reynolds number results in

$$\frac{\rho l_r^2}{\mu \Delta t_r} \frac{\partial u^*}{\partial t^*} + Re \left(u^* \frac{\partial u^*}{\partial x^*} + v^* \frac{\partial u^*}{\partial y^*} \right) = - \frac{l_r \Delta p_r}{\mu \Delta V_r} \frac{\partial P^*}{\partial x^*} + \left(\frac{\partial^2 u^*}{\partial x^{*2}} + \frac{\partial^2 u^*}{\partial y^{*2}} \right),$$

$$\frac{\rho l_r^2}{\mu \Delta t_r} \frac{\partial v^*}{\partial t^*} + Re \left(u^* \frac{\partial v^*}{\partial x^*} + v^* \frac{\partial v^*}{\partial y^*} \right) = - \frac{l_r \Delta p_r}{\mu \Delta V_r} \frac{\partial P^*}{\partial y^*} + \left(\frac{\partial^2 v^*}{\partial x^{*2}} + \frac{\partial^2 v^*}{\partial y^{*2}} \right) \quad (\text{B- 6})$$

The non-dimensional boundary conditions applied to the flow field are $P^*|_{R_1-R_4} = 0$, $\frac{\partial u^*}{\partial x^*}\Big|_{R_1, R_3} =$

$\frac{\partial v^*}{\partial x^*}\Big|_{R_1, R_3} = 0$, and $\frac{\partial u^*}{\partial y^*}\Big|_{R_2, R_4} = \frac{\partial v^*}{\partial y^*}\Big|_{R_2, R_4} = 0$. The initial conditions are also taken as $u^*, v^*|_{initial} =$

0. The slip wall velocities for $u_{w1,3}^* = \frac{u_{w1,3} - u_r}{\Delta V_r}$. Substituting electroosmotic velocity $u_{w1,3} = \frac{\mu_{eo} \partial \phi}{\partial x}$ for

the wall slip boundaries, one will get $u_{w_{1,3}}^* = \frac{(\mu_{e0}\Delta\phi_r/\Delta x_r)\frac{\partial\phi^*}{\partial x^*} - u_r}{\Delta V_r}$ and $v_{w_{1,3}}^* = 0$. Similarly for W_2, W_4 ,

we have $u_{w_{2,4}}^* = 0$ and $v_{w_{2,4}}^* = \frac{(\mu_{e0}\Delta\phi_r/\Delta y_r)\frac{\partial\phi^*}{\partial y^*} - v_r}{\Delta V_r}$.

In the non-dimensional Navier-Stokes (N-S) equations (B- 5), the coefficient of the pressure term is equal to $\frac{l_r\Delta p_r}{\mu\Delta V_r}$. By choosing $\Delta p_r = \frac{\mu\Delta V_r}{l_r}$, the coefficient of the pressure term becomes one. As shown in equations (B- 5), this coefficient comes from scaling the viscous term to one, through dividing the N-S terms by $\frac{\mu\Delta V_r}{l_r^2}$. Considering (10) and (11), the choice for Δp_r is $\Delta p_r = \frac{\mu\Delta V_r}{l_r}$.

Non-Dimensionalization of Concentration Field Equations and Boundary Conditions

Non-dimensionalization of equation (16) for the concentration field yields:

$$\frac{\Delta c_r}{\Delta t_r} \frac{\partial c^*}{\partial t^*} + \frac{\Delta V_r \Delta c_r}{l_r} [(u^* + u_{ep,i}^*) \frac{\partial c_i^*}{\partial x^*} + (v^* + v_{ep,i}^*) \frac{\partial c_i^*}{\partial y^*}] = \frac{D_i}{l_r^2} \Delta c_r \left(\frac{\partial^2 c_i^*}{\partial x^{*2}} + \frac{\partial^2 c_i^*}{\partial y^{*2}} \right) \quad (\text{B- 7})$$

Dividing (B- 7) by $\frac{D_i}{l_r^2}$ and rewriting $\frac{\Delta V_r l_r}{D_i} = \frac{\Delta V_r l_r}{\nu} \frac{\nu}{D_i}$ which is $Re_r Sc_i$, or Peclet number, Pe_i , one obtains

$$\frac{l_r^2}{\Delta t_r D_i} \frac{\partial c^*}{\partial t^*} + Pe_i [(u^* + u_{ep,i}^*) \frac{\partial c_i^*}{\partial x^*} + (v^* + v_{ep,i}^*) \frac{\partial c_i^*}{\partial y^*}] = \left(\frac{\partial^2 c_i^*}{\partial x^{*2}} + \frac{\partial^2 c_i^*}{\partial y^{*2}} \right) \quad (\text{B- 8})$$

The boundary conditions applied to the concentration field at the reservoirs are $c_{i,R_1}^* = \frac{c_{i,R_1} - c_r}{\Delta c_r}$, $c_{i,R_2,R_4}^* = 0$, $\frac{\partial c_i^*}{\partial x^*} \Big|_{R_3} = 0$, and $\frac{\partial c_i^*}{\partial n^*} \Big|_{\text{walls}} = 0$ for impermeable walls. The initial condition is shown by $c_i^* \Big|_{\text{initial}} = 0$.

Problem Parameters

The contributing parameters in this problem are listed in Table B- 2, based on the presented non-dimensional equations and boundary conditions.

Table B- 2: List of parameters

| | |
|-------------------------------------|---|
| Parameters in the problem | $x_r, y_r, t_r, \phi_r, u_r, v_r, c_r, l_r(\Delta x_r, \Delta y_r)$ $\Delta\phi_r, \Delta p_r, \Delta t_r, \Delta V_r(\Delta u_r, \Delta v_r), \Delta c_r$ |
| Parameters with preliminary choices | $x_r, y_r, t_r, u_r, v_r, \Delta p_r$ |

In the following, the parameters for the geometry, potential field, flow field, and concentration field are explored.

Geometric parameters x_r, y_r

In order to do the non-dimensionalization of the geometric parameters, the reference parameters need to be determined. Taking the center of cross-linked channels as the origin, $x_r = y_r = 0$, there is a little impact of this arbitrary choice on our problem, thus we non-dimensionalize the geometric parameters as $x^* = \frac{x}{\Delta x_r}, y^* = \frac{y}{\Delta x_r}$.

Potential field parameters $\phi_r, \Delta\phi_r$

The non-dimensional potential $\phi^* = \frac{\phi - \phi_r}{\Delta\phi_r}$ holds at each reservoir, and the choices of $\phi_r = \phi_3$ and $\Delta\phi_r = \phi_1 - \phi_3$ simplify the boundary conditions and reflect the effect of applied potential as a key parameter in the injection phase, one that controls the sample progression along the channel. For the injection phase, voltages are primarily applied at reservoirs R_1 and R_3 . If R_3 is set to ϕ_3 , then by applying various potentials at R_1 , the non-dimensional ϕ_1^* and ϕ_3^* become one and zero, respectively. This choice dramatically reduces the number of combinations/permutations necessary to fully grasp the influence of applied potential on injection and separation.

Flow field parameters $t_r, u_r, v_r, \Delta V_r, \Delta P_r$

In this transient problem, the initial time is set to $t_r = 0$, meaning that the initial time is before any application of voltage. For the velocity reference, because the problem is non-linear, particularly in the coupling between the flow field and the concentration field, an absolute reference simplifies the equations and their coupling. Therefore, the reference velocities are assumed to be $u_r = v_r = 0$. Another possible choice for the reference velocity would be the electroosmotic wall velocities, but there

is no uniform average velocity at the walls, so the absolute zero velocity is assumed as the reference velocity. The fluid is driven by the electroosmotic velocity at the boundaries with the applied voltages and electric field acting as driving parameters. Only in the vicinity of the cross will the flow penetrate the separation channel through a balance of shear forces and induced pressure. The driving velocity along the channel is the electroosmotic velocity, thus, it is an obvious choice for the velocity scale based on the nominal applied electric field, i.e. $\Delta V_r = \mu_{eo} E_r = \mu_{eo} \frac{\Delta \phi_r}{L_1 + L_3}$. For a typical microchannel, the injection channel length is 8 – 10 mm, the difference in the applied potential at R_1 and R_3 100 – 300 V, and μ_{eo} is in the order of 10^{-8} . Thus, the velocity scale will be on the order of $\Delta V_r = \mu_{eo} E_r = \mu_{eo} \frac{\Delta \phi}{L_1 + L_3} = (10^{-8}) \frac{\text{m}^2}{\text{s}} \left(\frac{200 \text{ V}}{10^{-2}} \right) = 0.2 \frac{\text{mm}}{\text{s}}$ or thereabouts.

Concentration field parameters $c_r, \Delta c_r$

Initially, the channels and reservoirs, except for R_1 , are filled with the buffer solution, which has zero concentration, and the sample, injected at R_1 with c_{i,R_1} , flows and diffuses into the channel. As a consequence, the reference concentration is set at $c_r = 0$. As shown in Figure B- 1, for most of the problem, c_{i,R_1} is the concentration flowing and diffusing into the buffer in the channels.

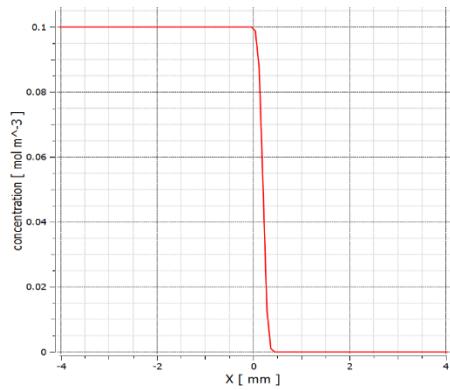


Figure B- 1: Sample concentration along the centerline of the injection channel (t=4.5s)

Taking $\Delta c_r = c_{i,R_1} - c_r = c_{i,R_1}$ simplifies the boundary conditions at R_1 to $c_{i,R_1}^* = 1$ and $c_{i,initial}^* = 0$. The parameters with obvious choices are listed Table B- 3. In this table, there are also two remaining parameters, Δt_r and l_r , with different choices and consequences.

Table B- 3: Parameters

| | | |
|-------------------------------------|--|--|
| Parameters with obvious choices | $x_r = 0, y_r = 0$ $\phi_r = \phi_3$ $u_r = 0, v_r = 0$ $c_r = 0$ | $\Delta p_r = \frac{\mu \Delta V_r}{l_r}$ $\Delta \phi_r = \phi_1 - \phi_3$ $\Delta V_r(\Delta u_r, \Delta v_r) = V_{eo}$ $\Delta c_r = c_{i,R1}$ |
| Parameters with non-obvious choices | $\Delta t_r, l_r(\Delta x_r, \Delta y_r)$ | |

Time scale Δt_r - Momentum consideration

The time scale Δt_r comes from the non-dimensional momentum and concentration equations. In this subsection, momentum consideration is explored, and in the next subsection, concentration consideration is explored. The non-dimensional momentum equation, using the choice for Δp_r , $\Delta p_r = \frac{\mu \Delta V_r}{l_r}$ is

$$Re \left(\frac{l_r}{\Delta V_r \Delta t_r} \frac{\partial \vec{u}^*}{\partial t^*} + \vec{u}^* \cdot \nabla^* \vec{u}^* \right) = - \frac{\Delta p_r l_r}{\mu \Delta V_r} \nabla^* P^* + \nabla^{*2} \vec{u}^* \quad (\text{B- 9})$$

On the left hand side of (B- 9), the Reynolds number $\frac{\rho l_r \Delta V_r}{\mu}$ appears as the coefficient of the inertia term. There are two possible choices for the reference time scale: (i) the diffusive time scale and (ii) the convective time scale.

Diffusive time scale: The coefficient of the transient term in N-S equation (B- 5) is $\frac{\rho l_r^2}{\mu \Delta t_r}$, which suggests a possible diffusive time scale of $\Delta t_{r,diff-v} = \frac{\rho l_r^2}{\mu} = \frac{l_r^2}{\nu}$. This renders the coefficient of the transient term unity and reflects the diffusion of momentum through shear forces. The coefficient of the inertia term is the Reynolds number, $Re = \frac{\rho l_r \Delta V_r}{\mu}$, and, by picking this diffusive time scale, the non-dimensional momentum equation becomes

$$\frac{\partial \vec{u}^*}{\partial t^*} + Re(\vec{u}^* \cdot \nabla^* \vec{u}^*) = - \frac{\Delta p_r l_r}{\mu \Delta V_r} \nabla^* P^* + \nabla^{*2} \vec{u}^* \quad (\text{B- 10})$$

Convective time scale: On the other hand, the coefficient of the transient term is $Re \frac{l_r}{\Delta V_r \Delta t_r}$. This suggests choosing a convective time scale, $\Delta t_{r,con.} = \frac{l_r}{\Delta V_r}$, which reflects the time scale for convective

transport of species . The dominant terms in the N-S equation and the subsequent choice of time scale are discussed in the following. For the fluid flow in the microchannel, which is flow with a balance between inertia, pressure, and viscous forces, with diffusion largely across the channel with length scale w_h , the Reynolds number is defined as $Re = \frac{w_h \Delta V_r}{\nu}$. The sample moves toward the cross and along the injection channel with the electroosmotic velocity scale $\Delta V_r = \mu_{eo} E_r = \mu_{eo} \frac{\Delta \phi_r}{L_1 + L_3}$ on the order of $0.2 \frac{\text{mm}}{\text{s}}$ and this leads to a Reynolds number on the order of $\mathcal{O}(10^{-2})$. For such a low Reynolds, the diffusive time scale of $\Delta t_{r,diff-v} = \frac{l_r^2}{\nu} = \frac{(50 \times 10^{-6})^2}{1 \times 10^{-6}} = 2.5 \text{ ms}$ is considerably smaller than that for the migration of the sample, for which the convective time scale is $\Delta t_{r,con.} = \frac{l_r}{\Delta V_r} = \frac{L_1 + L_3}{\Delta V_r} \cong \frac{10^{-2}}{0.2 \times 10^{-3}} \cong 50 \text{ s}$. Thus, by taking a convective time scale and $\Delta p_r = \frac{\mu \Delta V_r}{l_r}$, the left hand side of the momentum equation (B- 9) vanishes, which results in $-\nabla^* P^* + \nabla^{*2} \vec{u}^* = 0$. Consequently, (B- 9) reduces to a steady-state momentum equation with the pressure and viscous terms on the right hand side as the balance of pressure forces and shear forces. Depending on our choice of time scale, the non-dimensional momentum equation appears in different forms. Moreover, the choice of the length scale l_r not only affects our time scale, but also the non-dimensionalization of our geometric boundaries, governing equations, and boundary conditions for all three potential, flow and concentration fields. There are two choices for the geometric length scales: (i) the length of the injection channel in total $L_1 + L_3$ (or even part of it, L_1), (ii) the width of the separation channel $l_r = w_v$. As previously shown, the convective time scale is $\Delta t_{r,con.} = \frac{l_r}{\Delta V_r} \cong 50 \text{ s}$ when the sample moves from R_1 to R_3 . In contrast, a momentum diffusive time scale is $\Delta t_{r,diff-v} = \frac{l_r^2}{\nu} \cong 2.5 \text{ ms}$ through shear forces and this time scale is significantly smaller than the time that a sample is migrating along the channel. Consideration of the two choices, based solely on momentum considerations, suggests that the problem dynamics is such that the cross-channel diffusion (shear) establishes itself very quickly and that the problem is largely one of a quasi-steady balance between electroosmotic convection, diffusion, and induced pressure phenomena, and that the convective time scale is the preferable one to use. This situation is further examined below from the perspective of species transport.

Time Scale Δt_r - Concentration Consideration

The concentration equation in non-dimensional form is the following.

$$\frac{l_r^2}{\Delta t_r D_i} \frac{\partial c^*}{\partial t^*} + \frac{\Delta V_r l_r}{D_i} \vec{u}^* \cdot \nabla^* c^* = \nabla^{*2} c_i^* \quad (\text{B- 11})$$

Scaling the first term coefficient in (B- 11), $\frac{l_r^2}{\Delta t_r D_i}$, to unity we have the diffusive time scale; when $l_r = w_v$, then $\Delta t_{r,diff-D} = \frac{w_v^2}{D_i} = \frac{(50 \times 10^{-6})^2}{1 \times 10^{-10}} = 25$ s. The reason we use $l_r = w_v$, in the diffusive time scale, comes from the solution of the concentration solution for two semi-infinite bodies coming into contact Figure B- 2. The solution to a finite body is $c(x, t) = \frac{c_0}{2} \operatorname{erfc}\left(\frac{x}{2\sqrt{D_i t}}\right)$, where $\operatorname{erfc} = 1 - \operatorname{erf}$, and the interface concentration is maintained at $\frac{c_0}{2}$. This solution provides for diffusion of the sample and buffer solution on both sides of the interface. As illustrated in Figure B- 3, in the vicinity of the interface, the sample is dispersed into the vertical channel, but the main goal is to have a well-defined, distinct sample plug at the cross in preparation for the separation phase. Noting that $\operatorname{erfc}(0.5) = 0.48$, indicating significant diffusion has occurred, we then use $\frac{x}{2\sqrt{D_i t}} = 0.5$ as a guide. As noted above, the convection time scale for traversing the entire channel is 50 s, so the time for the sample to reach the cross is about 25 s. Using $t=25$ s, and $D_i = 10^{-10} \text{ m}^2/\text{s}$, the value of x corresponding to $\frac{x}{2\sqrt{D_i t}} = 0.5$ is $x = 50 \mu$, which is the same order as w_v . The solution to the concentration equation shows that at the interface, $x = 0$, there is half of the sample's initial concentration, $c(0, t) = \frac{c_0}{2}$, that is diluted on both sides with the buffer solution. From the above, w_v is an appropriate length scale to use in the diffusive time scale.

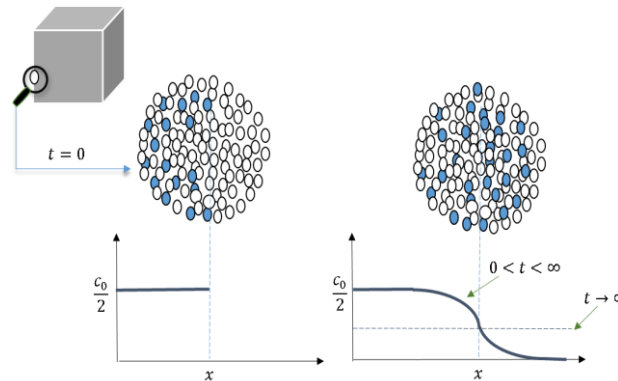


Figure B- 2: Illustration of the diffusion process and scales of diffusion (Gulliver 2007)

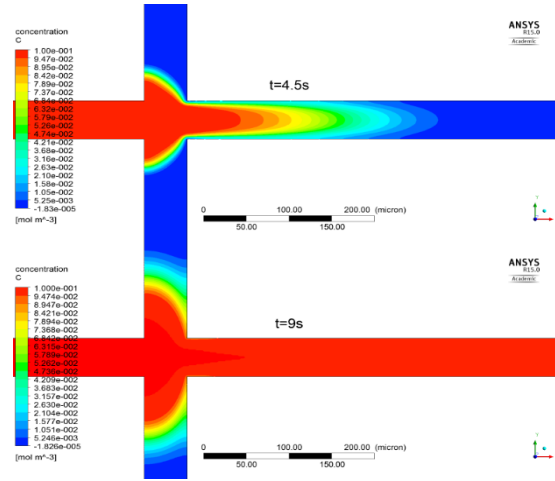


Figure B- 3: A sample concentration contour for a horizontal injection at t=4.5 and 9s

Similarly to the detailed description of time scale for the momentum equation, the coefficient of the second term in (B- 11) is the Peclet number, $Pe = \frac{\Delta V_r l_r}{D_i}$. Implementing a diffusive time scale of

$\Delta t_{r,diff-D} = \frac{w_b^2}{D_i}$, then results in

$$\frac{\partial c^*}{\partial t^*} + Pe(\vec{u}^* \cdot \nabla^* c^*) = \nabla^{*2} c_i^* \quad (B- 12)$$

Conversely, extracting the Pe number from the coefficient of the transient term, $\frac{l_r^2}{\Delta t_r D_i}$, we obtain

$\frac{l_r^2}{\Delta t_r D_i} = \frac{\Delta V_r l_r}{D_i} \frac{l_r}{\Delta V_r \Delta t_r} = Pe \frac{l_r}{\Delta V_r \Delta t_r}$. This again suggests a choice for the convective time scale of $\Delta t_r \cong$

50 s. The concentration equation then becomes

$$Pe \left(\frac{\partial c^*}{\partial t^*} + \vec{u}^* \cdot \nabla^* c^* \right) = \nabla^{*2} c_i^* \quad (B- 13)$$

A comparison of the diffusive and convective time scales through concentration and momentum equations reveals that the two time scales are of the same order. A simple calculation of the Pe number

will also result in $Pe = \frac{\Delta V_r l_r}{D_i} = \frac{(0.2 \times 10^{-3} \frac{m}{s}) 50 \times 10^{-6}}{10^{-10} \frac{m^2}{s}} = 100$, which is a significant number compared to

other coefficients scaled to one. Regardless of the choice of time scale, the Peclet number is a significant coefficient and the concentration equation will require the transient, inertia and diffusion terms. Since the net flux is independent of the time scale, the rate of concentration change is a net flux of the diffusion term and convection term multiplied by a significant Peclet number and can be written as $\frac{\partial c^*}{\partial t^*} =$

$\nabla^{*2}c_i^* - Pe(\vec{u}^* \cdot \nabla^*c^*)$. Using the convective time scale, the rate of concentration change becomes $\frac{\partial c^*}{\partial t^*} = \frac{1}{Pe}(\nabla^{*2}c_i^*) - \vec{u}^* \cdot \nabla^*c^*$, which reveals the insignificance of diffusion, by having a diffusion coefficient of $\frac{1}{Pe}$ compared to the convective term in changing the net concentration flux. The net effect of changing the time scale is to rate of passage of time.

Conclusion for Δt_r and Length scale: $l_r(\Delta x_r, \Delta y_r)$

As discussed above, both convective and diffusive time scales are of the same order. This means that during the migration of a sample along the injection channel over 25 s, it takes about 25 s for the sample to diffuse the width of the channel. In other words, for most cases, depending on the diffusivity and electroosmotic mobility of the sample, the convection happens fat about the same rate as diffusion and the convective time scale captures the dynamics of the sample transit during injection. Therefore, by choosing a convective time scale of $\Delta t_r = \frac{l_r}{\Delta V_r}$, the momentum and concentration equations will have the following final forms:

$$-\nabla^*P^* + \nabla^{*2}\vec{u}^* = 0 \quad (\text{B- 14})$$

$$\frac{\partial c_i^*}{\partial t^*} + \vec{u}^* \cdot \nabla^*c_i^* = \frac{1}{Pe} \nabla^{*2}c_i^* \quad (\text{B- 15})$$

As previously discussed at the end of length scale section, there are two options for length scale: the length of injection channel (or even first part of it before the cross), $L_1 + L_3$ (or L_1), or the width of the separation channel, w_p , (here both channels have the same width). Much of the literature takes the width of the microchannel as the reference length scale. Ren and Li, [127] also Erikson and Li [128] all took the width of the channel as the length scale in their non-dimensionalization of the problem. Yang et al. [129] took the height of the channels. Fu et al. [23] presented non-dimensional equations by taking the width of the microchannel as their reference length scale, and half of the channel width was considered for the length scale to non-dimensionalize the problem in research of Storey et al.[130]. The hydraulic diameter of the rectangular channel was taken as the length scale for a more convenient comparison of channels with different shapes [131], [132]. Table B- 4 shows a summary of the ranges for time scales and related parameters.

Table B- 4: Summary of Parameter Ranges

| $\Delta t_{r,diff-D} = \frac{l_r^2}{D_i}$ | $\Delta t_{r,con.} = \frac{l_r}{\Delta V_r}$ | $Re = \frac{\Delta V_r l_r}{\nu}$ | $Pe = \frac{\Delta V_r l_r}{D_i}$ |
|--|--|---|---|
| $l_r = 50 \times 10^{-6} \text{ m}$ | $l_r = 10^{-2} \text{ m}$ | $l_r: 50 \times 10^{-6} \text{ m}$ | $l_r = 50 \times 10^{-6} \text{ m}$ |
| $D_i = 10^{-10} \frac{\text{m}^2}{\text{s}}$ | $\Delta V_r = \mu_{eo} E_r = 10^{-8} \frac{\text{m}^2}{\text{V} \cdot \text{s}} * \frac{200 \text{ V}}{10^{-2} \text{ m}}$ $= 0.2 \frac{\text{mm}}{\text{s}}$ | $\Delta V_r = 0.2 \frac{\text{mm}}{\text{s}}$ | $\Delta V_r = 0.2 \frac{\text{mm}}{\text{s}}$ |
| | | $\nu: 1 \times 10^{-6} \frac{\text{m}^2}{\text{s}}$ | $D_i = 10^{-10} \frac{\text{m}^2}{\text{s}}$ |
| 25 s | 50 s | 0.01 | 100 |

In this study, regarding to the time scale conclusion and the choice of length scale, two cases including convective time scale, geometric length scale, and electroosmotic velocity scale are compared in the following.

$$1: \begin{cases} \Delta t_r = \frac{l_r}{\Delta V_r} & ; l_r = w_v \\ \Delta V_r = u_{eor} = \mu_{eo} E_r \end{cases} \quad 2: \begin{cases} \Delta t_r = \frac{l_r}{\Delta V_r} & ; l_r = L_1 + L_3 \\ \Delta V_r = u_{eor} = \mu_{eo} E_r \end{cases} \quad (\text{B- 16})$$

The complete set of non-dimensional equations is presented in (B- 17).

$$\begin{aligned} \frac{\partial^2 \phi^*}{\partial x^{*2}} + \frac{\partial^2 \phi^*}{\partial y^{*2}} &= 0 \\ \frac{\partial u^*}{\partial x^*} + \frac{\partial v^*}{\partial y^*} &= 0 \\ \frac{\partial^2 u^*}{\partial x^{*2}} + \frac{\partial^2 u^*}{\partial y^{*2}} &= \frac{\partial P^*}{\partial x^*} \\ \frac{\partial^2 v^*}{\partial x^{*2}} + \frac{\partial^2 v^*}{\partial y^{*2}} &= \frac{\partial P^*}{\partial y^*} \\ \frac{\partial c_i^*}{\partial t^*} + (u^* + u_{ep,i}^*) \frac{\partial c_i^*}{\partial x^*} + (v^* + v_{ep,i}^*) \frac{\partial c_i^*}{\partial y^*} &= \frac{1}{Pe_i} \left(\frac{\partial^2 c_i^*}{\partial x^{*2}} + \frac{\partial^2 c_i^*}{\partial y^{*2}} \right) \end{aligned} \quad (\text{B- 17})$$

Having $l_r = w_v$, leads to $Pe_i = Pe_{i,w_v} = \frac{\Delta V_r w_v}{D_i}$ that simplifies to $Pe_{i,w_v} = \frac{\mu_{eo} \Delta \Phi_r}{D_i} \frac{w_v}{L_1 + L_3}$.

Alternatively, taking the other length scale, $l_r = L_1 + L_3$, results in $Pe_i = Pe_{i,L_1+L_3} = \frac{\Delta V_r (L_1 + L_3)}{D_i}$

which simplifies to $Pe_{i,L_1+L_3} = \frac{\mu_{eo} \Delta \Phi_r}{D_i}$. Depending on the choice of l_r , the geometric parameters of Table B- 1 are divided by w_v or $L_1 + L_3$ and will take on differing values. Table B- 5 lists the non-

dimensional geometric parameters and shows that by picking the width of the separation channel as the length scale in the problem, we have one fewer geometric parameter since $w_v^* = 1$.

Table B- 5: Non-Dimensional Geometric Parameters

| | | |
|-------------------|---|---|
| $l_r = w_v$ | $L_1^* = \frac{L_1}{w_v}, L_2^* = \frac{L_2}{w_v}, L_3^* = \frac{L_3}{w_v}$ | $L_4^* = \frac{L_4}{w_v}, w_h^* = \frac{w_h}{w_v}, w_v^* = 1$ |
| $l_r = L_1 + L_3$ | $L_1^* = \frac{L_1}{L_1+L_3}, L_2^* = \frac{L_2}{L_1+L_3}, L_3^* = \frac{L_3}{L_1+L_3}$ | $L_4^* = \frac{L_4}{L_1+L_3}, w_h^* = \frac{w_h}{L_1+L_3}, w_v^* = \frac{w_v}{L_1+L_3}$ |

Furthermore, as shown in Table B- 6, the choice of length scale doesn't affect the electric potential parameters and two parameters of ϕ_{R2}^* and ϕ_{R4}^* are the controlling parameters in the injection phase. In separation phase ϕ_{R1}^* and ϕ_{R3}^* are the controlling parameters. (Figure B- 4)

Table B- 6: Non-Dimensional Potential Parameters

| | |
|-------------------|--|
| $l_r = w_v$ | $\phi_{R2,R4-inj}^*$ (For specified voltages instead of floating B.C.) |
| $l_r = L_1 + L_3$ | $\phi_{R2,R4-inj}^*$ (For specified voltages instead of floating B.C.) |

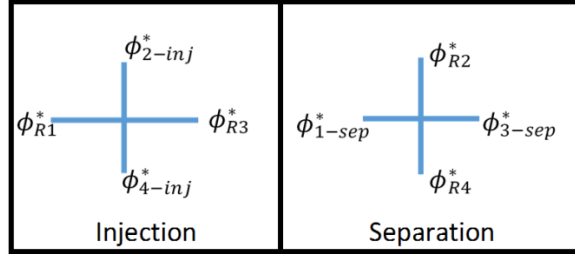


Figure B- 4: Controlling potentials at injection and separation

For the flow boundary conditions, the non-dimensional slip wall velocities in Table B- 7 include a geometric parameter for the case where $l_r = w_v$, whereas there is no geometric parameter for the case where the length scale is $l_r = L_1 + L_3$.

Table B- 7: Non-Dimensional Velocity Parameters

| | |
|-------------------|--|
| $l_r = w_v$ | $u_{w_{1,3}}^* = \frac{L_1+L_3}{w_v} \frac{\partial \phi^*}{\partial x^*}, v_{w_{2,4}}^* = \frac{L_1+L_3}{w_v} \frac{\partial \phi^*}{\partial y^*}$ |
| $l_r = L_1 + L_3$ | --- $(\frac{\partial \phi^*}{\partial x^*} \text{ and } \frac{\partial \phi^*}{\partial y^*})$ |

Finally, the contributing non-dimensional parameters in the concentration equation and boundary conditions are shown for both length scales in Table B- 8.

Table B- 8: Non-Dimensional Concentration Parameters

| | |
|-------------------|--|
| $l_r = w_v$ | $u_{ep,i}^* = -\mu_{ep,i}^* \frac{L_1+L_3}{w_v} \frac{\partial \phi^*}{\partial x^*}$, $\mu_{ep,i}^* = \frac{\mu_{ep,i}}{\mu_{eo}}$, $Pe_i = \frac{\mu_{eo} \Delta \phi_r}{D_i} \frac{w_v}{L_1+L_3}$ |
| $l_r = L_1 + L_3$ | $u_{ep,i}^* = -\mu_{ep,i}^* \frac{\partial \phi^*}{\partial x^*}$, $\mu_{ep,i}^* = \frac{\mu_{ep,i}}{\mu_{eo}}$, $Pe_i = \frac{\mu_{eo} \Delta \phi_r}{D_i}$ |

Both methods have the same number of parameters, 11. The first and second approach have 5 vs 6 geometric parameters and, 1 and 0 geometric parameters, in the velocity boundary conditions, respectively. Both methods have 2 potential parameters and 3 concentration parameters. The equal number of parameters is in accord with the Buckingham pi theorem. The first method, $l_r = w_v$, will be adopted here which mathematically has slightly easier geometric boundary specification.

Non-dimensionalization Conclusion

The current research presents a detailed examination of the non-dimensionalization of the governing equations and boundary conditions for the design of a microchip for sample injection and separation through electrophoresis. From the two phases of sample injection and separation, the governing equations and boundary conditions for the injection phase are specifically considered. The authors' focus is on the injection phase with the objective to develop as distinct, sharp, and clean a sample as possible. This objective is in concert with the desire to maximize species separation and resolution. The geometric boundaries as well as the equations and boundary conditions for the electric potential, fluid flow, and concentration fields are presented in detail. The advantage of the non-dimensionalization approach is to identify all governing parameters for the problem without making preliminary or arbitrary choices. Regarding the mathematics and the physics of the problem, some obvious choices are made. The difference in the applied potentials at the injection reservoirs is taken as the reference potential scale and the electroosmotic velocity is taken as the velocity scale. The options for a pressure scale are compared and that pressure reference was selected that places the non-dimensional momentum equations in a canonical form. In the momentum equations the emergence of the Reynolds number and associated typical values renders the inertial and transient terms of the equations inconsequential in relation to the viscous and pressure terms. The fluid flow problem is

essentially a quasi-steady flow of viscous shear balanced by induced pressure forces subject to the incompressibility constraint. Since the initial concentration of the injected sample is known, it is taken as the reference concentration scale and is measured against the buffer species concentration of zero. The Peclet number for species transport is of sufficient magnitude that the transient and advection terms of the species transport equations play a significant role. The complete transient species history must be computed starting from an initial non-dimensional species concentration of zero. The options for time scale and length scale in the problem are thoroughly discussed. It is shown through momentum and concentration considerations, both the convective and diffusive time scales are on the same order of magnitude and we choose the convective time scale to make the math of the problem somewhat cleaner. For the length scale option, two scales are considered: the width of the separation channel and the length of the injection channel, in its entirety. It is presented that with the former, there is one fewer geometric parameter while in the latter there is one fewer parameter in the velocity boundary conditions. With either choice, the number of parameters in the problem formulation is the same. This is consistent with the Buckingham pi theorem. The role of non-dimensionalization is to provide guidance in the study of microchip design whether the study be numerical or physical. Using the dimensionless parameters judiciously, the maximum information can be obtained from the least number of experiments, either numerical or physical. This, in turn, saves both time and cost of studies. In a similar way, the separation phase formulation is non-dimensionalized, but not presented to avoid repetition.

Numerical Simulation Tool and Solver

The results of numerical simulations presented in this research are based on using the ANSYS CFX software. This CFD tool is appropriate for microfluidics simulations and is based on the finite volume method (FVM). In a FVM model, the computational domain is divided in control volumes and conservation principles are applied to each control volume. This ensures conservation, both in each cell and globally in the domain, and is a great advantage of the FVM. Using unstructured grid is possible in FVM, although most of the microfluidic problems have simple geometries, computationally efficient enough with structured grid.

FVM Discretization

FVM model falls into two categories of center node based and vertex based models. All the governing equations are integrated over each control volume and then discretized to obtain one set of algebraic equations for each control volume/cell. In the center node based FVM approach, the value of each variable is stored in a node in the center of the cell. However, all the cell faces values are also available in discretized form. Interpolation methods are used to obtain approximate values at these positions with the impact of numerical stability, convergence rate and accuracy. For the vertex based model, which is used in ANSYS CFX, all the solution steps are performed for each vertex (cell corner) and the mesh vertices are used to store the variables. Since the control volume includes several mesh elements, discretization is done for each element and properties are distributed to the corresponding control volumes. Shape function approach is used for properties approximations.

Pressure-based Coupled Solver

In the discretized form of the governing equations the pressure and velocity is strongly coupled. Pressure distribution is required to solve these equations, and pressure gradients appear in the momentum equations. However, the momentum equations can be used to solve for the velocities if the pressure is known. Knowing that the continuity equation cannot be used directly to obtain the pressure field, the coupled pressure and velocity fields are should solved in CFD codes. Two main types of solvers exist for handling the pressure velocity coupling; segregated solvers and coupled solvers. A segregated solver makes use of a pressure correction equation. Firstly, the momentum equations are solved using a guessed pressure. If the resulting velocities do not satisfy the continuity equation a pressure correction equation is solved to update the pressure field. With the updated pressure, the velocity fields are also updated and this process is repeated until the obtained velocity fields satisfy both the momentum equations and the continuity equation. One of the most widely used pressure correction schemes is the SIMPLE (Semi Implicit Method for Pressure Linked Equations) scheme. Due to the fact that the equations are solved in a subsequent manner, only one discrete equation needs to be stored at a time which results in lower memory requirements. However, due to the iterative nature of the solution algorithm the convergence rate is often slower. In a coupled solver like ANSYS CFX, the momentum and continuity equations are solved simultaneously. As the discrete system of all equations needs to be stored at the same time the memory requirement is larger for a coupled solver and it takes

more time to complete one iteration loop. However, in return for taking more time for each iteration the total number of iterations to achieve convergence is usually lowered when using a coupled solver [133].

Geometry and Mesh

The first geometry and mesh are created in ANSYS Workbench. In this research we consider the problem two dimensional, assuming that no changes happens along the depth of the channel. Running a 2D simulation is not possible in CFX and the geometry is created in 3D form with the depth of $10\mu\text{m}$. Figure B-5 shows the first geometry of the studied microchannels. However, for the purpose of verification with experiments and also for a symmetric control of the sample, the injection and separation channels are switched. All the results in the next chapters are based on the sample injection vertically, from R_2 and performing the separation horizontally, in the channels between R_1 and R_3 .

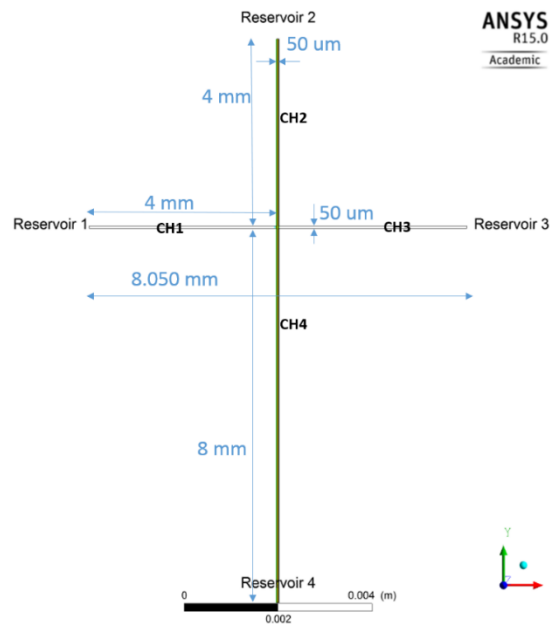


Figure B-5: Chip geometry (preliminary study)

Simulation Set-up and Temporal Analysis Type

After creating the geometry and generating the mesh, ANSYS CFX-pre is implemented for setting the simulation domain, boundary conditions, and the type of temporal analysis, the choice of solver, and

algorithms as well as output control parameters. Since the three sets of governing equations including the equations for the electric field, flow field and concentration fields are decoupled, the simulations for each case includes six files in total, consisting of the three electric, flow and concentration files for both injection and separation phases. The domain material consists of the sample and buffer solution, and all the physical properties are selected from the verification case discussed. As mentioned in the non-dimensionalization of the governing equations, electric and flow fields are steady state, but the concentration field must be solved in the non-steady form.

Boundary Conditions and Initial Conditions

Boundary conditions are presented in Figure B-6 and

Table B-9.

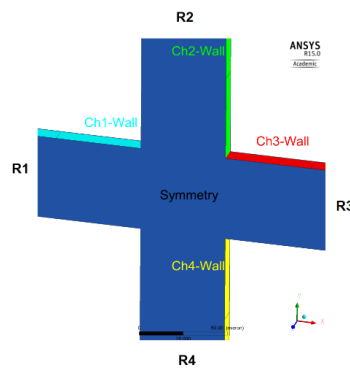


Figure B-6: Boundary conditions

Table B-9: Boundary Conditions

| name | location | Boundary type | comments |
|------------------|--|--|---|
| Ch_1 to Ch_4 | Walls of the injection and separation Channels | Walls with zero electrical flux (insulated), slip velocity, and zero concentration flux(impermeable) | slip velocity: electroosmotic velocity |
| R_1 to R_4 | Sample and buffer reservoirs | Opening open to atmospheric pressure, with flow direction normal to boundaries | Inlet/outlet which is defined by the applied electric field |
| Symmetry | Channels front and rear surfaces | Symmetry | |

Initial condition for the concentration equation is assumed the original sample concentration for the sample reservoir and zero for the buffer solution

Advection scheme: High resolution

The advection term requires the integration point values of a variable φ to be approximated in terms of the nodal values of φ [133]. The advection schemes implemented in ANSYS CFX [134] can be cast in the form:

$$\varphi_{ip} = \varphi_{up} + \beta \nabla \varphi \cdot \Delta \vec{r} \quad (\text{B- 18})$$

where φ_{ip} and φ_{up} are respectively the value at the integration and upwind points. \vec{r} is the vector from the upwind node to the ip. Particular choices for β and $\nabla\varphi$ yield different schemes as described below.

- 1st Order Upwind Differencing Scheme: A value of β yields a first order Upwind Difference Scheme (UDS). This scheme is very robust, but it will introduce diffusive discretization errors that tend to smear steep spatial gradients.
- Specified Blend Factor: By choosing a value for β between 0 and 1, and by setting $\nabla\varphi$ equal to the average of the adjacent nodal gradients, the discretization errors associated with the UDS are reduced. The quantity $\beta\nabla\varphi \cdot \Delta\vec{r}$, called the Numerical Advection Correction, may be viewed as an anti-diffusive correction applied to the upwind scheme. The choice $\beta = 1$ is formally second-order-accurate in space, and the resulting discretization will more accurately reproduce steep spatial gradients than first order UDS. However, it is unbounded, and may introduce dispersive discretization errors that tend to cause non-physical oscillations in regions of rapid solution variation.
- Central Difference Scheme: With the central difference scheme (CDS), β is set to 1 and $\nabla\varphi$ is set to the local element gradient. An alternative interpretation is that φ_{ip} is evaluated using the tri-linear shape functions $\varphi_{ip} = \sum_n N_n(S_{ip}, t_{ip}, u_{ip}) \varphi_n$. The resulting scheme is also second-order-accurate, and shares the unbounded and dispersive properties of the Specified Blend Factor scheme. An additional undesirable attribute is that CDS may suffer from serious decoupling issues. While use of this scheme is not generally recommended, it has proven both useful for LES-based turbulence models.
- Bounded Central Difference Scheme: The central differencing scheme described above is an ideal choice in view of its low numerical diffusion. However, it often leads to unphysical oscillations in the solution fields. In order to avoid these oscillations, the bounded central difference (BCD) scheme can be used as the advection scheme.
- High Resolution Scheme, which is used here, uses a special nonlinear recipe for β at each node, computed to be as close to 1 as possible without introducing new extrema. The advective flux is then evaluated using the values of β and $\nabla\varphi$ from the upwind node. The recipe for β is based on the boundedness principles used by Barth and Jespersen [135]. This methodology involves first computing a φ_{min} and φ_{max} at each node using a stencil involving adjacent nodes (including the node itself). Next, for each integration point around the node, equation (B- 18)

is solved for β to ensure that it does not undershoot φ_{min} or overshoot φ_{max} . The nodal value for β is taken to be the minimum value of all integration point values surrounding the node. The value of β is also not permitted to exceed 1. This algorithm can be shown to be Total Variation Diminishing (TVD) when applied to one-dimensional situations.

Convergence Criteria

Convergence criteria is set to RMS residual. At any stage of a calculation, each equation will not be satisfied exactly, and the “residual” of an equation identifies how much the left-hand-side of the equation differs from the right-hand-side at any point in space. If the solution is “exact,” then the residual is zero. This means that each of the relevant finite volume equations is satisfied precisely. However, because these equations only model the physics approximately, this does not mean that the solution exactly matches what happens in reality. If a solution is converging, residuals should decrease with successive time steps (ANSYS CFX USER’s Guide). The convergence behavior of many matrix inversion techniques can be greatly enhanced by the use of a technique called ‘multigrid’. The multigrid process involves carrying out early iterations on a fine mesh and later iterations on progressively coarser virtual ones. The results are then transferred back from the coarsest mesh to the original fine mesh. From a numerical standpoint, the Multigrid approach offers a significant advantage. For a given mesh size, iterative solvers are efficient only at reducing errors that have a wavelength of the order of the mesh spacing. So, while shorter wavelength errors disappear quite quickly, errors with longer wavelengths, of the order of the domain size, can take an extremely long time to disappear. The Multigrid Method bypasses this problem by using a series of coarse meshes such that longer wavelength errors appear as shorter wavelength errors relative to the mesh spacing. To prevent the need to mesh the geometry using a series of different mesh spacing, ANSYS CFX uses Algebraic Multigrid. Algebraic Multigrid [136] forms a system of discrete equations for a coarse mesh by summing the fine mesh equations. This results in virtual coarsening of the mesh spacing during the course of the iterations, and then re-refining the mesh to obtain an accurate solution. This technique

significantly improves the convergence rates. Algebraic Multigrid is less expensive than other multigrid methods because the discretization of the nonlinear equations is performed only once for the finest mesh. ANSYS CFX uses a particular implementation of Algebraic Multigrid called Additive Correction. This approach is ideally suited to the CFX-Solver implementation because, it takes advantage of the fact that the discrete equations are representative of the balance of conserved quantities over a control volume. The coarse mesh equations can be created by merging the original control volumes to create larger ones. The merged coarse control volume meshes to be regular, but in general their shape becomes very irregular. The coarse mesh equations thus impose conservation requirements over a larger volume and in so doing reduce the error components at longer wavelengths. [137]. A measure of how well the solution is converged can be obtained by plotting the residuals for each equation at the end of each time step. The RMS residual is obtained by taking all of the residuals throughout the domain, squaring them, taking the mean, and then taking the square root of the mean. This should present an idea of a typical magnitude of the residuals. For the flow and concentration fields targeting at $1e - 6$, whereas it is $1e - 14$ for the electric field [138].

